Volume 18, Number 6

June, 1965

SOVIET ATOMIC ENERGY

АТОМНАЯ ЭНЕРГИЯ

(ATOMNAYA ENERGIYA)

TRANSLATED FROM RUSSIAN

$\left(\dfrac{c}{b}\right)$ CONSULTANTS BUREAU

IMPORTANT NEW PHYSICS SERIES
FROM CONSULTANTS BUREAU

Place your standing order today for books in these series. It will ensure the delivery of new
volumes immediately upon publication; you will be billed later. This arrangement is solely
for your convenience and may be cancelled by you at any time.

REVIEWS OF PLASMA PHYSICS

Acad. M. A. Leontovich, Series editor

A systematic, multi-volume review of the present status of plasma theory, serving both as an introduction for students and for researchers entering the field, and as a convenient, authoritative, up-to-date presentation of current knowledge for workers in plasma physics. This continuing series, translated from Russian, is prepared by internationally known Soviet experts. Each volume contains a number of integrated tutorial reviews, covering in depth and in breadth specific aspects of theory. In many cases, new material is presented.

Volume 1

A comprehensive introduction to "classical" plasma physics, containing authoritative papers on: Motion of Charged Particles in Electromagnetic Fields in the Drift Approximation, by D. V. Sivukhin; Particle Interactions in a Fully Ionized Plasma, by B. A. Trubnikov; Transport Processes in a Plasma, by S. I. Braginskii; and Thermodynamics of a Plasma, by A. A. Vedenov. Much of the material in the first two papers is presented here for the first time. Although the theoretical analyses are quite advanced, the experimental aspects of the subject are kept firmly in view throughout.

326 pages   1965 $12.50

Volume 4

Contains three papers: Hydrodynamic Description of a Collisionless Plasma, by T. F. Volkov; Cooperative Phenomena and Shock Waves in Collisionless Plasmas, by R. Z. Sagdeev; and Coulomb Collisions in a Fully Ionized Plasma, by D. V. Sivukhin.

241 pages   1966 $12.50

Further volumes in this series will be published during 1966.

LEBEDEV PHYSICS SERIES

Acad. D. V. Skobel'tsyn, Series editor

Complete English translations of the Proceedings ("Trudy") of the famed Lebedev Physics Institute of the USSR Academy of Sciences published as Special Research Reports translated from Russian.

OPTICAL METHODS OF INVESTIGATING SOLID BODIES

"Trudy" Volume 25

Includes a major paper by N. D. Zhevandrov on polarized luminescence of crystals. The second paper, by the late V. P. Cheremisinov, reports a study of the vibrational spectra and structure of oxides; a final paper by L. A. Vainshtein concerns the calculation of cross-sections for excitation of atoms and ions by electron impact.

194 pages   1965 $22.50

COSMIC RAYS

"Trudy" Volume 26.

Contains an account of the experimental investigations into nuclear and electromagnetic interactions at high and ultra-high energies carried out in the last few years in the laboratories and research centers of the Lebedev Physics Institute.
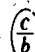
254 pages   1965 $27.50

RESEARCH IN MOLECULAR SPECTROSCOPY

"Trudy" Volume 27

Devoted to spectroscopic investigations into matter in various states of aggregation by the methods of Raman scattering and infrared absorption. A special section is devoted to the methodological problem of correcting measured quantities for instrumental errors.

206 pages   1965 $22.50

Further volumes in this series will be published approximately 6 months after their appearance in the original Russian.

(c/b) **CONSULTANTS BUREAU** 227 West 17th Street. New York. New York 10011

SOVIET ATOMIC ENERGY

A translation of **ATOMNAYA ÉNERGIYA**,

a publication of the Academy of Sciences of the USSR

Volume 18, Number 6   June, 1965

CONTENTS

CONTENTS (continued)

PHASE GROUPING OF A BEAM OF CHARGED PARTICLES
DURING CAPTURE INTO ACCELERATION IN THE OIYaI SYNCHROPHASOTRON*

(UDC 621.384.611)

G. S. Kazanskii, A. I. Mikhailov, N. B. Rubin, and A. P. Tsarenkov

The authors give a method for improving capture by means of preliminary imposition of a high-frequency accelerating field. The frequency of this field is varied according to the law of orbital deflection in "quasi-betatron" conditions. The accuracy and possible errors in the establishment of these conditions are estimated, and experimental results given.

It is known that a beam of particles injected into the chamber of a synchrophasotron has a certain angular and energy scatter.† This leads to the formation of a fairly complex structure in the proton beam in "quasi-betatron" conditions, causing some difficulty in effecting capture of the particles into synchrophasotron acceleration. It is known that 17% of the injected beam is captured from quasi-betatron into synchrophasotron conditions. This capture efficiency is determined [1] mainly by two factors:

1) particles with large amplitudes of radial betatron oscillation are unavoidably lost during capture and formation of a beam of accelerated particles in synchrophasotron conditions;

2) in synchrophasotron conditions, the particles are captured from part of the annular bunch, limited by the phase dimensions of the region of stability. For the OIYaI synchrophasotron, the latter extends about 200°.

In this paper we discuss a method for improving the efficiency of capture into synchrophasotron conditions by grouping the particles in the azimuthal direction [2]. This grouping is effected by bunching together that fraction of the particles which, in normal conditions, find themselves outside the stability region. If we create a stability region of which the phase width is 360°, and then displace it inwards along the radius and draw this region together to normal azimuthal dimensions, we can, in certain conditions, improve the efficiency of capture into synchrophasotron conditions. As far as we know, a similar program was studied for the Bevatron (USA).‡

Let us investigate the practicability of realizing this program. The equilibrium motion of the particles in accelerators of the "race-track" type is given by the following equations [3]:

$$
\left.
\begin{aligned}
\frac{dE_s}{dt} &= ec\beta_s \frac{V_0}{\Pi_s} \cos \varphi_s - \frac{2\pi}{\Pi_s \cdot c} \cdot \frac{\partial F_s}{\partial t}; \\
\frac{dE_s}{dt} &= \frac{E_s}{K_s} \left(-\frac{\dot{\omega}}{\omega} + \alpha_s \frac{\dot{B}_0}{B_0} \right); \\
\dot{\Pi}_s &= \alpha_s \Pi_s \left(\frac{\dot{E}_s}{E_s \beta^2} - \frac{\dot{B}_0}{B_0} \right), \\
z_s &= 0,
\end{aligned}
\right\}
\tag{1}
$$

---

* OIYaI = United Institute of Nuclear Research.
† For the OIYaI synchrophasotron, the energy scatter $\Delta W/W = 0.5\%$; the angular scatter $\alpha = \pm 5'$.
‡ The calculations of the Bevatron group were not made available to the present authors.

709
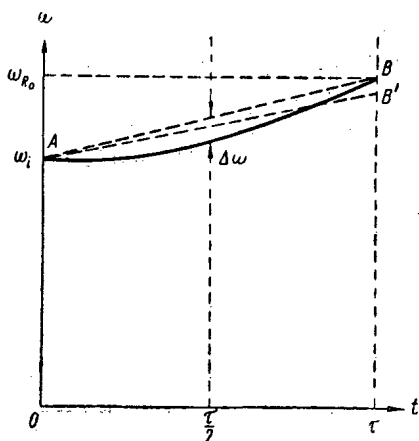
Fig. 1. Law of variation of frequency of accelerating potential in phase-grouping regime.
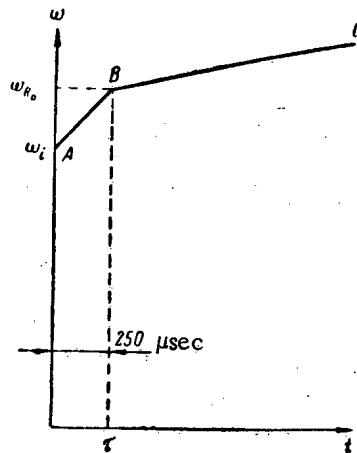
Fig. 2. Law of variation of frequency of accelerating potential during initial part of accelerating cycle with phase-grouping. AB) Law of frequency variation for phase-grouping conditions; BC) law of frequency variation for synchrophasotron conditions.

where E_s = equilibrium energy, B_0 = magnetic induction for z = 0 and some fixed radius in the electromagnet sectors, V_0 = amplitude of accelerating potential, φ_s = equilibrium phase, F_s = flux through area of orbit, c = velocity of light; $\beta_s = \dfrac{V}{C}$; $K_s = 1 + \dfrac{\alpha_s - 1}{\beta^2}$; $\alpha_s = \dfrac{1}{I(1-n)}$ (where n = index of fall in magnetic field, $I = 1 + \dfrac{4L}{2\pi r_s}$); $\Pi_s = 2\pi r_s + 4L$ = perimeter of equilibrium orbit (where r_s = equilibrium radius, L = length of straight-line section); ω = frequency of accelerating field.

We require that during capture the equilibrium energy shall not vary, i.e., we shall assume that $\dot{E}_s = 0$. We shall neglect the effect of the vortical electric field $\partial F_s/\partial t$.

From these conditions it follows that cos φ_s = 0 and $\varphi_s = \pi/2$. In this case the azimuthal dimension of the stability region is known to be 360°. Remembering this, from the 2nd equation in (1) we get the required law linking the frequency of the accelerating electric field with the changing magnetic induction during capture:

$$\frac{\dot{\omega}}{\omega} = \alpha_s \frac{\dot{B}_0}{B_0} .$$

Hence

$$\omega \approx \omega_i \left(\frac{B_0}{B_{0i}} \right)^{\alpha_s} = \omega_i \left(\frac{B_0}{B_{0i}} \right)^{\frac{1}{(1-n)\left(1+\frac{4L}{2\pi r_s}\right)}} , \qquad (2)$$

where i refers to the initial moment of time. From the 3rd equation in (1) we find the law of variation of r_s in the regime considered: $\dot{\Pi}_s = -\alpha_s \dfrac{\Pi_s \cdot \dot{B}_0}{B_0}$ or $\dfrac{\dot{r}_s}{r_s} = -\dfrac{\dot{B}_0}{B_0(1-n)}$, whence

$$r_s = r_{si} \left(\frac{B_0}{B_{0i}} \right)^{-1/1-n} . \qquad (3)$$

This equation represents the variation of the radius of the instantaneous orbit in normal quasi-betatron working.

Fig. 1 represents the law of variation of the electric field during capture (continuous curve). This law is of the form
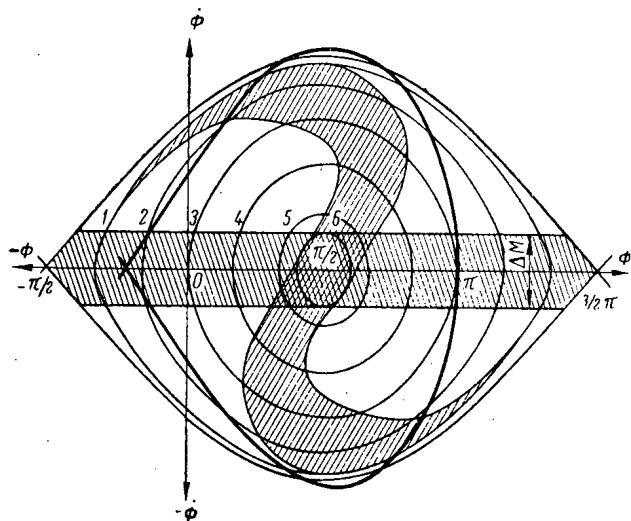
Fig. 3. Separatrix and phase trajectories of motion of particles during phase-grouping.
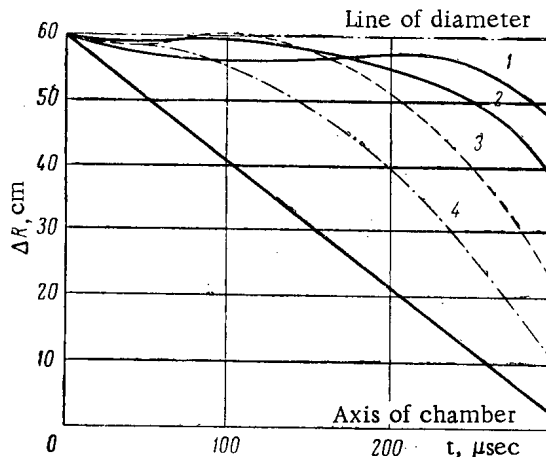
Fig. 4. Radial positions of particles with various initial conditions during phase-grouping. The straight line shows the radial compression of the particle orbits when the hf field is switched on.

$$\omega = \omega_i (1 + kt)^3, \tag{4}$$

so that $\dfrac{1}{(1-n)\left(1+\dfrac{4L}{2\pi r_s}\right)} \approx 3$ (see [2]) and $k = \dfrac{B_0}{B_{0i}}$.

For an interval of time equal to the duration of the phase-grouping regime τ, cubic parabola (4) was approximated by the straight line AB. With B_0 = 3600 gauss/sec and B_{0i} = 160 gauss, the maximum error due to the approximation, $\Delta\omega_{max}$, is $\dfrac{\Delta\omega_{max}}{\omega} = 5 \cdot 10^{-5}$ and corresponds to the time $t \approx \dfrac{\tau}{2}$. This error can be halved by approximating with the straight line AB'. The duration of phase-grouping, τ, is determined from the relation

$$\tau = (R_{inj} - R_0 - \Delta)\frac{(1-n)B_0}{R_0\dot{B}_0}, \tag{5}$$

where R_{inj} = radius of injector, R_0 = central radius, Δ = difference between radius of injector and radius of equilibrium orbit when the grouping electric field is switched on. At the initial moment it is convenient to take $\Delta \approx \dfrac{\Delta M}{2}$, where ΔM = radial dimension of region of instantaneous orbits corresponding to the energy spectrum of the injected beam, $\Delta W/W$.

The results of the calculation show that during phase-grouping the law of frequency variation can be taken as linear. For the OIYaI synchrophasotron, the rate of change of frequency during phase grouping is 14.3 Mc/sec, while the rate of change of frequency at the start of synchrophasotron conditions is 4.5 Mc/sec. At point B (Fig. 2), there must be a transition from one frequency law to the other. This imposes stringent requirements on the programmed frequency generator. Equally strict requirements are imposed on the amplitude of the hf potential which creates the hf electric field during phase grouping.

Let us examine in more detail the motion of particles in the separatrix during phase-grouping. In the general case, the first integral of the phase equation has the form

$$Q = \frac{\dot{\varphi}}{\omega_s \sqrt{\dfrac{eV_0 K_s}{\pi E_s}}} = \sqrt{(\sin\varphi - \varphi\cos\varphi_s) - (\sin\varphi_{init} - \varphi_{init}\cos\varphi_s) + Q^2_{init}} \tag{6}$$

711

Grouping field switched off at moment
when the particles are 10 cm from
injector

Capture of particles into syn-
chrotron conditions at central
radius R_0

50 μsec   *250 μsec*

t_0 t_1 t_2

Start of
injection

Switching in of frequency program-
mers and grouping-field amplitude
modulator

Switching in of accelerating field
modulator and switching out of fre-
quency programmer and grouping-
field amplitude modulator

Fig. 5. Sequence diagram of operations.

where Q_{init} and φ_{init} are the initial values of Q and φ, and φ and φ_s are the current and equilibrium phases.

Fig. 3 shows the separatrix for $V_0 = 10$ kV = const, and the phase trajectories of the moving particles during phase-grouping ($\varphi_s = \frac{\pi}{2}$). The same diagram shows the region of the instantaneous orbits ($\triangle M$) occupying a 20 cm radius at the moment of switching on the hf field. It is of interest to determine the particles distribution at the moment of their capture into synchrophasotron conditions. Using (6), we can find the positions of the particles in the phase region during a time interval τ such that

$$\int_{\varphi_{init}}^{\varphi_{fin}} \frac{d\varphi}{\sqrt{\sin \varphi - \sin \varphi_{init} + Q_{init}^2}} = \int_0^{\tau} \omega_s \sqrt{\frac{eV_0 K_s}{\pi E_s}} dt. \tag{7}$$

We can express the law of variation of eV_0 as a function of time and determine the value of φ_{fin} from (7), or alternatively, given φ_{fin} for the particles moving in a trajectory close to the separatrix, we can determine the value of eV_0. Figure 3 gives the position of the beam at time $t = \tau$ and $V_0 = 10$ kV = const. As seen from the diagram, up to the moment of capture into synchrophasotron conditions, the particles will mainly be grouped in the region of equilibrium phase, $\varphi_s = \pi/2$. Motion of particles is not observed in a narrow region near the separatrix. Particles distributed near the angular points of the separatrix ($-\frac{\pi}{2}, \frac{3\pi}{2}$), will evidently be slightly displaced, while particles with phases $-\frac{\pi}{2}$ and $\frac{3\pi}{2}$ will be the ideal case be stationary.

For the calculation, the initial conditions were chosen at the points designated by the numbers 1, 2, 3,. . ., $\varphi_{init} = +\frac{\triangle M}{2}$), and at the corresponding points with the same phases φ_{init} but with $\varphi_{init} = -\frac{\triangle M}{2}$.

The phase trajectories are the same for "similar" points differing only in the sign of φ_{init}. At the final moment ($t = \tau$), the particles from each pair give the limits of the position of the beam along its own trajectory. The number of particles captured into the acceleration regime is a maximum in the case when, at $t = \tau$, V_0 is instantaneously increased to 25 kV and the phase instantaneously changed by $\sim 30°$. (The position of the stability region for synchrophasotron working is shown on the same diagram by the thick line.) Figure 4 plots the time dependence of the radial positions of particles with different initial conditions. The curves are numbered to correspond with the initial conditions in Fig. 3. In the calculation, allowance was made for the time variation of the equilibrium orbits (3). As seen from the diagram, particles with certain initial conditions will, during phase-grouping, move in orbits near the injector. For this reason, the choice of amplitude for the hf field during grouping is very critical in its effect on the efficiency of capture into synchrophasotron conditions. On the one hand, it is necessary to choose V_0
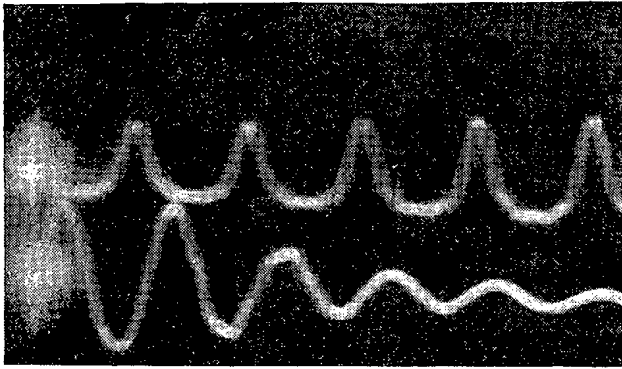
Fig. 6. Shape of grouped beam (upper curve) at time of switching out bunching field (lower curve).

large enough so that during phase-grouping the particles will succeed in distributing themselves near the equilibrium phase. On the other hand, excessive increase of V_0 will lead to increase in the region occupied by the grouped beam, and consequently to heavy losses of particles at the injector. Tuning of the phase-grouping setup thus reduces to the choice of $V_{0\ init}$ and the law of variation of V_0 during grouping.

To study phase-grouping, the electronics group of the LVE High-energy Laboratory of the OIYaI has developed a special apparatus including a frequency-modulated frequency generator with very rapid action in the modulation channel (delay 10 μsec) and elements effecting programmed control of the frequency and amplitude of the hf field during phase-grouping and transition to synchrophasotron working. The synchronization of the various elements of the apparatus is illustrated in Fig. 5.

The effect of phase grouping on capture of particles into synchrophasotron conditions was tested with acceleration time 30 msec. Capture with phase grouping was compared to capture without it. To eliminate a number of instabilities, a long series of statistical measurements was made. Account was taken of only those acceleration cycles for which the frequencies at the start of the grouping electric field and at the start of synchrophasotron working were maintained to within ± 0.1% of the optimum values. The optimum initial value and the law of variation of the hf potential amplitude during phase-grouping were chosen for maximum particle capture into synchrophasotron conditions.

The best results were obtained with a linear change of amplitude from $V_{0\ init} = 8$ kV to $V_{0\ init} = 12$ kV. At the end of phase-grouping, the amplitude V_0 was instantaneously increased to 20 kV (20 kV is the optimum amplitude for synchrophasotron acceleration conditions).

From this work, it was found that the use of phase grouping with the OIYaI synchrophasotron has enabled us to improve the capture of particles into synchrophasotron conditions by 30%. Figure 6 shows an oscillogram on which can be seen the grouped beam ($\Theta° \approx 270°$) at the moment of switching in the grouping electric field.

The following conclusions may be drawn:

1. An electric field excited in the accelerator chamber during particle injection creates an effect of phase-grouping, which leads to increased efficiency of capture into synchrophasotron conditions.

2. The efficiency of phase-grouping depends on the width of the energy spectrum and the angular scatter of the injected beam.

3. The conditions of phase grouping are relatively critical for tuning. For example, a frequency deviation of 0.3% from the set law practically cancels out the advantage gained.

4. In our opinion, the above results are promising for further work in this direction, and can be used in accelerators with long-duration and multiple injection.

The authors wish to thank A. B. Kuznetsov for helpful discussion and advice, and also their fellow-workers at the Radio Engineering Division of the High-Energy Laboratory of the OIYaI, G. A. Bokov, G. P. Puchkov, and S. N. Yurov, who helped in investigating the working conditions of the accelerator.

LITERATURE CITED

1. M. S. Rabinovich, Trudy FIAN SSSR, 10 (1958).
2. G. S. Kazanskii et al., Atomnaya Énergiya, 14, 153 (1963).
3. N. B. Rubin, Dissertation, OIYaI (1961).

IMPROVEMENTS IN THE CERN SYNCHROCYCLOTRON
OVER THE PAST THREE YEARS

(UDC 621.384.611.1)

P. Lapostol

European Nuclear Research Organization, Geneva
Translated from Atomnaya Énergiya, Vol. 18, No. 6,
pp. 559-565, June, 1965
Original article submitted June 26, 1964

Measures introduced to improve the intensity of the CERN synchrocyclotron 5 to 6 times are described.
The use of argon in the ion source gas, the use of a constant bias voltage across the central auxiliary
dee, modulation of the amplitude of the r-f voltage, the use of a vibrating target, and other features
are discussed. A program is presented for further experiments on the machine.

Over the past three years some improvement work has been done on the CERN synchrocyclotron. No substantial changes were made in the design of the machine proper, but the improvements do increase the synchrocyclotron intensity by a factor of 5 to 6 (Fig. 1), and the results of this work are of immediate interest, even if all the details are not definitively grasped. This report is needed right now since new and more fundamental improvements are being proposed for the immediate future.

Argon Added to the Ion-Source Gas

The ion source used for the CERN synchrocyclotron, a Penning type cold cathode source designed by R. Keller and L. Dick, operated on a hydrogen-helium mixture. News was received in 1961 that the intensity of the 150 MeV synchrocyclotron at Orsay (France) has been increased appreciably by the addition of trichloroethylene to the source plasma. Of course it would be undesirable to have C_2HCl_3 get into the chamber, from the standpoint of vacuum and chemical inertness, but this information still prompted the idea of using heavy inert gases, argon in particular. Since a gas mixture was already being used in the source, B. Hedin, who was in charge of this experiment, found no difficulty in replacing the helium with argon. The current maximum of the inner beam was obtained in an argon stream of $7 \cdot 10^{-3}$ torr · liter/sec (15 μg/sec), a hydrogen stream of $15 \cdot 10^{-3}$ torr · liter/sec (1.7 μg/sec), and in

Fig. 1. Increase in synchrocyclotron intensity: 1) internal beam intensity 0.3 μA; 2) argon impurity; 3) bias voltage across central dee; 4) magnetic field increased; 5) modulation of r-f voltage amplitude.

leakage of $14 \cdot 10^{-3}$ torr · liter/sec (22 μg/sec). Gas flowrate was determined by the pressure increment sensed by an ionization pressure gage whose readings were correlated for the specific gas [1]. Two pumps of 12,000 liters/sec each brought about a vacuum of $\approx 10^{-6}$ torr in the chamber.

Optimum extracted-beam currents were attained at a lower argon flowrate. This indicates that the argon enhances radial particle oscillations while suppressing vertical oscillations.

The physical processes responsible for the argon effect in enhancing beam intensity remain somewhat obscure. Nevertheless, argon did increase the average beam intensity from 0.3 to 0.55 μA, so that the source has been using argon since 1961. The volume of the gas stream is not very critical; the source operates with somewhat greater stability on argon than it did on helium.

714

Fig. 2. Center section of synchrocyclotron: 1) 4700 $\mu\mu$f capacitor, 7 kV; 2) dummy dee; 3) shielding; 4) 2250 V bias; 5) $\approx$2250 V bias across dee; 6) H_2 + A-mixture; 7) dee liner; 8) voltage supply cable; 9) ion source.

The Central Auxiliary Dee

Previous reports [2] described stochastic acceleration experiments conducted at CERN by R. Keller, L. Dick, and associates. At first, it had been proposed to achieve stochastic acceleration of protons with the aid of an auxiliary dee (cf. Fig. 2) to comparatively low energies, then to accumulate protons at that energy and later accelerate them to full energy by the usual method. Tentative investigations showed that the full intensity would be roughly doubled, but that the equipment would have to be so complicated as to be exorbitantly expensive to operate. But careful attention to the results showed that maintaining a strictly constant voltage across the stochastic dee could also have an effect.

We made an attempt to study the effect of constant bias across the auxiliary dee with appropriate high-frequency decoupling. These investigations were carried out by L. Dick. We found that when the voltage across the stochastic (auxiliary) dee was of the same sign and almost the same magnitude as the bias voltage across the main dee, the internal beam intensity increased by roughly 50% to near 0.8 μA. The auxiliary dee probably alters the vertical focusing of particles in the region free of magnetic focusing. This focusing improves orbit stability and accordingly improves beam acceptance. It is perfectly clear that there is no reason to consider the existing geometry the optimal one, and the research now underway on the Joint Institute for Nuclear Research synchrocyclotron (Dubna phasotron, USSR) showed that proper siting of the stochastic dee and selection of proper bias level are highly effective measures [3]. The results of that work emphasize the need for a systematic review of electrostatic focusing.

Auxiliary-dee experiments have shown the possibility of extra-fine control of circulating beam intensity by bias voltage. This method provides improved reproducibility superior to the usual beam defining method, and has less effect on beam quality. When the auxiliary dee bias voltage polarity is switched, the intensity varies by as much as 1/10 of the peak value. Auxiliary dee bias has been in use since 1961 on the CERN synchrocyclotron.

Modulating the R-F Voltage Amplitude

While stochastic acceleration investigations were in progress on the CERN synchrocyclotron, Lawson at Harwell (Britain) was studying various cyclotron type machines designed for beam stacking at the center [4]. Russell [5] advanced a definitive proposal for stepping up the beam intensity of the 275-cm Harwell synchrocyclotron. In this latest plan for increasing the accelerating field at the initiation of the acceleration cycle, when current limiting is almost achieved, r-f voltage opposed in phase to the voltage across the main dee is impressed across the auxiliary dee situated at the center of the machine.

The high-frequency system of the CERN synchrocyclotron has been described in an earlier report [6]. As we see in Fig. 3, the accelerating voltage amplitude ranges from 5 kV at the beginning of the cycle to 25 kV at the end.

f, Mcps
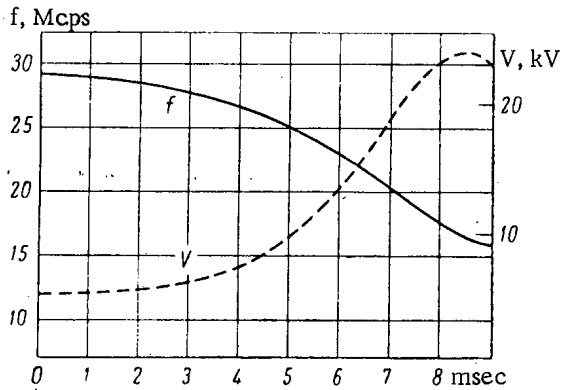
Fig. 3. Variation in frequency and amplitude of dee voltage during normal acceleration cycle with un-modulated r-f voltage amplitude.

This change is brought about by the properties of the tuning-fork modulated system. At first there were many gaps responsible for particle losses in the r-f voltage envelope, on account of resonances in the decoupling capacitors. New capacitors were designed, and have proven their worth in service. A third type of capacitor is now being introduced, designed for service at a still higher accelerating voltage. But at frequencies where the equilibrium phase is small, the beam load depresses the r-f voltage. A general rise in r-f voltage is out of the question because of sparking and damage in the feedback loop. The decision was therefore, to devise a modulator for the plate voltage of the oscillator tubes capable of varying the amplitude of the accelerating voltage as programmed.

In mid-1962, B. Hedin and H. Beger set up experiments to throw some light on a possible intensity increase. The r-f oscillator was switched on soon after initiation of the cycle, when a considerably higher voltage could be impressed across the dee than in normal operation. They found that not only the initial voltage but the initial rate of frequency change as well are essential parameters. The initial rate of frequency change may be selected by varying the amplitude of the tuning fork oscillations, or more simply by an equivalent variation of the magnetic field. The results plotted in Fig. 4 show the dependence of the beam current measured by a thermocouple placed at a radius of 110 cm (200 MeV) on the rate of frequency change at the onset of the cycle. Similar research on the Dubna phaso-tron was reported at the Dubna 1963 International Conference on Charged Particle Accelerators. A rotary capacitor aided in achieving results superior to the tuning fork arrangement.

We see from Fig. 4 that the intensity is maximized at some average accelerating voltage. But a voltage decrease over the entire cycle results in particle losses at the end of the acceleration, as mentioned earlier, and the optimum voltage amplitude at the cycle termination does not correspond under the existing law to the optimum in the capture mode. It was found, thus, that the amplitude modulator must decrease the voltage amplitude at the beginning of the cycle and maintain it at the maximum possible level at the end of the cycle. The first modulator tests were run in late 1962 by H. Beger and A. DeGroot. Beam intensity was stepped up almost 40% (see Fig. 5) when the anode voltage was varied linearly. Other forms of modulation might yield a slightly better increase.

The modulator was in continuous operation all during 1963. By having an amplitude modulator, we achieved an effect similar to the one reported by Lawson and Russell at Harwell: in response to a pulsed increase in the amplitude of the r-f voltage placed across the main dee during ignition of the ion source, the accelerating voltage was raised at the beginning of the cycle. But we observed no increased beam intensity. This finding is accounted for by the relative low optimum initial voltage.

Increase in Magnetic Field

It has already been noted that particles can be lost through insufficient voltage during the acceleration cycle. Furthermore, there exists in practice a point at which particles become lost through excitation of the transverse mode of oscillation. But a fraction of the particles will be lost on account of the meager vertical focusing. The number of target traversals in work with an internal target and the beam extraction efficiency depend largely on vertical focusing, which is directly proportional to the field index n or to the radial gradient of the field.

As the current flowing through the synchrocyclotron magnet is increased beyond the pre-1962 value of 1700 A, saturation effects cause the field to increase faster on the axis than at the fringes, so that n is increased.

Exact field measurements were carried out in mid-1962 by E. Braunersreuter and M. Van Goelick. Figure 6 shows the variation in field index n as a function of radius at various points. We might expect an increased yield of secondary particles, as well as increased intensity of accelerated protons in the transition to higher magnetic field values, on the basis of the results. This requires expansion of the r-f oscillator bandwidth, since the axial field increases at a faster rate than the peripheral field, and the initial frequency increases at a faster rate than the terminal frequency. These modifications and investigations of the machine were performed by H. Beger during 1962.

716
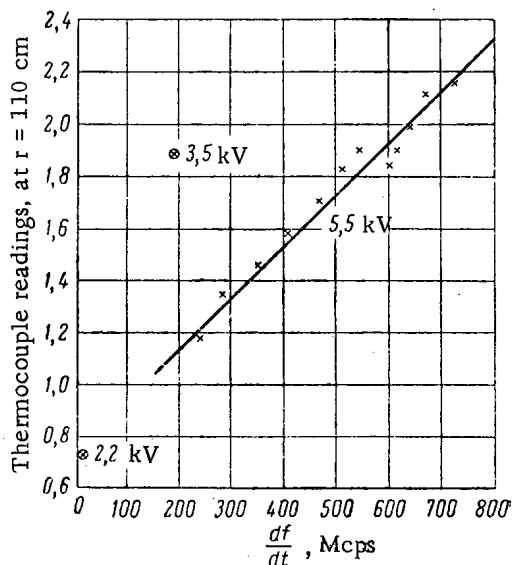
Fig. 4. Dependence of internal beam intensity on rate of frequency change at initial frequency.
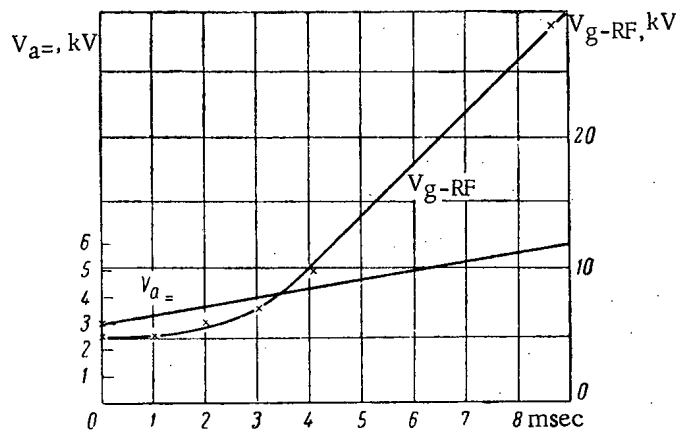
Fig. 5. Variation in plate voltage of oscillator and in amplitude of r-f voltage across dee when modulation is introduced.

Figure 7 clearly shows that the readings of the thermocouple placed at 210 cm radially are almost 50% higher, and that the π-meson intensity is stepped up by more than 60%.

Decreased intensity at higher current values is due to a fall-off in the current of the internal proton beam in the central section of the machine (probably brought on by changes in the distortions of the magnetic field in that section of the machine). The machine has been operated at higher magnetic fields since the end of 1962 in this way.

Vibrating Target

Ability to vary the time distribution of particles is of utmost importance in physical experiments. In normal synchrocyclotron operation, protons are accelerated in bunches of 200 μsec duration interspaced by 18 msec gaps, whereas most experiments profit from a continuous yield. The vibrating target is one of the devices intended to improve the time distribution of secondary particles released from an internal target. It was first installed on the synchrocyclotron of Columbia University, and has been described by J. Rosen [7].

The idea behind this method is that the accelerating voltage is switched off after the particles have been accelerated to a predetermined energy, and the target is gradually introduced into the freely circulating beam. If the target is vibrated at the pulse repetition rate (54 cps in our case), the beam will be displaced much more slowly relative to the beam than when a beam is accelerated to a fixed target. Detailed descriptions of this modification have been reported by B. Hedin who designed the target for the CERN synchrocyclotron [8].

Secondary particles have been obtained with the aid of this target, with a duty cycle from 4 to 2. When the target is properly positioned, the particle intensity in a long-duration pulse will be 90% of the intensity in a short pulse. If the frequency of the accelerating voltage is varied such that the acceleration terminates at the radius of the vibrating target but not in every cycle, the beam may then be divided between two internal targets. A further improvement suggested by S. Rabbi is the "jumping target" which is advanced into the beam over a time much shorter than the bunch width. This target is convenient for bubble-chamber experiments in parallel with other experiments. In combination with the stochastic extraction system described below, the jumping target arrangement is being used intensively to separate the beam between various experimental facilities employing counters.

Acceleration by means of a "Stochastic" Electrode

Another approach to improving the synchrocyclotron duty cycle has been put forth by R. Keller [2] and tried out on the Orsay synchrocyclotron [9] in line with suggestions by R. Keller and L. Dick. The accelerating voltage was turned off until the particles had acquired their peak energy, and then the beam was slowly accelerated by an auxiliary stochastic electrode excited according to a special program.

717
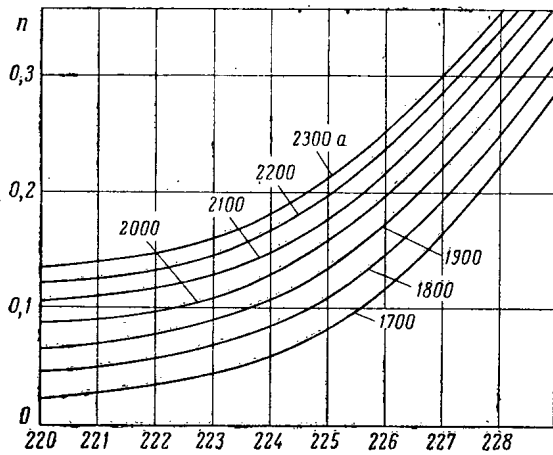
Fig. 6. Dependence of magnetic field index of syn-chrocyclotron on radius at various points on magnet.
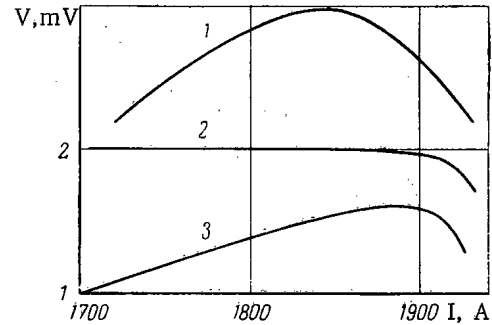
Fig. 7. Effect of magnet current on intensity of proton beam and π-meson beam: 1) thermocouple at r = 210 cm; 2) thermocouple at r = 110 cm; 3) π-meson count rate.

This device was designed and tested at CERN in 1961 by L. Dick, Y. Dupuis, and J. Vermeulen. A horseshoe electrode was placed between radii 205 cm and 230 cm, a voltage of amplitude 2.5 kV and frequency varied in saw-tooth pattern from 17.3 to 16.8 Mcps 500 times a second was placed across the electrode. The frequency program was not locked in phase with the basic program,* so that some of the protons slowed down and were lose. About 50% efficiency was achieved, but the duty cycle can be rendered slightly lower than two. The basic accelerating voltage must be shut off very quickly, otherwise an intense particle burst will hit the target. A timing device cur-rently in use prevents any rapid switch-over from internal target operation to extracted beam operation. Stationary equipment was installed in 1964.

Summary and Plans for the Future

Four sections of this article have described measures directed to obtaining increased intensity. What will be the next steps?

Parasitic Resonance at the Dee. As mentioned earlier, some portion of the beam becomes lost near r = 2 meters even before the coupling resonance at n = 0.2. These losses are due to the transverse mode of oscillations at the dee, excited by the second beam harmonic. The amplitude of voltage in this mode depends on beam intensity and tends to limit the beam intensity.

The proposal is to construct a new dee to prevent beam losses. Work on this was begun in 1964.

Central Section. High-energy operation of the synchrocyclotron depends on the conditions prevailing in the vicinity of the ion source. This holds not only for beam intensity, but beam quality as well, and is reflected in the successful extraction of both primary and secondary beams. It is now evident that the beam intensity of the CERN synchrocyclotron is acceptance-limited, and further that the source yields inordinately large radial betatron oscilla-tions. The mechanism underlying this limitation is still obscure, and we decided to initiate a careful study of this portion of the machine. Since the synchrocyclotron is run on an experimental program, its parts have a high level of radioactivity and control of the parameters of interest to us is of limited extent. The investigations will be con-ducted on a specially built model cyclotron. This model is now being fabricated, and experiments are scheduled to be underway in late 1964. The electromagnet in the model weighs 30 tons, pole diameter is 840 mm, pole gap 200 mm; the electromagnet will establish a field of 18 kG at 800 kVA. The r-f system has separate amplitude and frequency modulators. The terminal grounded-grid amplifier, 40 kW output and 26−28 Mcps bandwidth, will place a voltage of up to 7 kV amplitude across the dee.

* The system with auxiliary slow frequency program synchronized to the basic program was first developed at Berkeley by C. Crow; similar systems are now in use everywhere [10].

Activation. At the intensity now achieved ($1.6\,\mu$A) in the CERN synchrocyclotron, after the machine is shut off the radioactivity level inside the synchrocyclotron and near it will be extremely high [11]. The problem of activation, which seriously obstructs work on high-intensity machines, is now being studied at CERN by M. Barbier. Far-reaching sophistication making generous use of remote-control instrumentation will be required to ensure radiation safety in high-intensity work.

Beam Extraction. At present, the intensity of a beam of π-mesons obtained from internal and external targets is about the same. Increased beam efficiency would increase the yield of π-mesons from an external target without aggravating activation of the machine. There is some hope of achieving such extraction efficiency, which would appreciably cut down the fraction of particles lost inside the machine.

This problem calls for an over-all study of the central region capable of not only bringing about an increase in the number of particles accelerated, but also of improving beam quality and thereby rendering beam extraction easier.

A new beam extraction system is now being developed and will be tried out soon.

Secondary Beam Optics. Preliminary measurements have shown it be possible to effect an appreciable increase in the intensity of a beam of π-mesons by increasing the hole diameters in the shielding wall from 14 to 20 – 25 cm. But more measurements have to be made before work on this modification is ventured.

We are now reviewing the results of computer beam transport experiments with a view to improvements in focusing equipment [12].

Source of Polarized Protons. In conclusion, we must draw attention to a polarized proton source suggested by R. Keller, L. Dick, and M. Fidecaro which is now nearing completion. But installation of this instrument on the synchrocyclotron has been put off for some time.

The work described is the fruit of work by the entire synchrocyclotron section of CERN. Even though the text mentions only the names of those who bear the primary responsibility, our results have become possible thanks to the efforts of those physicists, engineers, and technicians who made their contributions.

LITERATURE CITED

1. Dushman, The Scientific Foundations of Vacuum Technique. New York (1949), p. 350.
2. R. Keller and K. Schmitter, Beam storage with stochastic acceleration and improvement of a synchrocyclotron beam. CERN 58 –13. R. Keller, L. Dick, and M. Fidecaro, Acceleration Stochastique dans un cyclotron de 5 Mev. Compt. rend. Acad. sci. Paris, 248, 3154 (1959); R. Keller, Experiments on stochastic acceleration. Intern. Conf. on High-Energy Accelerators, CERN (1959), p. 187; R. Keller, L. Dick, and M. Fidecaro, Les essais d'acceleration stochastique dans le synchrocyclotron de 600 MeV et leur interpretation. CERN 60 –43.
3. V. Danilov, et al., Proc. International Accelerator Conf. Dubna, Aug. 21-27, 1963. Moscow. Atom press [in Russian] (1964), p. 591.
4. J. Lawson, On the possibility of increasing the output of a synchro-cyclotron by means of a central high voltage Dee. AERE Report M 542 (1959).
5. F. Russell, Nature, 190, No. 4773, 335 (1961).
6. K. Schmitter and S. Kortleven, Rev. Techn. Philips, 22, No. 5, 165 (1961).
7. J. Rosen, Vibrating target for the improvement of synchro-cyclotron duty cycle. NEVIS –92 (1960).
8. B. Hedin, Longer Pulse length by a vibrating target in the CERN synchro-cyclotron. CERN 61 –21.
9. A. Cabrespine et al., J. phys. et radium, 21, 332 (1960).
10. E. Molthen, Peripheral Cee Beam Extractor for the Chicago 460 MeV synchro-cyclotron. EFINS 63 –50.
11. J. Blaser, Ch. Perret, M. Barbier, and J. Dutrannois, Shielding and activation of high-intensity cyclotrons. Intern. Conf. on Sector Focused Cyclotrons and Meson Factories, CERN 63 –19, April, 1963, p. 157; M. Barbier, Induced radioactivity in accelerators. Intern. Conf. on Accelerators for charged particles, Dubna (1963).
12. SCOPT –An IBM 7090 Code for Beam Optics Problems on the Synchro-cyclotron. CERN 64 –15, March (1964).
13. R. Keller, L. Dick, and M. Fidecaro, Une source de portons polarises. État actuel de la construction. CERN 60 –2; L. Dick, Ph. Lévy, and J. Vermeulen, Characteristics of the CERN polarized proton source. Intern. Conf. on Sector Focused Cyclotrons and Meson Factories. CERN 63 –19, April (1963), p. 127.

REDUCTION OF γ -RAY BACKGROUND FROM INDUCED ACTIVITY AT THE CERN PROTON SYNCHROTRON BY USING LOW ACTIVITY ABSORBERS

M. Barbier

CERN
Translated from Atomnaya Énergiya, Vol. 18, No. 6,
pp. 565-573, June, 1965
Original article submitted July 15, 1964

To reduce activation of the proton synchrotron pole tips and to reduce the γ -ray background from activated components, the use of marble to line the pole tips is proposed. It has been shown that marble, which is a rather good absorber, is but slightly activated. With the recommended arrangement of marble slabs in the interpolar space of the proton synchrotron, it is expected that the background intensity will be reduced by a factor of three within the chamber and by an order of magnitude in the neighborhood of the chamber.

Level of γ -Ray Background from Induced Activity at the CERN Proton Synchrotron After Machine Shutdown

In the present state of the CERN proton synchrotron, the rather frequent performance of work connected with operation, repair, and various alterations, both in the immediate vicinity of the proton synchrotron chamber and within it, is unavoidable.

To the group of operations within the chamber belong all alterations of the ion source and of the small dee system, the shifting of targets in accordance with the requirements of physicists and the precise measurement of target locations, the installation and adjustment of flip targets, the maintenance of thermocouples and of the springs on vibrating targets, the replacement of oil in the vacuum system, etc. It is necessary to carry out a large number of operations in the immediate vicinity of the chamber; among them are: leak detection (once every two weeks), routine maintenance of the rf system, installing and shifting units of the beam transport system.

The γ -ray background level several hours after shutdown of the proton synchrotron is 0.5 rem/hr near the chamber and 5 rem/hr inside it, and 18 days after machine shutdown, it is 1-2 rem/hr. At the present time, the maximum permissible dose for personnel exposed to radiation is 5 rem/yr and 3 rem per quarter, there being an additional rule at CERN which limits any single dose to 0.5 rem. Naturally, under these conditions, it is extremely difficult to carry out various operations on the proton synchrotron. Because of the requirement of the CERN rule with respect to single doses being not more than 0.5 rem, working time inside the chamber 18 days after machine shutdown is limited to 15 min. Such a situation is explained by the fact that, first, the intensity of the proton synchrotron at the present time is 5 times greater than the design value, and, second, as was generally the case at the time, no great significance was attached to the hazard from induced radiation in designing the machine (10 years ago). It is apparent that an increase in beam current by even a factor of three will complicate servicing of the proton synchrotron, and that maintenance will be generally impossible with a ten-fold increase. It should be noted that most of the work must be performed outside the chamber. Therefore, even a reduction of radiation dose only outside the chamber will significantly improve the situation.

The work to improve the use of the machine by experimenters and to reduce the radiation dose which is received by service personnel must proceed along two lines. First, it is necessary to increase the reliability and

TABLE 1. Comparison of Various Absorbers

Absorbent*	Hazard parameter for 650 MeV protons $\times 10^{-13}$ rad $\cdot$ cm^2	Density, g/cm^3	Half-valve thickness for neutrons with E > 200 MeV†	Cost per kg, Swedish franks
Water	1	1	110	—
Graphite	1.8	1.75	62	9.50
Alumina	28.5	2.1	56	1
Ordinary concrete	48	2.4	48.6	0.04 −0.17
Basalt	45	3.1	38	1
Barytes concrete	High	3.4	39	0.15 −0.2
Marble, CaCO$_3$	4	2.73	43.6	1.5 −2
Iron	66	7.8	18	0.5 −1
Copper	87	8.9	16.2	3 −4
Lead	~80	10.6	16.3	1 −1.40

* Organic materials were not considered since they are not radiation resistant.
† For energies above 200 MeV, neutron range is only slightly energy dependent.

radiation resistance of the various components of the machine, to simplify their construction, to establish cycling in probe operation, to reduce the changes in the beam transport-system, and, generally, to do everything possible to increase the reliability of the machine. Second, measures must be taken to reduce the level of the background from induced activity. The most radioactive components are the pole tips since almost the entire beam is lost in them both with the use of internal targets and with the use of an extracted beam. We investigated whether it was possible to choose materials with low induced activity for covering the pole tips.

Comparison of Absorbers

Since we are interested in radiation hazard after machine shutdown, it is very convenient to use the "hazard parameter" D [1] for the comparison of materials. It describes the radioactivity induced in a material by unit flux of incident particles, the absorption of the induced γ -rays within the volume of the material, and estimates the intensity of the γ -radiation in rads. The dimensions of the parameter D are rad $\cdot$ cm^2. If the hazard parameter is multiplied by the flux (number of particles per cm^2 per second), we obtain the γ -ray dose rate in rad/sec which is experienced by an individual standing in front of an infinitely thick wall of the given material which has been irradiated for an indefinitely long time. We arbitrarily excluded from D all activities with a half-life of less than one day, therefore, its use is valid for materials which are kept for not less than one day after the end of irradiation.

Other absorber characteristics of interest to us are density, range of high-energy particles (particularly neutrons), and cost. All this data is shown in Table 1. It is clear from the table that water and graphite are the safest materials from the point of view of induced activity. Marble has a higher density and somewhat greater activity; however, its induced activity is approximately 15 times less than the activity of iron. Alumina has a hazard parameter of the same order of magnitude as iron; it is even higher for concrete. Preliminary measurements for pure barium sulfate have shown that it possess an even higher activity. The hazard parameter for lead is still not known precisely. Several days after irradiation, it is equal to the hazard parameters for iron and copper; however, its activity falls much more rapidly, and becomes an order of magnitude less than the activity of copper and iron after two weeks. Because of the great weight of lead, more high-energy secondary neutrons are generated in it than are produced in materials with lower atomic weights. For that reason, we do not recommend the use of lead as an absorber. Thus, marble may prove to be the most suitable material for making shielding with low induced activity.

Some Properties of Marble

Below is given the composition of ordinary, veined white marble [2], %:

$$
\begin{array}{ll}
H_2O & 0.31 \\
SiO_2 & 0.71 \\
CaCO_3 & 98.45 \\
MgO & \text{~}0.32 \\
Al_2O_3 & \text{~}0.09
\end{array}
$$

721
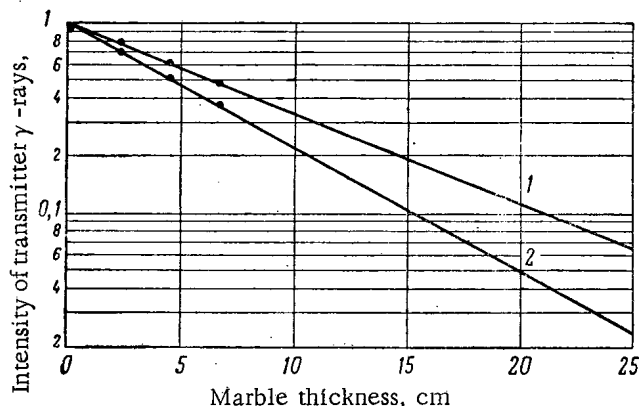
Fig. 1. γ -Ray absorption by marble: 1) CO^{60} γ -rays;
2) γ -radiation from a thick chunk of iron.
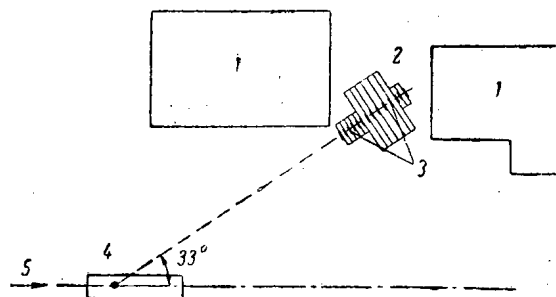
Fig. 2. Experimental arrangement for measuring the absorption of a neutron beam in marble (scale 1:10): 1) concrete shielding; 2) marble; 3) iron samples; 4) target; 5) 600 MeV proton beam.

It is clear that marble consists mainly of $CaCO_3$ and that the quantity of impurities is so small their activity can be neglected. The density of marble is 2.73, the tensile strength 44 kg/cm^2, and the compressive strength, 1200 kg/cm^2.

The cross section for the production of Na^{22} by irradiating Ca^{40} with 600 MeV protons is less than 3.5 mb, and for the production of Na^{24} it is 4 mb. For 155 MeV protons, the cross sections are 2.5 and 0.3 mb, respectively, according to measurements by Gusakov at Orsay (private communication). The magnetic susceptibility of a calcite crystal along the z axis is $0.4 \cdot 10^{-6}$ [3] so that marble does not perturb the magnetic field.

The emission of gases from the surface of marble after chemical purification and preliminary outgassing for some time at 200°C is 10^{-10} torr $\cdot$ liter/sec $\cdot$ cm^2, and therefore, it can be introduced into a vacuum system. At the present time, experiments are being performed to measure the emission of gases from large amounts of marble. The absorption by marble of CO^{60} γ -rays and the γ -radiation from thick chunks of activated iron is shown in Fig. 1. It is clear that the γ -radiation from the iron is attenuated by a factor e at a depth of 6.5 cm in marble and by a factor of 10 at a depth of 15.2 cm.

Experiments were performed at the CERN proton synchrotron to study the absorption of high-energy neutrons in marble. The neutrons were produced in a polyethylene target 40 cm long by irradiating it with an extracted beam of 600 MeV protons. A stack of marble slabs was located at an angle of 33ˇ to the target axis and 1.25 m from it. Pieces of iron foil, whose activity was measured after irradiation, were used as detectors; this was especially convenient because we also attempted to determine the attenuation of iron activation. The experimental arrangement is shown in Fig. 2, and the activity of the samples as a function of marble thickness (curve 1) is given in Fig. 3. Curve 2 in Fig. 3 was computed on the basis of the data from curve 1 with the exception of the $1/r^2$ factor which takes into account the reduction of neutron flux with distance, and it gives the activation of iron by all the neutrons emitted from the target as a function of marble thickness. A reduction in iron activation by a factor e is observed at a depth of 17.5 cm and by a factor of 10 at a depth of 54 cm.

Since there were no clearing magnets between the target and the stack of marble, we measured the activation induced by all cascade particles and also the attenuation of entire particle flux by the marble. In accordance with the data of Moyer and Wallace [4], the number of emitted neutrons and protons per bombarding proton is n/p = 1.4 and p/p = 2.1. However, the difference between the attenuation curves for the neutron and proton fluxes was small for absorber lengths less than the proton range.

Activation of the Proton Synchrotron

Preliminary studies have shown that the principal part of the radiation in the proton synchrotron hall at machine shutdown comes from the iron in the pole tips. Objects located within the chamber (dee, targets, extraction channel, stochastic dee, etc.) are also activated, but their mass is small in comparison with the mass of iron in which the particles are lost.
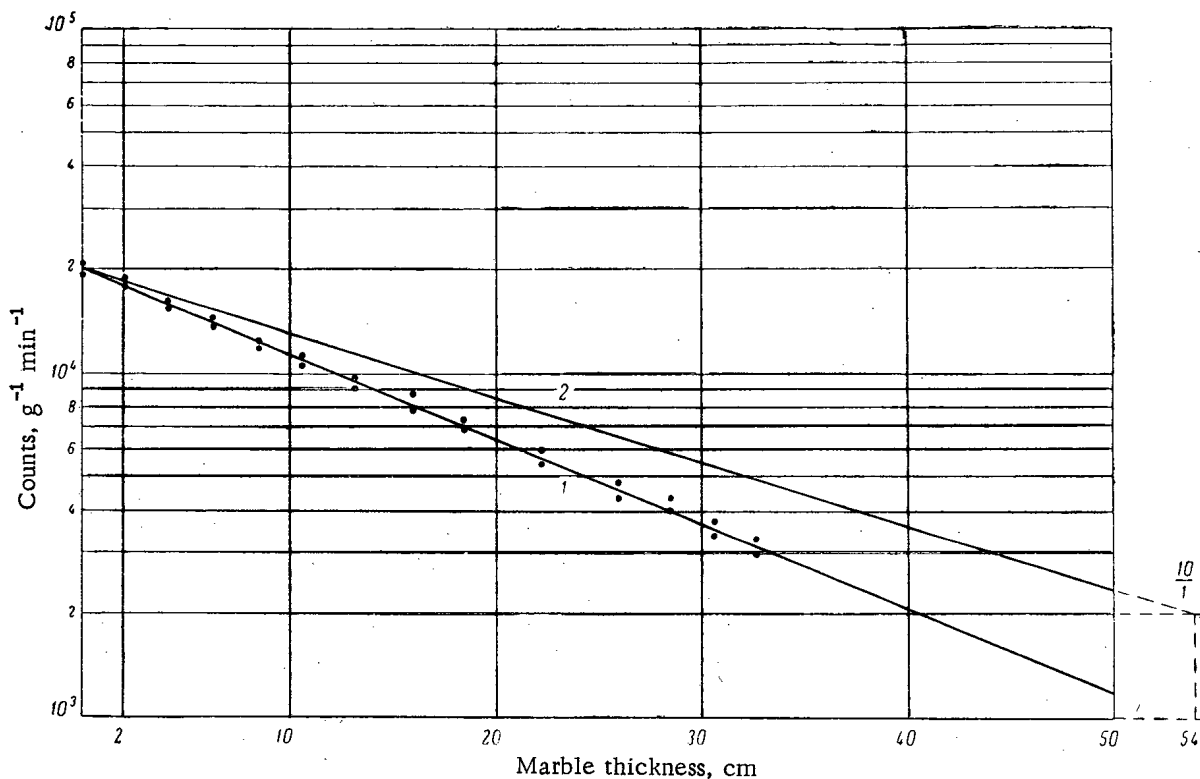
Fig. 3. Sample activation and attenuation of neutron radiation as a function of marble thickness.

The main radioactive isotopes with half-lives greater than one day which contribute to the activity of the poles are shown in Table 2, the partial hazard parameter being indicated for each one. Calculations which take into account the short-lived activities have shown that, for saturation conditions, the rate of decay at machine shutdown is increased insignificantly in comparison with the decay rate obtained for only long-lived elements [1]. Therefore, the short-lived activities may be neglected.

On the basis of the data in Table 2, one can compute the reduction in D over a long period of time. Such a curve is shown in Fig. 4; in the calculation, the contributions of Co^{56} and Cr^{51} were neglected because of their smallness, and the contribution of Sc^{48} was neglected because of the short half-life of this isotope. The computed reduction in D agrees well with the actual reduction in the activity of the proton synchrotron. From this same curve, one can obtain a curve for the activation of the machine (see curve 1). It is interesting to note that two thirds of the final value of the activity is reached at 14 days. This means that with the expected increase in intensity of accelerated protons, saturation will be reached very quickly. In this situation, the old level of activity at machine shutdown will be reached after a time equal to the activation time under the new conditions.

We consider the fluxes of activating particles in the proton synchrotron. First we determine the distribution of the protons and neutrons emitted from an internal target.

Elastic scattering of protons in the target. The protons stay in orbit; however, the amplitude of the vertical oscillations increases and the protons finish up in the pole tips along a circle with a radius equal to the radius of the target, being distributed uniformly in azimuth [1]. The isodose curves around the machine which were obtained by the rad-safe organization under the direction of Dr. Baarli have the shape of circles near the chamber.

One should note that these protons enter the iron at very small angles so that the entire proton range (180 g/cm^2 or 65 cm) is contained in even a thin slab of marble. The number of secondary particles produced in the marble is much less because its constituents have much lower atomic numbers than those in iron.

Protons produced by inelastic processes. Depending on their energy and angular distribution, these protons have circular trajectories which leave the target with various radii of curvature (from zero to the radius of the target). They form a flux which is directed inside the machine.

723

TABLE 2. Main Components in Iron Activity

Radioactive element	Half-life, days	$D, \times 10^{-13}$ rad$\cdot$cm^2
Co^{56}	77	0,65
Mn^{54}	300	8,6
Mn^{52}	5,5	46
Cr^{51}	28	0.5
V^{48}	16	2,36
Sc^{48}	1,8	2,05
Sc^{46}	85	5,9

Irradiation time, days

Time after irradiation, days

Fig. 4. Activation and reduction of activity for iron:
1) calculated increase in the parameter D with irradiation time; 2) calculated decrease in the parameter D with time after an infinite irradiation time; 3) Mn^{52} (5.5 days); 4) Mn^{54} (300 days); 5) Sc^{46} (85 days); 6) V^{48} (16 days);
----- $D_\infty = 64 \cdot 10^{-13}$ rad $\cdot$ cm^{-2}.

The neutrons which are produced as the result of inelastic processes also have a continuous energy spectrum up to the energy of the internal proton beam, and their trajectories, naturally, are straight lines. The neutron energy spectrum has been studied by many authors. The angular distribution of the neutrons produced by the interactions of 5 GeV protons has been investigated by Moyer [4] and is shown in Fig. 5. A good approximation is given by the expression

$$\frac{dN}{d\Omega} = C e^{-\frac{\theta}{\theta_0}}.$$

Here, C = 4.6 neut/sr-proton and θ_0 = 0.94 rad for $0 < \theta < 0.42$; C = 8.5 neut/sr-proton and θ_0 = 0.42 rad for $0.42 < \theta < \pi/2$, where θ is the angle between the directions of neutron and proton motion. For such a distribution, it is easy to compute the dependence on distance x from the target of the neutron flux incident on pole tips which are located h cm below the target. The dependence on the scale distance x/h of the product of the neutron flux per square centimeter per second, Φ, by the square of the height h divided by the number of protons is shown in Fig. 6. The maximum is located at $x_{max} = h/2\theta_0 = 1.2$ h since it is necessary to use the second set of constants. So close a location to the target for the maximum explains why the most active part of the pole tips of the proton synchrotron is found close to the target.

Reduction of γ-Ray Field Outside Chamber with Marble

We propose to line with marble slabs those portions of the pole tips on which particularly high fluxes of activating particles are incident. Primarily, this attenuates the flux of incident particles. The attenuation will be greatest for small angles of the incident particles, which are produced by elastic scattering of protons in the target and by inelastic processes at large distances from the target. In the immediate vicinity of the target, the particles are incident at large angles; therefore, the attenuation will be less. Even there, however, one should install sheets of weakly activatable adsorber although it may necessitate equipping them with rollers and removing them in order to carry out operations within the chamber. In the closed chamber, these sheets will absorb the iron γ-rays. The radiation field in the immediate vicinity of the chamber can be greatly reduced even by thin sheets because the γ-radiation emerges from the gap at small angles. With marble 6.5 cm thick, we have seen the intensity of γ-radiation from activated iron reduced by a factor e, and by a factor of 10 with a 15 cm thickness. At small angles, these values are achieved with sheets 5-10 cm thick which do not reduce the region for vertical oscillation of the particles determined by the dee aperture. Therefore, depending on the thickness of pole tip covering, it is possible to reduce the radiation dose in the danger zone outside the chamber by 3-10 times.

724
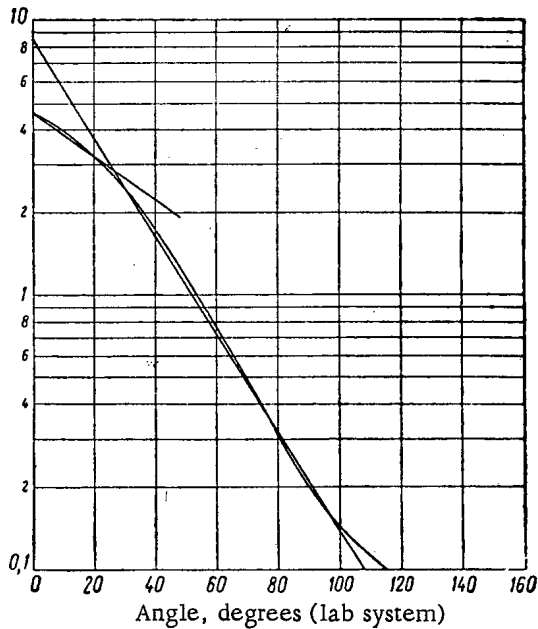
Fig. 5. Angular distribution in the neutron cascade according to Moyer.
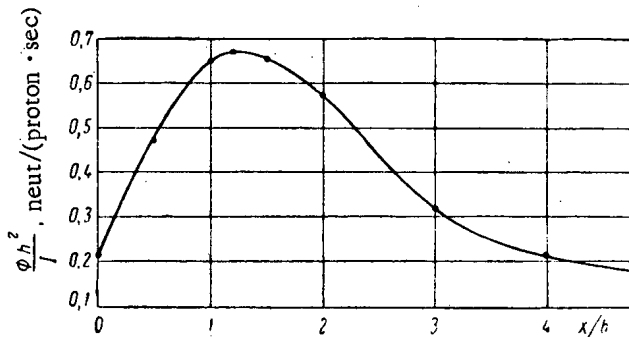
Fig. 6. Distribution of neutron flux incident on pole tips.

Arrangement of Marble Shielding Inside the Proton Synchrotron Chamber

Measurements of the radiation field within the chamber and studies of the locations where the proton and neutron beams are lost have shown that it is necessary to distribute the marble shielding uniformly in azimuth at the periphery of the pole tips. Effective shielding of the proton synchrotron is possible by making slight modifications of the targets as described below. The most suitable absorber arrangement inside the proton synchrotron chamber is shown in Fig. 7.

Marble is a material which is very easily formed to the required shape with ordinary machine tools. To prevent the absorption of moisture or gases when the chamber is opened, it is impregnated with inorganic materials (sodium silicate, or, better, potassium silicate). The side facing the pole pieces must have a rectangular network of grooves to assure the escape of gases during pumping down. To prevent electrostatic charging, the side facing the beam must be covered by a thin metallic foil (aluminum is recommended).

The disposition of the marble vertically must not limit the space for vertical oscillations established by dee construction. In the working areas, a marble absorber thickness up to 12 cm in each direction is permissible (see positions 1-4 in Fig. 7).

We shall consider the equipment which is located in that section of the pole tips which is not occupied by the dee. It is apparent that it will have to be simplified in the immediate future and made more effective not only from the point of view of absorber arrangement. Closest to the center are the monitor target and beam cutout. The monitor target is intended for a rough measurement of beam intensity with an ionization chamber installed on the west wall of the room. In practice, the target is not used for this purpose but is utilized for an abrupt interruption of the beam in working with short exposures for radiochemical investigations. From the practical point of view, this structure can be removed.

The beam cutout is used for slow and gradual regulation of beam intensity. It is necessary to keep it, having been combined with a new drive rod which has been introduced from the east side for remote control of the old ion source. Next follows a thermocouple located at a radius of 110 cm. This thermocouple, and one similar to it located at a radius of 210 cm, can be replaced by a single thermocouple mounted on the target probe. Since the latter can be shifted only up to a radius of 124 cm, it is necessary to equip it with an appropriate extension rod for the thermocouple. It is necessary to construct the target probe so that different targets can be mounted on its head when necessary. The neutron flip target at a radius of 175 cm can be eliminated. When necessary, a neutron beam can be obtained by using a beryllium block mounted on the target probe.

In accordance with present trends, the main target should be mounted on a Fermi carriage which makes it possible to eliminate manual adjustment of the target. It is desirable to locate on the carriage also, a vibrating target which is now used only for intercepting a part of the beam at a definite vertical location. If in the course of time a special flip target is required, it will always be possible to provide a cavity in the marble absorber. Modification of the Fermi carriage is inevitable and extremely desirable. To accomplish this, it is necessary that two
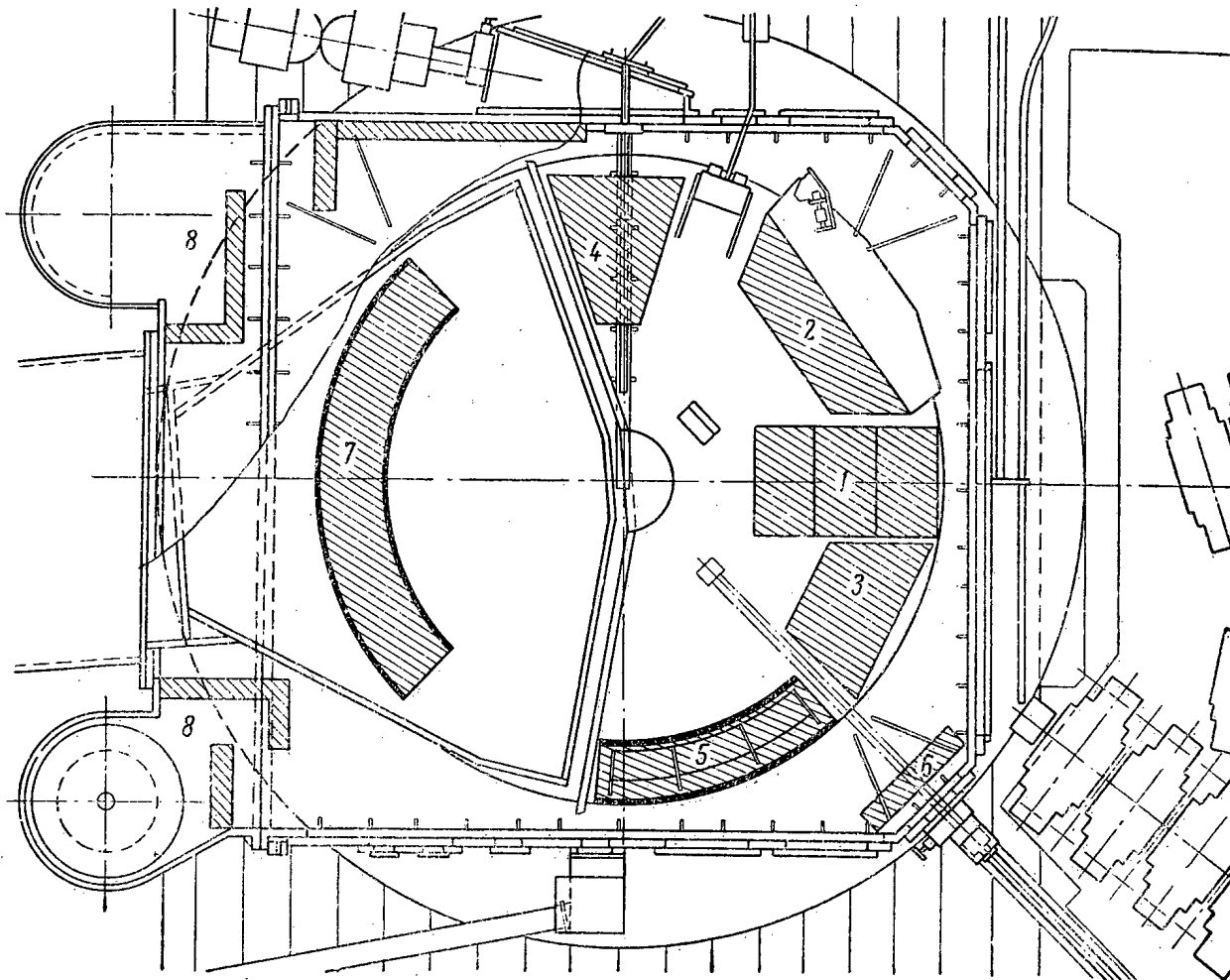
Fig. 7. Diagram of marble absorber arrangement in the proton synchrotron chamber.

rails be attached to the cylindrical outer surface of both pole tips. Only target holders will be located in positions on a line directed toward the center of the machine. Such a mobile system is more reliable than the presently use rack and pinion. At the present time, until the new system is assembled, the old system can be retained after having lined only the upper pole with marble. Finally, there remains the safety target which prevents entrance of the entire beam into an exit channel in the situation where a target drops. For this purpose, one can use the head of the experimental target placed in the required position.

In carrying out these recommendations, we will free the pole surfaces and nearly the entire area where targets are now located, and we will be able to arrange various marble slabs within the chamber in the manner shown in Fig. 7. The movable marble slabs 1 on rollers travel on rails which were intended for the introduction of the equipment for the polarized source located at the center of the machine. When necessary, these blocks are easily removed for inspection of the polarized source. Slabs 2 and 3 are bolted in place and remain in that position. In area 4, protons which have undergone elastic scattering in the target strike the pole tips. This region must be covered by absorber because the people who service the ion source are close by. Figure 7 does not show the channels and openings which must be drilled in the marble for mounting the ion source. The stochastic dee region, 5, is activated during proton synchrotron operation in the mode where the beam is deflected in a direction opposite the extraction direction. In this area, there will be people servicing the target probe; therefore, it is very important to protect them with an absorber, even of reduced thickness, located between the pole surface and the copper sheets forming the dee liner. A vertical slab, 6, 15 cm thick, shields the area for servicing the target probe from the target area. There are circular openings in this slab for the target probe. Position 7 is a most important one since it is in an area where

726

a large part of the beam is lost and where there exists the principal radiation source for the entire northern part of the proton synchrotron hall and for the rf system which is often needed for servicing. Here, the marble must be located between the pole surface and the dee liner, which must be modified. It is suggested that the capacity of the rf system be increased somewhat. In this position, one can be limited to a thin layer of marble since the protons enter it at very small angles. The selected thickness of marble must leave a clear gap (35 cm) for the dee liner. The vertical marble slabs 8 (15 cm thick) protect personnel servicing the pumps from chamber radiation while maintaining free passage for gases.

Thus, the problem of reducing the activity of the accelerator is extremely complex. Marble is a convenient high-density absorber because of the low activation of calcium. It has been found possible to arrange marble slabs in the chamber. A reduction in γ-ray background intensity by a factor of 3 inside the chamber and by a factor of 10 outside is expected. The flux geometries and radiation fields are so complicated that only by experimental means can one be convinced of the possibility of obtaining large attenuation coefficients. Since the present paper is a first attempt in a struggle against induced radioactivity in the accelerator, the author will be grateful for criticism and suggestions.

LITERATURE CITED

1. M. Barbier, Atomnaya tekhnika za rubezhom, No. 6, 30 (1965).
2. M. Pieri, I. Marmi d'italia, Universita di Pisa, Hoepli (1950).
3. E. Kohrausch, Praktische Physik. Bd. II. Ed. B. Teubner, Leipzig (1943).
4. R. Wallace, Nucl. Instrum. and Methods, 18, 405 (1962).

FLUX OF SECONDARY NEUTRONS PRODUCED BY 660 MeV PROTONS IN SHIELDING

(UDC 539.172.12:539.125.5)

V. A. Kon'shin, E. S. Matusevich, and S. S. Prokhorov

With the help of a set of threshold and resonance detectors, measurements were made of the spatial and energy distribution of secondary neutrons in graphite and nickel blocks. Absolute values of the neutron flux as a function of depth in an infinite slab were obtained for a plane, monodirectional proton source. The energy distribution of the secondary neutrons in the energy range $2.5 \cdot 10^{-8}$ to $6.6 \cdot 10^2$ Mev was represented by seven groups. The magnitude of the dose behind plane nickel and graphite shielding as a function of thickness was also determined. The results are discussed.

In recent years, there has been an increasing interest in theoretical and experimental studies of shielding against high-energy protons. The change in proton flux within shielding arising because of energy loss by ionization can be calculated rather exactly; however, because of the lack of complete data for the interaction cross sections of high-energy nucleons with nuclei and because of the lack of development of methods for computing the penetration of high-energy nucleons through matter, it is impossible to perform any kind of precise calculation of the fluxes and doses of secondary radiation. The experimental investigation of secondary radiation fields for the purpose of obtaining some integral characteristics such as the spatial distribution of flux or dose is presently the easiest, simplest, and most capable means of getting reliable information needed for the calculation of actual shielding.

EXPERIMENTAL METHOD

The measurements were made at the JINR synchrocyclotron. The proton beam emerging from the synchrocyclotron chamber was shaped by magnetic quadrupole lenses, and with the help of magnetic adapters and bending magnets, was brought out through a steel collimator 1 cm in diameter in a four-meter case iron wall behind which the targets were located in an experimental room. At the target, the beam diameter was 3 cm.

Monitoring of the proton beam incident on a target was done with a helium-filled ionization chamber. For absolute calibrations, the $\beta - \gamma$ coincidence counting method was used in measuring the activity induced in a plastic scintillator (polystyrene with added p-terphenyl) as a result of the $C^{12}(p,pn)C^{11}$ reaction. The cross section for this reaction was assumed to be 27 mb with an error of $\pm 5\%$ [1]. The proton flux was also determined by an independent method using the $Al^{27}(p, 3pn)Na^{24}$ reaction with a cross section of 11 ± 0.55 mb [1]. Absolute activity of the foils was determined by I. Yu. Levenberg who used absolute γ spectrometry. Both methods gave results agreeing within $\pm 10\%$. On the average, the proton flux was 10^{10} proton/sec.

The dimensions of the graphite targets were $120 \times 140 \times 160$, $60 \times 200 \times 200$, and $16 \times 200 \times 200$ cm; those for the nickel targets were $31 \times 80 \times 80$, and $2.4 \times 80 \times 80$ cm. Here, the first number is the thickness in the proton beam direction. The maximum thickness of both the nickel and graphite targets was greater than the ionization range of the primary protons. The proton beam impinged perpendicularly to the plane of the target, dividing its diagonal in the ratio 3:1.

The neutron flux was determined by means of a set of detectors: $In^{115}(n, \gamma)In^{116}$, $U^{238}(n, \gamma)U^{239}$, $Cu^{63}(n, \gamma)Cu^{64}$, $Al^{27}(n, \alpha)Na^{24}$, $Mg^{24}(n, p)Na^{24}$, $P^{31}(n, p)Si^{31}$, and $C^{12}(n, 2n)C^{11}$.

728
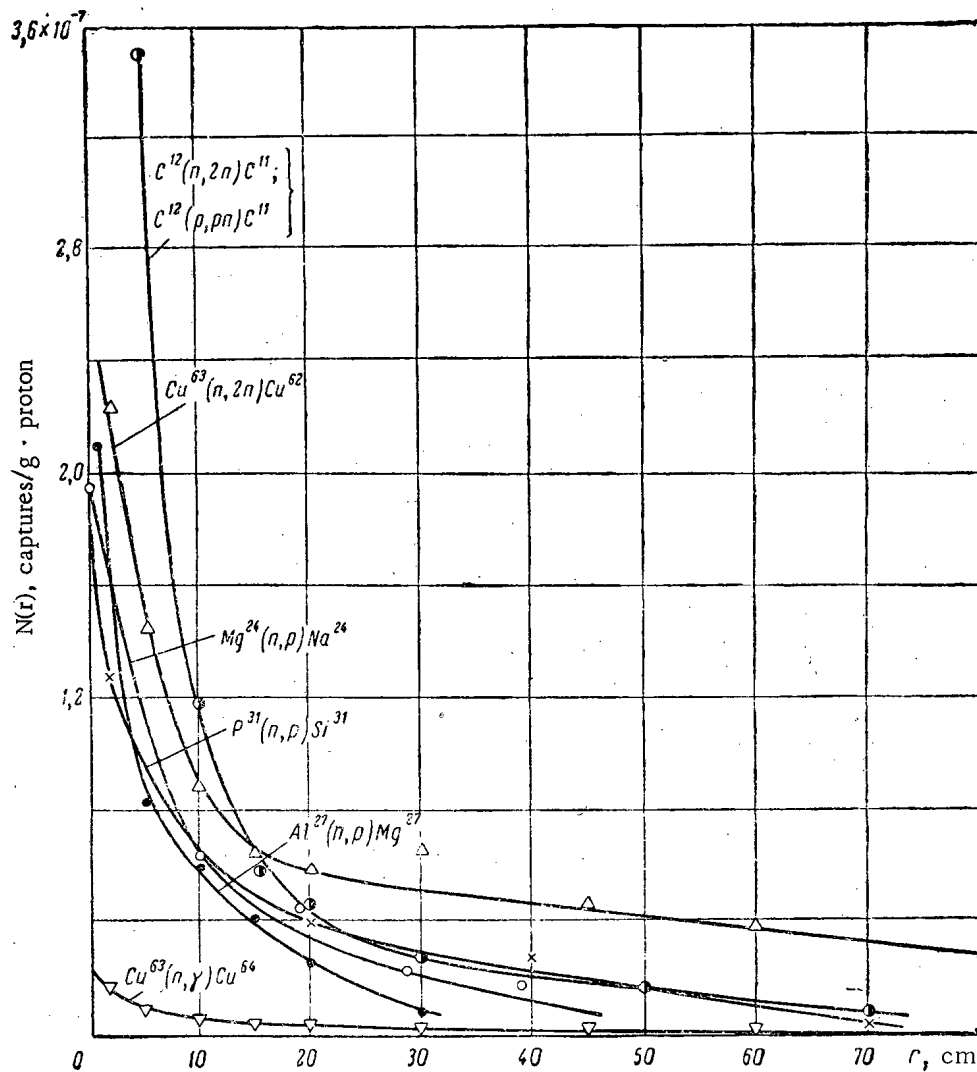
Fig. 1. Number of captures per gram of detector normalized to one incident proton.
(Data refers to the rear wall of the target with respect to the proton beam (z = 120 cm).)

Detector activation by irradiation is also possible in other reactions of the types (p, $\pi+$) and (p, $\pi+$p) with the formation of the same isotopes, but the cross sections for such reactions are small and their contribution negligible. In measurements based on the reaction Al^{27} (n, α)Na^{24}, consideration was given to the possibility of activation through the Al^{27} (p, 3pn)Na^{24} reaction (threshold ~50 MeV). The distributions measured with the carbon detectors characterize both the neutron and proton fluxes.

In determining the activity of U^{239}, it was chemically separated from fission fragments and decay products. The apparatus for counting induced activity was calibrated absolutely by independent methods: by determining the total capture in a large tank of water for a source of known intensity, by determining the number of counts from a $Y^{91}Cl$ β source of known activity, by determining the number of counts from an aluminum sample irradiated in a known neutron flux (Al^{27}(n, α)Na^{24} reaction), and, finally, by determining the induced activity of a copper detector for the Cu^{63}(n, γ)Cu^{64} reaction with a known thermal neutron flux. After introducing correction factors allowing for differences in the β-particle energies from the different detectors and for differences in the dimensions of the de-tectors, all the calibration methods gave efficiency values which agreed within 10%. The accuracy in determining the absolute count from the detectors was, on the average, ±10-15%.

RESULTS

For the measurements, the detectors were located in a plane perpendicular to the beam axis z along a radius vector r. A typical distribution of the number of captures N(r) measured at the exit side (z = 120 cm) of a graphite
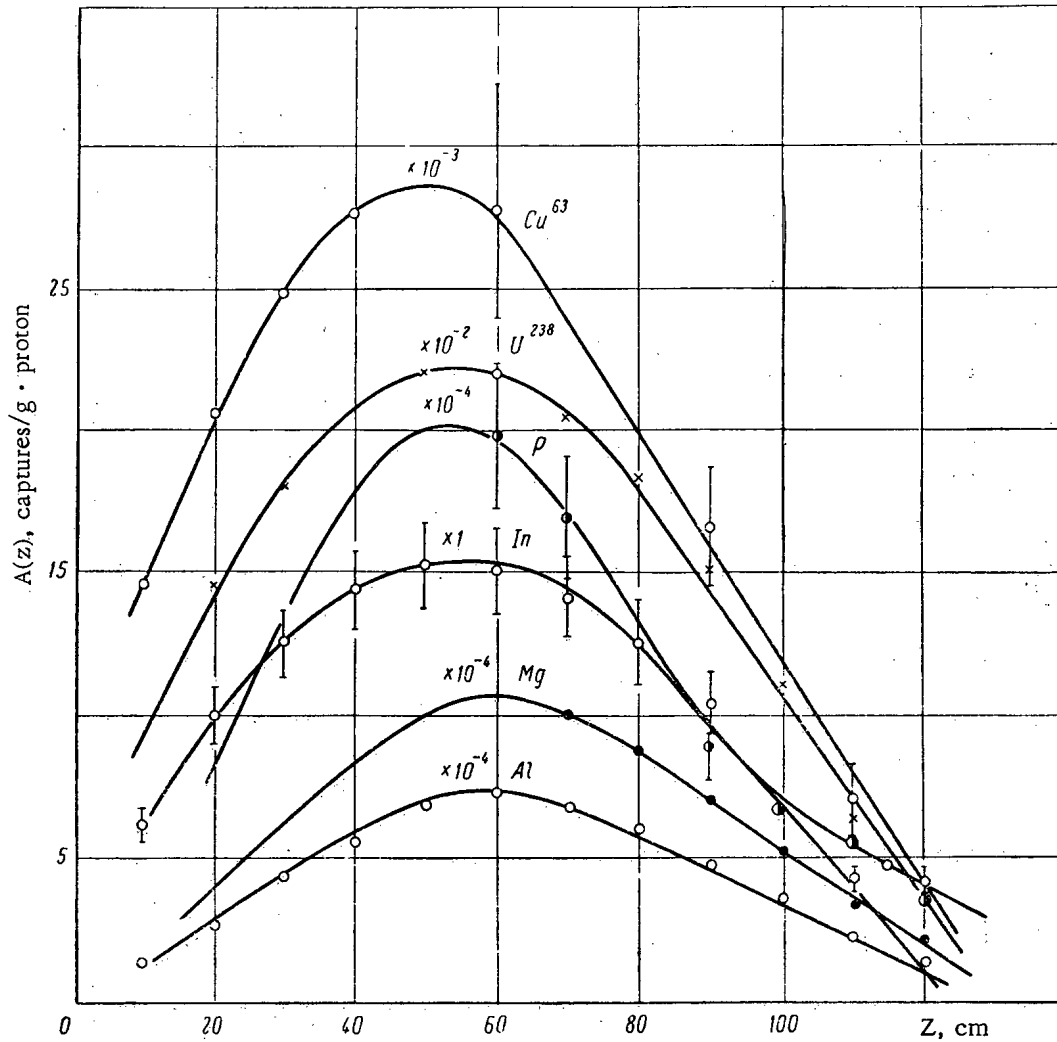
Fig. 2. Number of captures A(z) (plane, monodirectional proton source, proton/cm^2; detector activation in the reactions In^{115}(n, γ)In^{116}, U^{238}(n, γ)^{239}, Cu^{63}(n, γ)Cu^{64}, P^{31}(n, p)Si^{31}, Mg^{24}(n, p) Na^{24}, Al^{27}(n, α)Na^{24}).

block 120×140×160 cm in size is shown in Fig. 1. The distribution within this block and in other blocks generally had a shape similar to the one shown. To obtain the more significant quantity A(z), the number of captures from a plane, monodirectional source perpendicular to the plane of the target, the function N(r) was integrated over the

area of the target, i.e., the value of A(z) $= 2\pi \int\limits_{0}^{\infty} N\,(r,\ z)\ r dr$ was determined.

Generally speaking, one can only determine $\int\limits_{0}^{r_{max}} N\,(r,\ z)\ r dr$ from a measurement of N(r, z) and can com-

pute the quantity $\int\limits_{r_{max}}^{\infty} N\,(r,\ z)\ r dr$ defining the variation of N(r, z) as a function of r for r > r$_{max}$ by some arbi-

trary rule. However, the ratio $\int\limits_{r_{max}}^{\infty} N\,(r,\ z)\ r dr / \int\limits_{0}^{r_{max}} N\,(r,\ z)\ r dr$ did not exceed a few percent in all cases and
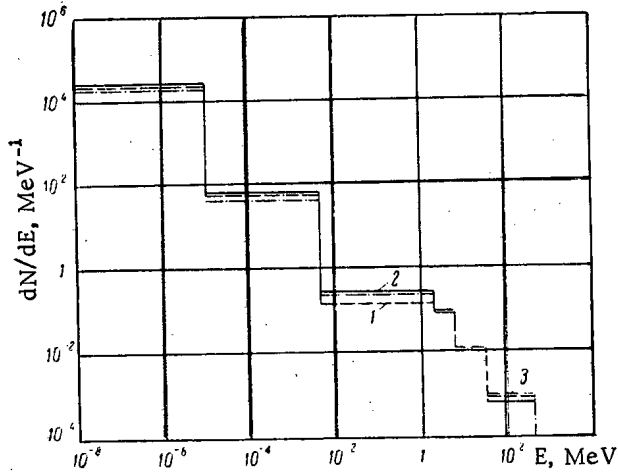
Fig. 3. Neutron energy distributions φ in a nickel prism (plane, monodirectional source; distribution normalized to total flux for z = 15.7); 1) z = 7.8 cm; 2) z = 15.7 cm; 3) z = 29.6 cm.
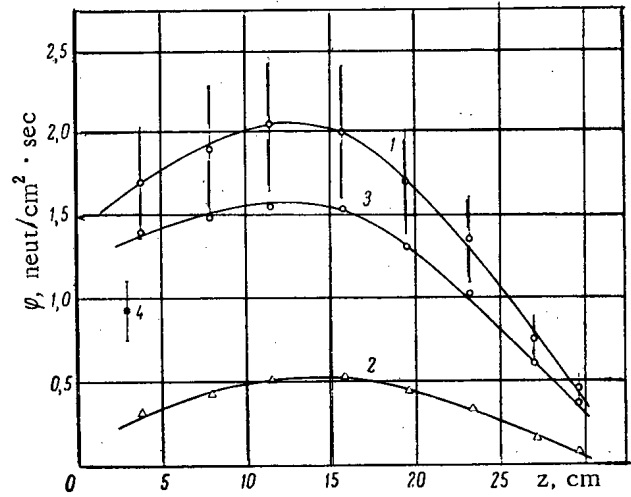
Fig. 4. Neutron flux distributions with depth z in a nickel prism (plane, monodirectional source with strength 1 proton/cm^2 · sec): 1) total flux; 2) flux in the range $2.5 \cdot 10^{-8} - 4.65 \cdot 10^{-3}$ MeV; 3) flux in the range $4.65 \cdot 10^{-3} - 6.6 \cdot 10^{3}$ MeV; 4) total flux behind prism 2.4 cm thick.

consequently, the approximate representation of N(r, z) as an exponential, for example, introduced no noticeable error.

The function A(z) is shown in Fig. 2, where z is the distance from the front face of the target, normalized to 1 g of detector for several detectors in the case of the graphite block 120×140×160 cm in size. In all cases (measurements with different blocks), the function A(z) had a maximum, and more or less resembled the curves shown in the figure on the whole. (For phosphorus and magnesium detectors, the function A(z) was obtained in the region z < 60 cm by assuming that the shape of A(z) was the same for all threshold detectors.)

The errors shown in Fig. 2 are basically determined by the errors associated with obtaining absolute values for detector activity. The errors in determining the relative values of the function A(z) are small.

The averaging of reaction cross sections to obtain values for neutron fluxes in the various energy groups was carried out over a neutron spectrum selected on the basis of several general considerations. In the elementary act of inelastic proton interactions with nuclei, it was assumed that the neutrons emitted with energies up to 20 MeV had a spectrum corresponding to an evaporation spectrum for a temperature which depended little on nucleus and proton energy [2, 3]. Above 20 MeV, the energy distribution of the emitted nucleons was assumed in accordance with previously published data [4-6]. For target thicknesses less than 0.2-0.3 of the proton nuclear range, the detector cross sections were averaged over the neutron spectrum for the elementary act. In determining neutron fluxes in thick graphite blocks, cross section averaging was carried out over a 1/E spectrum; for calculations of the flux in a nickel block, it was assumed the neutron flux was proportional to 1/E above 2 MeV, and a distribution previously measured [7] was used for lower energies. A certain inexactness in the assumed neutron spectra had an unimportant effect on the interpretation of the results because the averaged cross sections themselves depended little on the assumed spectra. Previously published reaction cross sections were used [8-14]. In measurements with resonance detectors, the effect of self-shielding was taken into account in accordance with [15].

The neutron energy range, $2.5 \cdot 10^{-8} - 6.6 \cdot 10^{2}$ MeV, was divided into seven intervals for graphite and into six for nickel in such a way that the principal part of the activity of each detector was produced by neutrons belonging to a single group. The selection of nonuniform intervals facilitated the determination of fluxes within the groups. Values of the fluxes were determined by the solution of a system of equations. As an example, the neutron energy distributions at three values of z are shown in Fig. 3 for a nickel prism.
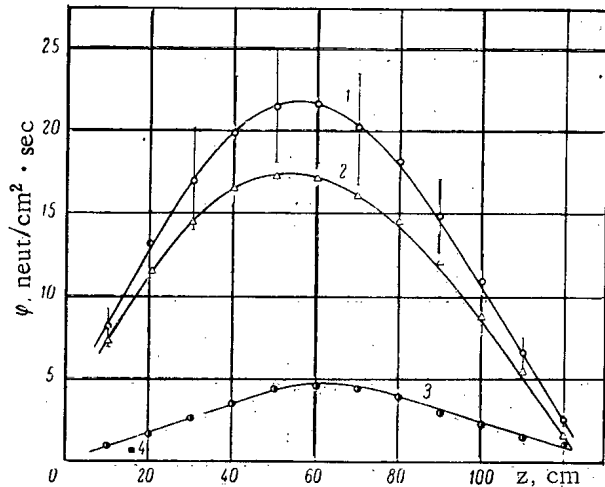
Fig. 5. Neutron flux distributions with depth z in a graphite prism 120×140×160 cm in size (plane, mono-directional source with strength 1 proton/cm^2 · sec): 1) total flux; 2) flux in the range $2.5 \cdot 10^{-8}$ – $4.65 \cdot 10^{-3}$ MeV; 3) flux in the range $4.65 \cdot 10^{-3}$ – $6.6 \cdot 10^2$ MeV; 4) total flux behind prism 16 cm thick.

Fig. 6. Dose behind plane shielding as a function of thickness for a plane, monodirectional source: ●) nickel; ○) graphite.

DISCUSSION OF RESULTS

In Figs. 4 and 5 are shown neutron flux distributions as a function of z in nickel and graphite for two energy intervals (E_n < and > 4.65 ke V); and also the total flux, for a plane, monodirectional proton source with an intensity of 1 proton/cm^2 · sec. The comparatively large errors in the determination of absolute values of neutron fluxes result from the very method of computing fluxes from measured detector activities. The principal contribution to the total flux in graphite is made by low-energy neutrons; in nickel, it is made by neutrons with energies above 4.65 keV. The excellent slowing down properties of graphite also explain the great difference in "soft" neutron fluxes (~30 times) in graphite and nickel; the fast neutron fluxes differ only by a factor of approximately three. The spatial distribution of the flux exhibits a maximum which is seen more clearly in the case of graphite and which is symmetric for graphite in contrast to the flux distribution in nickel. The appearance of a maximum is associated with the influence of two factors on which the spatial dependence of the neutrons depends, namely: the density of production of secondary neutrons by the primary proton beam, and development of nuclear cascades and of slowing down and dispersion processes involving the neutrons produced. The total flux at the symmetry axis of the graphite prism is about 20 neut/cm^2 · sec; such a large value for the flux is explained by the high albedo of graphite. As can be seen in Fig. 5, it is typical that the flux at z = 16 cm in a thick block is 11 neut/cm^2 · sec, while it is only 0.7 neut/cm² · sec behind a graphite wall 16 cm thick. For convenience in making comparisons, the neutron energy distributions in a nickel prism shown in Fig. 3 were normalized in terms of the total flux to the distribution for z = 15.7 cm. The largest number of low-energy neutrons is observed for z = 15.7 cm; more neutrons with higher energies are in the spectrum at the exit from the slab (at z = 29.6 cm). The same sort of characteristic for the dependence of energy distribution on z is also observed for graphite prisms.

The rem value of the dose behind plane shielding of graphite and nickel as a function of thickness, computed in accordance with the recommendations of [16], is shown in Fig. 6. Values of the relative biological effectiveness (RBE) were averaged within the energy groups over the assumed neutron spectrum. For graphite, the dose is practically independent of thickness, which can apparently be associated with two mutually compensating processes: the formation of neutrons by the primary proton beam, and neutron energy loss (and, therefore, reduction in RBE) through interaction of the secondary neutrons with carbon nuclei. Apparently, the second process is more important in nickel. It is natural that such an explanation has a particularly qualitative nature. It should be noted that the value for the dose behind shielding was obtained from the energy distribution of the flux and not from the neutron current, and that it corresponds to the dose at the surface. Far from the shielding, the dose value must be multiplied by some factor which depends on the angular distribution of the emitted neutrons and which lies in the range 0.5-1.0.

To compare the dose produced by secondary neutrons with the dose from primary protons, it is necessary to know rather precisely the relationship between the flux of 660 MeV protons and the rem dose produced by them. The recommendations which are contained in [16] do not make it possible to determine this relationship precisely.

However, if one assumes that equal fluxes of neutrons and protons with energies ~ 600 MeV present the same biological hazard, which is approximately true in the maximum depth dose case being considered, then the primary proton dose is approximately $12 \cdot 10^{-8}$ rem/proton, i.e., shielding with a thickness greater than the proton ionization range (~ 200 g/cm^2 for graphite, and 270 g/cm^2 for nickel) attenuates the dose from a plane monodirectional 660 MeV proton source by a factor of approximately four for a graphite wall and approximately six for nickel.

In conclusion, the authors are deeply grateful to S. G. Tsypin and G. N. Flerov for continuing interest, support, and fruitful discussions, to Yu. P. Kumekin and V. Stoletov for assistance in the accelerator work, to I. Yu. Levenberg who measured the absolute activities of the aluminum foils, and to V. P. Dzhelepov for making it possible to work with the JINR synchrocyclotron.

LITERATURE CITED

1. N. A. Perfilov, et al., Nuclear Reactions Induced by Nigh-Energy Particles, Moscow, Izd-vo AN SSSR (1962).
2. D. Skyrme, Nucl. Phys., 35, 177 (1962).
3. J. Dostrovsky, P. Rabinowitz, and R. Bivins, Phys. Rev., 111, 1659 (1958).
4. A. P. Zhdanov and P. I. Fedotov, ZhÉTF, 41, 1871 (1961).
5. N. Metropolis et al., Phys. Rev., 110, 204 (1958).
6. V. S. Kiselev and V. B. Flyagin, ZhÉTF, 38, 962 (1957).
7. I. I. Bondarenko et al., see this issue, p. 593.
8. L. P. Abagyan et al., Group Constants for Nuclear Reactor Calculations, Moscow, Atomizdat (1964).
9. P. Cuzzocrea et al., Nuovo cimento, 16, 450 (1960).
10. J. Crandl et al., Phys. Rev., 109, 425 (1958).
11. Buttler and Santry, Canada J. Phys., 41, 372 (1963).
12. P. Alboy et al., J. Phys. Rad., 23, 1000 (1962).
13. I. Yu. Levenberg, et al., ZhÉTF, 431, 1619 (1962).
14. N. G. Zaitsev, et al., ZhÉTF, 43, 1672 (1962).
15. G. I. Marchuk, Numerical Methods for Reactor Calculations, Moscow, Atomizdat (1958).
16. Health Rules for Working with Radioactive Materials and Sources of Ionizing Radiation, Moscow, Gosatomizdat (1960).

THE EFFECT OF DELAYED NEUTRONS ON THE TIME
OF ESTABLISHING A STABLE FISSION CHAIN

(UDC 621.039.51)

V. F. Kolesov

The stochastic process of delayed neutron multiplication is considered in limited fission chains in a reactor which is supercritical with respect to prompt neutrons. Equations are obtained for the instants of distribution of the output of delayed neutron precursors and for the mean square deviation.

The effect of delayed neutrons on the time of establishment of a stable fission chain is investigated. Equations are compiled and their approximate solutions are given. It is shown that for a small reactivity and with a weak source, the average time for establishing the first stable fission chain can be reduced by the delayed neutrons by a factor of 10 or more.

The processes which take place in a reactor are of a statistical nature. The initial increase of power is subjected to such considerable fluctuations that a description of the process by means of the usual kinetic equations, i.e., by means of average values, gives results in this region which are of little satisfaction. The kinetic equations are of significance for use only after the reactor has attained appreciable power.

Reactor power fluctuations and detector indications are being widely studied in connection with the development of methods for measuring the physical parameters of reactors [1-3], for evaluating the conditions for bringing a reactor safely to power [4-7] and also in connection with determining the amplitude spread of power pulses [7-8].

In [7], limited and infinite (stable) fission chains are brought into consideration for describing the initial stage of power increase in a reactor, supercritical with respect to prompt neutrons. This procedure is particularly suitable in considering fast reactors, in which a stable fission chain develops extremely rapidly [7]. It can be assumed that in a fast reactor the time for achieving an almost unlimitedly high power is equal to the time of formation of the first stable chain.

Expressions for the probability of establishing the first stable fission chain are derived in [7] by taking account of only the prompt neutrons. Similar expressions are obtained in the present paper which take the delayed neutrons into account. For this purpose, the multiplication process of delayed neutron precursors in limited chains and their contribution to the effective neutron source acting on the reactor is investigated.

We shall carry out the discussion within the framework of the often-used approximation for the zero lifetime of prompt neutrons [9]. We reduce the delayed neutrons to a single group with effective parameters γ and β_{eff}. In order to simplify the mathematical description we shall assume that the number of delayed neutron precursors m and the number of fissions in limited chains N can be assumed to be any, not necessarily integral, values.

The delayed neutron precursors are created in limited fission chains which fluctuate strongly in magnitude. As will be seen later, m(t) at low reactivity has an extremely extended distribution for any instant of time. We denote by means of the parameter ρ one of the possible realizations of the course of the dependence of m on time. The probability (or probability density) of realizing $m(\rho, t)$ we denote by $M(\rho)$. Then we can write

$$s(\varrho, t) = s_0(t) + \lambda m(\varrho, t);\qquad(1)$$

734
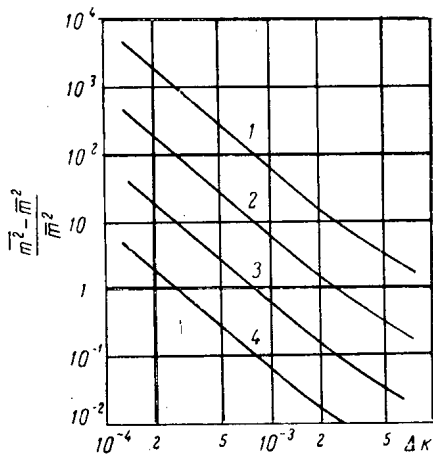
Fig. 1. Fractional mean square fluctuation $\dfrac{\overline{m^2}-\overline{m}^2}{\overline{m}^2}$ as a function of reactivity:
1) $s_0 = 10^2$; 2) $s_0 = 10^3$; $s_0 = 10^4$; 4) $s_0 = 10^5$.

$$W(\varrho,\, t) = W_0\,[s_0 + \lambda m(\varrho,\, t)]\exp\left\{-W_0\int_0^t [s_0 + \lambda m(\varrho,\, \xi)]\,d\xi\right\},\tag{2}$$

where s_0 and s are the strengths of the external and total neutron sources respectively; W_0 is the probability that a neutron source will initiate a stable fission chain; $W(\rho,\, t)$ is the probability density of the first stable fission chain originating at time t in the case when $m(t)$ has the form $m(\rho,\, t)$. The mean probability density will be determined by the expression

$$W(t) = \sum_\rho M(\varrho)\,W(\varrho,\, t)$$

$$\text{or}\quad \int_\rho M(\varrho)\,W(\varrho,\, t)\,d\varrho.\tag{3}$$

Thus, in order to determine $W(t)$, it is necessary to know all the possible realizations of $m(\rho,\, t)$ and their probability.

In order to simplify the problem we introduce into the discussion the quantity $P(m,\, t)$, which is the probability density of m delayed neutron precursors at time t. It is well-known that in a supercritical reactor the ratio $m(t)/\overline{m}(t)$ in course of time becomes time-independent and $P(m,\, t)$ will depend only on $m/\overline{m}$ [6]. After the distribution is stationary, each $m(\rho,\, t)$ will increase in accordance with the kinetic equations. It can be shown that in this case $m(\rho,\, t)$ is satisfied by the equation

$$\int_0^{m(\rho,\, t)} P(m,\, t)\,dm = \varrho,\qquad 0 \leqslant \varrho \leqslant 1.\tag{4}$$

We shall assume that relationship (4) holds approximately also for a nonstationary distribution. Then, considering Eq. (4) as the equation related to the upper limit we obtain

$$W(t) = W_0\int_0^1 [s_0 + \lambda m(\varrho,\, t)]\exp$$

$$\times\left\{-W_0\int_0^t [s_0 + \lambda m(\varrho,\, \xi)]\,d\xi\right\}d\varrho.\tag{5}$$

Consequently, in this approximation the problem is reduced to one of determining $P(m,\, t)$.

The Equation for P(m, t).

Distribution Moments

We denote by $W_n(N,\, t)$ the probability density of N fissions in a limited chain initiated by a single neutron source. In a limited chain of N fissions, νN prompt neutrons are formed and $\beta_{eff}\nu N/(1-\beta)$ sources of delayed neutrons, where ν is the average number of prompt neutrons per fission event; β is the actual fraction of delayed neutrons. The equation for $P(m,\, t)$ is obtained on the basis of considerations similar to those used in [10]:

$$\frac{dP(m,\, t)}{dt} = \lambda\int_0^\infty P(m - \gamma N + 1,\, t)\times(m - \gamma N + 1)\,W_n(N,\, t)\,dN$$

$$+ s_0\int_0^\infty P(m - \gamma N,\, t)\,W_n(N,\, t)\,dN - P(m,\, t)(s_0 + \lambda m);\ P(x,\, t) = 0\ \text{when}\ x < 0;\qquad \gamma = \frac{\beta_{eff}\,\nu}{1-\beta}\tag{6}$$

735
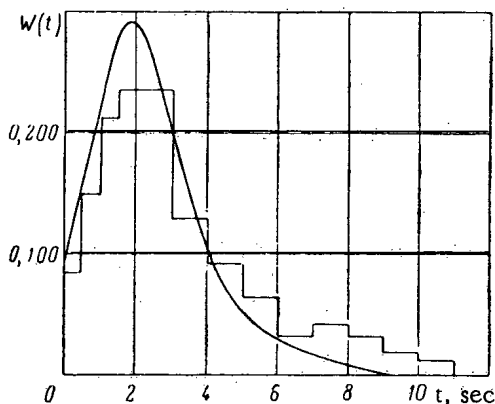
Fig. 2. Probability of initiation of the first stable fission chain as a function of time for $\triangle k = 3.5 \cdot 10^{-4}$ and $s_0 \approx 90$ n/sec (the curved line is the calculation and the histogram is the experiment [11]).

or

$$\frac{\partial G}{\partial t} = \varphi_1(p, t)\frac{\partial G}{\partial p} + \varphi_2(p, t)G(p, t) - K(p, t),$$

where

$$\varphi_1 = \lambda\,[1 - e^{p}g(\gamma p, t)]; \quad \varphi_2 = s_0\,[g(\gamma p, t) - 1]; \quad (7)$$

$$K(p, t) = \lambda e^{p} \int_0^{1/\gamma} W_n'(N, t)$$

$$\times e^{-\gamma N p} \int_0^{(1-\gamma N)} P(x, t)\,x e^{-px}\,dx\,dN; \qquad (8)$$

$G(p, t)$ and $g(p, t)$ are the Laplace transforms of the functions $P(m, t)$ and $W_n(N, t)$ respectively.

In all cases of application of Eq. (7) below, the term $K(p, t)$ is negligibly small in comparison with the other terms of the right hand side. Therefore, we shall assume that $K(p, t)$ is equal to zero.

It is not difficult to obtain from expression (7) the equation for any moment of distribution of $P(m, t)$. The equation for the n-th moment has the form

$$\frac{d\overline{m^n}}{dt} = n\lambda(\gamma\overline{N} - 1)\overline{m^n}$$

$$+ \sum_{k=1}^{n}\left[\frac{n(n-1)\ldots(n-k+1)}{k!}s_0\gamma^k\overline{N^k}\right.$$

$$\left.\frac{n(n-1)\ldots(n-k)}{(k+1)!}(-1)^k\lambda(1-\gamma z)^{k+1}\right]\overline{m^{n-k}},$$

$$z^l = \overline{N^l}. \qquad (9)$$

Here we assume that $\int_0^{} W_n(N)\,dN = 1$; in a precise determination $\int_0^{\infty} W_n(N)\,dN = 1 - W_0,$ but W_0 is small and it need not be taken into account. If s_0 and $\overline{N^k}$ are independent of time, then the solution of Eq. (9) has the form

$$\overline{m^n} = \sum_{j=0}^{n} b_{n,j}e^{jat}, \quad a = \lambda(\gamma\overline{N} - 1), \quad \overline{m^l}(0) = 0.$$

The coefficients of $b_{n,j}$ are determined from the following recurrent formulas:

$$b_{n,j} = -\frac{1}{a(n-j)}\sum_{k=1}^{n-j}\frac{n(n-1)\ldots(n-k+1)}{k!}\times\left[s_0z_1^k + \frac{n-k}{k+1}\lambda(z_1-1)^{k+1}\right]$$

$$\times b_{(n-k,\,j)} \text{ for } j < n;$$

$$b_{n,n} = \frac{1}{a}\sum_{k=1}^{n}\frac{n(n-1)\ldots(n-k+1)}{k!}\times\left[s_0z_1^k + \frac{n-k}{k+1}\lambda(z_1-1)^{k+1}\right]$$

$$\times\sum_{j=0}^{n-k}\frac{b_{(n-k),\,j}}{n-j}, \quad b_{0,0} = 1, \quad z_1^l = \gamma^l\overline{N^l}.$$

$$(10)$$
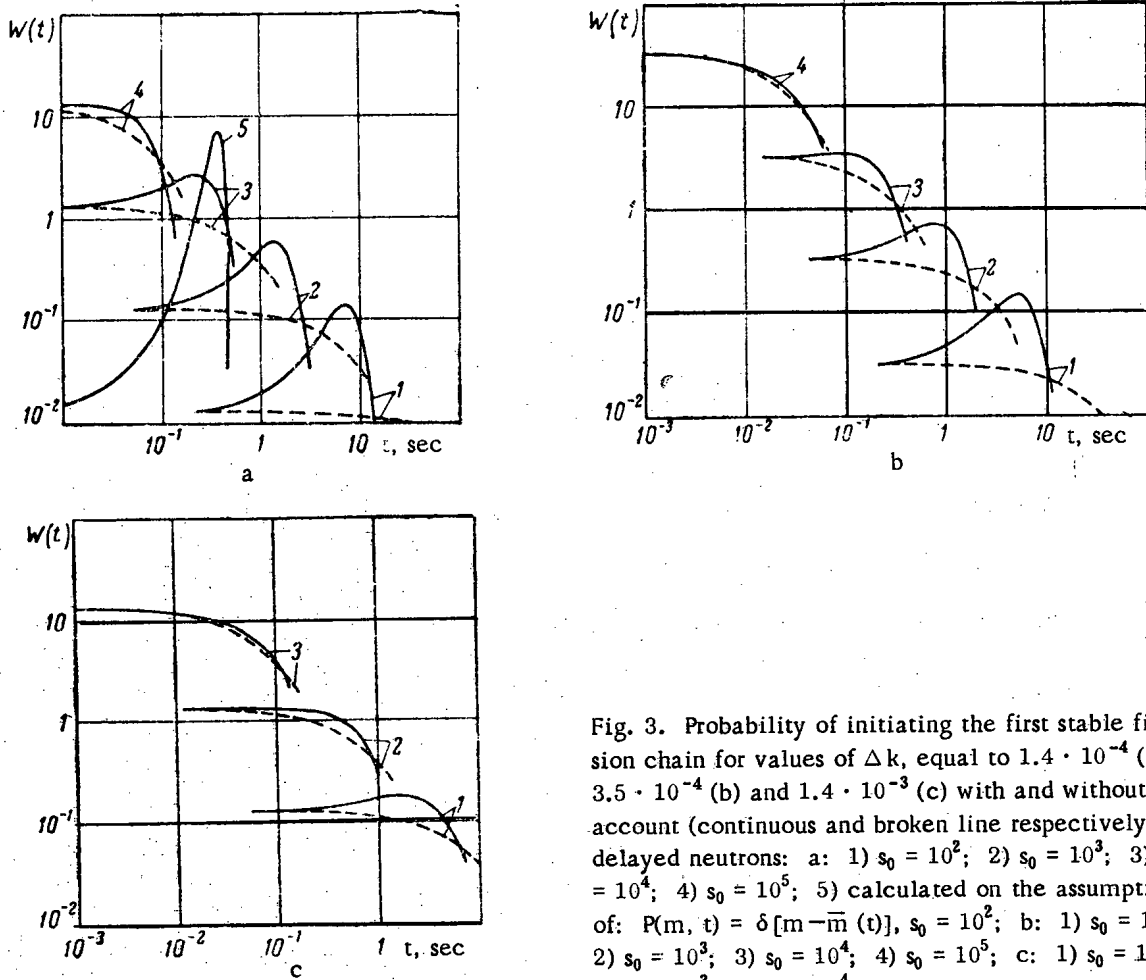
Fig. 3. Probability of initiating the first stable fission chain for values of Δk, equal to $1.4 \cdot 10^{-4}$ (a), $3.5 \cdot 10^{-4}$ (b) and $1.4 \cdot 10^{-3}$ (c) with and without account (continuous and broken line respectively) of delayed neutrons: a: 1) $s_0 = 10^2$; 2) $s_0 = 10^3$; 3) $s_0 = 10^4$; 4) $s_0 = 10^5$; 5) calculated on the assumption of: $P(m, t) = \delta[m - \overline{m}(t)]$, $s_0 = 10^2$; b: 1) $s_0 = 10^2$; 2) $s_0 = 10^3$; 3) $s_0 = 10^4$; 4) $s_0 = 10^5$; c: 1) $s_0 = 10^2$; 2) $s_0 = 10^3$; 3) $s_0 = 10^4$.

The moments of distribution of the number of fissions in the limited chains $\overline{N}^k$ occur in Eq. (9). Explicit expressions are also required below for $g(\gamma p)$ and W_0. Let us determine these expressions. We denote by $W_g(N)$ the probability density of N fissions in a limited chain excited by neutrons from a single fission, and we denote by k the prompt neutron multiplication factor. Taking into account that the probability of a neutron source causing fission is equal to k/ν, we can write

$$W_n(N, t) = \left(1 - \frac{k}{\nu}\right)\delta(N) + \frac{k}{\nu}W_g(N-1, t).$$

(11)

For W_0 and $W_g(N)$ we can use the following expressions obtained in [7]:*

$$W_0 \approx \frac{2.5(k-1)}{\nu};$$

(12)

---

* In the derivation of Eq. (13) a Poisson distribution is assumed for ν. This approximation introduces an additional inaccuracy into the result. However, the fluctuations being investigated are due to a large extent to the fact that each neutron can or cannot cause fission. For example, the fluctuation pattern remains the same qualitatively and in the case when ν neutrons are emitted in each fission event (see [7], p. 716). Consequently, the inaccuracy mentioned can be assumed to be unimportant.

$$W_g(N) = \frac{e^{-k}(ke^{-k})^N (N+1)^N}{(N+1)!} \cdot \tag{13}$$

We have altered formula (13) somewhat in view of our original assumptions: the factorial is replaced by its asymptotic expression and for the purpose of normalizing $W_g(N)$ to unity and the δ-function for $N = 0$ is added to the altered distribution. As a result we obtain

$$g(\gamma p) \approx 1 - \frac{k}{v}$$
$$+ \frac{1}{v}\left\{k - \sqrt{\frac{2}{\pi}}\left[1 - \sqrt{\pi}\alpha_0 + \alpha_0 - \frac{\alpha_0^2}{6}\right]\right\} e^{-\gamma p}$$
$$+ \frac{1}{v}\sqrt{\frac{2}{p}}\left(1 - \sqrt{\pi}\alpha + \alpha - \frac{\alpha^2}{6}\right); \tag{14}$$

$$\overline{N^n} \approx \frac{1 \cdot 3 \ldots (2n-3)}{v \, |\Delta k|^{2n-1}}, \tag{15}$$

where $\alpha_0 = k - \ln k - 1$; $\alpha = \alpha_0 + \gamma p$; $\Delta k = k - 1$. The numerator in Eq. (15) is equal to unity for $n = 1$.

The distribution m is suitable for characterizing a fractional mean square fluctuation F:

$$F = \frac{(\overline{m^2} - \overline{m}^2)}{\overline{m}^2}.$$

For constant values of k and s_0, the quantity F has very simple expressions. For a stable distribution, i.e., for $t \to \infty$ and for zero initial values of the moments

$$F(\infty) = \frac{A}{2B}\left(\frac{D}{B} + \frac{C}{A}\right) - 1 \quad \text{for} \quad \gamma\overline{N} > 1;$$
$$F(\infty) = \frac{A}{2B}\left(\frac{C}{A} - \frac{D}{B}\right) - 1 \quad \text{for} \quad \gamma\overline{N} < 1, \tag{16}$$

where $A = \lambda(\gamma\overline{N} - 1)$; $B = \gamma\overline{N}s_0$; $C = \lambda + 2\gamma\overline{N}(s_0 - \lambda) + \lambda\gamma^2\overline{N}^2$; $D = s_0\gamma^2\overline{N}^2$. The fluctuation $F(\infty)$ strongly decreases with increase of Δk and s_0: $F(\infty) \sim 1/s_0(\Delta k)^2$. The dependence of $F(\infty)$ on Δk for values of s_0 equal to 10^2, 10^3, 10^4, and 10^5 n/sec is represented in Fig. 1. The following values for the parameters are used in the calculation: $\lambda = 1$ sec^{-1}; $\beta_{eff} = 3 \cdot 10^{-3}$; $v = 2.63$.

Determination of P(m, t) and W(t)

In order to determine W(t) it is necessary to find the explicit form of P(m, t). The function P(m, t) can be obtained by solving Eq. (7) by the method of characteristics and the inverse Laplace transformation. However, this route would need a very large number of calculations. We have solved the problem approximately, having aimed at reproducing only the most probable sections of the distribution. The distribution P(m, t) was represented by an expression of the form

$$P(m, t) = \left(1 - \sum_{l=0}^{n} \frac{a_l}{b^l q}\right)\delta(m) + \sum_{l=0}^{n} a_l e^{-b^l qm}, \tag{17}$$

where q and a_l are time-dependent quantities; b is a constant factor; $\delta(m)$ is a delta-function.

In this representation, Eq. (7) is transformed into a system of (n + 2) ordinary differential equations for the unknown functions q, $a_0, \ldots, a_n$:

$$\sum_{l=0}^{n}\left[f_l^{(1)}(p_i)\frac{dq}{dt} + f_l^{(2)}(p_i)\frac{da_l}{dt}\right] = \Phi(p_i), \tag{18}$$

738

where

$$f_i^{(1)}(p_i) = \frac{a_l p_i (2b^l q + p_i)}{b^l q^2 (b^l q + p_i)^2} \; ;$$

$$f_i^{(2)}(p_i) = -\frac{p_i}{b^l q (b^l q + p_i)} \; ;$$

$$\Phi(p_i) = \varphi_2(p_i) - \sum_{l=0}^{n} \frac{a_l}{(b^l q + p_i)} \left[\frac{p_i \varphi_2(p_i)}{b^l q} + \frac{\varphi_1(p_i)}{b^l q + p_i} \right] , \; i = 1, 2, \ldots, (n+2)$$

Here, $p_1, p_2, \ldots, p_{n+2}$ are fixed values of the parameter p. The values of p_i should be chosen such that the most important parts of the distribution $P(m, t)$ are obtained with a high degree of accuracy. It is desirable to do this so that $\log p_i$ is of a single order from $\log(\lambda/s_0)$. If, for example, $n = 3$, $\lambda/s_0 = 10^{-3}$, then we can take $p_1 = 10^{-1}$, $p_2 = 10^{-2}$, $p_3 = 10^{-3}$, $p_4 = 10^{-4}$, and $p_5 = 10^{-5}$.

In the chosen representation, $m(\rho, t)$ is determined in the following way:

1) for $\quad \varrho \leqslant 1 - \sum_{l=0}^{n} \frac{a_l}{b^l q} \qquad m(\varrho, t) \equiv 0;$ (19)

2) for $\quad \varrho > 1 - \sum_{l=0}^{n} \frac{a_l}{b^l q} \quad m(\varrho, t)$ is equal to the root of unity of the equation

$$\sum_{l=0}^{n} \frac{a_l}{b^l q} e^{-b^l q m(\rho, t)} = 1 - \varrho.$$ (20)

Equations (5), (18) - (20) are solved numerically.

The experimental value of $W(t)$, obtained on the American "Godiva" reactor [11] is compared in Fig. 2 with the value of $W(t)$ calculated from Eqs. (5), (18) - (20) for $n = 0$. The experiment was carried out for $s_0 = 90$ n/sec (spontaneous fission). The reactivity $\Delta k \approx 3.5 \cdot 10^{-4}$ was injected rapidly after maintaining the reactor for 15 sec at the level of delayed criticality. The additional source from decay of the delayed neutron precursors, accumulated during the 15 sec of holding, was approximately 200 n/sec. The following values for the parameters are used in the calculations: $\lambda = 0.313$ sec^{-1}; $\beta_{eff} = 5.43 \cdot 10^{-3}$; $s_0 = 90$ n/sec; $\nu = 2.63$; $\Delta k = 3.5 \cdot 10^{-4}$; $p_1 = 3 \cdot 10^{-3}$; $p_2 = 3 \cdot 10^{-4}$. The initial distribution (17) was established with respect to the moment (9), calculated for the holding time of 15 sec. It can be seen that even with the rough representation for $n = 0$, the calculated distribution $W(t)$ is very close to the actual distribution.

The most simple representation in the form of Eq. (17) has the form

$$P(m, t) = q e^{-q m}.$$ (21)

For constant values of s_0 and Δk the problem can be solved analytically. Comparison with more precise calculations shows that a rough solution for $P(m, t)$ in the form of Eq. (21) gives a qualitatively correct estimate of the distribution $W(t)$. In this case

$$W(t) = \frac{W_0}{r} \left(s_0 + \frac{\lambda}{rq} \right) e^{-W_0 s_0 t},$$ (22)

where

$$q(t) = \varphi_3 \left[\left(\frac{\varphi_3}{q(0)} - \frac{\varphi_2}{p} \right) e^{\varphi_3 t} + \frac{\varphi_2}{p} \right]^{-1} ;$$

$$r(t) = \frac{\lambda W_0}{\varphi_3} \left(\frac{1}{q} - \frac{1}{q(0)} + \frac{\varphi_2 t}{p} \right) + 1.$$

The distributions $W(t)$ obtained by means of Eq. (22) for different values of Δk and s_0 are shown in Fig. 3a, b

739

and c. It is assumed in the calculations that for $\Delta k = 1.4 \cdot 10^{-4}$, $s_0 = 10^2$ and 10^3 and for $\Delta k = 3.5 \cdot 10^{-4}$, $s_0 = 10^2$ $\lambda = 0.313$ sec^{-1}, $\beta_{eff} = 5.43 \cdot 10^{-3}$; in the remaining cases $\lambda = 1$ sec^{-1} and $\beta_{eff} = 3 \cdot 10^{-3}$. Calculations made without taking account of delayed neutrons are shown by broken line. It can be seen from the figures that for small values of Δk and s_0 the delayed neutrons significantly change the course of $W(t)$. For example, for $\Delta k = 1.4 \cdot 10^{-4}$ and $s_0 = 10^2$, the delayed neutrons shorten the average time for establishing the first stable chain by a factor of 11.

We shall show, in conclusion, how important it is to know the distribution $P(m, t)$ for calculating $W(t)$. If we calculate the increase in intensity of the delayed neutrons by means of the usual kinetic equations, then we should have

$$W(t) = W_0 \left[s_0 + \frac{\lambda B}{A}(e^{At} - 1) \right] \exp \left\{ -W_0 \times \left[\left(s_0 - \frac{\lambda B}{A} \right) t + \frac{\lambda B}{A^2}(e^{At} - 1) \right] \right\} . \qquad (23)$$

Curve 5 in Fig. 3a represents $W(t)$, calculated by Eq. (23) for $\Delta k = 1.4 \cdot 10^{-4}$ and $s_0 = 10^2$. Comparison shows that the average time for establishing the first stable chain in the given case, calculated by means of the kinetic equations, is approximately 20 times less than the actual time. Be increasing Δk and s_0 the magnitude of $P(m, t)$ becomes increasingly less extensive and the distribution (23) approaches the actual value. By means of Eq. (23) the range of values of Δk and s_0 can be established for which there is no point in taking account of the delayed neutrons; they can be neglected is the condition

$$\frac{\lambda \beta_{eff} \nu}{s_0 (\Delta k)^2} \leqslant 1$$

is fulfilled.

LITERATURE CITED

1. W. Matthes, Nucleonik, 4, 213 (1962).
2. V. G. Zolotukhin and A. I. Mogil'ner, Atomnaya énergiya, 15, 11 (1963).
3. L. Pal, J. Nucl. Energy, Parts A/B, 17, 395 (1963).
4. H. Hurwitz et al., Nucl. Sci. and Engng, Part I, II, 15, 166, 187 (1963).
5. G. Bell, Ann. Phys., 21, 243 (1963).
6. G. Bell, W. Anderson, and D. Galbraith, Nucl. Sci. and Engng, 16, 118 (1963).
7. G. Hansen, Nucl. Sci. and Engng, 8, 709 (1960).
8. A. B. Govorkov, Atomnaya énergiya, 13, 152 (1962).
9. D. McMillan and M. Storm, Nucl. Sci. and Engng, 16, 369 (1963).
10. E. Courant and P. Wallace, Phys. Rev., 72, 1038 (1947).
11. T. Wimett et al., Nucl. Sci. and Engng, 8, 691 (1960).

THE SHAPE OF THE SPECTRUM OF MODERATED NEUTRONS IN ABSORBING MEDIA

(UDC 539.125.52)

V. N. Avaev

An approximate method is discussed for solving the kinetic equation for an infinite homogeneous medium with uniformly distributed sources for the conditions $\Sigma_s = \text{const}$ and $\Sigma_c \approx \dfrac{1}{\sqrt{E}}$.

A simple analytical expression is obtained for determining the shape of the spectrum. The shape of the spectrum, calculated on the basis of this expression, has been compared with that obtained experimentally.

The shape of the spectral distribution of moderated neutrons gives some valuable information which is essential for an accurate calculation of the characteristics of a nuclear reactor and its biological shielding.

The space-energy distribution of the moderated neutrons is described by the Boltzmann kinetic equation, which for the stationary state is written in the form

$$\Omega\nabla\varphi + \Sigma\varphi = \int_{u-\epsilon}^{u} du' \int d\Omega' \Sigma_s \varphi(\mathbf{r}, \Omega', u') f(\mu_0, u-u') + S(\mathbf{r}, \Omega, u). \qquad (1)^*$$

Equation (1) in the general form is insolvable, and therefore it is not possible to find an analytical relationship by means of which the shape of the spectral distribution can be determined, and also the fluxes of neutrons of various energies in arbitrary media. For infinite homogeneous media with uniformly distributed sources, Eq. (1) is simplified somewhat:

$$\Sigma\varphi = \int_{u-\epsilon}^{u} du' \Sigma_s \varphi(u') f_0(u-u') + S(u). \qquad (2)$$

It is well-known that a precise solution of Eq. (2) is possible only in the case when the single moderating element is hydrogen.† For heavier moderators ($\mu > 1$) there is no precise solution of Eq. (2). Approximate solutions of Eq. (2) are described in [3]. A discussion of the results of approximate methods of solving Eq. (2) is given below.

Approximate Method of Solving the Kinetic Equation for an Infinite Medium

In order to discuss the approximate method of solving Eq. (2) we shall assume that 1) $\Sigma_s = \text{const}$ and is entirely governed by elastic scattering; 2) Σ_c varies according to a $1/\sqrt{E}$ law; 3) the probability of a neutron with lethargy u' having a lethargy u after scattering is described by the equation

---

* The conventional symbols of [1] are used.
† The precise solution of Eq. (2) for elements of arbitrary mass without absorption is given in [2].

741
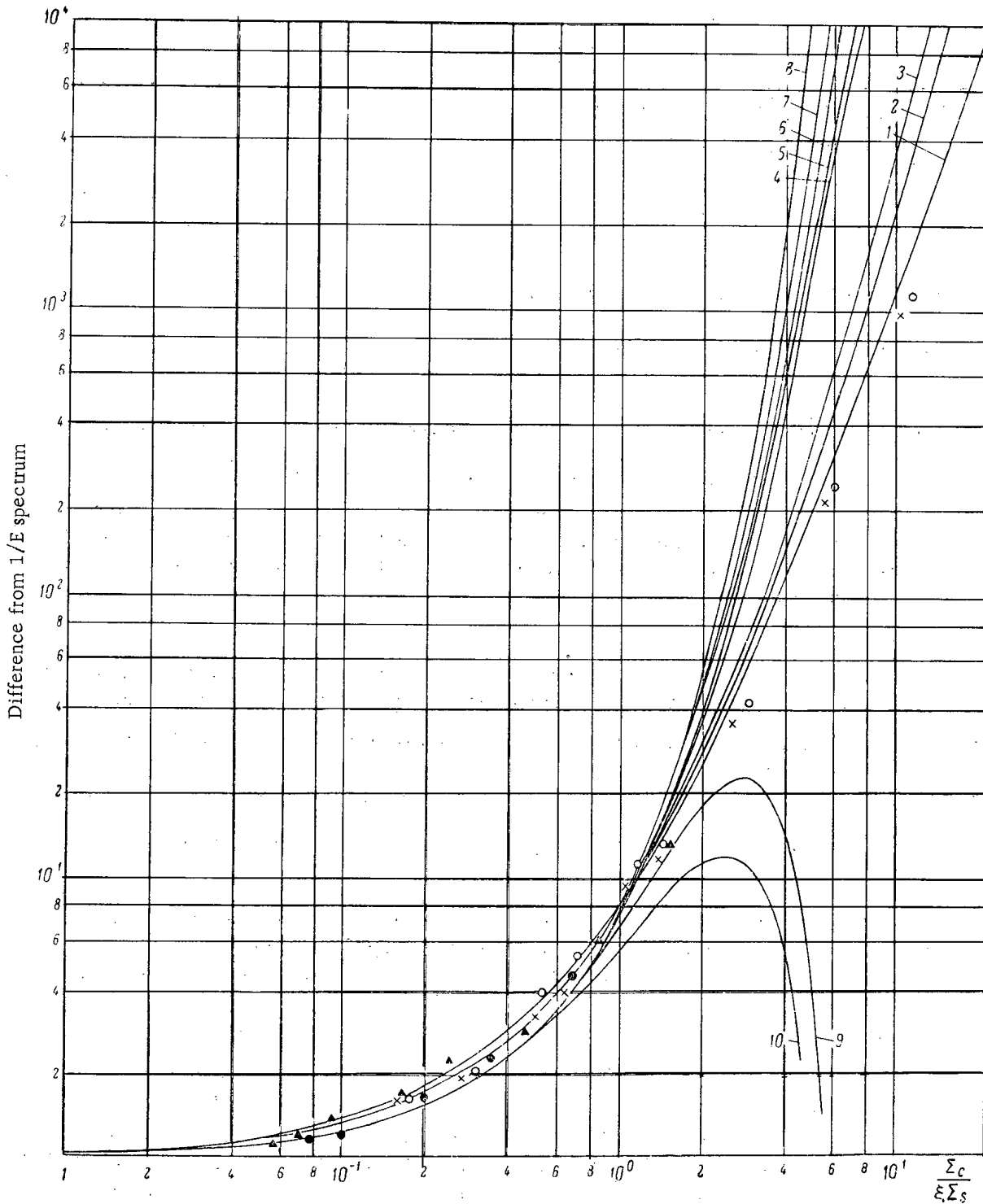
Difference from a 1/E spectrum as a function of $\Sigma_c/\xi\,\Sigma_s$. Calculated data: 1) approximation of this paper; 2, 4, 6) Wigner approximation for $\xi = 0.72$; 0.2 and 0.1 respectively; 3, 7) Grühling - Hertzel approximation for $\xi = 0.72$ and 0.1 respectively; 5, 9, 10) calculated on the basis of Eq. (17) for $\xi = 0.157$; 0.72 and 1.0 respectively; 8) Fermi approximation. Experimental data: ▲) shape of spectrum in iron; ●) shape of spectrum in a mixture of iron, polethylene and boron; ×) shape of spectrum in a mixture of boron with carbon; O) shape of spectrum in a mixture of iron with boron carbide.

$$f(u - u') = \frac{1}{1-\alpha} e^{-(u-u')}. \tag{3}$$

where α is the minimum value of the ratio of the neutron energy after scattering to its energy prior to scattering. The function $f(u - u')$ is determined from Eq. (3) over the range $u' \geq u \leq u' + \ln 1/\alpha$ and over the remaining range $f(u - u') = 0$. This conditions is allowed for by choosing the integration limits in Eq. (2). After differentiating Eq. (2) with respect to the variable u and after several transformations we obtain

$$\Sigma \frac{d\varphi}{du} + \left(\frac{\Sigma_c}{2} - \frac{1}{1-\alpha}\Sigma_s\right)\varphi(u) + \int_{u-r}^{u} du' \sum_s \varphi(u') \frac{1}{1-\alpha} e^{-(u-u')} + \frac{e^{-r}}{1-\alpha}\sum_s \varphi(u-r) = \frac{dS}{du}. \tag{4}$$

Having used Eq. (2) we convert expression (4) to the form

$$\Sigma \frac{d\varphi}{du} + \left(\frac{3}{2}\Sigma_c - \frac{\alpha}{1-\alpha}\Sigma_s\right)\varphi(u) + \frac{e^{-r}}{1-\alpha}\Sigma_s \varphi(u-r) - S = \frac{dS}{du}. \tag{5}$$

The expression $\varphi(u - r)$ is expanded in Taylor series

$$\varphi(u - r) = \varphi(u) - r\frac{d\varphi}{du} + \frac{r^2}{2!} \cdot \frac{d^2\varphi}{du^2} + \cdots \tag{6}$$

We limit Eq. (6) to the first two terms of the expansion and we take into consideration that $r = \ln\left(\frac{\mu+1}{\mu-1}\right)^2$, $\alpha = \left(\frac{\mu-1}{\mu+1}\right)^2$ and $\xi = 1 + \frac{(\mu-1)^2}{2\mu}\ln\left(\frac{\mu-1}{\mu+1}\right)$. Then expression (5) is written in the form

$$(\Sigma_c + \xi\Sigma_s)\frac{d\varphi}{du} + \frac{3}{2}\Sigma_c\varphi = S + \frac{dS}{du}. \tag{7}$$

We introduce the function $\psi(u)$ which is related to $\varphi(u)$ by the relationship

$$\psi = \varphi(\Sigma_c + \xi\Sigma_s). \tag{8}$$

We express $d\varphi/du$ via $d\psi/du$ in Eq. (7) and, using the relationship connecting the moderation density q(u) with $\varphi(u)$ we obtain the system of equations:

$$\left.\begin{array}{l} \dfrac{d\psi}{du} + \Sigma_c\varphi = S + \dfrac{dS}{du}; \\[2mm] \dfrac{dq}{du} + \Sigma_c\varphi = S. \end{array}\right\} \tag{9}$$

On the basis of this system of equations we can write

$$\psi(u) = q(u) + S(u); \tag{10}$$

$$\frac{dq}{du} + \frac{\Sigma_c}{\Sigma_c + \xi\Sigma_s} q(u) = \frac{\xi\Sigma_s}{\Sigma_c + \xi\Sigma_s} S(u). \tag{11}$$

The solution of the differential Eq. (11) has the form

$$q(u) = \int_{-\infty}^{u} S(u') \frac{\xi\Sigma_s}{\xi\Sigma_s + \Sigma_c(u')} e^{-\int_{u'}^{u}\frac{\Sigma_c(u'')}{\xi\Sigma_s + \Sigma_c(u'')}du''} du'. \tag{12}$$

Taking into account that $\Sigma_s = \text{const}$ and Σ_c $1/\sqrt{E}$, we write Eq. (12) in the form

$$q(u) = \int_{-\infty}^{u} S(u') \frac{\xi\Sigma_s [\xi\Sigma_s + \Sigma_c(u')]}{[\xi\Sigma_s + \Sigma_c(u)]^2} du'. \tag{13}$$

743

In the case of a point source, for which $S(u) = S_0 \delta(u - u_0)$, we obtain the expressions for $q(u')$ and $\varphi(u)$:

$$q(u) = \frac{S_0 \xi \Sigma_s [\xi \Sigma_s + \Sigma_c(u_0)]}{[\xi \Sigma_s + \Sigma_c(u)]^2} \; ; \tag{14}$$

$$\varphi(u) = \frac{S_0 [\xi \Sigma_s + \Sigma_c(u_0)]}{(\xi \Sigma_s)^2 \left(1 + \frac{\Sigma_c(u)}{\xi \Sigma_s}\right)^3} + \frac{S_0 \delta(u - u_0)}{\xi \Sigma_s + \Sigma_c(u)} \; . \tag{15}$$

It should be noted that expressions (12) – (15) for $\xi = 1$ completely coincide with the analagous expressions obtained by the precise solution of Eq. (2) when hydrogen is the sole moderating element.

The method of solving Eq. (2) given above was considered for a medium consisting of similar nuclei. If, however, the medium consists of nuclei of different elements then, assuming that $\psi = \varphi \left(\sum\limits_{k} \Sigma_{ck} + \sum\limits_{k} \xi_k \Sigma_{sk} \right)$,

where the suffix k refers to a nucleus of the n-th species, in order to determine q(u) we obtain an expression similar to Eq. (11)

$$\frac{dq}{du} + \frac{\sum\limits_{k} \Sigma_{ck}}{\sum\limits_{k} \Sigma_{ck} + \sum\limits_{k} \xi_k \Sigma_{sk}} q(u) = \frac{\sum\limits_{k} \xi_k \Sigma_{sk}}{\sum\limits_{k} \Sigma_{ck} + \sum\limits_{k} \xi_k \Sigma_{sk}} S(u). \tag{16}$$

It is easy, from Eq. (12), to obtain the relationships similar to expressions (13)-(15) for media consisting of a mixture of different nuclei.

We compare the expressions obtained for fluxes of moderated neutrons with the results of the solution of Eq. (2) by various methods. We carry out the comparison for a point source on the assumption that the absorption cross section for the energy of the source neutrons is greater than the energy of the neutron fluxes being determined. These assumptions are introduced for convenience of calculation as well as for the possibility of comparing the results of the calculation with experiment. The results of this comparison are given in the figure and show by what factor the neutron flux is reduced in the medium with absorption in comparison with the neutron fluxes in the same medium but without taking account of absorption.

Curve 1 (see figure) is drawn on the basis of the solution of Eq. (2) for a pure hydrogen moderator and, according to the data of this paper, for a moderator of any composition. The figure also shows the curves obtained on the basis of the Fermi, Wigner and Grühling-Hertzel approximations. In addition, the spectral distributions were calculated by the equation

$$\varphi(u) = \frac{1}{\xi(\Sigma_s + \Sigma_c)} e^{-\left\{\left(\mu + \frac{1}{\xi}\right)\frac{\Sigma_c}{\Sigma_s} - \frac{1}{3}\mu\left(\frac{\Sigma_c}{\Sigma_s}\right)^2\right\}} \; . \tag{17}$$

This expression is the asymptotic solution of Eq. (2) $\dfrac{\Sigma_c}{\Sigma_s} = \dfrac{\text{const}}{\sqrt{E}}$ and neglects the terms $\left(\dfrac{\Sigma_c}{\Sigma_s}\right)^2$ and

$\mu\left(\dfrac{\Sigma_c}{\Sigma_s}\right)^2$. It can be seen from the figure that the difference from a 1/E spectrum, i.e., the shape of the spec-

trum, for the ratio $\Sigma_c/\xi \Sigma_s$ changing from 0 to 1.3 - 1.4 is almost identical for all the approximations, with the exception of the approximation in which Eq. (17) is used. With this approximation, agreement is observed for a value of $\Sigma_c/\xi \Sigma_s < 0.8$. The maximum difference in the shape of the spectrum amounts in these regions to about 20%; the least difference from the 1/E spectrum is given by the Fermi approximation and the maximum difference by the approximation used in this paper. For values of $\Sigma_c/\xi \Sigma_s > 1.4$ (and for the results obtained by using Eq. (17) for $\Sigma_c/\xi \Sigma_s > 0.8$) the shape of the spectrum determined by the various methods differs considerably, and this difference increases with increase of the ratio $\Sigma_c/\xi \Sigma_s$. It should be noted that the shape of the spectrum determined by the Wigner and Grühling-Hertzel approximations and also from Eq. (17) depends significantly on the quantity ξ for a constant value of $\Sigma_c/\xi \Sigma_s$. It can be seen from the figure that with the same ratio $\Sigma_c/\xi \Sigma_s$ the difference from the 1/E spectrum for these approximations increases with increase of ξ.

744

Experimental Verification

The spectral distribution of the neutrons was studied on a water-cooled/water-moderated research reactor. In order to carry out the measurements, the material being studied was loaded into an experimental box located in the reactor shielding.

The shape of the neutron spectrum in the range of energies from 0.46 eV to 6 keV was determined by resonance indicators. For processing the results the method of "subtraction of the $1/\nu$ contribution" was used, and the shape of the spectrum was determined by the method of comparing with the 1/E spectrum. The detailed characteristics of the indicators are given in [4] and also the special features of the method used for determining the shape of the spectrum. We shall recount briefly the main propositions of paper [4].

The use of resonance indicators for determining the shape of the spectrum in strongly-absorbing media is associated with the need for taking into account accurately the contribution of secondary resonances in the total activity of the indicator. The point is, that the characteristics of secondary resonances of high energies are not always well-known. In order to investigate the feasibility of using the resonance indicator method in strongly absorbing media, control experiments were carried out in which the shape of the steady-state spectrum was measured in mixtures of polyethylene with boron carbide with a weight ratio of 1:1.5 and 1:4 respectively. From the fact that the ratio

$$\frac{\Sigma_s \text{ (hydrogen)}}{\xi\Sigma_s(\text{boron}) + \xi\Sigma_s \text{ (carbon)}}$$
is equal to 20 for the first mixture and 7.2 for the second mixture, it was assumed that

the spectral shape was not changed significantly as a result of moderation by carbon and boron and, with quite good accuracy, can be calculated on the basis of the equation defining the shape of the spectrum in a pure hydrogen-containing medium. Comparison of the experimental and calculated spectral shapes showed that for indicators with energies of 18.8 eV and above there is good agreement. For indicators which determine the flux of neutrons with energies of 1.46 eV (indium) and 4.9 eV (gold), the discrepancy was attributed to the contribution of secondary resonances with unknown characteristics, whose effect was not taken into account in calculating the spectral shape. In [5], the presence of resonances was indicated over the range of energies 100 and 300 eV for indium and gold respectively. In view of the fact that these resonances are found over quite a narrow energy range, they were substituted arbitrarily by a single resonance. The resonance energy for indium was taken as 100 eV and for gold −300 eV. On the basis of the calculated shape of the spectrum the characteristics of these resonances were determined for the first mixture. The fluxes of neutrons with energies of 1.46 and 4.9 eV were calculated for the second mixture, using these characteristics, and proved to be close to the calculated values. An indicator with a resonance at 0.46 eV (europium) was found unsuitable for determining the neutron fluxes for these media, since the difference between the total activity of the indicator and the activity due to secondary resonances is comparable with the measurement error.

It should be noted that prior to proceeding with measurements of the spectral distributions in mixtures of polyethylene and boron carbide, despite the evidence, the applicability of the above-mentioned theoretical results towards actual experimental conditions was verified. For this, the spectral distributions were measured in iron and in mixtures of iron with polyethylene and boron, for which $\Sigma_c / \xi \Sigma_s = 1.4$, and the shape of the spectrum is almost independent of the approximation used.

As would be expected, at a distance of several mean free paths from the source the steady-state shape of the spectrum is in good agreement with the shape of the spectrum calculated on the basis of Eq. (2) for point sources of neutrons with energies greater than the energy of the neutron fluxes being determined. Moreover, for the majority of indicators, the calculated contribution of secondary resonances to the total activity was found to be insignificant. Consequently, the characteristics of the secondary resonances could have no significant influence on the measurement results.

The experimental verification of the applicability of the various methods of approximation for solving Eq. (2) for $\Sigma_c / \xi \Sigma_s > 1.4$ was carried out in two media: a mixture of graphite and boron (about 7% by weight of boron) and a mixture of iron with boron carbide (~1.65% by weight of B_4C).

The stable shape of the spectrum in these media (see figure) within the limits of experimental measurement errors, and also of the errors associated with some inaccuracy in determining the concentration of boron in these mixtures, coincides with the shape of the spectrum calculated on the basis of the approximate solution of this paper.

The method proposed for solving the kinetic equation without taking account of the space dependence of the neutron flux enabled an analytical expression to be found for determining the spectral shape in uniform media in which Σ_s = const and $\Sigma_c \approx 1/\sqrt{E}$. The experimental verification confirmed the feasibility of using the expression obtained for media with a maximum value of the ratio $\Sigma_c/\xi\Sigma_s$, equal to 10. The applicability of the expression obtained for determining the spectral shape of moderated neutrons in media with $\Sigma_c/\xi\Sigma_s > 10$ requires further experimental proof.

The author expresses his thanks to Yu. A. Egorov for assistance in the project, to M. E. Netech, A. V. Nikitin, and Yu. V. Orlov for useful discussion of the results obtained, and also to A. I. Vasil'ev and G. G. Moiseev for assistance with carrying out the experiment.

LITERATURE CITED

1. G. I. Marchuk, Numerical methods of calculating nuclear reactors, Moscow, Atomizdat [in Russian] (1958).
2. Placrek, Phys. Rev., 69, 429 (1946).
3. Nuclear Reactors, [Russian translation], Moscow, Izd-vo IL, Vol. 1 (1956).
4. V. N. Avaev, Yu. A. Egorov, In the collection: Problems of dosimetry and radiation shielding, Atomizdat [in Russian], Moscow (1965).
5. D. Hughes and L. Harvey, Neutron Cross Sections, BNL—325, New York (1958).

A NEW METHOD OF RECONSTRUCTING TRUE SPECTRA

(UDC 621.039.519.22)

A. N. Tikhonov, V. Ya. Arsenin, A. N. Dumova,

L. V. Mayorov, and V. I. Mostovoi

Translated from Atomnaya Énergiya, Vol. 18, No. 6,
pp. 588-593, June, 1965
Original article submitted June 15, 1964

A new method of solving first order integral equations is proposed, which enables spectra distorted by the measuring instrument to be reconstructed with some meaning. This method is used for processing the results of measuring the energy spectrum of slow neutrons in a uranium-water lattice.

As a result of the great demands for accuracy of experimental data in various problems of reactor physics, it is extremely interesting to study the possibilities which are opened up by mathematical processing of measurement results. Such processing may reduce the demands on the resolving power of the instruments with which the experiments are undertaken and they may indicate what characteristics of the instruments it is necessary to improve in order to obtain the optimum information.

Problems of processing experimental data are related, as a rule, to the class of so-called error problems which up to now have been little studied. In this paper, two examples of the use of the new method of solving error problems are introduced, as developed by A. N. Tikhonov for the Fredholm integral equations of the first order [1].

In the first example we consider the problem of reconstructing the true energy spectrum of epithermal neutrons in the uranium block of a reactor by the results measured with a mechanical selector. The second example is devoted to calculation of the scaler energy flux of thermal neutrons in the moderator of a heterogenous lattice by the measured directional flux. The examples presented illustrate the possibilities of solving certain error problems of reactor physics.

Reconstruction of the True Energy Spectrum in the Uranium Assembly of a Reactor by the Results Measured with a Mechanical Selector

Formulation of the problem and method of solution. Measurements of the energy spectrum of slow neutrons in a heterogeneous reactor assembly becomes more difficult, as is well-known, according to the extent of advancement into the region of resonance absorption. In this region, deep and sharp troughs in the spectrum are observed, which correspond to resonance absorption. Therefore, in order to avoid a large loss of information it is necessary to use instruments with very good resolution. This, in its turn, leads to a reduction in intensity of the radiation being measured, as a result of which the statistical errors of the experiment are increased.

Mathematical processing of the measurement results can reduce the demand on the resolving power of the experimental apparatus. In this paper, preliminary results are presented of this processing of a spectrum in the energy range 0.2 - 200 eV, measured by means of a mechanical selector. The beam of neutrons was emitted from the uranium block of a subcritical uranium-water lattice, parallel to the axis of the block [2].

The general description of the method of measuring neutron spectra by means of a mechanical selector is given in [3], for example, and will not be discussed here.

Distortion of the true spectrum as a result of measurements by mechanical selection methods occurs as a consequence of a number of reasons, of which we shall take into account only the effect of the finite pulse width of the neutrons leaving the rotor and the finite channel width of the time analyzer (the indeterminacy in the flight path,
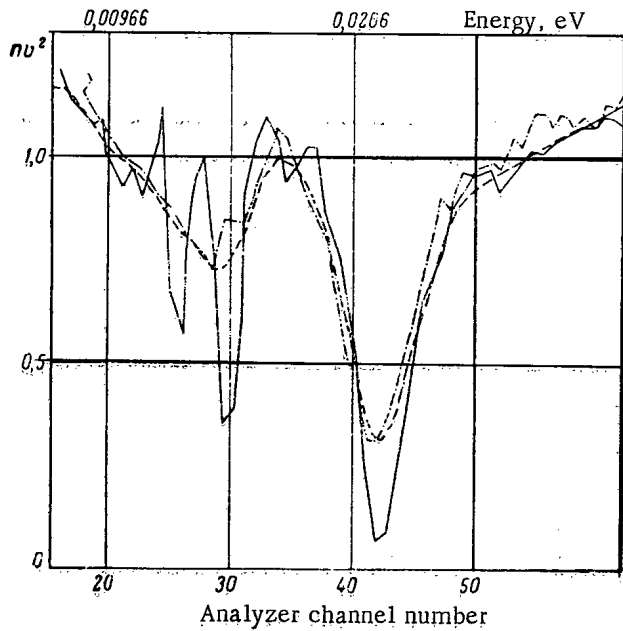
Fig. 1. Spectrum of neutrons in a uranium assembly, measured by means of mechanical selectors with different resolving power σ. The solid line corresponds σ≈4 μsec; the dash-dot line corresponds to σ≈17 μsec; the dotted line represents a simulated spectrogram $u_i^{(3)}$.
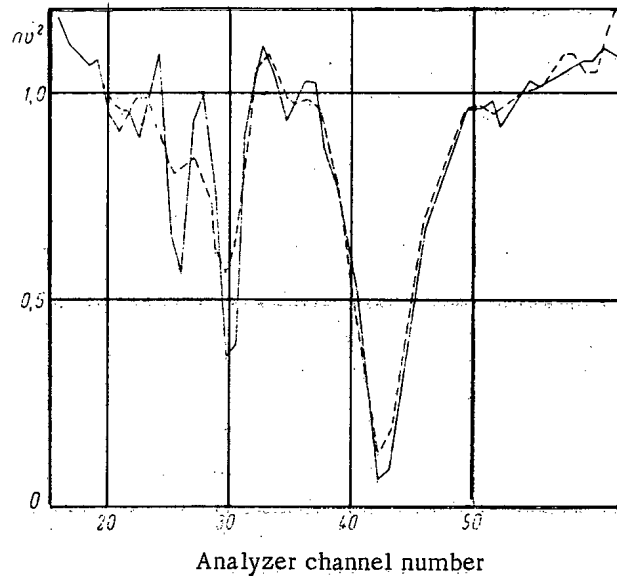
Fig. 2. Reconstruction of the "true" spectrum by the spectrogram. The solid line corresponds to the true spectrum; the dotted line represents the solution of Eq. (8), in which the left hand side is a stimulated spectrogram.

associated with the finite length of the counter, will be neglected). The transmission function of the rotor is taken as equal to unity, since corrections for the neutrons emitted by the rotating rotor, for the energy dependence of the counter sensitivity, losses in air etc., were made in the preliminary processing of the experimental data [2].

In the assumptions made, the number of neutrons u_i, recorded by the i-th channel of the time analyzer is related to the true spectrum of the neutrons emerging from the block, n (t), by the equation

$$u_i = \int_{-\tau/2}^{\tau/2} dt' \int_{-\Delta}^{\Delta} n\,(t_i + t' - t'')\,K\,(t'')\,dt'', \tag{1}$$

Here, i is the channel number; τ is the channel width of the time analyzer; Δ is the half-width of the pulse of neutrons emerging from the rotor of the mechanical selector; $t_i - \tau/2$ is the instant of time corresponding to the start of neutron recording by the i-th channel of the analyzer; n(t) is the neutron density corresponding to the true spectrum of the neutrons incident on the rotor [$t_i = i\tau$ is the time expended by neutrons with a given velocity ν_i on the flight path L between the rotor and the recording counter (L = $t\nu_i$]; K(t") is the pulse shape.

By substituting variables in the integrals of Eq. (1), we reduce it to the form

$$u_i = \int_{t_i-\Delta}^{t_i+\Delta} dt K\,(t_i - t)\,z\,(t), \tag{2}$$

where

$$z\,(t) = \int_{t-\tau/2}^{t+\tau/2} n\,(t')\,dt'. \tag{3}$$

748
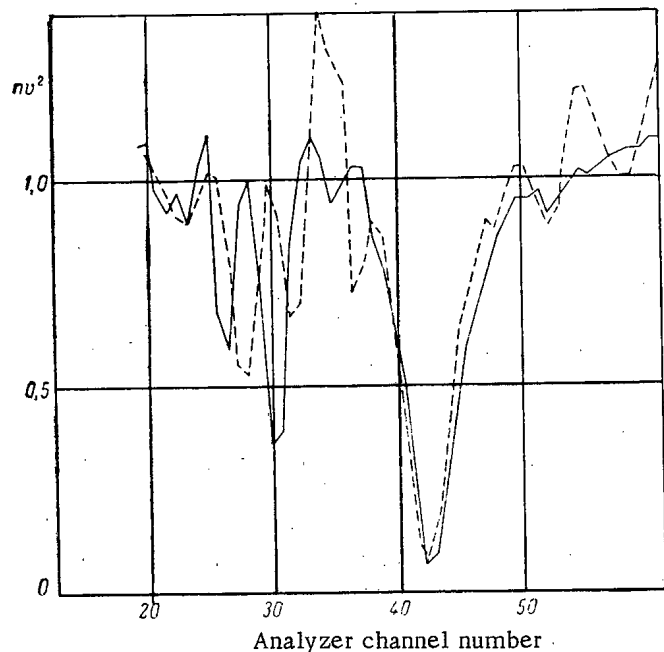
Fig. 3. Reconstruction of the true spectrum by the experimental spectrum ($u_i^{(2)}$). The solid line corresponds to the true spectrum; the dotted line represents the spectrum of neutrons in a uranium assembly, obtained by reconstructing the true spectrum according to the distortion, as a result of measurements by means of a mechanical selector ($\sigma \approx 17\,\mu$sec).

Thus, by solving Eq. (2) it is possible to determine only the integrated averages with respect to an interval of order of the channel width, which better approximate the true spectrum, the lower is the value of τ. These integrated averages $z(t)$ are the solution of an integral equation of the first order, which is solved by the method of regularization [1]. The concept of the method consists in the fact that we find as an approximate value of $z(t)$ the function $z_\alpha(t)$, the realization minimum of the functional

$$F(z) = \int dt \int [K(t,\ t')\,z(t')\,dt' - u(t)]^2\,dt + \alpha\Omega(z).$$

Here, α is a small numerical parameter defined by the mean square measurement error, and

$$\Omega(z) = \int \left(\frac{dz}{dt}\right)^2 p(t)\,dt$$

is the regularizer which enables $z_\alpha(t)$ to be found in a class of quite smooth functions. The problem at the minimum of the functional $F(z)$ reduces to Euler's equation, which is solved by finite-difference methods.

Results. The kernel of Eq. (2) is usually approximated by a Gaussian function of the form $(2\pi\sigma)^{-1/2}$ $\exp(-t^2/2\sigma^2)$ where σ is chosen such that

$$\int_{-\Delta}^{\Delta} K(t)\,t^2\,dt = \frac{1}{\sqrt{2\pi\sigma^2}} \int_{-\infty}^{\infty} t^2 e^{-t^2/2\sigma^2}\,dt. \tag{4}$$

If the rotor of the selector has a rectangular slit, then the width of the neutron pulse (to quite high accuracy) is

$$2\Delta = \frac{s}{\omega R}. \tag{5}$$

Here s is the width of the rotor slit; ω is the angular speed of rotation; R is the rotor radius. At sufficiently high neutron velocities, the shape of the pulse emerging from the rotor is close to triangular [3], therefore,

$$\sigma^2 = \int_{-\Delta}^{\Delta} \frac{1}{\Delta}\left(1 - \frac{|t|}{\Delta}\right) t^2\,dt = \frac{\Delta^2}{6} \tag{6}$$

or

$$\sigma \approx \frac{\Delta}{\sqrt{6}} \approx \frac{s}{\omega R 2\sqrt{6}}. \tag{7}$$

Thus, we obtain the final form of the equation for the function $z(t)$ corresponding to a rotor with a triangular slit:

$$u_i = \int_0^{\infty} \frac{1}{\sqrt{2\pi\sigma^2}}\exp\left[-\frac{(t_i - t)^2}{2\sigma^2}\right] z(t)\,dt. \tag{8}$$

This equation can be solved quite accurately if, firstly the function $z(t)$ varies within the interval of the length τ, and secondly, if the errors of the function u_i being determined experimentally are not too large.

749
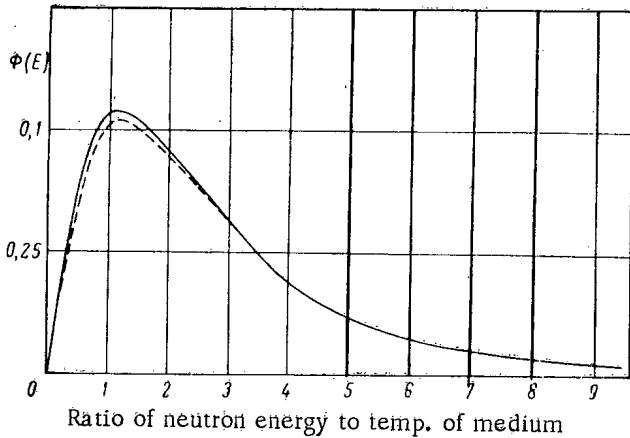
Fig. 4. Directional (——————) and scalar (— — — — —)
neutron fluxes in a uranium-water lattice.

It is necessary to fulfill the requirement of Eq. (1) in order that the integral in the right hand side of Eq. (8) can be represented with good accuracy by some quadratic formula, which gives it an approximate value. No more than N values of the function can be used in this formula, at points separated one from the other by a distance of order τ, since the function u_i as a result of measurement is known at the points t_i: $i = 1, 2, \ldots, N$; $t_i = i\tau$. On the other hand, the kernel of Eq. (8) can differ from zero for $|t_i - t| > \tau$, since in the contrary case it can be considered simply as a δ-function, and it can be assumed that $u_i \approx z(t_i)$.

Processing of the two experimental spectra, corresponding to one and the same true spectrum, measured by means of selectors having different resolving powers. The neutron pulses were recorded by an analyzer with a channel width of $\tau \approx 6$ μsec.

The first experimental ("apparatus") spectrum is obtained on a selector with quite good resolution $\sigma = \sigma_1 = 4$ μsec (s = 0.1 cm; R = 6.76 cm; $\omega = 0.104 \cdot 10^{-2}$). Since in this case $\sigma < \tau$, the "true" spectrum $z^{(1)}(t)$ should differ slightly from the measured spectrum. The function $u_i^{(1)}$ is plotted in Fig. 1 as the solid line.

The second experimental spectrum $u_i^{(2)}$ is obtained on a selector with a worse resolution $\sigma = \sigma_2 = 17$ μsec (s = 0.1 cm; R = 6.76 cm; $\omega = 0.224 \cdot 10^{-3}$ μsec). The function $u_i^{(2)}$ is plotted in Fig. 1 by the dash-dot line and, obviously it is a smoother curve than $u_i^{(1)}$.

In order to verify the validity of the assumptions about the kernel of the integral equation and the accuracy of the experimental data about the spectrum $u_i^{(2)}$, the integrals

$$u_i^{(3)} = \int_{-\infty}^{\infty} \frac{1}{\sqrt{2\pi\sigma_2^2}} e^{-\frac{(t'-t_i)^2}{2\sigma_2^2}} u^{(1)}(t')\,dt'$$

were evaluated.

If $u_i^{(1)}$, in fact, can be assumed to be the true spectrum, then the function $u_i^{(3)}$ should coincide with the measured spectrum $u_i^{(2)}$. The function $u_i^{(3)}$ is plotted as a dotted curve in Fig. 1. It is very close to the experimental spectrum $u_i^{(2)}$, which indicates the validity of the specification of the kernal, but somewhat smoother than $u_i^{(2)}$. The discrepancy, which is observed particularly clearly for channels with numbers $i \approx 30$-35, can be explained by the measurement errors. Consequently, it is not very hopeful that by solving the integral Eq. (2) the true spectrum $u_i^{(1)}$ will be successfully and accurately reconstructed by the spectrum $u_i^{(2)}$ in the vicinity of $i \approx 30$.

In order to demonstrate the feasibility of the method of regularization of the solution of the integral Eq. (2), the spectrum $u_i^{(1)}$ was reconstructed by the simulated spectrum $u_i^{(3)}$. The results are shown in Fig. 2. The fine structure of the spectrum is reconstructed quite well for $i \approx 40$ and somewhat less well for $i \approx 30$. The latter is explained by the fact that the number of points (i.e., the number of analyzer channels), by which the experimental spectrum is defined, is inadequate for describing it accurately, and consequently, the errors of integration with respect to a small number of points give an excessively smooth curve in this region.

On the basis of calculations carried out, it can be concluded that the fine structure of the spectrum can be determined not only by means of more detailed experiments but also by means of a more complete mathematical processing of the measurement results. In this case, bearing in mind the subsequent mathematical processing, it is necessary to improve some or other parameters of the instrument by the appropriate method, by selecting the optimum relationships between them (in the given case these parameters are the speed of rotation of the rotor, the analyzer channel width and the magnitude of the statistical errors).

750

Calculation of the Scalar Energy Flux in a Moderator by the Measured Directional Flux

In measurements of the energy spectrum of thermal neutrons in a reactor lattice the neutron beam, as a rule, is extracted from a certain point of the lattice, parallel to the axis of the block. Thus, the energy spectrum of the directional neutron flux is measured, which may be significantly different from the energy spectrum of the scalar neutron flux and which, in practice, is the most interesting.

For a one-dimensional lattice with isotropic neutron scattering, the scalar energy flux $\Phi(E, r)$ at the point r is related with the energy spectrum of neutrons in the direction of the lattice axis $\Phi_{\parallel}(E, r)$ by the relationship

$$[\Sigma_s(E) + \Sigma_a(E)] \varphi_{\parallel}(E, r) = \int_0^{E\,\lim} \Sigma_s(E, E', r) \Phi(E', r) dE' + S(E, r) \tag{9}$$

(all the symbols here are universal).

If the directional flux $\Phi_{\parallel}(E, r)$ at the point and the characteristics of the medium $\Sigma_a(E)$, $\Sigma_s(E, E')$, $S(E, r)$, are known, the scalar flux at the same point can be determined by solving Eq. (1). The method described above enables a stable solution of this equation to be found.

The determination of the scalar flux in uranium-water lattices are of particular interest. In [4], the directional flux was determined for these lattices by calculating the scalar flux and it was compared with the measured flux. It was shown in this paper that the calculated spectra are slightly sensitive to scattering anisotropy in water. Thus, in order to find the scalar flux in water by the measured directional flux, Eq. (9) can be used.

We shall consider by way of example, a uranium-water lattice for which the energy spectra of the directional flux were measured in [2] at different points of the cell.

The differential scattering cross section of neutrons in water was calculated by the UPRAS (Universal Program for Calculation of Cross sections) program on the assumption that water is described by a crystal model having an acoustic spectrum which is determined experimentally [6], and an optical spectrum with frequencies $\omega_1 = 0.2$ eV and $\omega_2 = 0.4$ eV. The calculated inelastic scattering cross sections agree well with the experimental data. The thermal neutron sources were assumed to be isotropic and they were calculated on the assumption that for an energy $E > 0.25$ eV the epithermal neutron spectrum has a Fermi form CE^{-1} and is independent of the angle. The quantity C was defined as the limit of the experimental directional flux, multiplied by $E [C = E \Phi_{\parallel}(E)]$ at high energies.

Figure 4 shows the graph of the measured directional and calculated scalar neutron fluxes in water at the boundary with the block.

In conclusion, it should be noted that as a result of reconstructing the true spectrum the errors, which distorted the shape of the experimental curve, are increased generally speaking. The problem concerning the optimum choice of the parameter α is associated with how much the measurement data, containing errors, permits the true spectrum to be reconstructed. With too small a value of α, the errors in the reconstructed spectrum become so large that they lead to buildup of the solution obtained. Paper [7] is devoted to the estimation of the errors in the reconstructed spectrum. In addition, a special paper will be devoted to this.

LITERATURE CITED

1. A. N. Tikhonov, Dokl. AN SSSR, 149, 529 (1963).
2. V. I. Mostovoi et al., Atomnaya Énergiya, 13, 547 (1962).
3. V. I. Mostovoi, M. I. Pevzner, and A. I. Tsitivich, In the book: Data of the International Conference on the Peaceful Uses of Atomic Energy, Geneva, 1955, [in Russian], Moscow, Izd-vo AN SSSR (1957), p. 19.
4. H. Honeck and H. Tacahashi, Nucl. Sci. Engng, 15, 115 (1963).
5. L. V. Mayorov, V. F. Turchin, and M. S. Yudkevich, Report No. 360, presented by USSR at the Third International Conference on the Peaceful Uses of Atomic Energy [in Russian], Geneva (1964).
6. P. Egelstaff et al., Proc. Simp. Chalk-River, Vol. 1 (1962), p. 343.
7. A. N. Tikhonov and V. B. Glasko, Zh. vychislitel'noi i matematicheskoi fiziki, 4, 564 (1964).

MEASUREMENT OF NEUTRON SPECTRA IN NICKEL, IRON, AND STAINLESS STEEL

(UDC 621.039.538/539.125.52)

I. I. Bondarenko, V. G. Liforov, V. N. Morozov,

M. N. Nikolaev, V. A. Parfenov, and V. A. Semenov

Measurements of neutron spectra in various media, obtained by the transit-time method in the fast pulse reactor IBR with a resolution of 0.04 μsec/m, are presented. The spectra of neutrons emerging from iron and nickel prisms of various thickness and also those from stainless-steel prisms are studied. The "fine structure" due to the resonance character of the cross sections of the media studied was clearly seen in the spectra measured. The experimental neutron spectra are compared with calculations made with a multigroup system of constants allowing for resonance self-screening of the cross sections. The reasons for the slight discrepancies found are analyzed.

The most widespread methods of measuring space-energy distributions of fast and intermediate neutrons in various media are those based on measuring the spatial dependence of the rates of reactions possessing different energy/cross section relationships [1-5]. Conclusions based on the results of such measurements are not always unequivocal, since at certain points of the set studied it is often necessary to determine the energy spectrum of the neutrons with more precise (and complex) direct methods of neutron spectroscopy, by means of photoemulsion [1, 2], the Wilson chamber [1], He^3 chambers and counters [2, 3], or in some cases by means of resonance detectors [3-5].

All these methods, however, lack the resolving power needed to reveal the "fine structure" of the neutron spectrum, associated with the resonance nature of the cross section, explicitly in the experimental results. At the same time, a study of just this structure is extremely important for checking and developing ideas on the propagation of neutrons in media containing neutron-resonance scatterers and absorbers. I. I. Bondarenko first showed the necessity of considering the resonance structure of cross sections when calculating fast reactors in 1957. Since then a great deal of work has been done on developing methods of allowing for the resonance structure of cross sections in reactor calculations [6-12], studying the influence of resonance effects in macroscopic experiments [13, 14], and developing methods for determining the mean cross-section characteristics needed to allow for resonance effects in reactor calculations [12, 15]. In all these papers, however, the influence of the resonance structure of the cross sections on the propagation of neutrons in matter was considered only from the point of view of determining integral characteristics. Detailed neutron spectra in the resonance region were not examined.

At the present time, the only experimental method making it possible to measure neutron spectra with a high resolving power is the transit-time method. Use of this method for studying the spectrum of fast neutrons retarded in matter is complicated by the fact that the minimum pulse length is determined by the statistical indeterminacy of the slowing -down time, which for nuclei with mass number ~50 is ~15 μsec. Thus, for such investigations we need a pulse source of high intensity, making it possible to increase the resolution on account of the greater transit-time base. Owing to the absence of such a source, it appeared, until recently, impossible to use the transit-time method for studying fast-neutron spectra.

Such a possibility re-emerged with the arrival of the fast pulse reactor IBR [16]. The pulse length of the IBR reactor, equal to ~36 μsec, is great enough for the slowing down of the neutrons in a heavy moderator not to lead to serious prolongation of the pulse. At the same time, the high intensity of the pulse makes it possible to use an

752
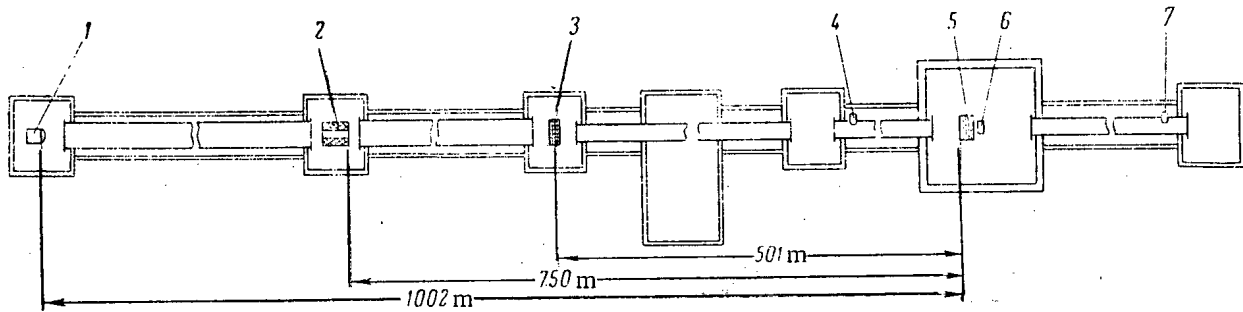
Fig. 1. General arrangement of the experiment: 1) scintillation detector; 2) collimator; 3) boron-counter detector; 4) monitor on 50-m base; 5) prism of material studied; 6) active zone of IBR reactor; 7) monitor on 100-m base.
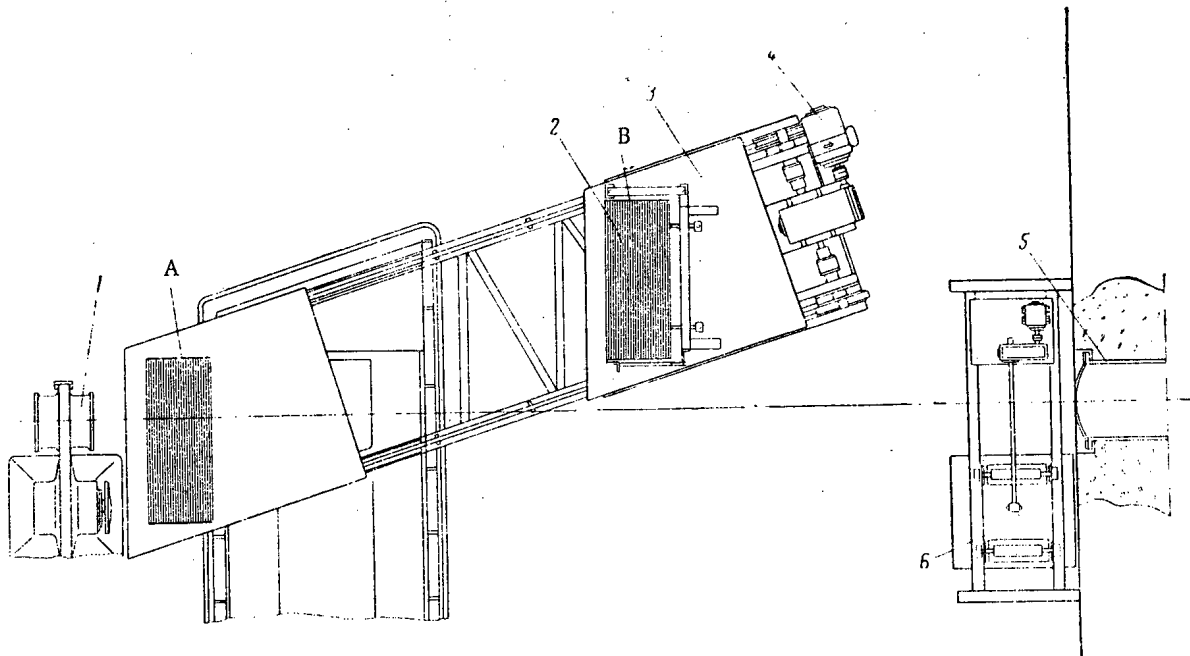
Fig. 2. General view of the disposition of the prism in the reactor room: 1) active zone of IBR reactor; 2) prism of material being studied; 3) platform for moving prism; 4) motor for moving platform; 5) neutron guide; 6) slide; A) position of prism "at the zone;" B) position of prism "at the wall."

extremely large transit-time base (1 km) and thus, ensure a high resolving power of the system. It was, therefore, decided to make a cycle of experiments to study the spectra of neutrons emerging from blocks of nickel, iron, and stainless steel. The choice of materials was based on the following considerations.

As we know, the resonance structure of the nuclei of nickel and iron appears right up to energies of the order of several MeV [4], and in the region of several keV it is extremely strong [6]. A characteristic feature of the resonances in the keV range of energies is the presence of deep interference minima, which exert a very great influence of the diffusion and slowing-down of the neutrons [10]. The effect of interference between resonance and potential scattering arises most strongly in the distribution of neutrons in media containing even-even nuclei (iron, nickel), especially in those cases where one isotope predominates in the natural mixture (iron).

Study of the slowing-down spectrum of neutrons in stainless steel is interesting from the point of view of checking the accuracy of existing methods of describing the propagation of neutrons in a mixture of resonance scatterers [6]. In the choice of materials for study, of course, the important fact that iron, nickel, and stainless steel are widely used in reactor construction was borne in mind.

753
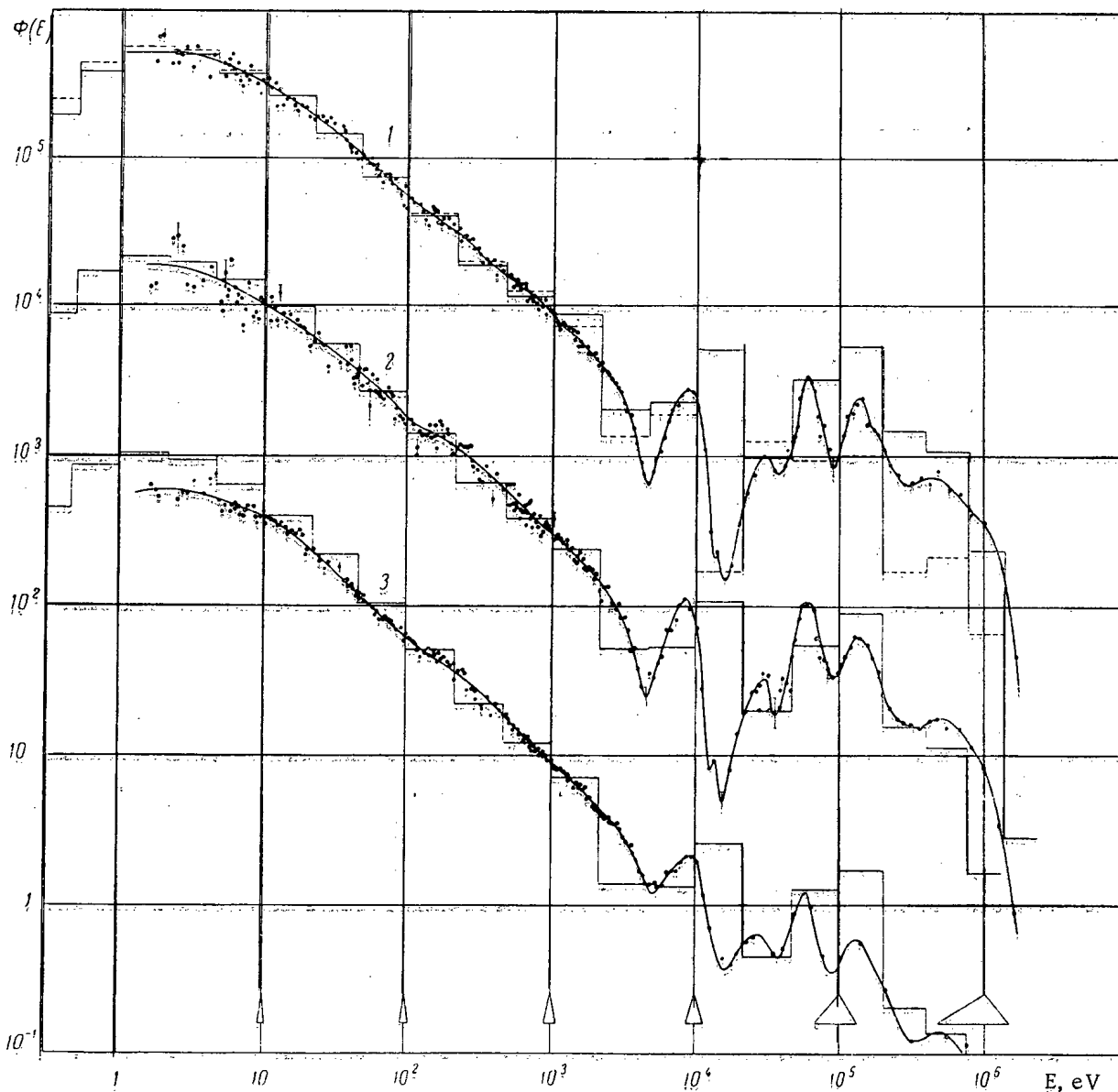
Fig. 3. Spectrum of leakage neutrons from nickel (curves 1, 2, 3, correspond to prism thicknesses of 31, 52, 77 cm).

The spectra of neutrons emerging from nickel prisms 306, 515, and 770 mm thick, iron prisms 300, 480 mm thick, and stainless-steel prisms 300 and 490 cm thick were measured. The transverse dimensions of the nickel prisms were 800×800 mm, and those of the iron and stainless-steel prisms 700×800 mm.

Measuring Methods

The work was conducted on the IBR reactor, which, thanks to high neutron intensity in the pulse ($\sim 10^{17}$ sec^{-1}), made it possible to measure the spectra by the transit-time method at a high resolution ~ 0.04 μsec/m, i.e., to study the neutron spectra for energies below 1 MeV. At 100 keV the resolution was 35%.

The arrangement of the experiment appears in Figs. 1 and 2.

The active zone of the reactor is in the center of a room 10×10×10 mm at a height of 2 m from the floor. The dimensions of the active zone are 250×250×250 mm. The prism of the material to be studied is placed on a platform controlled from the control panel of the reactor. The platform is moved on horizontal rails at an angle of 18° to the axis of the neutron guide. The minimum distance from the active zone to which the prism could be moved is 300 mm. In the other extreme position (at the wall), the prism completely uncovers the neutron guide.

754
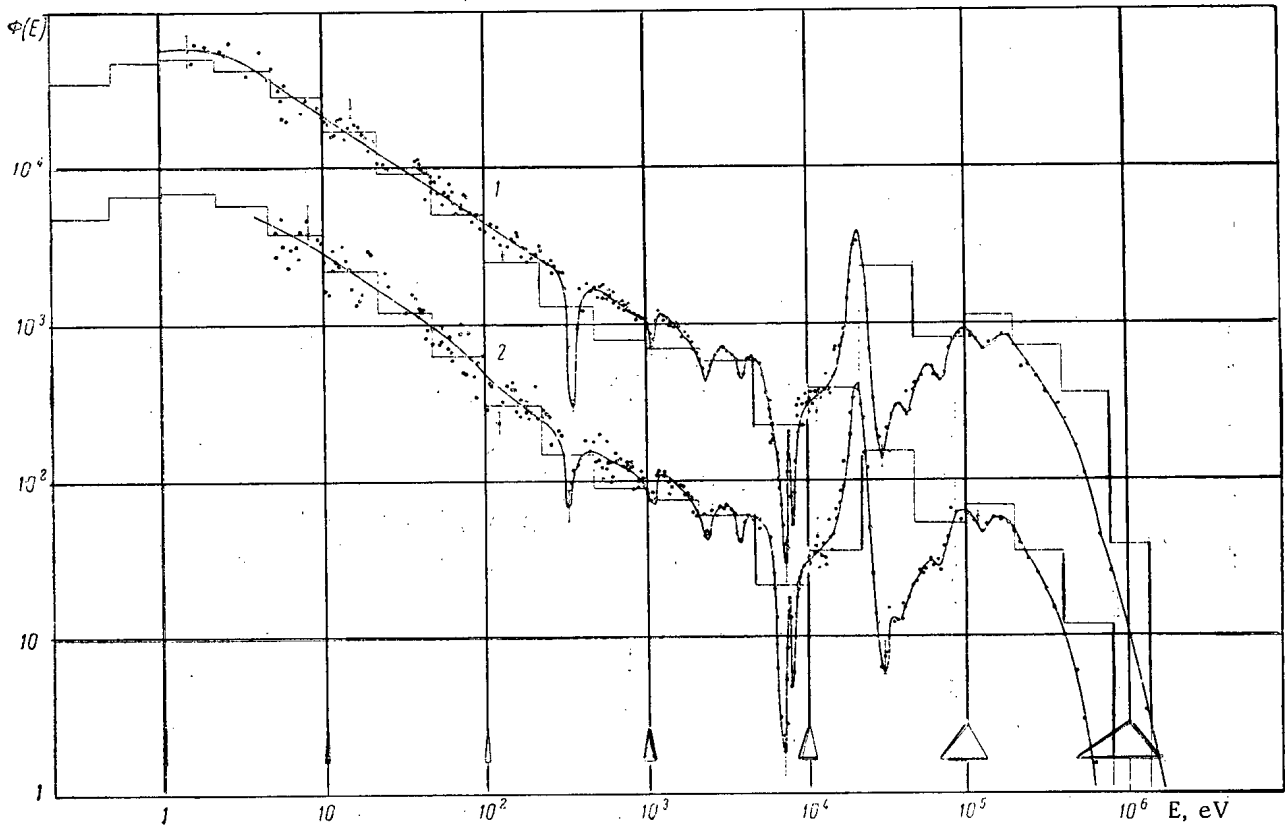
Fig. 4. Spectrum of leakage neutrons from iron (curves 1 and 2 correspond to prism thicknesses of 30 and 49 cm).

The detector lies at the end of the kilometer base (see Fig. 1) at 1002 m from the surface of the prism. The neutrons travel the distance from the reactor to the detector through an evacuated neutron guide. The liquid methylborate scintillation detector used in the measurements is described in [17]. The pulse length of the detector is 1.5 μsec. The thickness of the scintillator in the direction of the beam is 3 cm. The area of the detector is 415 cm^2. The energy dependence of the detector efficiency was determined by comparison with the efficiency of a boron counter. The variation of the cross section for reaction $B^{10}(n, \alpha)$ with neutron energy was taken from the atlas [18].

Measurements were made on a 1024-channel analyzer having a dead time of 24 μsec [19]. For measurements in the energy range above 20 keV the breadth of the analyzer channel was 8 μsec, and for measurements below 20 keV it was 32 μsec.

The power of the reactor was regulated by monitors. Corrections connected with variation in the reactor power did not exceed a few percent. The resolution was 0.04 μsec/m for energies below 20 keV. Below 100 eV the resolutions worsened somewhat owing to the indeterminacy in the neutron slowing-down time. Estimates showed, however, that this effect was not great ($\sim 10\%$) [20], and thus, had hardly any influence on the form of the spectrum at low energies.

The transit-time was calibrated from the known position of the nuclear levels of the elements studied. The effect of recyclic neutrons was removed for the 8-pulse/sec frequency used by means of a cadmium filter.

In determining the neutron spectrum, the prism lay at a distance of 300 mm from the surface of the active zone. For subtracting the background, a measurement was made in which the prism lay at 870 mm from the active zone. The spectrum under investigation was obtained as the difference between these two measurements. The measurement for the prism displaced to 870 mm was made in order to allow for the so-called correlated background, i.e., the background of scattered neutrons which, after second scattering at the prism, fly out of it at the same time (within the limits of the resolution function) as the neutrons of the effect being studied, and also of neutrons passing through the prism without collision. The ordinary (uncorrelated) background of the detector, the background of γ -radiation from the active zone, and the background of delayed neutrons were measured by means of resonance
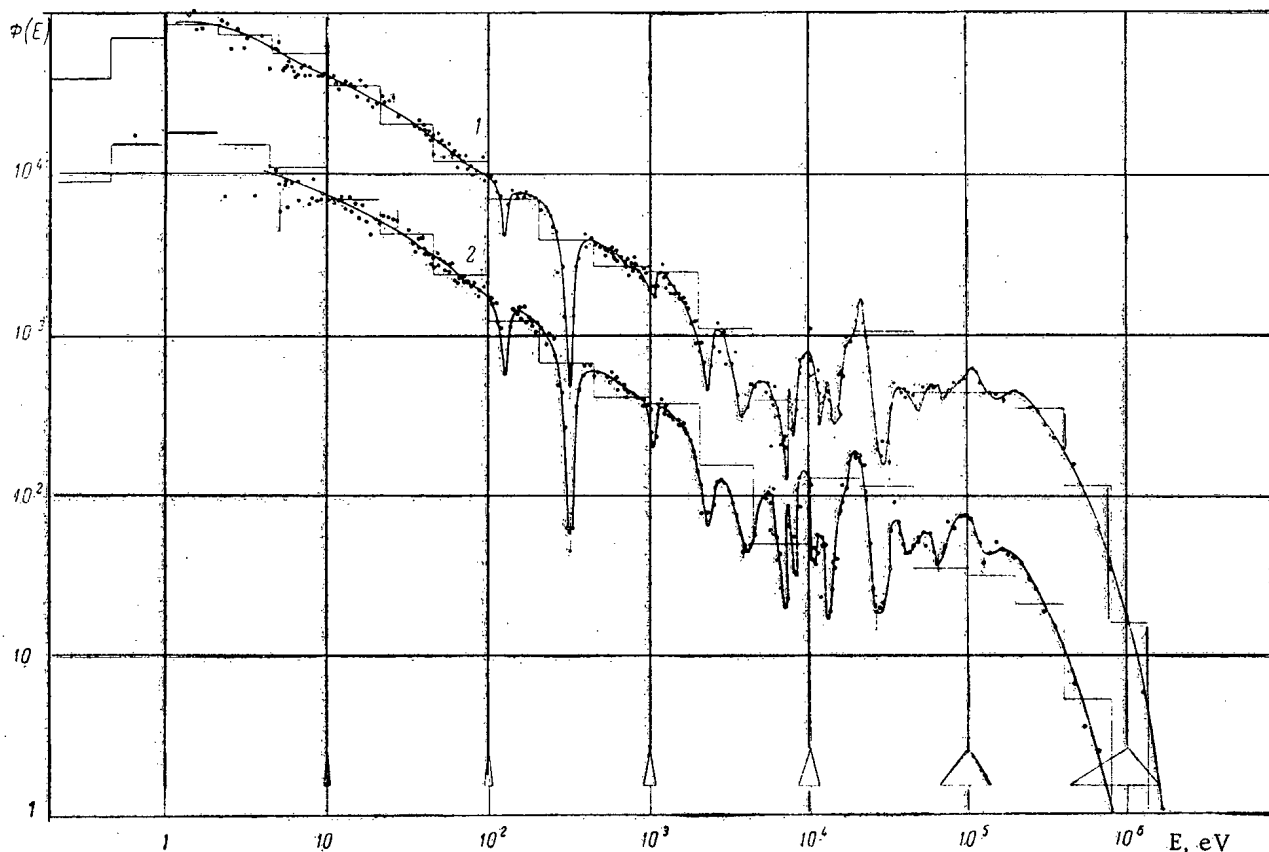
Fig. 5. Spectrum of leakage neutrons from stainless steel (curves 1 and 2 correspond to prism thicknesses of 30 and 48 cm).

filters of manganese, cobalt, and cadmium. In the measurements for the more distant prism, the effect itself was only half that found with the prism at 300 mm from the active zone. Meanwhile the background fell very little, since 75% of it was contributed by the actual detector.

The total background in the region of 5 eV was equal to the effect itself, falling with increasing energy roughly as $1/\sqrt{E}$. Thus, in the region of 1 keV the background was smaller than 7% of the effect. As a result of the measurements, a correction was introduced for distortion of the form of the spectrum by the aluminum stoppers of the neutron guide, the cadmium filter, and the air gaps. This correction was only important in energy ranges where these materials have strong resonances. In this case it was determined by measuring spectra smooth in these energy ranges. In all the rest of the energy region measured, the correction was estimated by calculation. The maximum errors did not exceed 40%.

Results of Measurements

Nickel. The spectra of neutrons emerging from nickel prisms, calculated for unit energy interval, are shown in Fig. 3. On the scale used, the Fermi slowing-down spectrum is shown by a straight line with 45° slope. The experimental spectrum clearly shows features due to the resonance nature of the nickel cross section. Clearly visible are dips for the Ni^{62} level at 4.5 keV, the unresolved Ni^{60}, and Ni^{58} levels at 15 and 17 keV, and the Ni^{60} level at 30 keV. For higher energies, individual resonances are not resolved. There only appear surges of neutron flux in the regions 60 and 150 keV, where the total cross section of nickel is small owing to the coincidence of interference minima in the cross sections of the main isotopes [21]. For E ~100 keV there is a dip in the spectrum connected with coinciding levels of Ni^{58} and Ni^{60}. The interference minimum caused by these resonances coincides, within the limits of the resolution function, with the group of resonances at 65 keV, so that detailed structure of the cross sections in the 60-to-100 keV region is not observed in the spectrum under study.

756
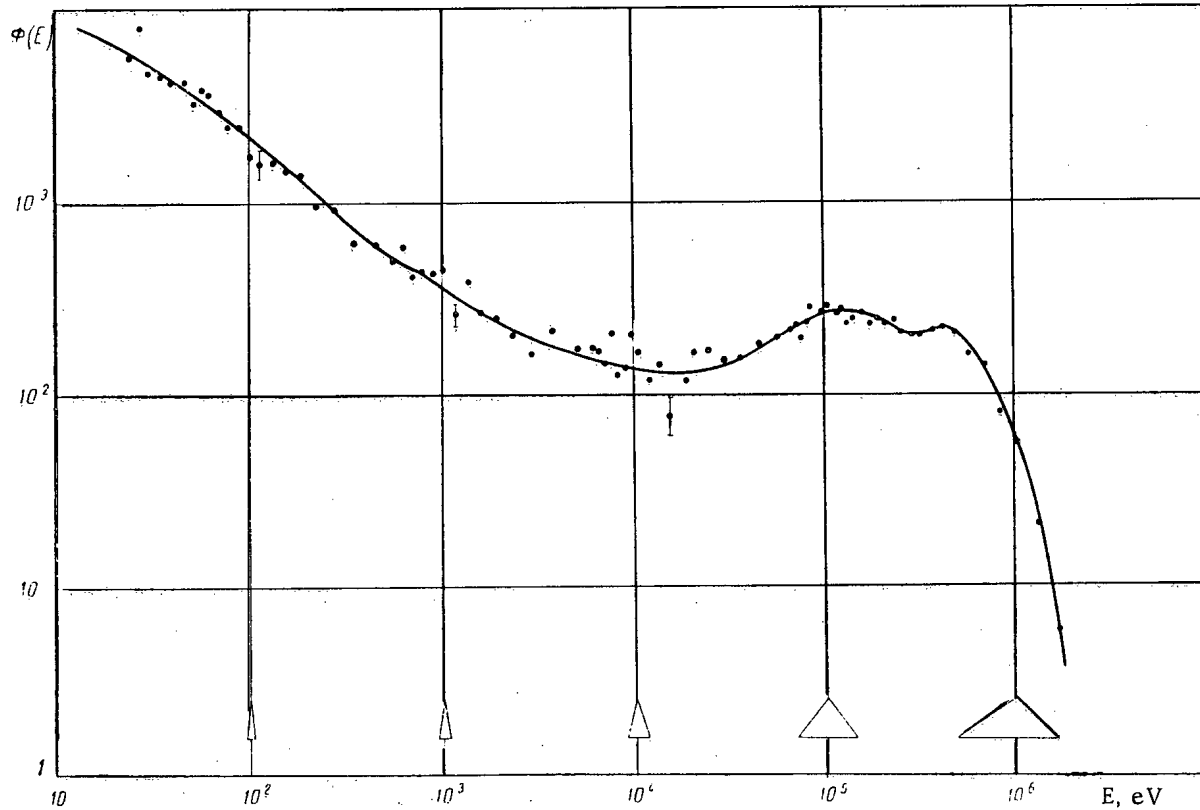
Fig. 6. Neutron spectrum of the IBR reactor.

Iron. The spectra of neutrons emerging from iron prisms are shown in Fig. 4.

The experimental spectra clearly show dips corresponding to the Fe^{57} level at 3.9 keV, the Fe^{54} at 7.25 and 8.00 keV, the Fe^{56} at 28 keV, and the Fe^{54} at 52.5 keV. The Fe^{54} and Fe^{56} levels at 72 and 74 keV were also revealed, though they could not be resolved. In the 140-keV region we see a group of Fe^{54} and Fe^{56} levels. Very evident is the strong surge of neutron flux due to the interference minimum of the Fe^{56} level at 28 keV. Furthermore, clearly visible in the spectrum are dips at energies 335 ev, 1.1 keV, and 2.35 keV, due to manganese impurity (the prism material was St. 3).

Stainless Steel. The spectra of neutrons emerging from the stainless-steel prisms are shown in Fig. 5. Apart from features associated with the presence of iron, manganese, nickel, and chromium, the spectrum also shows a dip at energy 132 eV due to cobalt impurity.

In the region below the energy of the first strong level, the neutron spectra observed in all the media studied have a character typical for a slowing-down spectrum in a weakly-absorbing medium. The maximum of the spectrum is in the region of 1 eV. For lower energies, the spectrum should fall sharply owing to the heavy increase in radiation capture.

In the region of energies where the total cross section is constant, the spectrum of leakage neutrons should evidently not differ greatly from the neutron spectrum in the medium. For calculating the latter, we may use the fact that the resonance neutrons constituting sources for the soft part of the spectrum have, owing to the interference dips in the cross section, a considerably greater relaxation length than the migration distance of neutrons slowed down through the resonance region. Hence, the neutron spectrum in the energy range below that of the resonances will be close to the equilibrium spectrum, i.e., the spectrum in the infinite medium [1]. This spectrum may be calculated for smoothly-changing cross sections from the formula

$$\Phi(E) \sim \frac{P(E)}{E \Sigma(E)} ,$$

(1)

where $\Sigma(E)$ is the total cross section of the medium, P(E) being the probability of a neutron's escaping capture on

slowing down to energy E, which in the case of a slowly-varying absorption cross section is determined by the well-known Greuling-Hertzel formula

$$P(E) = \exp\left(-\int_E^{E_0} \frac{\sigma_a}{\xi\delta_s + \gamma\sigma_a} \frac{dE}{E}\right).$$

(2)

Here E_0 is the energy of the source, and the value of γ for large mass numbers equals 2/3 ξ. If σ_s is constant, and σ_a varies as $1/\sqrt{E}$, i.e.,

$$\sigma_a = \frac{\sigma_a'}{\sqrt{E}},$$

(3)

then the integral of expression (2) may easily be calculated, and then

$$\Phi(E) \sim \frac{1}{E\left(1 + \frac{\alpha}{\sqrt{E}}\right)\left(1 + \frac{2}{3}\frac{\alpha}{\sqrt{E}}\right)^{3/\xi}},$$

(4)

where

$$\alpha = \frac{\sigma_a'}{\sigma_s}.$$

The spectrum calculated from this formula in all cases coincided with experiment, within the limits of error, below the energy of the first level. In Figs. 3-5 these spectra do not deviate from the continuous curves drawn through the experimental points in the region in question.

In the resonance region, comparison of the measured leakage spectrum with the equilibrium spectrum is not permissible. The spectrum of neutrons passing through the prism and emerging normal to its surface was, therefore, calculated on the 25-group approximation. The calculation was made for plane geometry in the s_8-approximation of the s_n method. The leakage of neutrons through the side surfaces of the prism was allowed for in the diffusion approximation. The spectrum of the neutrons falling from the reactor on to the surface of the prism was taken from experiment (Fig. 6), and their angular distribution was regarded as isotropic. The anisotropy of neutron scattering in the prism was considered on the transport approximation. Here, computing formulas of the s_n method obtained in the way set out in [22] were used. The constants allowing for the self-screening of the cross sections and required for the calculation were constructed from the data and recommendations of [6]. The results of the calculation are shown in Figs. 3-5 in the form of histograms. In the energy ranges where the cross sections are constant or vary slowly, the results of the multigroup calculations coincide both with the experimental results and those calculated by formula (4). In the resonance region there are considerable discrepancies between the experimental and computed results, the main reason for this being imprecision in allowing for the resonance self-screening of the cross sections, especially in groups corresponding to the region of the interference minima. Such imprecision is not unexpected, since certain experimental data on cross sections in this region contain large errors.

This relates especially to nickel, which chiefly contains two isotopes with similar concentrations. The minimum cross sections of natural nickel, calculated from the theoretical course of the cross sections for the individual isotopes (Breit-Wigner formula), change considerably on varying the parameters of the levels over the limits of the errors made in determining them. Thus, the position of the minimum in the cross section before the Ni^{58} and Ni^{60} resonances (17 and 15 keV), calculated from the resonance parameters, occurs at an energy above 10 keV. The group constants [6] were also obtained on this assumption. In reality it proved that the cross section reached a minimum in the neighboring group. The cross section in the neighborhood of this minimum was also determined imprecisely. An analogous error arises in the 100-to-200 keV group, where the part played by resonance self-screening also proved to be too high. For iron, the form of the spectrum in the resonance region is described fairly well by the computed histogram. The ratio of the neutron fluxes with energies above and below that of the Fe^{56} level at 28 keV, however, is determined imprecisely in the calculation. This discrepancy may also be explained by inexactitude in accounting for the structure of the cross sections in the region of this resonance. These inexactitudes in allowing for the resonance self-screening of the cross sections only have a large effect when considering the propagation of neutrons in media consisting of pure iron or nickel [13, 14]. On diluting these elements with others, the role of the inexactitudes diminishes sharply. For example, the neutron spectra in stainless steel 1Kh18N9T (18% Cr, 9% Ni) are described fairly well by the calculated histogram.

On comparing the experimental data with the results of multigroup calculations, we must also bear in mind the essential inaccuracy of the multigroup method associated with the indeterminacy of calculating the cross section

758

for the elastic slowing of neutrons from one group into another. As noted in [6], these cross sections depend greatly on the accepted form of the intragroup spectrum and hence, require correction in the process of computation. However, if the average fluxes in the groups vary irregularly, the introduction of a correction into the elastic-slowing-down cross section for the form of the intragroup spectrum from the data of the multigroup calculation is based on the arbitrary description of the calculated histogram by a smooth curve. This circumstance limits the accuracy of the multigroup method and makes it difficult to use this for describing the structure of the spectrum.

Finally, we note that the computational data also contain a slight error due to insufficient accuracy of assigning the boundary conditions in the s_8 approximation.

CONCLUSION

These results on measuring the spectra of neutrons emerging from thick blocks of matter by the transit-time method made it possible to detect the resonance structure of the spectra in the region of several keV. The analysis made of these spectra (comparison with multigroup calculation and simple-model calculations in the region of constant cross sections) is only preliminary. However, even such analysis enables us to draw certain conclusions on the precision of calculating spectra in matter by multigroup methods.

For a more complete understanding of the physics of neutron propagation in matter and an explanation of the causes underlying discrepancies, it is of great interest to make a more detailed analysis, so as to determine the dependence of the structure of the spectrum on the energy dependence of the total cross section. In order to make such an analysis, the whole energy range must be divided into such a large number of groups as will allow the structure of the cross section to be described with fair accuracy. In an energy range where the cross section of the medium is measured with insufficient resolution, the method of subgroups set out in [15] may be used.

At the present time, constants are being prepared for detailed computation of the spectra. The results of the detailed analysis of the spectra will be published after this work has been completed.

In conclusion the authors use this opportunity of thanking O. D. Kazachkovskii, L. N. Usachev, and V. V. Orlov for valuable discussions, F. L. Shapiro and Yu. S. Yazvitskii for useful advice and kind permission to use the neutron detector and multichannel time analyzer of the Laboratory of Neutron Physics in the United Institute of Nuclear Studies, and also the servicing staff of the IBR reactor under the direction of S. K. Nikolaev for help in the work. The authors are very grateful to V. Z. Nizik, Z. A. Aleksandrova, and L. M. Serede who participated in analyzing the experimental data.

LITERATURE CITED

1. A. I. Leipunskii et al., In the book: Transactions of the Second International Conference on the Peaceful Use of Atomic Energy. Contributions of Soviet scientists [in Russian], Moscow, Atomizdat, 2 (1959), p. 377.
2. I. Holmes et al., In the book: Material of the International Conference on the Peaceful Use of Atomic Energy (Geneva, 1955), [Russian translation], Moscow, Izd. AN SSSR, 401 (1956).
3. A. I. Leipunskii, Atomnaya énergiya, 11, 498 (1961).
4. M. N. Nikolaev et al., Physics of fast and intermediate reactors, IAEA, Vienna, 1 (1962), p. 403.
5. V. I. Golubev, Atomnaya énergiya, 18, 469 (1965).
6. L. P. Abagyan et al., Systems of Group Constants for Fast and Intermediate Neutrons [in Russian], Moscow Atomizdat (1964).
7. A. A. Luk'yanov and V. V. Orlov, Influence of the Resonance Structure of Cross Sections on the Diffusion of Neutrons. In the Collection: Neutron Physics [in Russian], Moscow, Gosatomizdat (1961), p. 105.
8. A. A. Luk'yanov and V. V. Orlov, In the Collection: Theory and Methods of Calculating Nuclear Reactors [in Russian], Moscow, Gosatomizdat (1962).
9. A. A. Luk'yanov and V. V. Orlov, Atomnaya énergiya, 10, 262 (1961).
10. A. A. Luk'yanov, Dissertation [in Russian] (1963).
11. S. B. Shikhov and L. P. Abagyan, In the collection: Theory and Methods of Calculating Nuclear Reactors [in Russian], Moscow, Gosatomizdat (1962).
12. L. P. Abagyan et al., Contribution No. 357 presented by the USSR to the Third International Conference on the Peaceful Use of Atomic Energy [in Russian], Geneva (1964).
13. G. A. Batyrbekov et al., Atomnaya énergiya, 17, 294 (1964).

759

14. A. I. Leipunskii et al., Contribution No. 368, presented by the USSR to the Third International Conference on the Peaceful Use of Atomic Energy [in Russian], Geneva (1964).

15. M. N. Nikolaev and V. V. Filippov, Atomnaya énergiya, 15, 493 (1963).

16. G. E. Blokhin et al., Atomnaya énergiya, 10, 437 (1961).

17. I. Vizi et al., Liquid Scintillation Detectors for Recording Neutrons. Conference on Nuclear Electronics Belgrade (1961).

18. D. Joos and R. Schwartz, Atlas of Neutron Cross Sections [Russian translation], Moscow, IL (1958).

19. L. A. Metalin et al., Pribory i tekhnika éksperimenta, No. 3 (1960).

20. A. A. Bergman et al., See [2], Vol. 4, p. 166.

21. I. V. Gordeev, D. A. Kardashev and A. V. Malyshev, Handbook on Nuclear-Physics Constants for Reactor Calculations [in Russian], Moscow, Atomizdat (1964).

22. V. N. Morozov, In the collection: Theory and Methods of Calculating Nuclear Reactors, [in Russian], Moscow, Gosatomizdat (1962).

SELF-DIFFUSION IN THE α AND β PHASES OF URANIUM *

A. A. Bochvar, V. G. Kuznetsova, V. S. Sergeev, and F. P. Butra

Results of studying the self-diffusion of uranium were first communicated to the Second Geneva Conference on the Peaceful Use of Atomic Energy, where results on the self-diffusion of the cubic γ phase of uranium were set out and values of the self-diffusion coefficients and activation energy presented [1]; these were in good agreement with later work [2, 3]. Results on self-diffusion in the α and β phases were published in [5-9].

The low symmetry of the α-uranium lattice suggests that the rate of self-diffusion depends on the crystallographic direction. This view was first discussed in [4], where it was concluded, on the basis of a theoretical analysis of the crystal lattice of α uranium, that the self-diffusion coefficients along the a, b, and c axes would be in the ratio 1:0:0.8, and a diffusion mechanism for the radiation growth of uranium was proposed. Experimental studies of self-diffusion in α uranium were reported in [5, 6, 9]. In [5], self-diffusion was studied in single crystals in the three principal crystallographic directions. The self-diffusion coefficient was determined from the rate of change of α activity on the surface of the single crystals in the annealing process (absorption method). The radioactive indicator was U^{233}. The intensity of α radiation from the surface of the sample was determined by counting the number of α particle tracks in photographic emulsion. In this way the following values were obtained for the coefficients in cm^2/sec: $D_{[100]} = 1.8 \cdot 10^{-14}$; $D_{[010]} = 0.72 \cdot 10^{-14}$; $D_{[001]} = 0.66 \cdot 10^{-14}$; it was noted that the difference between the coefficients lay within measuring error. In [6] polycrystalline α uranium was studied. The indicator was U^{235}. The temperature variation of the self-diffusion coefficient was found in the form

$$D = 2 \cdot 10^{-3} \exp (40\,000/RT).$$

Autoradiographic investigations indicated preferential self-diffusion along grain boundaries (especially for temperatures below 600°C). There was no support for a variation in the self-diffusion coefficient with crystallographic direction, as in [5]. A difference between the self-diffusion coefficients in the principal crystallographic directions was detected in [9]. According to this investigation, the values of the coefficients along the [100] and [001] directions were the same and equal to $1.95 \cdot 10^{-13}$ cm^2/sec, while that along the [010] direction was $\leq 10^{-14}$ cm^2/sec.

Results of studying self-diffusion in the β phase were given in [7, 8]. In [7], the temperature dependence of the self-diffusion coefficient was given as $D = 1.35 \cdot 10^{-2} \exp (42,000/RT)$, and in [8] it was asserted, on the basis of an analysis of the penetration curves and an autoradiogram of one sample, that self-diffusion in β uranium was anisotropic. Thus, data on the nature of self-diffusion in α and β uranium are contradictory.

In the present investigation, main attention was devoted to a study of the dependence of the self-diffusion rate on the crystallographic direction in both low-temperature phases of uranium by the autoradiography method, which under certain conditions gives the most reliable results.

EXPERIMENTAL METHOD

Preliminary study of self-diffusion in polycrystalline α uranium showed that the coefficient at 650°C was smaller than 10^{-11} cm^2/sec. In view of the comparatively low value, the method of diffusion out of a thin layer into semiinfinite space was used. The coefficient was calculated from the rage of change of % radioactivity on the surface of the sample in the process of annealing (absorption method), and also from autoradiograms taken from the sample surface. The methods of calculating the self-diffusion coefficient from the change in % activity and from the autoradiograms are given in an appendix. The radioactive indicator used was U^{233}.

* Contribution No. 333 presented by the USSR to the Third International Conference on the Peaceful Use of Atomic Energy. Geneva, 1964.
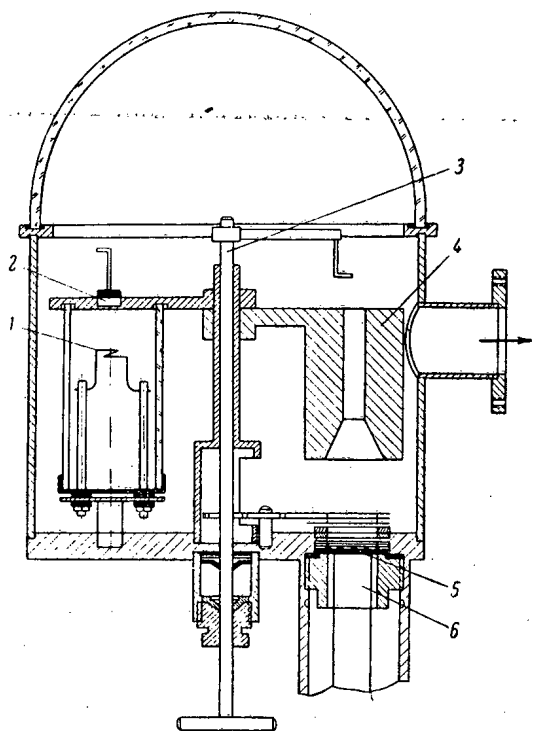
Fig. 1. Main arrangement of the apparatus for studying self-diffusion by the absorption method: 1) tungsten spiral; 2) sample; 3) rod for loading samples into the furnace; 4) furnace; 5) scintillator; 6) photoelectron multiplier.

In diffusion from a thin layer, the main error in measuring the coefficient may result from oxidation of the surface layer. In view of the great tendency of uranium to oxidation, an apparatus was prepared so that such operations as depositing the thin layer of isotope on sample surfaces, annealing, and measuring the α activity in the course of annealing could be carried out without breaking the vacuum in the system. The vacuum for all the operations was kept equal to $(4 \text{ to } 6) \cdot 10^{-7}$ mm Hg. The main arrangement of the apparatus is shown in Fig. 1. Inside the framework is placed a device for thermally evaporating the U^{233} from a tungsten spiral, and an annealing furnace. At the bottom of the framework are mounted the luminophore and photomultiplier for recording the α radiation. The samples are loaded into the furnace and unloaded from it by means of a movable rod introduced into the system by way of a vacuum seal. The samples were annealed at 640°C, the annealing time being 10 to 50 h.

The investigations were made on single crystals, polycrystalline samples with large, perfect grains, and polycrystalline samples with enlarged, imperfect grains. All the samples were prepared from metal of the following chemical composition:

Element	Fe	Si	Mn
Content, wt. %	$8,1 \cdot 10^{-3}$	$1,1 \cdot 10^{-2}$	10^{-4}

Element	Cu	Al	Ni	C
Content, wt. %	$1,6 \cdot 10^{-4}$	10^{-3}	$3 \cdot 10^{-3}$	$9 \cdot 10^{-3}$

Imperfect single crystals were obtained by phase recrystallization. As shown by Laue photographs, the single crystals consisted of individual subgrains, the difference in the orientation of which did not exceed 3°. Quenching the single crystals from the β phase and subsequent annealing at 620 to 640°C led to the formation of polycrystalline specimens with coarse grains. The dimensions of individual grains reached 2 to 3 mm. The grains constituted perfect single crystals, oriented in very different crystallographic directions with respect to the outer surface of the sample. The crystallographic orientation of the single crystals and individual grains in the polycrystalline material were determined from back-reflection Laue photographs. The samples of single crystals and polycrystalline samples with perfect grains formed plates 5×5×0.5 mm in size. The surface of the samples was electropolished before depositing the isotope in an electrolyte of composition 10 m/liter H_2CrO_4, 10 m/liter CH_3COOH, 30 m/liter H_2O.

After annealing, in the course of which the α activity from the surface of the sample was measured, the distribution of the isotope in the polycrystalline samples was examined by successively removing layers from the surface and taking autoradiograms. This layers 0.5 to 1 μ thick were removed electrolytically in the electrolyte specified above. In taking the autoradiograms, the surface of the sample was brought into immediate contact with the emulsion of the photoplate. Fine-grain emulsions were used, with a large silver-halide content. The thickness of the emulsion layer on the plates did not exceed 10 μ. The blackening density was measured on a microphotometer.

EXPERIMENTAL RESULTS

Self-Diffusion in α Uranium. Determination of the self-diffusion coefficients in single crystals by measuring the α activity in the course of annealing showed that the coefficient was the same along the [100] and [001]

762
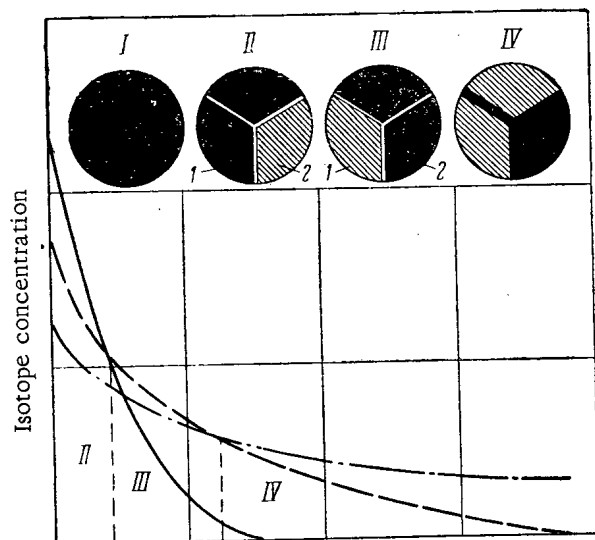
Fig. 2. Schematic representation of autoradiograms in the presence of anisotropic self-diffusion:————— in grain 1;— — — — in grain 2;—·—·—·— along the grain boundaries.

directions and equal to 4 to 6) · 10^{-13} cm^2/sec. Along the [010] direction, the self-diffusion coefficient could not be determined by this method, since in the course of annealing for the time mentioned no change was observed in the α activity of a single crystal with this orientation. This result is in good agreement with the data of [9].

The autoradiography method was developed on the following basis. If there is a dependence of the rate of self-diffusion in the α uranium crystal lattice on the crystallographic direction (anisotropy of self-diffusion), then after annealing the distribution of the isotope will be different in differently-oriented grains of the polycrystalline sample. The smaller the self-diffusion coefficient, the smaller the depth to which diffusion of the isotope will proceed, and on the autoradiogram obtained from the original surface of the polycrystalline sample after annealing this grain will give a larger blackening density. Figure 2 gives exemplary curves for the variation in isotope concentration in grains 1 and 2 and along the grain boundaries, together with the character of the autoradiograms. The autoradiogram of the sample surface before annealing indicates uniform blackening density (position I); after annealing, the autoradiogram from the same surface will have the form of II. Grain 1 gives a large blackening density, since in this, the self-diffusion coefficient is larger than in grain 2. If now we remove layers from the sample surface and take autoradiograms from the newly-revealed surfaces, then a similar blackening-density distribution is preserved in grains 1 and 2 roughly up to the point at which the concentration-distribution curves intersect. Then the picture should reverse position III), since the concentration in grain 1 at this distance from the original surface will become smaller than in grain 2. If the rate of self-diffusion along the grain boundaries is larger than in the body of the grain, then at a greater depth the maximum blackening density will be given by the grain boundaries (position IV). Such a distribution of blackening density on the autoradiograms is a convincing proof of the anisotropy of self-diffusion in α uranium.

Figure 3 shows autoradiograms of a polycrystalline sample after annealing. As may easily be seen, the distribution of blackening density on these autoradiograms corresponds to the scheme just described. Grain 1 in Fig. 3a gives maximum blackening density, while at a depth of even 1.5 μ (see Fig. 3b) the concentration of the isotope is practically zero, which indicates the low value of self-diffusion coefficient in this grain. A similar picture is found in other samples.

Figures 4 and 5 present autoradiograms of polycrystalline samples with perfect grains. The nature of the blackening-density distribution in these is the same as in Fig. 3. The table gives the self-diffusion coefficients

Fig. 3. Autoradiograms of polycrystalline sample after annealing at 640°C for 10 h: a) from original surface; b) at depth 1.5 μ; c) at depth 8 μ.

763

Fig. 4. Autoradiograms of polycrystalline sample with perfect grains after annealing at 640°C for 40 h: a) from original surface; b) at depth 0.7 μ; c) at depth 3 μ; d) at depth 7 μ.

Fig. 5. Autoradiograms of polycrystalline sample with perfect grains after annealing at 640°C for 30 h; a) at depth 1.7 μ; b) at depth 7 μ.

calculated from the autoradiograms for individual grains of the sample (see Fig. 4) and crystallographic orientations of the grains. Figure 6 gives Laue photographs of several grains. From the autoradiograms of Fig. 4 we see that the smallest depth of penetration of the isotope occurs in grains 2 and 8. These grains are oriented with the (010) plane parallel to the sample surface. The greatest depth is found in grain 3, oriented with the (001) plane parallel to the surface. Although the method of varying $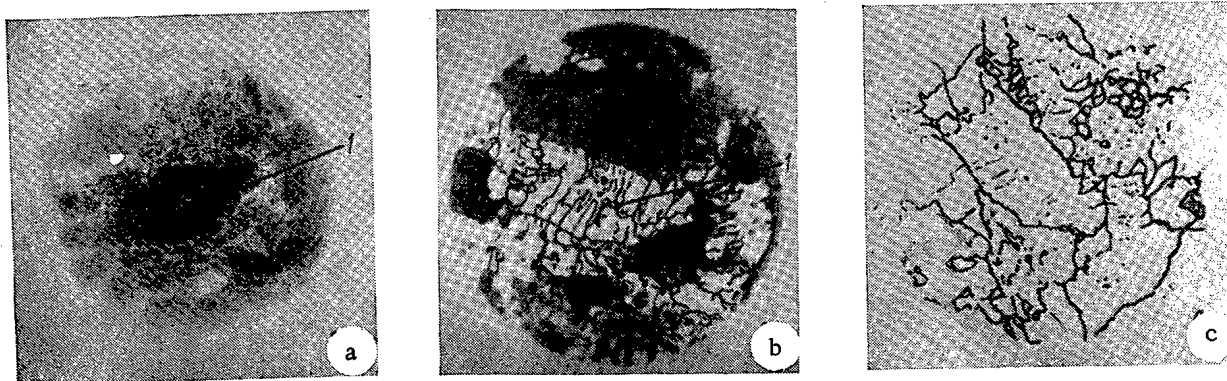\alpha$ activity gave the same value of self-diffusion coefficient in the [100] and [001] directions, we see from the autoradiograms of Fig. 5 that even in these directions the penetration depth of the isotope differs a little. The difference in the self-diffusion coefficients was not determined quantitatively. It was not found possible to determine the value of the coefficient in the [010] direction by this method any more than from the variation of α activity, owing to the small penetration of the isotope. An approximate estimate gave the value $\leq 10^{-14}$ cm^2/sec. The analytical relationship for the variation in α activity on the grain surface, and hence, the blackening density, as a function of distance from the original surface, is given in the Appendix. The equation obtained makes it possible to calculate the self-diffusion coefficients in various grains graphically from the blackening densities which they create in the autoradiograms.

Analysis of the autoradiograms obtained from many samples leads to the conclusion that the self-diffusion coefficient along any crystallographic direction depends on the angle between the given crystallographic direction and the [010] axis, and to a first approximation does not depend on the angles made with the [100] and [001] axes. The minimum value of the coefficient is found for the direction [010] and the maximum for the [100] and [001]. The coefficient along these directions, equal to 2.10^{-13} cm^2/sec, agrees closely with that found in [9] (1.95 · 10^{-13} cm^2/sec). The table gives the values of the self-diffusion coefficients in α uranium along various crystallographic directions. The autoradiograms presented indicate preferential self-diffusion along the grain and subgrain boundaries, and also a relation between the rate of self-diffusion along the boundaries and the mutual orientation of the grains. The latter follows from Fig. 3b and c. The penetration depth of the isotope along the subgrain boundaries inside grain 1 is far smaller than along the boundary between this grain and its neighbors.

Self-Diffusion in β Uranium. Self-diffusion in β uranium was studied by the same methods as in α uranium. Figure 7 shows autoradiograms of a sample annealed at 720°C for 3 h. The character of these autoradiograms is the same as for the α uranium. This indicates anisotropy and preferential self-diffusion along the grain boundaries in β uranium. Since the study was made with pure uranium, in which the β phase is not fixed at room temperature, it was not possible to establish directions with maximum and minimum self-diffusion coefficients. The coefficient for the temperature range 700 to 750°C obtained from the variation of α activity in the course of annealing lies between (2-6) · 10^{-11} cm^2/sec.

Discussion of Results. The experimental results presented convincingly indicate the presence of anisotropy of self-diffusion in the α and β phases of uranium. In α uranium the rate of self-diffusion along any crystallographic direction depends on the angle between that direction and the [010] axis, and to a first approximation is independent

764

Fig. 6. Laue photographs of grains 2 and 3 in the sample (see Fig. 4).

Values of Self-Diffusion Coefficients in Various Crystallographic Directions in α Uranium

No. of grain	Crystallographic direction	Self-diffusion coefficient, cm²/sec
2	[010]	$\leqslant 10^{-14}$
8	[010]	$\leqslant 10^{-14}$
1	[021]	$6,3 \cdot 10^{-14}$
5	[240]	$6,4 \cdot 10^{-14}$
7	[130]	10^{-13}
6	[153]	$1,6 \cdot 10^{-13}$
4	[111]	$1,8 \cdot 10^{-13}$
3	[001]	$2,1 \cdot 10^{-13}$
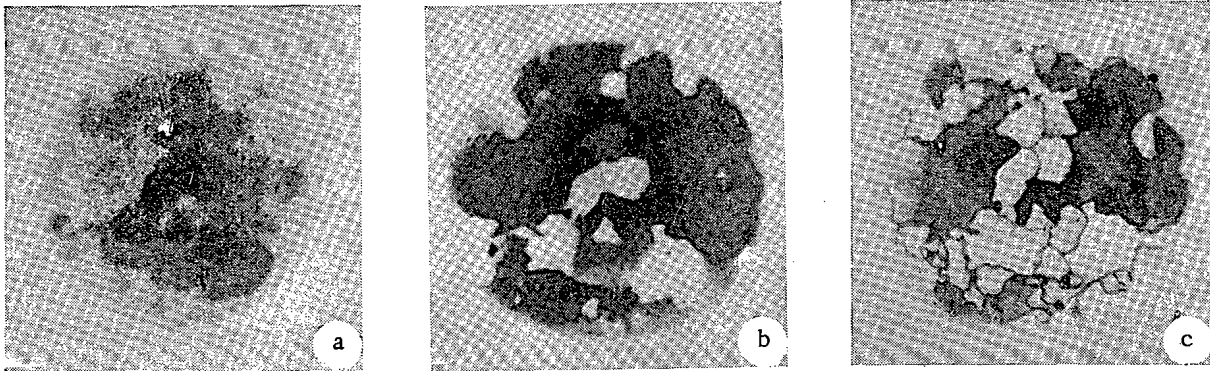
Fig. 7. Autoradiograms of a sample annealed at 720°C for 3 h: a) from original surface; b) at depth 4 μ; c) at depth 12 μ.

of the angles made with the a and c axes. This means that the self-diffusion coefficients along crystallographic directions lying on the surface of a cone with axis [010] are the same. The minimum self-diffusion coefficient is that along the [010] direction; approximate estimates give $D \leq 10^{-14}$ cm²/sec, at 640°C. Along the [100] and [001] directions, $D = 2.10^{-13}$ cm²/sec in good agreement with the results of [9]. The anisotropy and boundary self-diffusion make the self-diffusion coefficient very sensitive to the structure of the samples. The finer the structure, the larger contribution is made to the diffusion flow by the grain boundaries. The same relation is also found on reducing the temperature. The structural dependence of the self-diffusion coefficient will not allow a physically-significant activation energy to be determined in polycrystalline samples. In studying fine-grained samples, the activation energy can to a certain extent, characterize just the boundary diffusion. The activation energy of 40 kcal/g · atom obtained in [6] evidently corresponds to this case, since, judging by the autoradiogram presented, the authors used fine-grained uranium for their studies.

It should be noted that the study of self-diffusion in α uranium presents great experimental difficulties. This is primarily connected with the great oxidizability of uranium. The tendency of uranium to interact actively with gas may well be one reason why no self-diffusion anisotropy was found for α uranium in [5].

Thus, the results obtained convincingly confirm the dependence of the self-diffusion coefficient in α- and β-uranium on the crystallographic direction. These results might have lent support to the diffusion mechanism of the radiation growth of uranium proposed in [4], but for the fact that the sharp increase in the coefficient of radiation growth at low temperatures obtained in [10] forbids this conclusion.*

---

* The results of a fairly recent experimental study [11] indicate the absence of any marked radiation growth in uranium single crystals at temperature 110°K, and thus, contradict the earlier-published information. If these latter results are confirmed, the relation found to exist between the self-diffusion coefficient and the crystallographic direction will enable the process of radiation growth to be regarded as the result of anisotropic migration of defects arising in the course of irradiation.

765

Recently, after certain methodical improvements, the self-diffusion coefficients of α uranium were measured along directions perpendicular to planes close to the (100 and (001) planes in the temperature range 560 to 660°C. The results obtained made it possible to determine the activation energy of self-diffusion along these directions. This proved equal to 67 ± 2.5 kcal/g · atom. The temperature dependence of the self-diffusion coefficient along the directions in questions is described by the equation

$$D = 9.1 \cdot 10^2 \exp\left(-67\,000/RT\right) \text{ cm}^2/\text{sec}$$

A tendency for the activation energy to fall on reducing the angle between the given direction and the [010] was revealed.

APPENDIX

Methods of Calculating Self-Diffusion Coefficients

Absorption Method. In studying diffusion by the absorption method, a thin layer of radioactive isotope is deposited on the surface of the sample investigated. In the course of annealing, part of the isotope passes off into the depths of the sample, as a result of which the α radioactivity on the surface diminishes. The change of radioactivity with time will be given by the equation

Fig. 8. Scheme for deriving the computing equation: 1) sample; 2) scintillator.

$$\frac{A}{A_0} = \text{erf}(\varepsilon) - \frac{1}{\varepsilon\sqrt{\pi}}(1 - e^{-\varepsilon^2}), \qquad (1)$$

where A is the radioactivity of the surface after annealing for time t, A_0 is the original radioactivity,

$$\varepsilon = \frac{\lambda}{2\sqrt{Dt}};$$

λ is the range of the α particles, and

$$\text{erf}(\varepsilon) = \frac{2}{\sqrt{\pi}}\int_0^{\varepsilon} e^{-x^2}\,dx.$$

Equation (1) is valid when the activity is measured over a solid angle of 2π. In our case the α radiation is recorded for a solid angle $< 2\pi$ and, hence, Eq. (1) cannot be used. The variation of α activity on the sample surface will only be recorded by the counter system when the maximum emergent angle of the α particles at the surface of the sample becomes smaller than the counting angle (Fig. 8). The equation in this case takes the form

$$A = \int_0^{a} c(x, t)\,dx + \int_0^{\lambda_{\text{eff}}} c(xt)\left(1 - \frac{x}{\lambda}\right)dx,$$

where α is the distance from the sample surface for which the maximum angle of emergence of the α particles (angle α in Fig. 8) will equal the counting angle θ, λ_{eff} is the effective range of the α particles in the sample,

$a = \lambda k$; $k = \cos\theta$; $c(xt) = \dfrac{A_0}{\sqrt{\pi Dt}}e^{-x^2/4Dt}$. After integrating we obtain

$$\frac{A}{A_0} = \left[\text{erf}(p) - \frac{1}{p\sqrt{\pi}}(e^{-q^2} - e^{-p^2})\right], \qquad (2)$$

where $p = \dfrac{\lambda}{2\sqrt{Dt}}$; $q = \dfrac{k\lambda}{2\sqrt{Dt}}$. For k = 0, i.e., $\theta = 90°$, expression (2) takes the form of (1); for k = 1, i.e., for $\theta = 0$ (corresponding to the recording of a collimated beam) we obtained the expression

$$A = A_0\,\text{erf}(p), \qquad (3)$$

766

Thus, expressions (1) and (3) are particular cases of Eq. (2).

The self-diffusion coefficient in Eq. (2) is calculated graphically from the experimentally-obtained value of A/A_0. The effective range was determined experimentally.

Method of Autoradiography. If there is a dependence of the rate of self-diffusion in the α uranium lattice on the crystallographic direction, then, on an autoradiogram taken from the surface of a polycrystalline sample after annealing, individual grains will give different blackening densities. By removing layers of definite thickness from the surface, we can obtain a complete picture of the distribution of the isotope in separate grains. The variation of activity on the surface of the individual grain, and hence, also the blackening density due to this grain, with distance from the original surface will be described by the equation

$$\frac{A}{A_0} = \int_{a'}^{a'+\lambda} c(xt)\left(1 - \frac{x}{\lambda}\right) dx; \quad c(xt) = \frac{1}{\sqrt{\pi Dt}} e^{-x^2/4Dt}.$$

Integration gives

$$\frac{A}{A_0} = \left(1 + \frac{a'}{\lambda}\right)\left\{[\mathrm{erf}(z+p) - \mathrm{erf}(z)] - \frac{1}{p\sqrt{\pi}}(e^{-z^2} - e^{-(z+p)^2})\right\}, \tag{4}$$

where a' is the distance from the original surface, and

$$z = \frac{a'}{2\sqrt{Dt}}; \quad p = \frac{\lambda}{2\sqrt{Dt}}.$$

A series of autoradiograms from surfaces situated at different distances from the original enables us to calculate the coefficients of self-diffusion in individual grains graphically by using Eq. (4).

LITERATURE CITED

1. A. A. Bochvar, V. G. Kuznetsova, and V. S. Sergeev, In the book: Transactions of the Second International Conference on the Peaceful Use of Atomic Energy. Contributions of Soviet Scientists [in Russian], Moscow, Atomizdat, 3 (1959), p. 370.
2. I. Adda and A. Kirianenko, J. Nucl. Mat., 3, 120 (1959).
3. S. Rothman, L. Lloyd, and A. Harkness, Trans AIME, 218, 605 (1960).
4. L. Seigle and A. Opinsky, Nucl. Sci. Engng, 2, 38 (1957).
5. R. Resnick, L. Castleman, and L. Seigle, J. Nucl. Mat., 5, 5 (1962).
6. I. Adda, A. Kirianenko, and C. Mairy, Compt. rend., 253, No. 3 (1961).
7. I. Adda, A. Kirianenko, and C. Mairy, J. Nucl. Mat., 1, 300 (1959).
8. S. Rothman, J. Gray, and A. Harkness, J. Nucl. Mat., 3, No. 1 (1961).
9. S. Rothman, J. Hines, J. Gray, and A. Harkness, J. Appl. Phys., 33, No. 6 (1962).
10. Y. Quéré and J. Doulat, Compt. rend., 252, 1305 (1961).
11. B. Loomis et al., J. Appl. Phys. Lett., 5, 135 (1964).

STUDY OF THE MECHANICAL PROPERTIES OF BERYLLIUM

(UDC 546.45.001.2)

N. N. Davidenkov, B. A. Sidorov, L. M. Shestopalov, N. F. Mironov,

N. M. Bogograd, L. A. Izhvanov, and S. B. Kostogarov

Thanks to its high strength density ratio and good nuclear properties, beryllium is attracting increased attention from scientists as a construction material for use in aviation, rocket, and atomic technology. We here describe methods for mechanical (tensile and compression) tests in vacuum on beryllium and set out results for beryllium prepared by metal-powder and casting methods, measured at 20 to 1000°C.

Methods of Testing. The mechanical (tensile and compression) tests in the range 20 to 1000°C were carried out on the testing machine IM-4R with vacuum chamber mounted on the lower loading screw of the machine between its supports.* The arrangement of the apparatus used for tensile tests is shown in Fig. 1. For compression tests a reverser was placed inside the vacuum chamber. With the help of a centering device the sample was set up outside the chamber between the supports of the reverser, after which it was gripped with forceps and together with the reverser carried into the chamber.

The temperature of the tests was monitored by a Nichrome-nickel thermocouple (diameter of thermoelectrode 0.1 mm). The "hot" junction of the thermocouple was fixed directly to the side surface of the sample, while the "cold" junction was thermostated outside the chamber. The thermo-emf was measured by a potentiometric method with an accuracy of 0.5°C. The temperature drop in the working part of the sample along its axis was not greater than 0.5 to 1.0°C after normal holding for 0.5 h at the given test temperature. The required temperature was maintained by regulating the heating current by means of an autotransformer. All the tests at elevated temperatures were conducted with a vacuum of 10^{-4} mm Hg, which prevented oxidation of the samples.

TABLE 1. Impurity Content in Various Kinds of Beryllium, Wt. %

Impurity	Characteristics of material					
	Distilled, $-50\,\mu$	Distilled, $-500\,\mu$	Magnesium thermal, $-50\,\mu$	Magnesium thermal, $-500\,\mu$	Electrolytic, $-500\,\mu$	Cast from distilled
Iron	0,06	0,035	0,3	0,17	0,023	0,03
Manganese	0,02	0,018	0,015	0,033	0,0025	0,01
Chromium	0,01	0,004	0,2	0,004	0,005	Not detd.
Aluminum	0,05	0,032	0,03	0,110	0,010	0,05
Magnesium	<0,002	0,003	0,02	0,05	0,005	0,004
Silicon	0,006	0,009	0,03	0,037	0,064	0,004
Nickel	0,002	0,002	0,004	0,008	0,020	0,002
Copper	Not detd.	0,003	0,01	0,012	0,016	0,0015
Carbon	0,07	0,35	0,06	0,30	Not detd.	0,30
Oxygen	0,22	0,10	0,3	0,12	0,41	Not detd.
Nitrogen	<0,005	Not detd.	0,01	0,01	0,018	»

* A. L. Shakh-Budagov and V. N. Dyn'kov took part in constructing the test system.
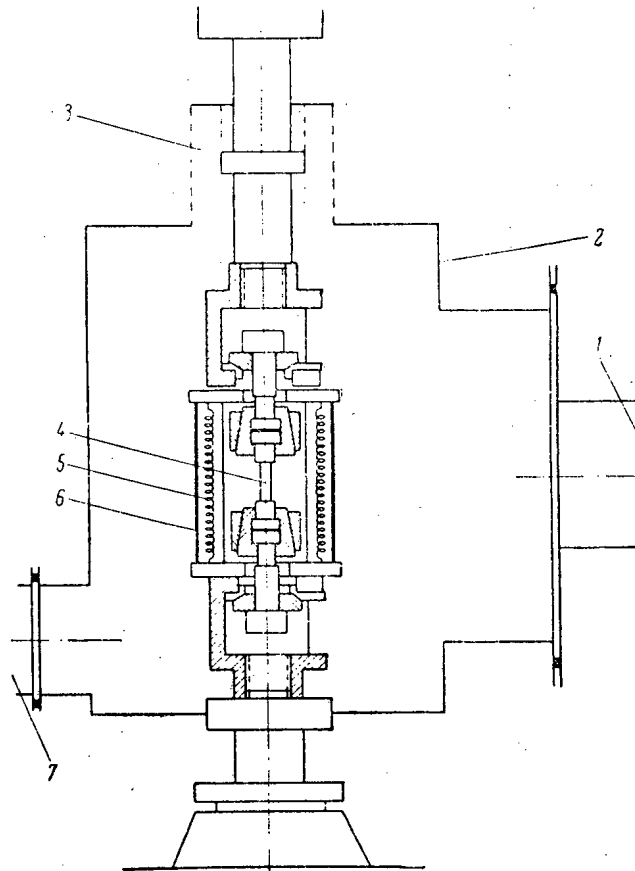
Fig. 1. Arrangement of vacuum chamber for mechanical tensile tests: 1) flange for opening the chamber; 2) vacuum chamber with water jacket; 3) double bellows; 4) sample; 5) Nichrome heater; 6) nickel screen; 7) diffusion-pump tube.

In this investigation, the effect of the technology of preparing the beryllium on its mechanical properties was studied. Metal prepared in the following ways was examined: magnesium-thermal reduction of beryllium fluoride, vacuum distillation, and electrolysis of beryllium chloride [1].

Compact beryllium was prepared by metal-powder methods from powders of coarseness —500 μ and also from finely-dispersed powders of coarseness —50 μ (in the latter case only from distilled and magnesium-thermal metal). Samples were also prepared from centrifugally-cast distilled beryllium. Table 1 presents data on the impurity content of the types of beryllium studied. The properties of beryllium were studied for samples of material obtained by the following technological schemes.

1. Pressing beryllium powder at 20°C and pressure 10 ton/cm^2. Sintering in vacuum $1 \cdot 10^{-3}$ mm Hg at temperature 1180 to 1200°C for 2 h. Gage pressing at temperature 500°C and pressure 10 ton/cm^2. Density of resultant material was 1.75 to 1.82 g/cm^3.

2. Hot pressing of beryllium powder in vacuum $1 \cdot 10^{-3}$ mm Hg at temperature 1160 to 1180°C and pressure 30 to 50 kg/cm^2 in graphite press molds with 45 min holding. Density close to theoretical.

3. Hot pressing of beryllium powder in air at temperature 1120 to 1140°C and pressure 110 kg/cm^2 with 45 min holding.

4. Extrusion from a sintered billet obtained by technological scheme

Fig. 2. Samples for tests in tension and compression.
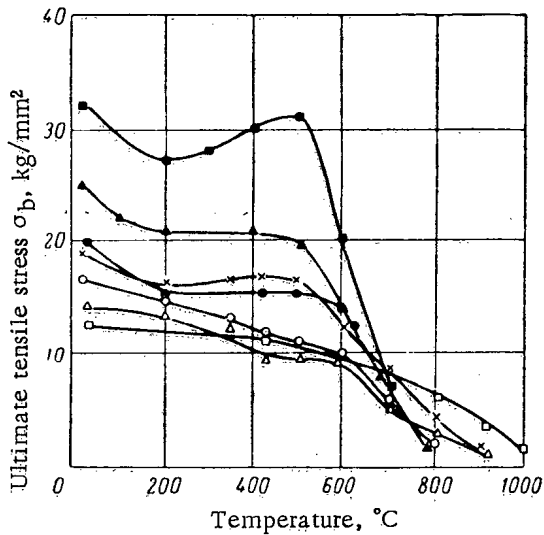
Fig. 3. Temperature dependence of the ultimate tensile stress of beryllium: $\times$ cold-pressed and sintered, magnesium-thermal, from $-500\,\mu$ powder; $\bullet$) hot-pressed in vacuum, magnesium-thermal, from $-500\,\mu$ powder; $\bigcirc$) hot-pressed in vacuum, distilled, from $-500\,\mu$ powder; $\triangle$) hot-pressed in vacuum, electrolytic, from $-500\,\mu$ powder; $\blacktriangle$) hot-pressed in vacuum, distilled, from $-50\,\mu$ powder; $\blacksquare$) hot-pressed in vacuum, magnesium-thermal, from $-50\,\mu$ powder; $\square$) cast from distilled metal.

1, temperature 450 to 500°C, reduction 75%. Density close to theoretical.

5. Extrusion from a hot-pressed billet obtained by technological scheme 2, temperature 450 to 500°C, reduction 75%. Density close to theoretical.

The finely-dispersed powder was obtained by grinding the material in an inert medium and treated by technological schemes 2 and 5.

The tests in tension and compression were conducted on cylindrical samples (Fig. 2). The samples for tension were shortened (ratio of working length l_0 to diameter d_0 was around 2.5), which made it possible to prepare identical samples oriented both along and across the direction of extrusion or of pressing the billets. For convenience in carrying out the compression tests, samples having $l_0/d_0 = 1.4$, were chosen.

It should be noted that, on passing over to standard five- or ten-fold samples, i.e., on changing the geometrical similitude of the samples, the average values of all the mechanical properties fell by a quantity which, as a rule, did not exceed the scatter in the values from sample to sample within the limits of one batch (for example, the temporary resistance or breakdown point σ_b fell by 3% for ten-fold samples). The change in the mechanical properties is evidently due to the appearance of a certain "scale effect," in that the strength and other mechanical characteristics depend on the size of the deformed volume V of material. The only exception is the total elongation, which also depends on the geometrical similitude of the samples. If we follow the static theory of strength, then
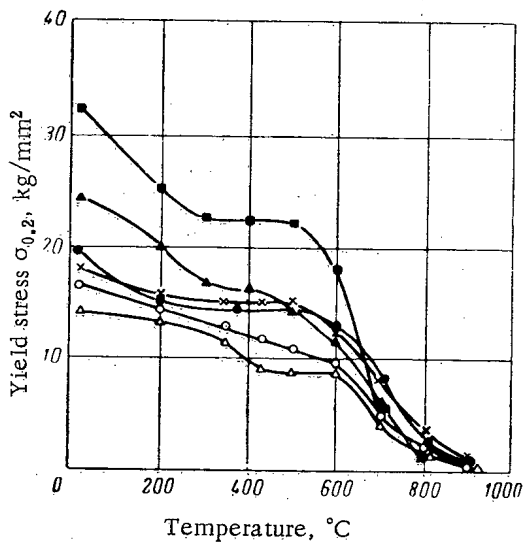
Fig. 4. Temperature dependence of the yield stress of beryllium under tension.
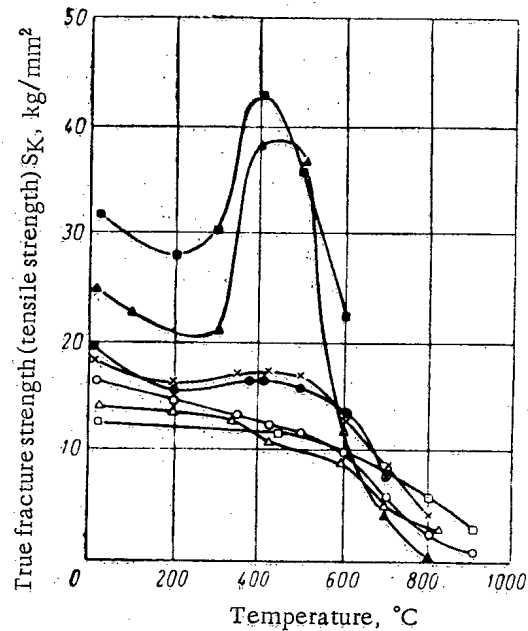
Fig. 5. Temperature dependence of the true tensile stress of beryllium.

770
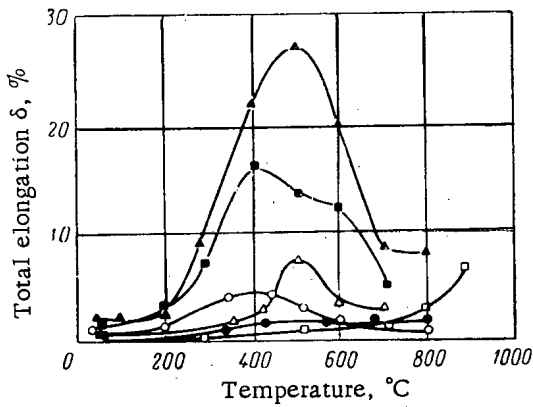
Fig. 6. Temperature dependence of total rela-
tive elongation of beryllium under tension.
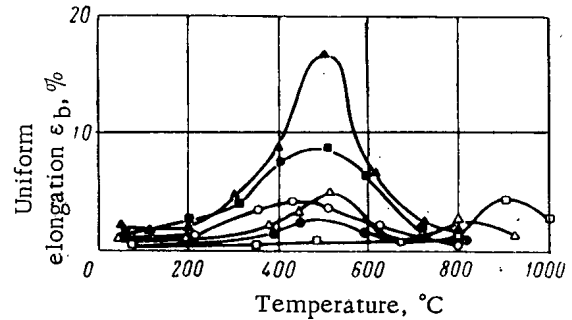
Fig. 7. Temperature dependence of uniform rela-
tive elongation of beryllium under tension.
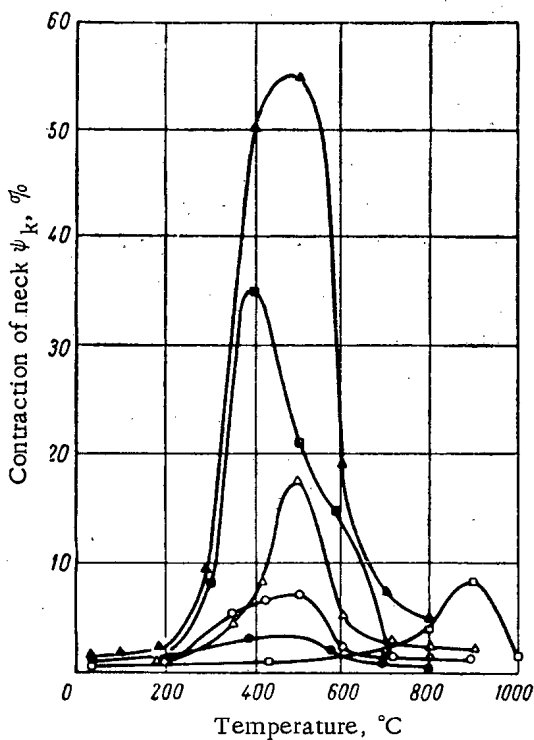
Fig. 8. Temperature dependence of relative
contraction of beryllium under tension.
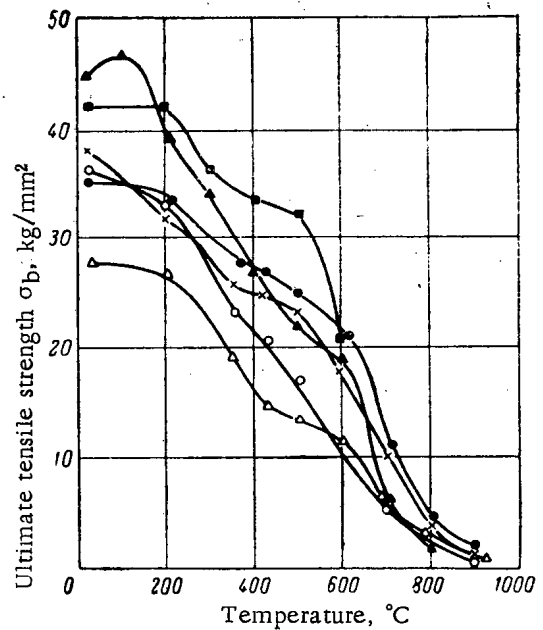
Fig. 9. Temperature dependence of the ultimate
tensile stress of extruded beryllium.

$$\frac{\sigma_b}{\sigma_{b2}} = \left(\frac{V_2}{V_1}\right)^{1/m},$$

in which for extruded beryllium at 20°C the following were obtained: $m \approx 20$ (σ_b, S_k); $m \approx 37$ ($\sigma_{0\,2}$); $m \approx 3.5$ to 4.5 (ε_b, ψ_k). With increasing temperature, the influence of the scale factor diminished, and for 400°C it could not be neglected.

After mechanical treatment, all the samples were annealed in vacuum at 850°C for 1 h, and then electro-polished with the removal of a layer around 20 μ.

The majority of samples for tensile tests were cut along the directions of pressing and extrusion and the axis of symmetry of the casting. Samples for compression tests were cut both along these directions and perpendicular to

771
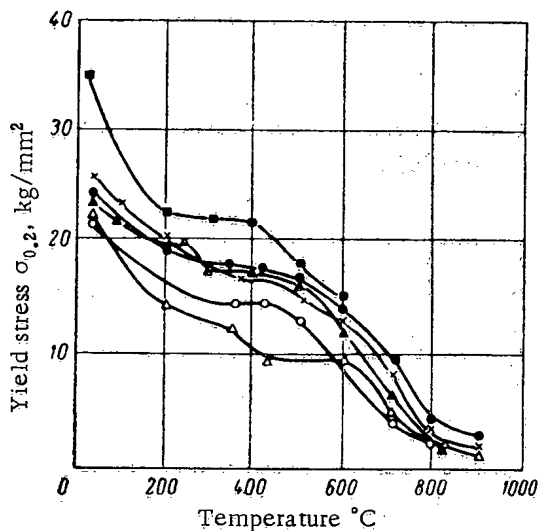
Fig. 10. Temperature dependence of the yield stress of extruded beryllium under tension.
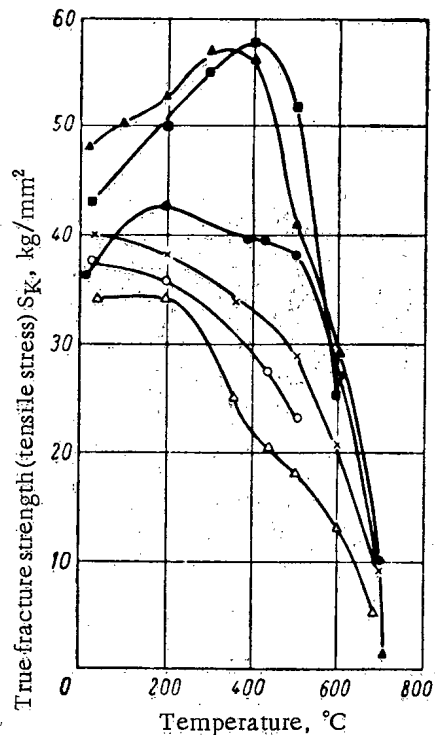
Fig. 11. Temperature dependence of the true tensile stress of extruded beryllium.
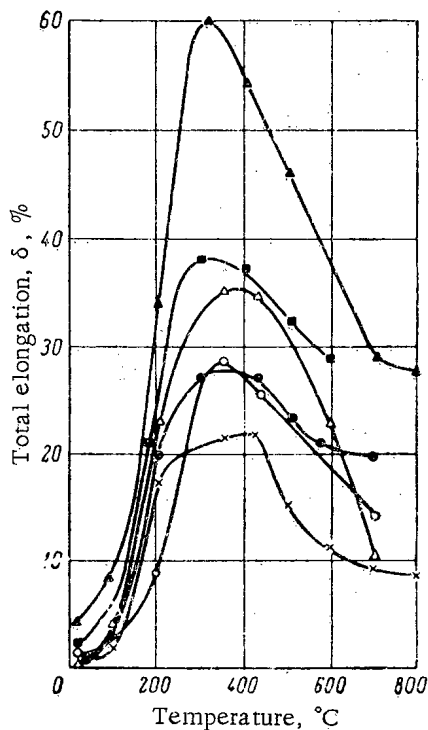
Fig. 12. Temperature dependence of the total relative elongation for extruded beryllium under tension.

them. The mechanical characteristics were determined in the usual way on the basis of strain diagrams. The strain rate was 7%/min for tension and 10%/min for compression.

Results of the Tests. The tensile tests were made at temperatures 20, 200, 350, 425, 500, 600, 700, 800, 900, and 1000°C. Figures 3-14* show graphs relating the mechanical properties of the tested materials to test temperature; these are constructed from values averaged over 3-5 samples for each temperature point.

The compression tests were made, in the main, only at 20°C and the temperature of maximum ductility of the material in question, as found from the tensile tests. Table 2 shows the average values of the mechanical properties of metal-powder ($-500\,\mu$ powder) and cast beryllium obtained during compression tests at 20°C and higher temperatures. As a rule, at high temperatures there was a warping of the samples without a fall in the load on the strain diagram. The strength and strain characteristics in this case were, therefore, determined arbitrarily from the diagram for the moment when a macroscopic crack, intersecting almost the whole side surface of the sample, appeared.

It follows from the tensile-test results given that at 20°C the beryllium studied had limited ductility, not exceeding a few percent. In all kinds of metal-powder beryllium, the ductility rose sharply on raising the temperature to 400 ot 500°C, but fell on further temperature rise. This was also noted by other authors [2-4].

A considerable influence is exerted on the ductility and strength of beryllium prepared by the metal-powder method by the degree of

---

* In Figs. 4-14 the notation of the points is the same as in Fig. 3.

772
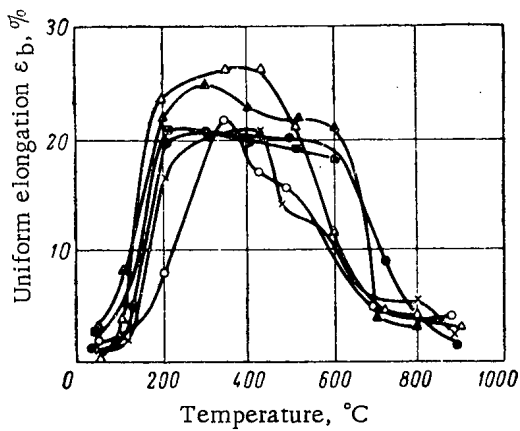
Fig. 13. Temperature dependence of the uniform relative elongation for extruded beryllium under tension.
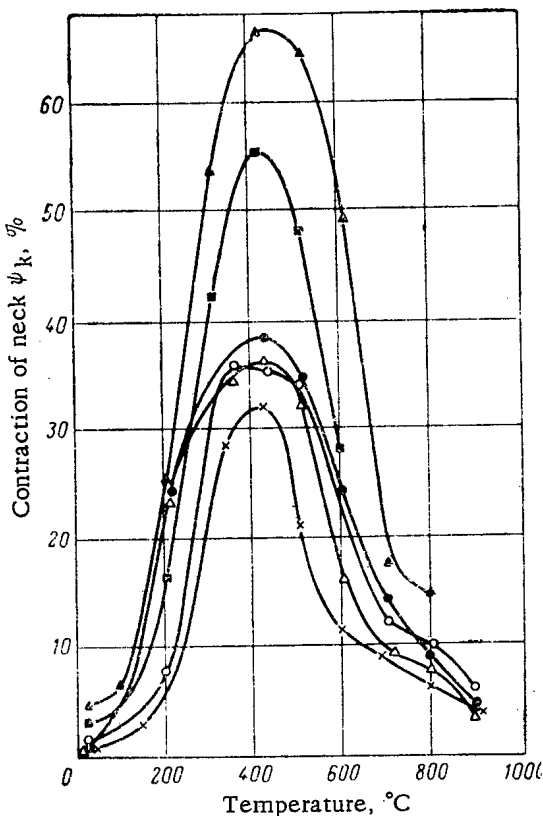
Fig. 14. Temperature dependence of relative contraction of extruded beryllium under tension.

refinement of the original powder particles. The metal obtained by extrusion from a hot-pressed billet, itself prepared from fine powder crushed in an inert medium, had the highest ductility and strength, both at room temperature (δ, ψ_k up to 5%; σ_b, S_k up to 50 kg/mm^2) and at elevated temperatures up to 600°C (ε_b up to 25%, ψ_k up to 66%, δ up to 60%).

For the same degree of refinement (-500μ), relatively high ductility at elevated temperatures was found in samples of distilled and electrolytic (chloride) metal (see Figs. 6-8 and 12-14), which may be associated with the greater purity of the metal.

On analyzing the effect of the means of preparation of the beryllium samples on the mechanical properties, it is not hard to see that the ductile and strength properties of the sintered and hot-pressed, unextruded billets were comparatively low. This may be explained by the aggregation of impurities and other inhomogeneities of structure along the grain boundaries of the metal obtained by the metal-powder method, especially for the case of a coarse-grained original powder, which is confirmed by metallographic analysis. After extrusion, the ductility and strength of beryllium at 20°C increased by a factor of two to three, while the yield stress changed rather less. This is explained mainly by the collapse of the oxide film and other inhomogeneities on pressure treatment, the establishment of favorble orientation in the remaining inhomogeneities, and also the development of grain texture, which, judging from x-ray diffraction study, also remains to a certain degree in the annealed metal.

The mechanical properties of sintered beryllium differ little from those of the hot-pressed coarse-grained material, though hot-pressing in vacuum is preferable nevertheless, owing to the absence of compressed air.

Metal-powder beryllium obtained by hot pressing in air had low mechanical properties under tension. Clearly the sintering of the powder particles was made difficult by the additional oxidation of their boundaries (these data are not shown in the graphs).

The cast metal proved more brittle than the metal-powder material. Brittle failure ensued even on heating to 400°C. This may be connected with the presence of coarse and nonequiaxial grains in the cast material, which is supported by metallographic data. Whereas in all the investigated types of metal-powder beryllium, obtained from coarse powders, the average grain diameter in the prepared samples was roughly the same and equal to 100 μ, in the cast metal the grain size was more than 300 μ across and 5.0 mm along. We note that beryllium single crystals can be strained by a considerable amount both at room and elevated temperatures, but only for definite orientations of the single crystal and reduced impurity content [5-8].

Tensile tests were not made on ingots and bars extruded from them at high temperatures. On the basis of tests made in the range 20 to 200°C we may conclude that, as a result of grain refinement on extrusion, the mechanical properties of this material will approach those of samples extruded from metal-powder billets.

773

TABLE 2. Mechanical Properties of Metal-Powder (Powder $-500\,\mu$) and Cast Beryllium on Compression

Characteristics of material	Temp. of tests, °C	Direction of tests	Ultimate compressive stress, kg/mm²	Yield stress kg/mm²	Relative contraction, %	True fracture strength kg/mm²
Cold-pressed and sintered, magnesium-thermal	20	Along	118	33,4	27	85
	20	Across	109	32,2	23	84
	425	Along	73	17,7	45	41
	425	Across	70	16,2	45	40
Hot-pressed in air, magnesium-thermal	20	Along	62	33	17	52
	20	Across	56	32,5	14	49
	425	Along	42	19,4	30	29
	425	Across	43	18,8	28	31
Hot-pressed in vacuum, magnesium-thermal	20	Along	88,7	28,8	20	71
	20	Across	93,0	29,1	21	74
	425	Along	60	17,1	35	35
	425	Across	60	18,0	35	35
Hot-pressed in vacuum, distilled	20	Along	91	25,2	24	69
	20	Across	91	26,1	23	70
	425	Along	50	13,5	45	29
	425	Across	50	11,6	40	28
Hot-pressed in vacuum, electrolytic	20	Along	81	23,7	23	63
	20	Across	75	21,4	21	60
	500	Along	54	9,3	51	25
	500	Across	34	9,4	34	22
Extruded from cold-pressed and sintered magnesium-thermal metal	20	Along	148	36	30	104
	20	Across	109	37	16	91
	425	Along	80	17,6	50	44
	425	Across	85	20,4	40	48
Extruded from vacuum-hot-pressed magnesium-thermal metal	20	Along	160	32,8	32	109
	20	Across	118	37	19	96
	425	Along	100	17,6	50	50
	425	Across	100	21,3	50	50
Extruded from vacuum-hot-pressed distilled metal	20	Along	137	32,0	29	99
	20	Across	86	38,1	12	75
	350	Along	55	15,7	50	27
	350	Across	65	23,0	40	38
Extruded from vacuum-hot-pressed electrolytic metal	20	Along	134	26,8	34	89
	20	Across	128	26,1	31	88
	425	Along	73	12,4	62	28
	425	Across	69	10,6	56	27
Cast metal	20	Along	60	23,8	13	52
	20	Across	61	24,6	14	52
	500	Along	40	14,1	30	28
	500	Across	42	14,7	28	30
Extruded from cast metal	20	Along	147	30,8	26	109
	20	Across	72	23,2	18	58
	800	Along	8	5,8	30	6

The temporary and true fracture strength in hot-pressed beryllium and ingots in the range 20 to 500°C depend little on temperature. As temperature rises from 20 to 200°C, there is a rise in the strength of extruded beryllium, which was explained in [9] a by the greater negative influence, at room temperature, of surface defects arising on mechanical treatment and leading to stress concentrations on loading samples not submitted to additional annealing, and b) by surface cold-hardening.

The highest strength characteristics belong to samples of extruded, not-pressed, distilled beryllium, prepared from powder of 50 μ coarseness (average diameter 20 to 25 μ). At room temperature, the temporary resistance to fracture was 45 kg/mm^2, and the true fracture strength 48 kg/mm^2. The same samples had the greatest ductility at room temperature: total elongation 3.6%, uniform elongation 3.6%, neck contraction 4.0%; at the temperature of maximum ductility these were respectively 60, 25, and 66%. In the mechanical testing of the beryllium there was a considerable scatter of results both from batch to batch and within each batch.

In compression tests (see Table 2), the lowest values of strength and ductility occurred in the cast metal and in billets hot-pressed in air, and the highest in the extruded metal. The strength and ductility under compression were considerably higher than under tension; hence, all operations connected with the deformation of beryllium are carried out under conditions favorable to the creation of volume compressive stresses in the material. The yield stress under compression was on average 10 to 20% higher than under tension, which to some extent was due to friction at the ends of the sample on compression.

Comparison of data obtained in compression tests for samples cut along and across the directions of pressing or extrusion, or the casting axis, show that hot-pressed billets have no marked anisotropy of properties along and across the pressing direction. This is confirmed in tensile tests. The mechanical properties under compression at 20°C for annealed samples of beryllium, extruded from hot-pressed or cast billets, proved higher in the longitudinal direction than in the transverse (in individual cases this difference reached 200%). A similar difference was observed for tensile tests, the anisotropy falling with rising temperature. The anisotropy of the mechanical properties in extruded beryllium are connected with the earlier-mentioned features in the structure of this metal.

Metallographic data showed that beryllium obtained by hot-pressing in vacuum fractured, during tensile tests at temperatures below 300 to 400°C, mainly through the grain, and at temperatures above 500 to 600°C along the grain boundaries. This transformation could also be established by the form of the fracture: for failure along the grain boundaries, the fracture was darker than for failure by way of the grain.

The brittleness of beryllium at low test temperatures is reminiscent of the behavior of certain cold-short metals with body-centered lattices, which show crystalline fractures. Increasing the grain size led to brittle failure being observed at higher temperatures. The nature of the cold-shortness of beryllium is not yet sufficiently understood. The cold-shortness of beryllium is connected in [7] with the stopping of dislocations along slip planes, especially the (1010) planes, by obstacles due both the impurities and structural inhomogeneities. This braking action with falling temperature is connected with the diminution of thermal fluctuations facilitating the overcoming of these obstacles during deformation.

Brittleness at high temperatures is caused by the weakening of the grain boundaries of the metal or an increase in the rate of flow along the boundaries, which is explained by peculiarities in the grain-boundary structure of metal-powder beryllium, by oxide inclusions, porosity, etc. Special heat treatment (for example, annealing with subsequent slow cooling at a rate of 3 to 5°/h) can change the character of the impurity distribution and reduce the tendency to form cracks along the grain boundaries during deformation at high temperatures [7].

Thus, the highest values of ductility and strength were obtained for samples prepared by the vacuum hot-pressing of finely-dispersed powder (−50 μ) of distilled metal with subsequent extrusion. A rather-reduced ductility occurred in metal-powder samples made from coarser powders (−500 μ) of distilled and chloride-electrolytic metal. The introduction of extrusion raises all the mechanical properties of beryllium, especially in the direction of flow of the metal.

LITERATURE CITED

1. G. A. Meerson et al., Atomnaya énergiya, 5, 6 (1958).
2. W. W. Beever and K. G. Wickel, Beryllium [Russian translation], Collection of translations, Editor M. B. Reifman. Moscow, IL, 4 (1956), p. 65.

3. Beryllium, Editors, D. White and J. Burke, [in Russian], Moscow, IL (1960).

4. J. Darwin and J. Baddery, Beryllium [Russian translation], Moscow, IL (1962).

5. R. I. Garber, I. A. Gindin, and Yu. V. Shubin, Fiz. metal. i metalloved., 12, 437 (1961).

6. D. L. Tower and A. R. Kaufman, Beryllium, Editors, E. White and J. Burke, [Russian translation], Moscow, IL, (1960), p. 332.

7. M. Herman and G. Spangler, Material of the International Conference on the Metallurgy of Beryllium [Russian translation, London, October 16-18 (1961).

8. V. M. Amonenko et al., Fizika tverdogo tela, 3, 796 (1961).

9. A. R. Kaufman, P. Gordon, and D. W. Lilly, Beryllium, Collection of translations, Editor, M. B. Borisov [Russian translation], Moscow, IL, 2 (1953), p. 46.

THERMOGRAPHIC INVESTIGATION OF UO$_2$, UCl, AND KCl TERNARY AND BINARY SYSTEMS

(UDC 546.791.4)

N. S. Martynova, I. V. Vasil'kova, and M. P. Susarev

The systems UCl$_4$–KCl, UO$_2$–KCl, UO$_2$–UCl, and UO$_2$–UCl$_4$–KCl were investigated thermographically.

The presence of compounds K$_2$UCl$_6$ and UOCl$_2$ in the binary systems UCl$_4$–KCl and UO$_2$–UCl$_4$ allows a breakdown of the ternary system UO$_2$–UCl$_4$–KCl into the subsystems UOCl$_2$–K$_2$UCl$_6$–UCl$_4$, UO$_2$–UOCl$_2$–K$_2$UCl$_6$, and UO$_2$–K$_2$UCl$_6$–KCl. The first of these has the lowest melting point and is regarded as an independent ternary system.

The use of fused salts as a reaction medium is becoming increasingly frequent in industry and in laboratory research. In uranium chemistry, fused salts can be employed in the regeneration of spent nuclear fuel [1] and in the conversion of oxides to chlorides [2, 3]. Reports have also appeared on studies of the uranium tetrachloride—potassium chloride system [4-6]. Barton et al., [6] report the existence, alongside of congruently melting K$_2$UCl$_6$, of two incongruently melting compounds, KUCl$_5$ and KU$_3$Cl$_{13}$, in this system. The melting point of K$_2$UCl$_6$ ($\sim 600°C$) is 50°C below the figure reported earlier.

A thermographic investigation was performed by a method not requiring a comprison standard [7], cooling curves were recorded with the aid of a FPK-55 thermograph using a combination thermocouple [8]. Laboratory-synthesized UO$_2$ and UCl$_4$ were used in the work, as well as chemically pure potassium chloride. Uranium dioxide was obtained by reduction of UO$_3$ in a hydrogen stream. Uranium tetrachloride was obtained by chlorination of uranium dioxide with carbon tetrachloride, after which impurities were driven off in vacuum. The uranium content in the resulting compounds was determined vanadatometrically [9], the chlorine content was determined mercurimetrically [10]. Deviations from theoretical predictions remained within 0.1 to 0.3%. Oxygen content in the UO$_2$ was not determined. The mixtures were prepared in a dry box. The initial substances were mixed in the required amounts (total weight 0.2 to 0.3 g) and loaded into quartz ampules. Ampules containing mixtures were sealed off in vacuum and left to stand for 8-10 h at a temperature above the phase transition temperature so as to arrive at equilibrium in the alloys. The results of thermographic experiments run on the systems UCl$_4$–KCl, UO$_2$–KCl, and UO$_2$–UCl$_4$ appear in Tables 1 to 3 and in Figs. 1-3.

TABLE 1. The UCl$_4$–KCl System

UCl$_4$	KCl	Thermal arrests, °C			
100,0	0	565	536	—	—
100,0	0	567	547	480	—
90,8	9,2	515	485	388	—
83,5	16,5	505	483	386	320
80,5	19,5	486	385	330	—
77,6	22,4	453	376	318	—
77,3	22,7	467	392	315	—
74,6	25,4	—	388	318	—
71,4	28,6	454	372	314	—
66,6	33,4	408	396	328	—
63,0	37,0	—	390	328	—
59,0	41,0	—	387	314	—
57,0	43,0	328	—	—	—
56,4	43,6	330	—	—	—
56,1	43,9	331	—	—	—
51,7	48,3	321	—	—	—
51,5	48,5	—	298	—	—
50,2	48,8	320	297	—	—
46,1	53,9	316	310	—	—
45,3	54,7	319	—	—	
42,6	57,4	368	300	—	
41,0	59,0	374	302	—	
39,3	60,7	460	305	—	
39,0	61,0	464	314	—	
37,5	62,5	518	—	412	
33,6	66,4	600	—	408	
33,2	66,8	602	—	408	
32,6	67,4	610	—	410	
32,5	67,5	598	535	409	
28,7	71,3	—	537	420	
25,0	75,0	560	—	425	
24,1	75,9	524	522	426	
22,2	77,8	540	520	418	
22,2	77,8	573	528	418	
17,5	82,5	646	—	408	
12,1	87,9	680	518	402	
5,3	94,7	750	510	407	
0	100,0	773			

777

Fig. 1. Phase diagram of UCl_4-KCl system.

TABLE 2. The UO_2-KCl System

Alloy comp. mole, %		Thermal arrests, °C		Alloy comp. mole, %		Thermal arrests, °C	
UO_2	KCl			UO_2	KCl		
0	100.0	773	—	23.7	76.3	759	755
1.4	98.6	764	761	23.5	76.5	—	757
2.6	97.4	765	761	30.1	69.9	—	758
5.0	95.0	763	758	38.2	61.8	758	756
7.0	93.0	752	749	38.8	61.2	—	760
11.3	88.7	—	758	40.5	59.5	—	751
12.2	87.8	—	756	49.2	50.8	—	750
15.8	84.2	—	760	56.5	43.5	—	750
16.7	83.3	—	750	68.6	31.4	—	751
20.4	79.6	761	756	71.5	28.5	—	744
21.0	79.0	757	747	81.0	19.0	—	731

TABLE 3. The UO_2-UCl_4 System

Alloy comp. mole, %		Thermal arrests, °C		Alloy comp. mole, %		Thermal arrests, °C	
UO_2	UCl_4			UO_2	UCl_4		
0	100.0	565	—	50.3	49.7	860	—
4.3	95.7	542	537	51.9	48.1	870	—
5.6	94.4	548	536	53.8	46.2	—	851
10.9	89.1	584	559	54.6	45.4	—	852
13.5	86.5	—	537	55.6	44.4	863	857
14.3	85.7	—	545	56.2	43.8	860	—
19.8	80.2	715	530	58.3	41.7	—	850
20.4	79.6	752	542	59.5	40.5	865	—
25.0	75.0	798	548	60.6	39.4	—	848
29.8	70.2	822	542	60.8	39.2	—	843
34.4	65.6	847	521	71.2	28.8	—	857
37.9	62.1	846	542	71.3	28.7	—	818
42.8	57.2	856	—	71.7	28.3	—	826
43.0	57.0	867	542	81.3	18.7	—	812
50.0	50.0	865	—				

The liquidus agrees with the melting point phase diagram [6] in the case of the UCl_4-KCl system. The existence of the congruently melting compound K_2UCl_6 with its melting point of 605°C and polymorphic at 418°C was confirmed. The 66-80 mole % range of UCl_4 showed the existence of a congruently melting compound hindering the polymorphic transformation at 320°C. A more exact statement of the composition and confirmation of the proposition in [6] on the temperature of the polymorphic transformation of this compound matching the temperature of the peritectic reaction of $KUCl_5$ formation would require further research. Table 4 lists data on the invariant points in the system UCl_4-KCl.

The systems UO_2-KCl and UO_2-UCl_4 were studied in the 400-900°C range (below the melting point of uranium dioxide). Parts of the liquidus corresponding to separation of pure UO_2 do not show up on the thermograms. This could possibly be accounted for by the fact that the heat evolved in the crystallization of small amounts of solid when there is only a slight departure from the eutectic composition will not be recorded by the thermocouple, while

778
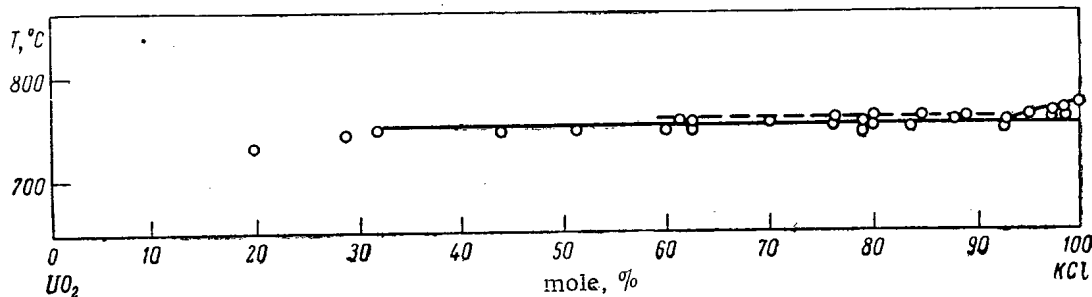
Fig. 2. Phase diagram of UO_2—KCl system.
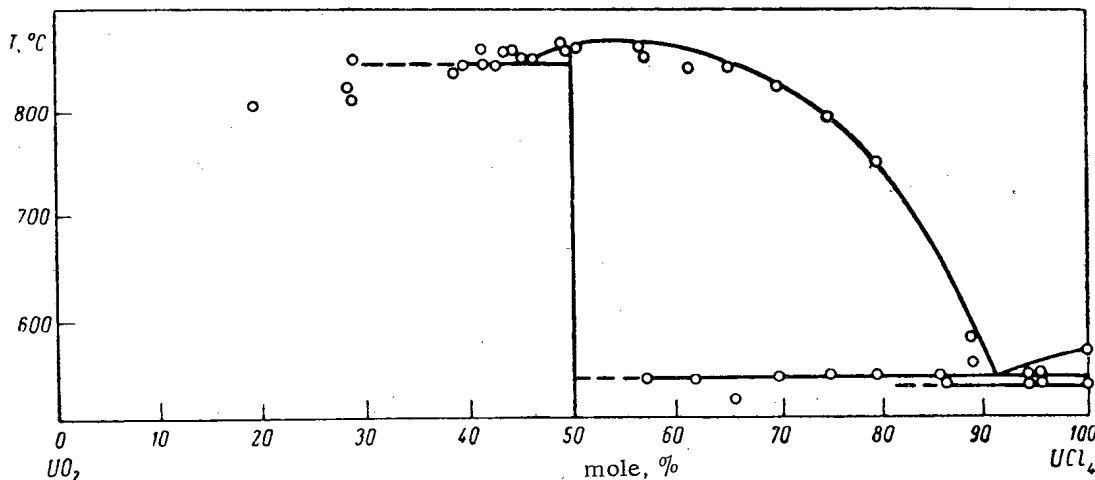
Fig. 3. Phase diagram of UO_2—KCl_4 system.

TABLE 4. Invariant Points of System UCl_4—KCl

Thermal arrests, °C	UCl_4 content, mole, %	Solid phases	Characteristic of point
529	24	K_2UCl_6, KCl	Eutectic
605	33.3	K_2UCl_6	Dystectic
418	41	α-K_2UCl_6, β-K_2UCl_6	Transitional
300	43	β-K_2UCl_6, β-$KU_2Cl_9^*$	Eutectic
320	52	α-KU_2Cl_9, β-KU_2Cl_9	Transitional
384	61	α-KU_2Cl_9, UCl_4	»
485	100	α-UCl_4, β-UCl_4	»
540	100	β-UCl_4, γ-UCl_4	»

* Composition arbitrary.

the steepness of the liquids (t_{melt} UO_2 = 2878° [11]) hinders detection of the solids when larger amounts of the solid phase separate out.

In the case of the UO_2—KCl system, the phase diagram belongs to the eutectic type, the eutectic point is shifted toward the lower-melting KCl component. In the transition from KCl to mixtures of KCl and uranium dioxide we observe a depression of the melting point from 773° to 755°C when the UO_2 content in the mixture is near 7 mole %. As the UO_2 content in the mixture increases, this thermal arrest is observed within the range of compositions studied. When the KCl content in the mixture is less than 30 mole %, the part of UO_2 remaining in the solid phase over the studied temperature range is not wetted by the KCl bath and becomes freely interspersed in the ampule

after the latter has been heated. For that reason, these specimens were not studied thermographically. Clearly, in that portion of Fig. 2 corresponding to a UO_2 content greater than 7 mole %, we observe some thermal effects at a temperature slightly higher than the eutectic, along with the eutectic thermal arrest, in some instances. There is no way of explaining the origin of these effects without further investigation.

No compounds other than the familiar uranium oxychloride $UOCl_2$ appear in the initial mixture in the composition region 43—100 mole % UCl_4 on the phase diagram for the UO_2—UCl_4 system. The markedly smeared peak on the diagram reflects the tendency of uranium oxychloride to disproportionation, which is responsible for the difficulty in obtained $UOCl_2$ free of decomposition products. We may assume that over the composition range 0—50 mole %

Fig. 4. Phase diagram of the system $UOCl_2 - K_2UCl_6$.

TABLE 5. Invariant Points of System $UO_2 - UCl_4$

Thermal arrest, °C	UCl_4 content, mole %	Solid phase	Characteristic of point
851	~46	UO_2, $UOCl_2$	Eutectic
865	50.0	$UOCl_2$	Dystectic
540	91.0	$UOCl_2$, UCl_4	Eutectic

TABLE 6. The System $UOCl_2 - K_2UCl_6$

Alloy comp. mole, %		Thermal arrest, °C			Alloy comp. mole, %		Thermal arrest, °C		
$UOCl_2$	K_2UCl_6				$UOCl_2$	K_2UCl_6			
100,0	—	865	—	—	50,0	50,0	491	460	—
94,4	5,6	819	—	—	43,4	56,6	—	463	370
87,6	12,4	768	460	—	37,0	63,0	—	455	—
78,4	21,6	697	453	—	25,0	75,0	567	458	—
66,7	33,3	598	480	355	12,1	87,9	602	470	—
56,0	44,0	489	461	370	—	100,0	605	—	—
51,5	48,5	524	478	360					

UCl_4 (in the $UO_2 - UOCl_2$ system) the phase diagram is of the eutectic type with the liquidus branch corresponding to the separation of uranium dioxide sloping even steeper than that of the $UO_2 - KCl$ system. Invariant points of the $UO_2 - UCl_4$ system are listed in Table 5.

The existence of the stable compounds K_2UCl_6 and $UOCl_2$ enables us to break up the ternary system $UO_2 - UCl_4 - KCl$ into the subsystems: $UOCl_2 - K_2UCl_6 - UCl_4$; $UOCl_2 - K_2UCl_6 - UO_2$; $UO_2 - K_2UCl_6 - KCl$. We consider the first of these as an independent ternary system. This system is a low-melting one, so that it lends itself to practical use.

The phase diagram of the system $UOCl_2 - K_2UCl_6$ was studied in order to fill in gaps in knowledge of the binary systems. Results of thermographic studies appear in Table 6 and Fig. 4. The phase diagram of the system $UOCl_2 - K_2UCl_6$ is of the eutectic type. The eutectic contains 57 mole % K_2UCl_6 and melts at 462°C. Thermal arrests at 360° to 370°C are probably due to some process occurring in the solid phase.

The $UOCl_2 - K_2UCl_6 - UCl_4$ ternary system, therefore, encompasses two eutectic type binary systems and a third system ($UCl_4 - K_2UCl_6$) with a phase diagram characterized by the presence of an incongruently melting compound. These ternary systems usually feature a ternary eutectic.

The range of the ternary eutectic may be estimated from data on the eutectics of the binary systems which are limiting cases of this ternary system, and from the comparative characteristics of pairwise interaction of the components. If we recall that the eutectic resembles the minimum heteroazeotrope, we may make use of the regularities found for azeotropic systems [12, 13]. These regularities are the following, for eutectic systems: the ternary eutectic
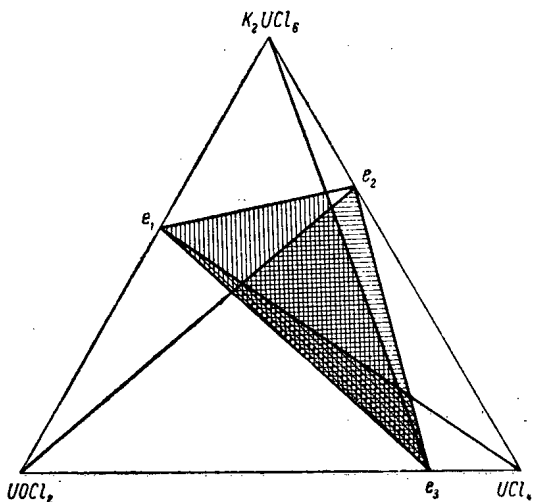
Fig. 5. Range of the ternary eutectic in the system $UOCl_2 - K_2UCl_6 - UCl_4$.
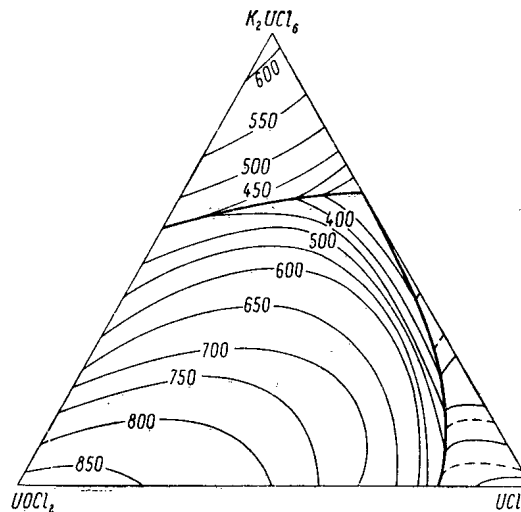

Fig. 6. Phase diagram of $UOCl_2 - K_2UCl_6 - UCl_4$ system.

TABLE 7. The $UOCl_2 - K_2UCl_6 - UCl_4$ System

Alloy composition, mole %			Thermal arrest, °C	Alloy composition, mole %			Thermal arrest, °C
$UOCl_2$	UCl_4	K_2UCl_6		$UOCl_2$	UCl_4	K_2UCl_6	
100,0			865	22,7	16,2	61,1	485
85,7	10,3	4,0	854	22,0	72,5	5,5	672
77,6	17,3	5,1	830	20,0	30,0	50,0	591
75,0	12,5	12,5	793	16,8	49,3	33,9	609
75,0	12,5	12,5	800	16,1	77,8	6,1	484
69,5	22,9	7,6	832	15,8	80,1	4,1	507
66,6	27,8	5,6	812	14,6	64,0	21,4	628
60,0	30,5	9,5	792	12,5	75,0	12,5	527
57,4	20,9	21,7	734	11,1	83,2	5,7	503
53,9	37,5	8,6	800	10,6	86,4	3,0	511
50,1	37,0	12,9	788	9,9	16,0	74,1	478
49,7	38,1	12,2	788	9,5	21,4	69,1	468
44,8	49,6	5,6	782	9,3	29,7	61,0	322
44,0	50,6	5,4	812	8,4	31,0	60,6	310
40,7	18,4	40,9	615	8,3	42,5	49,2	322
40,2	10,5	49,3	556	8,2	36,9	54,9	339
40,0	10,0	50,0	563	8,0	46,2	45,8	322
33,3	33,3	33,4	684	7,0	60,0	33,0	354
33,0	33,6	33,4	680	6,3	87,0	6,7	512
28,6	50,0	21,4	674	6,1	71,7	22,2	442
27,2	54,1	18,7	710	4,8	82,4	12,8	495
25,1	62,1	12,8	448	4,2	90,1	5,7	509
24,9	62,8	12,3	686				

lies within a triangle whose apices are on that side of the tie line connecting the apex of the composition triangle to the binary eutectic where the binary system whose components have lesser chemical affinity, so that the tendency to chemical interaction is expressed more sharply, is found. This method of estimating the range of the ternary eutectic has been used in studying the systems $NaCl - KCl - K_3VCl_6$ and $VCl_3 - NaCl - KCl$ [14, 15].

Now consider the possible range of the ternary eutectic of the $UOCl_2 - K_2UCl_6 - UCl_4$ system. Of the binary systems formed by uranium tetrachloride, the system with least chemical affinity of the components will be the $UCl_4 - K_2UCl_6$, in which an incongruently melting compound forms. With respect to the $e_1 - UCl_4$ tie line (Fig. 5), the ternary eutectic, if such exists, must lie in that part of the triangle bounded by points e_1, UCl_4, and K_2UCl_6. On comparing the binary systems formed by the K_2UCl_6 component, we draw the conclusion that the ternary eutectic must be in the sector delineated by e_3, K_2UCl_6, UCl_4, since even in that case, and for the same reason, the system $K_2UCl_6 - UCl_4$ will have a stronger tendency to form the compound. Of the pair of components including $UOCl_2$, the pair with greater affinity will be $UOCl_2 - UCl_4$, since $UOCl_2$ is a product of the interaction of UCl_4 and UO_2. The greater affinity of this pair is seen in that the eutectic they form is less pronounced than the eutectic in the system $UOCl_2 - K_2UCl_6$. The ternary eutectic must, therefore, lie in the sector $e_2 - UOCl_2 - K_2UCl_6$. The portions in the triangle $e_1e_2e_3$, within which the ternary eutectic cannot range are hatched. The diagram clearly shows a small part of the triangle $e_1e_2e_3$ adjacent to the binary eutectic e_2 which was left unhatched.

Findings of a thermographic study of the system $UOCl_2 - K_2UCl_6 - UCl_4$ appear in Table 7 and in Fig. 6. Complete mutual solubility of the components in the liquid phase is observed in this system. Most of the phase diagram is occupied by the crystallization field of $UOCl_2$. The region of lowest temperatures is actually adjacent to the eutectic of the binary system $K_2UCl_6 - UCl_4$, in conformity with the theoretical estimate. The composition
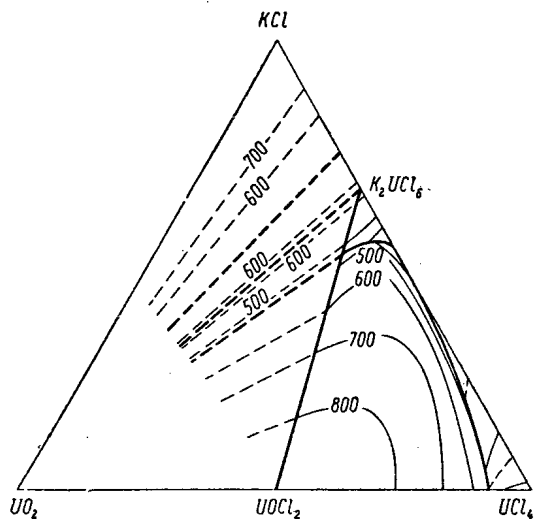
781

Fig. 7. Phase diagram of system UO_2–UCL_4–KCl.

TABLE 8. Subsystems $UOCl_2$–K_2UCl_6–UO_2 and UO_2–K_2UCl_6–KCl

Alloy composition, mole %			Thermal arrest, °C	Alloy composition, mole %			Thermal arrest, °C
UO_2	UCl_4	KCl		UO_2	UCl_4	KCl	
50,0	10,0	40,0	634	15,0	28,0	57,0	619
50,1	19,9	30,0	622	10,0	20,0	70,0	586
50,0	29,9	20,1	702	10,0	30,0	60,0	610
50,0	40,0	10,0	816	10,0	30,0	60,0	623
39,9	10,0	50,1	662	10,1	40,2	49,7	556
40,0	30,0	30,0	645	5,8	18,9	75,2	566
30,1	10,0	59,9	685	5,1	31,2	63,6	619
30,0	20,0	50,0	566	5,0	15,0	80,0	645
20,0	30,0	49,9	540	5,0	25,0	70,0	515
20,0	26,5	53,5	618	4,2	27,2	68,6	508
20,1	10,0	69,9	686	2,3	17,4	80,3	627
17,6	22,4	60,0	497				

corresponding to the lowest temperature deviates from the binary eutectic composition by amounts not exceeding experimental error, and for practical purposes may be considered identical to the eutectic.

Consider that portion of the ternary system UO_2–UCl_4–KCl bounded by the quadrangle with vertices lying at points corresponding to the compounds UO_2, $UOCl_2$, K_2UCl_6, and KCl. This region is bounded on two sides by the systems UO_2–KCl and UO_2–$UOCl_2$, with similar phase diagrams. This similarity lies in the fact that the eutectic points shift markedly toward the lower-melting components KCl and $UOCl_2$ on account of the large difference in the melting points of the components of these systems (t_{melt} UO_2 is higher than the melting point of KCl, and that of $UOCl_2$ is higher than 2000°C) and the associated steep slope of the liquidus branch corresponding to separating out of uranium dioxide. The melting points of the binary eutectics depart from the melting points of those components by only 15° to 20°C. This is evidence that the surface of the UO_2 field liquidus must have a steep incline. Under our experimental conditions, then, the only points of this surface that could be obtained on the thermograms (in our work the temperature did not go above 900°C) would be points lying in the immediate vicinity of the joint crystallization lines of the component pairs UO_2 and KCl, UO_2 and K_2UCl_6, UO_2 and $UOCl_2$. But in these instances the amounts of uranium dioxide separating out and the related thermal effects are insignificant and are not picked up on the thermogram. Only thermal arrests corresponding to the joint crystallization of two solid phases appear on the thermograms. The liquidus appears only in regions corresponding to the crystallization phase fields of KCl, K_2UCl_6, and $UOCl_2$. Thermographic findings for this portion of the ternary system UO_2–UCl_4–KCl appear in Table 8 and Fig. 7. Unbroken lines in Fig. 7 indicate isotherms characterizing the liquidus surface. The broken lines indicate nodes where a solid uranium dioxide phase coexists with ternary melts in equilibrium with solid binary solutions with a KCl, K_2UCl_6, or $UOCl_2$ base.

Thermographic investigations of the interaction between UO_2 and uranium tetrachloride and potassium chloride at temperatures to 900°C revealed that uranium dioxide interacts chemically only with the tetrachloride, to form the oxychloride $UOCl_2$. Uranium dioxide forms no compounds under the conditions investigated with potassium chloride, with the K_2UCl_6 complex, or with the oxychloride $UOCl_2$, and instead dissolves in their melts to limits of 5-7%. The presence of UO_2 in melts containing KCl, K_2UCl_6, and $UOCl_2$ has practically no effect on the mutual solubility of those compounds, as we see.

Of greatest importance in the ternary system UO_2–UCl_4–KCl is the subsystem $UOCl_2$–K_2UCl_6–UCl_4. The results obtained may be utilized in work with melts of chlorine-containing uranium compounds.

LITERATURE CITED

1. G. Benidict et al., New Nuclear Materials Including Non-Metallic Fuels, Vienna, IAEA (1963), p. 21.
2. N. P. Galkin et al., Atomnaya énergiya, 12, 531 (1962).
3. R. Canning, Australian Atomic Energy Symposium, Melbourn University Press (1958), p. 115.

4. J. Katz and E. Rabinowitch, The chemistry of uranium. McGraw-Hill, New York, 1951. [Russian translation], Moscow, Foreign Lit. Press (1954), p. 392.

5. T. Kuroda and T. Susuki, J. Electrochem. Soc. Japan., 26, 416 (1958).

6. C. Barton et al., Quoted in: E. Levin and M. McMurdie. Phase diagrams for ceramists, Part II, No. 1270 (1959).

7. L. G. Berg, Introduction to thermography. Moscow, USSR Academy of Sciences [in Russian], (1961), p. 101.

8. E. Deving and F. Richardson, Trans. Faraday Soc., 55, 611 (1959).

9. Yu. V. Morachevskii and I. A. Tserkovnitskaya, Collection of papers on radiochemistry. Leningrad, Leningrad gos. univ., [in Russian], (1955), p. 171.

10. R. D. Glukhovskaya and N. A. Ugol'nikov, Uchenye zapisi Tomsk., Univ., 29, 124 (1959).

11. W. Lambertson and M. Mueller, J. Amer. Ceram. Soc., 36, 329 (1953).

12. L. S. Kudryavtseva and M. P. Susarev, Izvestiya akad. nauk Eston. SSR. Seriya fiz.-mat. i tekhn. nauk, 12, 212 (1963).

13. L. S. Kudryavtseva and M. P. Susarev, Zhur. priklad. khim., 36, 2239 (1963).

14. I. V. Krivousova, I. V. Vasil'kova, and M. P. Susarev, Zhur. priklad. khim., 37, 2198 (1964).

15. I. V. Krivousova, I. V. Vasil'kova, and M. P. Susarev, Zhur. priklad. khim., 37, 2348 (1964).

REMOVAL OF RADIOACTIVE ISOTOPES FROM SEWAGE

(UDC 621.039.7)

F. V. Rauzen and Z. Ya. Solov'eva

Data are cited on the purification of sewage from radioactive isotopes by methods of coagulation and ion exchange.

It is shown that by the successive use of the indicated methods, low-activity sewage may be purified to the maximum permissible concentration (MPC) for all radioactive isotopes.

The removal of radioactive isotopes from waste solutions by ion exchange resins is directly dependent on the salt composition of the solutions.

As has already been reported [1], in the creation of an experimental industrial purification station, ion exchange has been used as the basic method for removing radioactive isotopes from sewage. The sewage is preliminarily coagulated to remove suspended and colloidal particles.

Operating experience of the station has shown that sewage contains varied radioactive isotopes, the relative amounts of which vary within a broad range. In practice, the sewage sent for purification from physical, chemical, and biological laboratories may contain all known radioactive isotopes at various times.

The literature contains no quantitative indices of the removal of individual radioactive isotopes from sewage. In [2], cited in certain books [3, 4], indices of purification on cation exchange resins from the radioactive isotopes Cs^{137}, $Sr^{90}-Y^{90}$, $Re^{106}-Rh^{106}$, and $Ce^{144}-Pr^{144}$ are cited; however, their content in the initial solution was very low, sometimes lower than the maximum permissible concentration (MPC). Coefficients of purification from certain radioactive isotopes, obtained during the process of coagulation of sewage, are cited in [5-7], but the number of these isotopes is small, and the conditions of coagulation differed from those used at the purification station.

To ascertain that the technological scheme of the purification station may guarantee removal of any radioactive isotopes from sewage, we conducted special experiments with solutions containing one or several radioactive isotopes, specially added to the solutions. The direct quantitative determination of radioactive isotopes entering with sewage and remaining in the solution after purification is hindered by the great variety of the emitters and by their low concentrations.

TABLE 1. Purification of Solutions from Radioactive Isotopes During Coagulation

Radioactive isotope	pH	Conc. radioactive isotopes, curies/liter		Purification factor
		before coagulation	after coagulation	
Cs^{137}	8÷9	$2 \cdot 10^{-6}$	$1,4 \cdot 10^{-6}$	1,4
Sr^{90}	8÷9	$5 \cdot 10^{-7}$	$2 \cdot 10^{-7}$	2,5
Y^{90}	8÷9	$1,6 \cdot 10^{-7}$	$1,1 \cdot 10^{-9}$	146
$Ce^{144}-Pr^{144}$	7	$3,1 \cdot 10^{-6}$	$1,6 \cdot 10^{-8}$	194
$Ce^{144}-Pr^{144}$	9	$3,1 \cdot 10^{-6}$	$3,5 \cdot 10^{-9}$	885
$Zr^{95}-Nb^{95}$	8	$1,1 \cdot 10^{-4}$	$1,4 \cdot 10^{-7}$	785
$Zr^{95}-Nb^{95}$	8	$7,6 \cdot 10^{-5}$	$2,9 \cdot 10^{-7}$	260
$Zr^{95}-Nb^{95}$	8	$3,2 \cdot 10^{-5}$	$1,8 \cdot 10^{-7}$	178
Po^{210}	8÷9	$3,1 \cdot 10^{-7}$	$6,9 \cdot 10^{-9}$	45
Pu^{239}	8	$3,1 \cdot 10^{-7}$	$1,3 \cdot 10^{-9}$	239
C^{14}	8	$7,0 \cdot 10^{-6}$	$4,1 \cdot 10^{-6}$	1,7
S^{35}	8	$1,4 \cdot 10^{-5}$	$1,3 \cdot 10^{-5}$	1,1
I^{131}	8	$1,1 \cdot 10^{-5}$	$1,0 \cdot 10^{-5}$	1,1
P^{32}	10	$4,0 \cdot 10^{-8}$	$2 \cdot 10^{-8}$	2,0

PROCEDURE

The following reagents were introduced (mg/liter) into tap water to simulate the salt composition of sewage sent to the purification station [1]: 130 Na_2CO_3; 120 soap; 20 NaOH; 90 kerosene catalyst. 4 $FeCl_3$;

784

TABLE 2. Purification Factors in Two-Step Ion Exchange

Radioactive isotope	Stage of treatment				Conc. of radioactive isotopes in purified sol. curies/liter	Total purification factor	MPC, curies/liter [13]
	ca. exchange resin of 1st stage	anion exchange resin of 1st stage	ca. exchange resin of 2nd stage	anion exchange resin of 2nd stage			
Cs^{137}	100	1,5	100	1,2	$0,7 \cdot 10^{-10}$	$1,8 \cdot 10^{4}$	$4 \cdot 10^{-9}$
Na^{24}	100	1,5	100	1,2	$1 \cdot 10^{-10}$	$1,8 \cdot 10^{4}$	$8 \cdot 10^{-10}$
Sr^{90}	10 000	1,2	20	1,2	$1 \cdot 10^{-12}$	$2,9 \cdot 10^{5}$	$3 \cdot 10^{-11}$
Y^{90}	30	2,0	10	3,0	$< 1 \cdot 10^{-11}$	$1,8 \cdot 10^{3}$	$6 \cdot 10^{-9}$
$Ce^{144}—Pr^{144}$	115	1,6	10	1,5	$< 1 \cdot 10^{-10}$	$2,7 \cdot 10^{3}$	$3 \cdot 10^{-9}$
$Zr^{95}—Nb^{95}$	25	5	10	1,1	$< 1 \cdot 10^{-11}$	$1,4 \cdot 10^{3}$	$5 \cdot 10^{-11}$
Po^{210}	1,5	15	4	10	$< 1 \cdot 10^{-10}$	$9 \cdot 10^{2}$	$2 \cdot 10^{-7}$
C^{14}	1,4	3,5	1,5	2	$2 \cdot 10^{-7}$	15	$7 \cdot 10^{-9}$
S^{35}	1,1	100	10	400	$< 1 \cdot 10^{-10}$	$4,4 \cdot 10^{-5}$	$2 \cdot 10^{-9}$
I^{131}	1,5	100	2	50	$6 \cdot 10^{-10}$	$1,5 \cdot 10^{4}$	$6 \cdot 10^{-10}$
P^{32}	1,2	10	1,2	20	$< 1 \cdot 10^{-10}$	$2,9 \cdot 10^{2}$	$5 \cdot 10^{-9}$

80 HNO_3. One or a group of radioactive isotopes were added to the prepared solution in the form of salts or acids (the concentration of the carriers did not exceed 0.01-0.1 mg/liter). It was noted that radioactive isotopes of certain elements are strongly sorbed on the walls of the vessels during the first days (Y^{90}, Ce^{144}, Zr^{95}, and Nb^{95}); hence, work with the solution was begun after the specific activity of the solution became constant (after 10-15 days).

A 5% solution of ferric sulfate, in a dose of 100 mg/liter, was introduced into the solution for coagulation, and a 10% sodium hydroxide solution was added to pH = 8-9. After mixing for 30 min and standing overnight, the solution was decanted from the precipitate and passed successively through cation and anion exchange resins. The ion exchange resins KU-2, AN-2F, and ÉDÉ-10P, which are used at the purification station, were used in the experiments.

The initial solution, solution after coagulation, and filtrates after the columns were analyzed according to the general procedures for determining summary activity [8], content of ions [9], pH level and specific electric conductivity [10, 11]. The latter characterized the total content of salts in the solutions.

During the process of filtration of the solutions through the ion exchange resins, several samples were collected to determine the dependence of the composition of the filtrate obtained on the volume of the filtered solution. The data obtained were depicted in the form of effluent curves.

In the presence of several radioactive isotopes in solution, the content of each of them was determined by the method of analyzing the curves of the absorption of β radiation in aluminum [12].

Removal of Radioactive Isotopes from Solutions During Coagulation

Table 1 presents average results on the purification of solutions from various radioactive isotopes. Here, as in our subsequent exposition, the purification factor denotes the ratio of the specific activities of the initial solution and the solution obtained after precipitation or filtration. From Table 1 it is evident that chiefly radioactive isotopes of the elements forming hydroxides or insoluble compounds under the given conditions are removed during coagulation. For the other radioactive isotopes, the purification factors do not exceed 2.5.

Removal of Radioactive Isotopes from Solutions During their Filtration through Ion Exchange Resins

From Fig. 1, which presents the effluent curves obtained for a number of radioactive isotopes, it is evident that purification of the solutions from most of the isotopes is directly dependent upon the removal of salts from the solution.
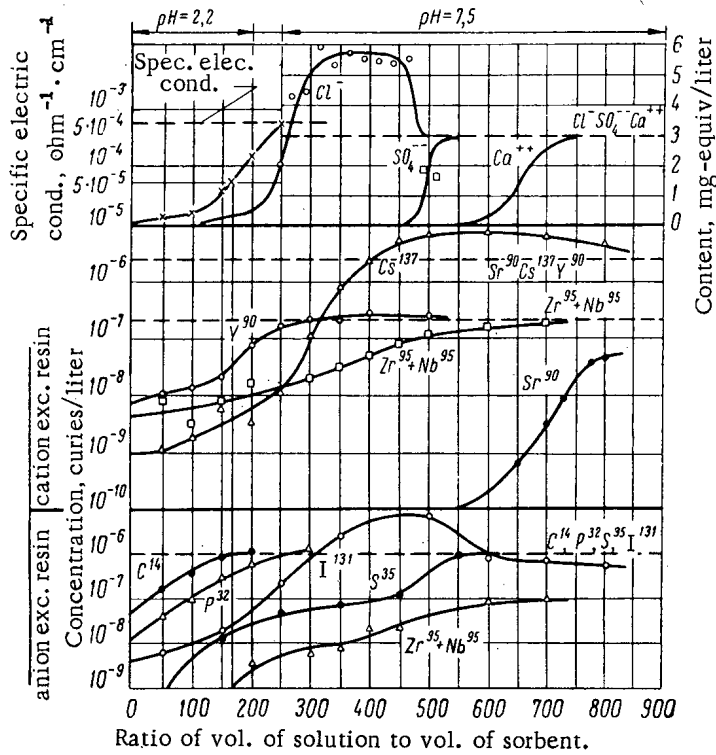
785

Fig. 1. Variation of the ion concentration in the filtrate as a function of the volume of the solution passed through (dotted line —concentration in initial solution).
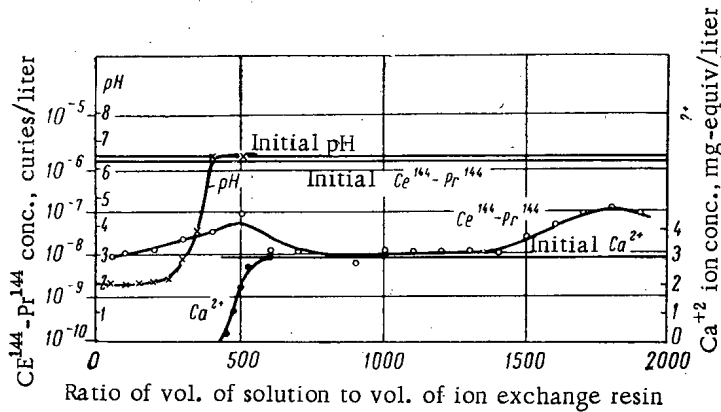

Fig. 2. Variation of the Ce^{144}-Pr^{144} concentration in the filtrate as a function of the volume of the solution passed through.

The most profound purification is achieved when there is still a large reserve capacity on the ion exchange resins, and the filtrates contain negligible amounts of the salts (at a specific electric conductivity of the filtrate less than $5 \cdot 10^{-5}$ $ohm^{-1} \cdot cm^{-1}$).

When all the hydrogen ions saturating the cation exchange resin, capable of exchange, are replaced by cations from solution, the content of radioactive isotopes in the filtrate increases. This pertains not only to the isotopes forming cations in solution, but also to the isotopes forming anions, since the weakly basic anion exchange resins AN-2F and ÉDÉ-10P possess very low exchange capacity in neutral and weakly alkaline media (Fig. 1 at the top indicates the pH of the filtrate after the cation exchange resin).
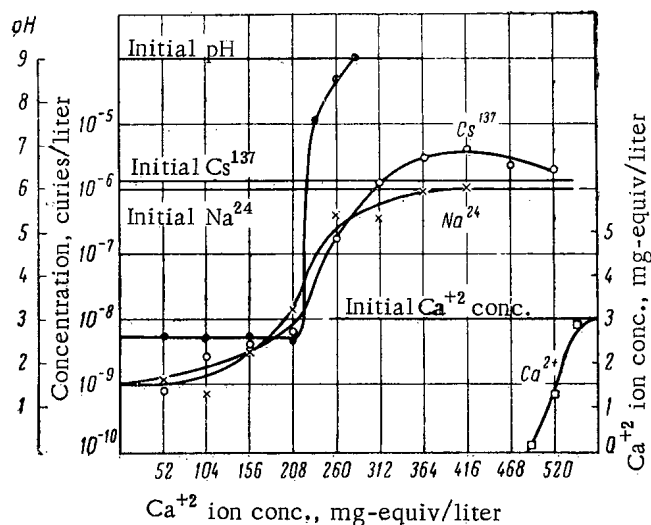
Fig. 3. Variation of Cs^{137} and Na^{24} concentration in the filtrate as a function of the volume of solution passed through.

The different affinities of the chemical elements for ion exchange resins are also manifested in such a dilute state as that of the radioactive isotopes in our experiments. From Fig. 1 it is evident that the sorption of Sr^{90} continued even after the cation exchange resin was saturated with sodium ions, i.e., when the pH of the filtrate became equal to 7.5. The isotope Ce^{144} is absorbed by the cation exchange resin even when the entire capacity of the cation exchange resin has been exhausted, and the salt compositions of the initial solution and filtrate have become virtually identical (Fig. 2).

The experiments showed also that radioactive and nonradioactive isotopes close in chemical properties are removed identically from solutions. Close purification factors of the solutions from Sr^{90} and the cations of hardness (Ca^{45} was used as the radioactive tracer to determine the latter) were found. The results of purification from Cs^{137} and from sodium ions are also close, which is evident from Fig. 3: the removal of sodium ions, the concentration of which is 3 mg-equiv/liter, may be judged according to the decrease in the Na^{24} concentration.

As a result of the experiments, it was established that in the system used, at the stage of purification when the ion exchange resins are used only in the H^+ and OH^- forms, maximum purification from radioactive isotopes is achieved. The capacity of the ion exchange resins with respect to radioactive isotopes, if there are no salts in solution, is very great; hence, the introduction of the second stage of ion exchange into the process guarantees the production of high sewage purification factors.

Table 2 shows the purification factors that may be achieved in two-step ion exchange if the content of radioactive isotopes in the initial solution (after coagulation) corresponds to the values indicated in Table 1, and the total salt content does not exceed 0.7 g/liter.

On the basis of the above, the following conclusions may be drawn:

1. It was shown that in the successive treatment of low-activity sewage by the methods of coagulation and two-step ion exchange, the concentrations of radioactive isotopes may be reduced below the MPC.

2. The removal of radioactive isotopes from waste solutions by ion exchange resins is directly dependent upon the salt composition of the solution.

3. With increasing salt content in the filtrates after the ion exchange columns, the concentration of radioactive isotopes in them increases.

LITERATURE CITED

1. K. A. Bol'shakov et al., In the book: Transactions at the Second International Conference on the Peaceful Uses of Atomic Energy, Reports of the Soviet Scientists [in Russian], Moscow, Atomizdat, 4 (1959), p. 189.
2. H. Swope and E. Anderson, Industr. and Engng. Chem., 47, 78 (1955).
3. Collection: Ion Exchange Technology [Russian translation], Editors, F. Nakhoda and J. Shubert. Moscow, Metallurgizdat (1959).
4. Collection: Waste Products of the Atomic Industry [Russian translation]. Editor E. Glueckhauf. Moscow, Gosatomizdat (1963).
5. V. V. Pushkarev, Zh. Neorganich. Khimii, 1, 170 (1956).
6. S. A. Boznesenskii et al., Ibid., 3, 233 (1958).
7. P. F. Dolgikh, Zh. Prikl. Khimii, 35, 995 (1962).
8. V. Bochkarev et al., Measurement of the Activity of Sources of Beta and Gamma Radiations [in Russian], Moscow, Izd. AN SSSR (1953).

787

9. Collection: Analysis of Mineral Raw Materials [in Russian], Editors, Yu. N. Knipovich and Yu. V. Morachevskii, Leningrad, Goskhimizdat (1956).

10. A. Weisberg, Physical Methods of Organic Chemistry [Russian translation], Moscow, Izd. Inostr. Lit., 4 (1954).

11. V. I. Perel'man, Concise Chemists' Handbook [in Russian], (1955).

12. M. E. Tsvetaeva and M. N. Brusentsova, Collection of Radiochemical and Dosimetric Procedures [in Russian]. Editors, N. G. Gusev et al., Moscow, Medgiz (1959).

13. Sanitary Regulations for Work with Radioactive Substances and Sources of Ionizing Radiations [in Russian], Moscow, Atomizdat (1960).

All abbreviations of periodicals in the above bibliography are letter-by-letter transliterations of the abbreviations as given in the original Russian journal. *Some or all of this periodical literature may well be available in English translation.* A complete list of the cover-to-cover English translations appears at the back of this issue.

NOTES ON ARTICLES SUBMITTED

WAVEGUIDE ACCELERATOR-BUNCHER INTENDED TO PRODUCE A MONOKINETIC ELECTRON BEAM

(UDC 621.384.621)

G. I. Zhileiko and V. A. Snedkov

In order to obtain minimum electron-energy scatter at the output of an accelerator-buncher, various ways of integrating the equations of motion and field equations are considered. In certain cases, when the dynamics of electrons deviating little from the equilibrium trajectory are being studied, it is convenient to use analytical solution of the equations. The equations may be reduced to the form

$$\frac{d^2\xi}{du^2} + f(u)\xi = 0,$$

(1)

where

$$f(u) = \frac{kU_0 \operatorname{ctg} \varphi_s}{E_{acc}(u)(\sqrt{(u+1)^2 - 1})^3},$$

(2)

and to the equation

$$\psi = \operatorname{tg} \varphi_s \frac{d\xi}{du}.$$

(3)

Here ξ and ψ are small deviations of the energy and phase from the equilibrium values. In Eq. (1), $f(u)$ is determined by the variation of the accelerating electric field along the buncher, which must be found by calculation for given u and ξ. For certain forms of $f(u)$, solutions of (1) are known in trigonometrical and cylindrical functions. Variations of $E_{acc}(u)$, corresponding to practically acceptable accelerating-field strengths $10 < E_{acc} < 150 \text{kV/cm}$ take place for $f(u) = u^{-n}$, where n = 0 to 4. The known solutions of (1) exhaust the variety of ways in which the field strength varies along the buncher. On choosing the optimum relationship $E_{acc}(u)$, ensuring a monoenergetic electron beam, the forms relating to a small or very large length of the buncher drop out. The former are impracticable owing to the too-large accelerating-field strengths in any region of the buncher, and the latter owing to the inconveniences connected with large linear dimensions of the accelerator. As a result of the selection, relationships between the accelerating-field strength and the length of the buncher were obtained for identical initial and final energies and for $\xi k = 0$.
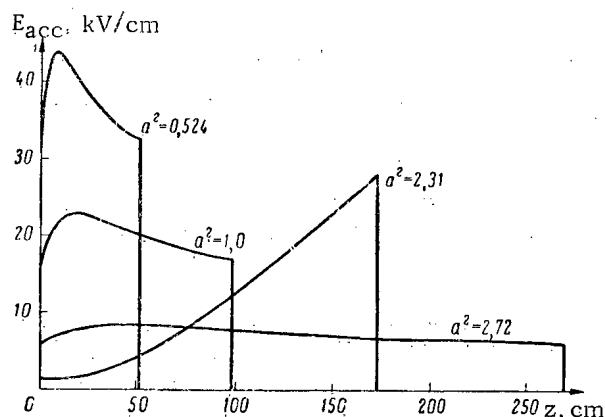
Variation of the accelerating field with longitudinal coordinate of the accelerator z for various coefficients a^2 (for each curve the final energy of the electrons equals 2 MeV).

If $f(u) = \left(\frac{a}{u+b}\right)^2$, then the optimum variant is $a^2 = 0.524$ (see figure).

MAXIMUM EFFICIENCY AND LIMITING CURRENT OF AN ELECTRON
BEAM IN A HEAVY-CURRENT WAVEGUIDE ACCELERATOR

(UDC 621.384.62)

G. I. Zhileiko

The efficiency $\eta = \dfrac{P_E}{P}$ of an accelerating waveguide (P_E = electron-beam power) is defined with due allowance for the variation in dimensions of the accelerating waveguide, determined from the conductivity function

$$\Gamma = \frac{P}{E^2} = \int_0^{2\pi} \int_0^{a} E_r H_\varphi \, r dr d\varphi \qquad (P = \text{uhf power flow, } E = \text{amplitude of accelerating field on waveguide axis, } a =$$

radius of apertures in diaphragms, E_r and H_φ = transverse field components, r = radius, φ = azimuthal coordinate), the attenuation factor of the field in the waveguide metal α, the coefficient $\delta = E_I / E_F$ (indices indicate initial and final values), the length L of the waveguide, and the radiation field $E_{rad. f}$:

$$\eta = 1 - \frac{\Gamma_F}{\delta^2 \Gamma_I} e^{2\alpha L} - \frac{E^2_{rad.f}}{E^2_I} \ .$$

The limiting current of the beam for given P, kinetic energy U, $\Gamma_F / \delta^2 \Gamma_I e^{2\alpha L} \ll 1$, $\delta \approx 5$, $\alpha \ll 1$ and $\Gamma_F \leq \Gamma_I$ is

$$I_{\lim} \approx \frac{P}{U} \cdot \frac{1 - \dfrac{\Gamma_F}{\Gamma_I} \cdot \dfrac{E^2_{rad.f}}{E^2_I}}{1 + \dfrac{\alpha U}{\xi E_F (\delta \sin \theta_I + \sin \theta_F)}} \ .$$

Here $\xi = \dfrac{U}{E_I \sin \theta_I + E_F \sin \theta_F) L}$ is the averaging coefficient of the accelerating field along the length of the accelerator, θ is the equivalent equilibrium phase, defined as $\sin \theta = (1 - \dfrac{E_{rad}}{E \sin \Phi}) \sin \Phi$, where Φ is the equilibrium phase without allowing for the radiation field.

The expressions for η and $I_{\lim}$ are valid when all the quantities coming into the formulas rise or fall monotonically with increasing z. If not, the waveguide is divided into two sections, for which the calculations are made separately.

For calculating the radiation field, we consider the excitation of an electromagnetic E_{01} in the accelerating waveguide by groups of electrons for phase velocities $\nu_\Phi = a + bz$, $\nu_\Phi = \sqrt{m} + nz$ and $\nu_\Phi = $ const of the exciting current (current of the accelerated electron beam) varying along the waveguide. Formulas are given for the radiation fields and the total field, and the fundamental harmonic of the beam current is determined.

The formulas obtained for the radiation fields show that the field has a maximum in the region of $\nu_\Phi \approx 0.6$ to 0.85, if a nonbunched beam ($E_{rad} \approx 8.5$ kV/cm for P = 2 MW, $E_{acc} \approx 20$ kV/cm, I = 0.5 A) is introduced into the accelerator. If a bunched beam is introduced, the radiation field rises rapidly at the beginning of the waveguide ($E_{rad} \approx 15$ kV/cm for the same data) and falls with increasing phase velocity.

DOSE RATE FROM A UNIDIRECTIONAL SOURCE OF GAMMA QUANTA CLOSE TO THE GROUND-AIR INTERFACE

(UDC 539.171:539.12)

Yu. I. Bublik, S. M. Ermakov, B. A. Efimenko,

V. G. Zolotukhin, and E. E. Petrov

The dose rate from a unidirectional, mono-energetic gamma-quantum source close to the earth-air surface has been calculated by the Monte-Carlo method (i.e., by calculating the flux locally, separating analytically the contribution of single scattering, and treating in parallel the results of statistical tests for many points in space). The statistical accuracy of the dose-rate determination is 6-8%.
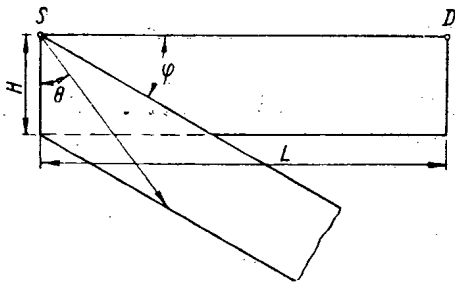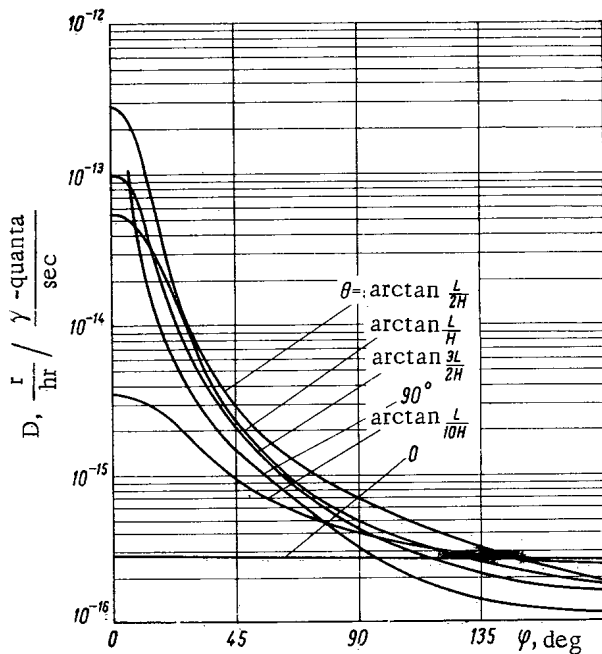
A comparison is made with experimental results [1, 2] obtained with a Co^{60} source. The agreement is satisfactory.

In the calculations it was assumed that the earth and the air are two semi-infinite media separated by a plane boundary. The composition of the ground was taken as SiO_2 (density $2.0 \cdot 10^3$ kg/m³), of the air as 21 wt. % oxygen and 79 wt. % nitrogen (density 1.29 kg/m³). The source S and detector D were placed at the same height H and spaced apart by a distance L. The geometry of the calculation is shown in Fig. 1.

Fig. 1. Geometry of calculation.

The calculations were performed for initial beam energies 0.1, 0.5, 1.25, 2.7, 5.0, and 8.0 MeV, distances L of 5, 15, 30, 50, and 100 m, and heights H of 1, 4, 7, 10, 12, 16, 20, 30, 40, 50, and 60 m. The angles θ and φ were varied in the ranges $[0, \pi/2]$ and $[0, \pi]$ respectively.

All the results are reduced to the integral dose rate,

$$D\,(L, H, \theta, \varphi, E_0) = \int_0^{E_0} \psi\,(L, H, \theta, \varphi, E_0, E) \times A\,(E)\,dE,$$

where $\psi(L, H, \theta, \varphi, E_0, E)$ is the energy spectrum of the scattered gamma quanta in the beam, and $A(E)$ the conversion coefficient from flux to dose rate.

Figure 2 plots the dose rate versus the angles of orientation of the primary beam for H = 4 m and L = 50 m. Figure 3 plots the dose rate versus H for $\theta = 0°$ and L = 15 m (1) or L = 50 m (2). Figure plots the dose rate versus φ for various initial gamma quantum energies E_0 for $\theta = \arctan L/H$, L = 15 m and H = 4 m.

Fig. 2. Dose rate of scattered gamma radiation versus direction of primary beam (E_0 = 1.25 MeV).
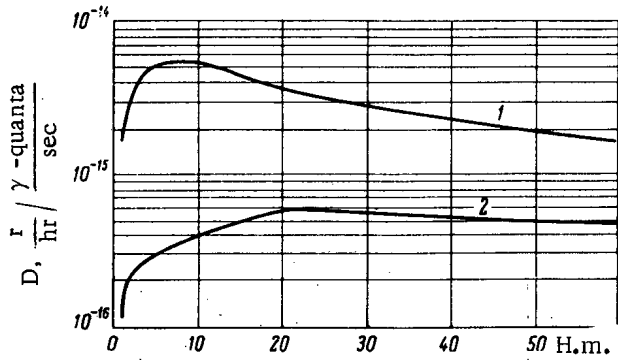
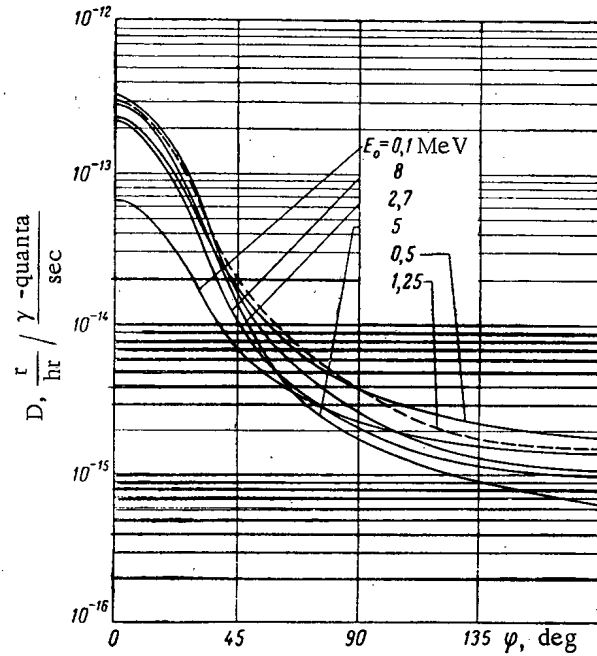Fig. 3. Dose rate versus height.

Fig. 4. Dose rate versus φ for various initial energies E_0.

The above information can be used to calculate the dose rate from an anisotropic gamma-ray source near the earth's surface.

LITERATURE CITED

1. E. Blizard, Reactor Handbook, 3, ch. 15, 271 (1962).
2. S. M. Ermakov et al., Atomnaya énergiya, 18, 416 (1965).

AGES OF NEUTRONS FROM MONO-ENERGETIC AND MULTI-ENERGETIC SOURCES IN A UNIFORM MODERATOR

(UDC 539.125.52)

D. A. Kozhevnikov

The author calculates the age (square of the moderation length) of neutrons, from the space-energy distribution function found in [1] for neutrons in a uniform moderator of any isotopic composition. The expression found is much more convenient for numerical calculation than the results of the momentum method:

$$\tau_s(u) = \frac{1}{3}\,\overline{\lambda^2}(u)\left[v_0^2 + \frac{u + v_0\,\overline{\cos\vartheta_0} + 1 - \overline{\xi}_0}{\xi(1 - \overline{\cos\vartheta})} + \frac{3 - 5\,\overline{\cos\vartheta}}{3\,\xi(1 - \overline{\cos\vartheta})^2}\right].$$

The neutron characteristics contained in this formula, and the method of their calculation, are described in [1]. A scheme is given which makes clear the physical meaning of the individual terms in the formula. Each term has an analogue in the formulae obtained by the momentum method; however, the awkwardness of the latter hinders the direct interpretation of their physical meaning. The origin of errors in the calculation is established, using the models of Selenguth-Hertzel, Plachek, and others.

The author gives a graph of the calculated ages of neutrons in water and graphite versus their initial energies. Calculations are made both with and without allowing for diffraction anisotropy of neutron scattering at the oxygen in water. A comparison is drawn up between the results of calculations by the Monte-Carlo method, by multi-group Fourier-transform programs, by the method of momenta, etc.

From an analysis of the experimental data on the energy spectra of fission neutrons from U^{235} and from (α, n) isotope sources (Po-Be, Ra-Be, Pu-Be, Po-B), the author draws up a detailed table of normalized weight functions and mean energies of the spectra of these sources.*

From the tabulated weight functions for the above sources, the author calculates the age of neutrons from the sub-indium resonance in water; experimental data are given.

The calculated results are in good agreement with experiment. It is shown that the diffraction anisotropy and inelastic scattering of neutrons in oxygen lead to changes in neutron ages which are quite close in value, but opposite in sign. The magnitude of the age is sensitive to changes in the shape of the source spectrum; experimental errors in measuring the spectrum cause marked scatter of the calculated values.

The references include 49 items.

LITERATURE CITED

1. D. A. Kozhevnikov, Atomnaya Énergiya, 17, 34 (1964).

---

* A knowledge of the spectral weight functions is necessary for calculating the space-energy distribution and neutron ages for multi-energy sources.

HEAT TRANSFER AND TEMPERATURE FIELDS IN BUNDLES
OF ROD-SHAPED HEAT-EMITTING ELEMENTS, PARALLEL
TO THE LAMINAR FLOW OF A LIQUID IN WHICH THEY ARE IMMERSED
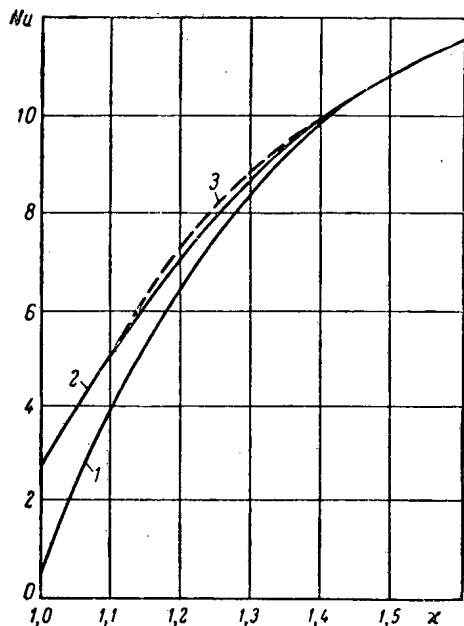
(UDC 621.039.517.5)

M. Kh. Ibragimov and A. V. Zhukov

The study of heat exchange in reactor cores with laminar coolant flow is of importance in investigating the conditions of shut-down cooling or of nominal power output.

Reactor cores often consist of cylindrical fuel elements arranged in a square grid with small spacing ($\varkappa$ = 1.1-1.2). In this case, the temperature field and heat exchange depend not only on the physical properties and flow conditions of the coolant, but also on the construction of the fuel elements—heat conductivities of the can and fissionable material and can thickness. There are no data on this question in the literature. The solution derived by Sparrow et al., [1] is only a partial one; it is derived only for one boundary condition, t_c = const.; and does not take into account the influence of fuel-element construction on heat exchange and temperature field. To allow for this influence, we have to solve simultaneously the equations of heat conduction and heat exchange in the fissionable material (f), can (c), and coolant (l),

$$\left. \begin{array}{l} \nabla^2 t_f + \dfrac{q_v}{\lambda_f} = 0; \\[2mm] \nabla^2 t_c = 0; \\[2mm] \nabla^2 t_l = \dfrac{u}{a_l} \cdot \dfrac{\partial t_l}{\partial z} \end{array} \right\} \qquad (1)$$

for the appropriate boundary conditions.

By solving these equations, we get expressions for the temperature distribution and heat flux, and also for the mean Nu number in the bundle of fuel elements:

$$\dfrac{t_c - \bar{t}_c}{q r_0} \lambda_l$$

$$= \sum_{m=1}^{\infty} A_{c_m} \left[1 + \dfrac{\lambda_c - \lambda_f}{\lambda_c + \lambda_f} \left(\dfrac{r_1}{r_0} \right)^{12m} \right] \cos 6m\,\varphi \ldots; \qquad (2)$$

$$\dfrac{q_c}{\bar{q}_c} = 1 - \dfrac{\lambda_c}{\lambda_l} \sum_{m=1}^{\infty} 6m A_{c_m}$$

$$\times \left[1 - \dfrac{\lambda_c - \lambda_f}{\lambda_c + \lambda_f} \left(\dfrac{r_1}{r_0} \right)^{12m} \right] \cos 6m\varphi \ldots; \qquad (3)$$

$$Nu = \dfrac{2 \left(\dfrac{2\sqrt{3}}{\pi} \varkappa^2 - 1 \right)}{M \left(\dfrac{3}{64\varkappa^2} - \dfrac{\sqrt{3}}{4\pi} \right) - D} \ldots \qquad (4)$$

Nu plotted versus relative spacing $\varkappa$: 1) boundary conditions q_c = const.; 2) boundary condition t_c = const. (authors' data); 3) boundary condition t_c = const. (data from [1]).

794

Here r_1 and r_0 are the internal and external radii of the can, and M is a parameter to allow for the velocity distribution. The coefficients A_{c_m} and D are found from the solution of (1).

From (2)-(4) the temperature fields, heat fluxes and mean Nu numbers are calculated for bundles of fuel elements with $\varkappa$ = 1.0, 1.1, 1.2, and 1.5, with boundary conditions at the surface of the fuel element t_c = const. and q_c = const. The calculated values of Nu, represented in the diagram, give two limiting estimates for the heat trans- in the bundles of fuel elements. The upper curve corresponds to limitingly high heat conductivity of the fuel ele-

ment $\left[\dfrac{\lambda_c - \lambda_f}{\lambda_c + \lambda_f} \left(\dfrac{r_1}{r_0} \right)^{12m} \to -1 \right]$, and the lower curve to limitingly low conductivity $\left[\dfrac{\lambda_c - \lambda_f}{\lambda_c + \lambda_f} \left(\dfrac{r_1}{r_0} \right)^{12m} \to 1 \right]$.

For actual fuel elements, the values of Nu lie between these curves and can be calculated from (4).

LITERATURE CITED

1. E. Sparrow et al., Trans. ASME, November, 415 (1961).

795

THE ROLE OF DIFFUSION IN THE MIGRATION
# OF RADIOACTIVE CONTAMINANTS

(UDC 621.43)

V. M. Prokhorov

Radioactive fission products falling on the Earth's surface will in time migrate into the soil. One cause of this migration is free diffusion —a slow but steady process, which can, over a long time, redistribute the radioactive isotopes in the soil or ground.

The author suggests a method of estimating the contribution made by diffusion to the vertical migration of an isotope; it is based on measurements of the isotope content in the surface layer of soil. It is provisionally supposed that the isotope can penetrate into the soil only by diffusion. Three variants are discussed for the variation of isotope concentration at the surface; these are the closest approximations to natural conditions: (1) once-only arrival; (2) constant concentration; (3) concentration increasing linearly with time. For these conditions, formulae are derived which give the fraction q of an isotope (of its total content in the soil) which remains in the upper layer of soil of thickness 1, in terms of a dimensionless parameter $y = l/(2\sqrt{Dt})$, where D is the diffusion coefficient and t the time. The diagram plots this relation for the three variants mentioned above: from this we can calculate the actual diffusion coefficient. By processing the published data on the distribution of Sr^{90} in the soil in natural conditions, it is shown that the mean actual diffusion coefficient is close to the value derived by the authors in laboratory experiments, and, as a rule, lies between $3 \cdot 10^{-8}$ and $2.5 \cdot 10^{-7}$ cm^2/sec. This shows that diffusion plays an important part in the vertical migration of Sr^{90}, and, therefore, it is partly a formal procedure to regard the migration as a diffusion process. By approaching the migration of a radioactive isotope as a diffusion process, we can predict its distribution in the soil. The table gives results of such a calculation, for the case of linear increase of concentration at the soil surface (see diagram, curve 3).

Variation of Sr^{90} Content in Upper Soil Layer
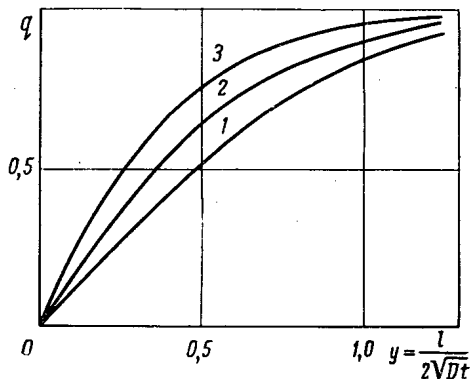
Fraction q of isotope in upper layer versus parameter $y = l/2\sqrt{Dt}$. 1) Once-only contamination of soil; 2) constant concentration at surface; 3) linear increase of surface concentration with time.

Thickness of layer, cm	Actual diff. coef. cm^2/sec	Sr^{90} content in upper layer (% of total amount)			
		1953	1959	1965	1971
0—5 0—10 0—15	$4.5 \cdot 10^{-8}$	93 100 100	84 98 100	77 96 100	71 93 99
0—5 0—10 0—15	$9 \cdot 10^{-8}$	84 98 100	71 93 99	64 88 97	57 84 94
0—5 0—10 0—15	$18 \cdot 10^{-8}$	71 93 90	57 84 94	49 76 90	44 71 85

A 10 MeV WAVEGUIDE SYNCHROTRON

(UDC 621.384.612)

A. A. Vorob'ev, A. N. Didenko, A. I. Lisitsyn, B. N. Morozov,

Yu. I. Potekhin, L. G. Salivon, and R. M. Filatova

For some years the Tomsk Polytechnic Institute has been studying the waveguide synchrotron [1]. The accelerating system in this, is a smooth or loaded waveguide, closed into a circle, in which is excited an electromagnetic wave with an azimuthal component of the electric field. The dimensions of the waveguide are chosen so that, at one radius, the phase velocity of an electromagnetic wave of the required mode is equal to the velocity of light; this also synchrozines the electric field with the accelerated particles.

In the Nuclear Physics Research Institute of the Tomsk Polytechnic Institute, work has been done on the theory of accelerators of this type. Studies have been made of the dispersion properties of curved septate waveguides [2] and smooth systems [3], the dynamics of electrons in such waveguides [4, 5], and their economic efficiency [6]. Under certain conditions, the efficiency of a waveguide system can be an order of magnitude higher than that of the most modern accelerating systems in high-energy synchrotrons. It is shown that, in high-energy waveguide synchrotrons, it is necessary to use decelerating systems of the symmetrically-loaded waveguide type [2] and various rod systems [7], while, in low-energy accelerators, sufficient effectiveness can be attained with smooth curved waveguides and curved waveguides with diaphragms along the outer curved wall. To attack the problems arising in the construction of this type of accelerator, we have planned and built a 10 MeV waveguide synchrotron for electrons. With instructions of priority from the Tomsk workers, work on the efficiency of cyclic waveguide accelerators has also been going on at the Institute of Vacuum Electronics in Czechoslovakia [8], where a 1.5 MeV waveguide synchrotron, based on a smooth curved waveguide, has been built and put into service.

In the 10 MeV synchrotron at Tomsk, the accelerating system is a rectangular waveguide bent into a circle, with diaphragms on the outer wall, in which is excited a wave of mode H_{018} with $\pi/2$ vibrations. The radius of the equilibrium electron orbit, at which the phase velocity of the H_{018} wave is equal to that of light, is 13 cm. The interaction area is 6 X 6 cm. The quality factor is $Q \approx 300$, the shunt resistance $R_{sh} \approx 0.07$ Megohm. The waveguide has two radial sections at nodes of the HF current. After injection by a Kerst gun with injection potential 300 keV, the electrons are accelerated in betatron conditions up to 3 MeV. On switching on the HF generator, the particles are captured into the synchrotron regime and accelerated to the final energy of 10 MeV. The guiding magnetic field is produced by an electromagnet with three-leg core, its windings being powered from an ac network at 50 cps. To reduce the effect of the conductive coating on the waveguide, which is located within the magnetic field, the interpole gap at the equilibrium radius is widened to 12 cm, and the wall thickness of the curved waveguide is made equal to 30 μ. In connection with this, the accelerating chamber is a glass shell, finished to high accuracy, and following the decelerating structure in its inner surface, onto which is evaporated a silver coating. The construction of the waveguide presents certain difficulties. Our experiments showed that the required accuracy and finish of a curved waveguide may be much less than those initially planned. To ensure mechanical strength of the system, it was considered convenient to enclose it in a vacuum-tight casing with dimensions chosen to correspond with the interpole gap.

The source of electromagnetic waves was a pulsed HF generator working in the ten-centimeter range, generating pulses of duration 5000 μsec and power 400 watt. With our chosen acceleration time, this power is necessary, not to obtain the required energy increase, but for transfer of particles from betatron to synchrotron conditions. High-frequency power is fed to the accelerating chamber via a waveguide channel, with a ferrite bypass and flexible waveguide connector, which mechanically separates the glass chamber from the channel. The vacuum line to
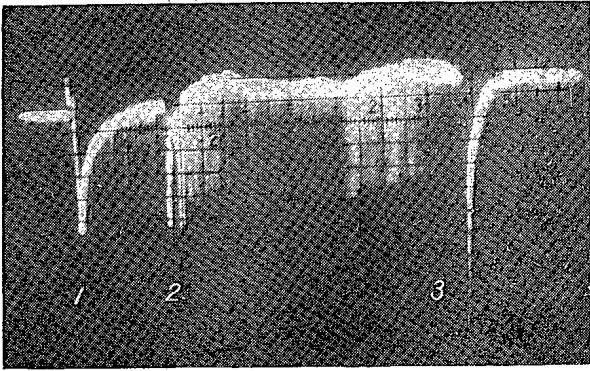
Monitor oscillogram of acceleration: 1) injection of electrons; 2) switching on of HF field; 3) pulse for diverting electrons on to target.

the accelerator chamber is also led in via the flexible waveguideconnector. To get quick, reliable pumping out, and to eliminate possible pressure build-ups in the accelerating chamber and vacuum casing, due to the complex surface of the chamber, one of the nipples of the casing has a second pump.

The generator and elements of the waveguide channel have remote control for adjusting the accelerator to maximum radiation.

At the end of December 1963, the apparatus was brought into betatron and synchrotron operation. Synchrotron operation was achieved on the second day after betatron operation was begun. The transition from betatron to synchrotron operation is reliable; tuning up is simple; and the accelerator works stably at pressures of $2 \cdot 10^{-5}$ mm Hg.

The figure gives a monitor oscillogram of acceleration. It displays the process of betatron acceleration, the moment at which the HF field is switched on, and, quite clearly, the capture and acceleration of electrons by synchrotron working. In working, the accelerator shows a characteristic curve for the current captured into the synchrotron operation versus the power of the HF generator, frequency and time of switching on the HF field.

In conclusion, we should like to thank V. I. Zhuravlev, A. M. Voloshin, P. I. Matyazh, A. A. Kush, and A. N. Pershin, students at the Tomsk Polytechnic Institute, who helped in tuning and adjusting the equipment, and also E. S. Kovalenko and A. P. Ol'shanskii, who took part in developing the theory of the accelerator, the preparation of the plans and the measurements on the models.

LITERATURE CITED

1.　A. A. Borob'ev, Izv. vyssh. uchebn. zavedenii. Élektromekhanika, 5, 106 (1958).
2.　B. N. Morozov, Radiotekhnika i élektronika, 6, 1496 (1961).
3.　E. V. Padusova, V. I. Shimanskii, and E. V. Milyutina, Izv. Tomsk. politekhnichesk. in-ta, 105, 81 (1960).
4.　E. S. Kovalenko, Izv. vyssh. uchebn. zavedenii, Fizika, 6, 85 (1959).
5.　E. S. Kovalenko, Ibid, No. 3, 175 (1960).
6.　A. N. Didenko and E. S. Kovalenko, Atomnaya énergiya, 10, 69 (1961).
7.　A. A. Vorob'ev and A. N. Didenko, Atomnaya Énergiya, 12, 242 (1962).
8.　J. Datlov et al., Czechosl. J. Phys., 12B, 894 (1962).

PASSAGE THROUGH THE CRITICAL ENERGY
IN AN AUTOMATICALLY CONTROLLED ACCELERATOR

(UDC 621.384.60)

É. A. Zhil'kov

In cyclic accelerators there is now widespread use of a system of automatic frequency tuning of the accelerating field by the beam, which can considerably improve the stability of synchrotron oscillations against various disturbances [1-3]. In this letter we examine the influence of an automatic control system on a small bunch of particles which it goes through the critical energy in an acclerator with strong focusing. The problem is problem is discussed by the method of momenta [4, 5]. The equations for the combination of momenta are derived in [5]. To describe the behavior of the bunch on approaching the critical energy, we use a linearized system of momentum equations. We can, thus, discuss the passage of the center of the bunch through the critical point and its resultant changes in dimensions.

A small phase oscillation of the center of the bunch is described by the equations [5, 6]:

$$\left. \begin{array}{l} \dfrac{d\Delta E}{dt} = -\dfrac{eV_0\omega_s \sin \varphi_s}{2\pi}\, \eta; \\[3mm] \dfrac{d\eta}{dt} = \omega_0 \left[K(t) + \dfrac{\gamma^2}{\gamma^2-1}\beta_\lambda \right] \dfrac{\Delta E}{E_s} + \omega_0 \beta_\eta \eta + \delta, \end{array} \right\} \tag{1}$$

where β_λ and β_η are the real coefficients of the feedback links via the momentum, $\lambda = \Delta p/p$, and phase $\eta = \varphi - \varphi_s$, respectively; the term δ allows for the action of external disturbances. All the remaining symbols are explained in [7]. The solution of (1) without automatic control near the critical point has been fully studied [7]. The main feature of this solution is a phase jump of $-2\,|\varphi_s|$ in the accelerating field at time $t = t_k$; otherwise, the acceleration conditions are disturbed. The automatic control system alters the nature of the phase motion. Merely by analyzing the motion of the center of the bunch, it is impossible to draw any conclusion on the phase change of the accelerating field during transition through the critical energy. With intense feedback, the vibration frequency of the center of the bunch is mainly determined by β_λ, and is independent of the sign of K(t). However, the frequencies of all higher momenta, on which the automatic control system has a weak action [5, 8], become imaginary. The bunch can be kept stable only if there is a change in the phase of the acceleration. A direct consequence of the phase change is a change in sign of β_λ after the critical point. This is in agreement with [2, 4]. At the critical point β_λ must vanish, i.e., the feedback link via momentum must be interrupted.

Let us examine the effect of β_η on the vibrations of the center of the bunch. For a wide-band system of automatic control, near the critical point (1) must take the form

$$\frac{d^2\Delta E}{d\tau^2} \mp \omega_0 \beta_\eta \frac{d\Delta E}{d\tau} - \Omega_1^2 \tau \Delta E = -\frac{eV_0 \sin \varphi_s}{2\pi}\delta, \tag{2}$$

where

$$\tau = t - t_k; \qquad \Omega_1^2 = \frac{eV_0 q\omega_s^2 \sin \varphi_s K'(t_k)}{2\pi E_s}.$$

As seen from (2), β_η does not change sign after the transition. The solution of (2) for $\delta = 0$ can be expressed in

terms of the Bessel function of order $\pm^{1}/_{3}$:[*]

$$\Delta E = \frac{3}{2} \cdot \frac{E_s \Omega_0^2}{q \omega_s K_1'} w^{1/3} \exp\left\{ -\frac{3}{2} \lambda (\omega^{2/3} + \lambda^2) \right\} \times [C_1 J_{-1/3}(w) - C_2 J_{1/3}(w)], \tag{3}$$

where

$$\Omega_0 = \left(\frac{2}{3} \Omega_1^2\right)^{1/3}; \quad w = \frac{2}{3\Omega_1^2}\left(\Omega_1^2 \tau - \frac{1}{4} \omega_0^2 \beta_\eta^2\right)^{3/2}; \quad \lambda = -\frac{\omega_0 \beta_\eta}{2\Omega_0}.$$

Constants C_1 and C_2, which are determined by the initial conditions have been chosen so that, when $\lambda \to 0$, (3) reduces to the solution without an automatic control system. For the critical point we get

$$\left(\frac{\Delta E}{E_s}\right)_{w\to 0} \longrightarrow \frac{3\Omega_0^2 e^{-3/2\lambda^3}}{2^{2/3}\Gamma(^2/_3) q\omega_s K'} C_1.$$

To study the behavior of the phase at the critical point, we shall use (1) and (3), from which we get

$$\eta = w^{1/3} \exp\left[-\frac{3}{2} \lambda (w^{2/3} + \lambda^2) \right] \times \left\{ C_1 [w^{1/3} J_{2/3}(w) + \lambda J_{-1/3}(w)] + C_2 [w^{1/3} J_{-2/3}(w) - \lambda J_{1/3}(w)] \right\}.$$

At the critical point, the phase deviation reaches the following limiting value:

$$(\eta)_{w\to 0} \longrightarrow \left[\frac{2^{2/3}}{\Gamma(^1/_3)} C_2 + \frac{2^{1/3}\lambda}{\Gamma(^2/_3)} C_1 \right] e^{-3/2\lambda^3}. \tag{6}$$

Using the asymptotic Bessel function, we get an expression for the phase at a great distance from the critical point (the adiabatic approximation):

$$\eta = \sqrt{\frac{2}{\pi}} e^{-3/2\lambda w^{2/3}} \left\{ C_1 \left[w^{1/6} \sin\left(w - \frac{\pi}{12}\right) \right. \right.$$

$$\left. + \lambda w^{-1/6} \cos\left(w - \frac{\pi}{12}\right) \right] + C_2 \left[w^{1/6} \cos\left(w + \frac{\pi}{12}\right) - \lambda w^{-1/6} \cos\left(w - \frac{5\pi}{12}\right) \right] \right\}. \tag{7}$$

As we should expect, small phase oscillations are strongly damped, both in the adiabatic region and at the critical point ($\lambda > 1$).

Let us estimate the action of a disturbance on the phase motion of the center of the bunch. The excitation of phase vibrations by a disturbance is represented by the equation

$$\frac{dC_{1,2}}{dw} = \pm \frac{\pi}{3\Omega_0} \delta(w) \exp\left\{ \frac{2}{3} \lambda w^{2/3} \right\} J_{\pm 1/3}(w). \tag{8}$$

If the disturbance is stable in the critical region (e.g., a disturbance of frequency $\delta = \Delta\omega_0$), we get for the increments in $C_{1,2}$

$$\Delta C_{1,2} = \pm \frac{\pi \Delta\omega_0}{3\Omega_0} \int_{w_0}^{w} e^{2/3\lambda w^{2/3}} J_{\pm 1/3}(w')\, dw'. \tag{9}$$

Putting $\omega_0 \to -\infty$, while $\omega \to 0$, and calculating the integral approximately for the case $\lambda > 1$, we have

$$\Delta C_1 \approx 2.5 \frac{\Delta\omega_0}{\omega_0} \cdot \frac{\Omega_0}{\omega_0 \beta_\eta^2}; \qquad \Delta C_2 \approx 3.7 \frac{\Delta\omega_0}{\omega_0 \beta_\eta}. \tag{10}$$

---

[*] We are considering the case where $\tau > 0$.

In particular, for $\beta_\eta \simeq 10^{-2} - 1$ (these values of β_η are typical for the automatic control system of the 7 BeV accelerator at the Institute of Theoretical and Experimental Physics [3]) the permissible perturbations in the accelerating field frequency are much reduced. The same applies to perturbations in the magnetic field $\Delta <B_z>_s$, for which $\Delta\omega_0/\omega_0$ in (10) must be replaced by $-\alpha \, \Delta<B_z>_s/<B_z>_s$. Thus, in an accelerator with automatic control, the over-all pattern of phase motion of the bunch's center on going through the critical point remains qualitatively the same. At the critical point, the limiting energy, phase and tolerance depend on the parameters of the automatic control system, and can be much reduced by rational choice of the latter.

Let us consider how the dimensions of the bunch behave near the critical point. As the principal characteristics of the bunch dimensions, we shall use the second moments $\Psi = \overline{\eta^2}$, $V = \overline{\Delta E^2}$, $W = \overline{\eta \Delta E}$. For small oscillations of the bunch dimensions, equations [5] are of the form

$$\dot{\Psi} = \frac{2q\omega_s K(t)}{E_s} W; \quad \dot{V} = -\frac{eV_0\omega_s \sin \varphi_s}{\pi} W; \quad \dot{W} = \frac{q\omega_s K(t)}{E_s} V - \frac{eV_0\omega_s \sin \varphi_s}{2\pi} \Psi. \tag{11}$$

Solving (11) in the neighborhood of the critical point, we get

$$
\begin{aligned}
\Psi &= v^{4/3} [A_1 J_{2/3}^2 (v) + A_2 J_{2/3} (v) J_{-2/3} (v) \\
&\quad + A_3 J_{-2/3}^2 (v)]; \\
W &= \frac{E_s g^2}{2q\omega_s K'} v [2A_1 J_{2/3} J_{-1/3} \\
&\quad + A_2 (J_{-1/3} J_{-2/3} - J_{1/3} J_{2/3}) - 2A_3 J_{1/3} J_{-2/3}]; \\
V &= \frac{eV_0 \sin \varphi_s E_s g}{2\pi q K'} v^{2/3} [A_3 J_{1/3}^2 (v) \\
&\quad - A_2 J_{1/3} (v) J_{-1/3} (v) + A_1 J_{-1/3}^2 (v)];
\end{aligned}
\tag{12}
$$

where

$$\Omega^2 = \frac{eV_0 q\omega_s^2 \sin \varphi_s K'(tk)}{2\pi E_s}; \quad v = \frac{2}{3} \Omega\tau^{3/2}; \quad g = \frac{2}{3} \Omega^{2/3}.$$

The constants A_i are about one-tenth of the C_i. As seen from (12), in the adiabatic region ($v \gg 1$), the bunch dimensions oscillate at twice the oscillation frequency of the bunch center; during acceleration, the phase dimensions of the bunch, ψ, are adiabatically reduced, while the energy scatter V adiabatically increases. Expanding the Bessel function in a series, we find the following values for the dimensions of the bunch at the critical point:

$$(\Psi)_{c\to 0} \to \frac{2^{4/3}}{\Gamma^2 (1/3)} A_3; \quad \left(\frac{V}{E_s^2}\right)_{v\to 0} \to \frac{2^{2/3}eV_0 \sin \varphi_s g A_1}{\Gamma^2 (2/3) 2\pi q E_s K'}; \quad \left(\frac{W}{E_s}\right)_{v\to 0} \to \frac{g^2 A_2}{\Gamma (1/3) \Gamma (2/3) q\omega_s K'}. \tag{13}$$

Let us calculate the increase in the orbit corresponding to increase in the bunch's energy scatter at the critical point:

$$\frac{\overline{\Delta R^2}}{R^2} = \alpha^2 \left(\frac{eV_0 \sin \varphi_s \omega_s}{2\pi E_s q}\right)^2 \frac{2^{2/3}}{\Gamma^2 (2/3)} A_1. \tag{14}$$

Let us put $\alpha \approx 10^{-2}$, $eV_0 = 10^4$eV, $E_s = 5 \cdot 10^9$ eV, $\omega_s = 10^6$ cps, $g \approx 3 \cdot 10^2$, $R \approx 3 \cdot 10^4$ cm: then $\overline{\Delta R^2} \approx 0.1A_1$. Hence, we may conclude that the increase in bunch size in the critical region is not hazardous, because even at the critical point the dimensions do not exceed the square of the amplitude of free vibrations of the bunch's center outside the critical region in the absence of automatic control.

In the linear approximation, the automatic control system has no effect on the bunch size. In [8], taking account of non-linearity outside the critical region, an expression was obtained for the vibration frequency of the bunch dimensions, for uniform distribution with respect to energy:

$$\omega = 2 - \frac{\varepsilon}{2} \left(1 + \frac{5}{3} \operatorname{ctg}^2 \varphi_s\right) - i \operatorname{ctg} \varphi_s \varepsilon \times \frac{\left[\frac{\operatorname{ctg} \varphi_s}{6}\left(\omega_0\beta_\eta \pm \frac{2i\gamma^2}{\gamma^2-1} \cdot \frac{\beta\lambda}{K(t)}\right) \pm \beta_\Psi \mp \beta_V - i\beta_W\right]}{3 + 2i\omega_0\beta_\eta \mp \frac{\gamma}{\gamma^2-1} \cdot \frac{\beta\lambda}{K(t)}}.$$

In this formula, the frequency is expressed in terms of that of linear synchrotron vibrations, and account is taken of the changes in sign of the momentum and dimension feedback coefficients after the critical point is passed. From (15) it follows that, for $|\beta| > 1$, it is possible to achieve stability of the bunch purely on account of the automatic control system with respect to the center $|\beta_\lambda, \beta_\eta|$ both before and after the transition. The stability of the bunch can be increased by introducing feedback via the dimensions. For other distributions, when there is natural damping, it is necessary to analyze the parameter ξ [5, 6] before and after the critical energy is reached, as done, for example, in [6]. Owing to the non-linearity of the equations, the bunch's center does not coincide with the equilibrium phase, but is displaced relative to it by an amount equal to the equilibrium dimensions of the bunch [5]. The center of the bunch must be displaced. The results obtained are valid for bunches of small dimensions in the linear approximation. To solve the non-linear problem, special discussion is required.

LITERATURE CITED

1. K. Johnsen and C. Schmelzer, Proc. of Int. Conf. on High Energy Accel. CERN (1956), p. 395.
2. W. Schnell, Proc. of Int. Conf. on High Energy Accel. CERN (1959), p. 485.
3. Yu. S. Ivanov and A. A. Kuz'min, Pribory i tekhnika éksperimenta, 4, 106 (1962).
4. H. Hereward, Proc. of Int. Conf. on High Energy Accel. Brookhaven (1961), p. 236.
5. É. A. Zhil'kov and A. N. Lebedev, Atomnaya Énergiya, 18, 22 (1965).
6. É. A. Zhil'kov, Pribory i tekhnika éksperimenta, 1, 17 (1965).
7. A. A. Kolomenskii and A. N. Lebedev, Theory of Cyclic Accelerators [in Russian], Ch. IV, Moscow, Fizmatgiz (1962).
8. É. A. Zhil'kov, Atomnaya Énergiya, 18, 58 (1965).

PARTICLE LOSSES DUE TO PASSAGE THROUGH NONLINEAR
RESONANCES IN ACCELERATORS AND STORAGE DEVICES

(UDC 621.384.61)

A. A. Kolomenskii

Reports have recently appeared concerning projects for large proton storage systems, designed to effect collisions between intersecting beams [1, 2]. Our aim in this paper is to analyze one of the possible mechanisms of particle losses which must be allowed for in developing and applying systems of this type.

A characteristic property of cyclic accelerators and storage rings is the existence of dangerous resonance combinations of the parameters, determined by the relations

$$q_r\nu_r + q_z\nu_z = m \quad (q_{r,\,z},\, m \quad \text{are integers}), \tag{1}$$

where ν_r, ν_z = frequencies of radial and vertical betatron vibrations (expressed in terms of the frequency of revolution ω). The resonance order k is determined by $k = |q_r| + |q_z|$. The permissible limits follow from the requirements that the working point ν_r, ν_z on the stability diagram shall not come close to the edges of the cell determined by the linear resonance bands ($k \le 2$). This cell is crossed by bands of non-linear resonance ($k > 2$), caused by disturbances in the magnetic field. The effects of these resonances are usually not very dangerous, because when the working point is stationary they are compensated for by non-linear displacement of the vibration frequency. However, if the working point, though remaining within the cell, wanders and passes through non-linear resonance bands owing to instabilities of the magnetic field, the amplitude of betatron vibrations may rise to dangerous values, leading to loss of particles. There is especial danger that such losses may arise from repeated passage through non-linear resonances when these occur in storage rings, in which the particles have to circulate for very long times of an hour or more, several orders greater than those usually found in accelerators.

We shall confine ourselves to systems with strong focusing, having proton storage rings in mind. For electrons, an important part is played by relativistic electromagnetic radiation, which (with suitable choice of focusing system) damps the vibrations and limits the effects of various disturbing factors. For protons, this radiation is practically nonexistent, and there is no damping of the vibrations, so that in storage rings the particle energy and magnetic field remain practically constant.

If a nonlinear resonance is crossed slowly enough, there may be "coupling hysteresis" of the fraction of particles in the resonance, accompanied by marked increase in the amplitude, even for a single non-repeated passage [3]. However, it is estimated that in practice passage is comparatively rapid. There is, thus, no coupling hysteresis, and increases in amplitude will arise in those short periods during which there is synchronism between particle vibrations and harmonic disturbances of the magnetic field.

The increases in amplitude due to rapid passage through non-linear resonances can be calculated from known formulae (see [3], ch. III, §8).

It is characterized by the coefficient $J = \dfrac{a^2}{a_i^2}$, where a_i, a are the amplitudes of vibration before and after transmission, respectively. Using the method of stationary phases, we obtain for J the expression

$$J = \left[1 - \left(\frac{k}{2} - 1\right) G \sqrt{\frac{2\pi}{|\delta'|}} \sin\left(kw_0 \pm \frac{\pi}{4}\right) \right]^{\frac{2}{2-k}}. \tag{2}$$

Here k = order of resonance (k > 2); ω_0 = phase at moment of transmission;

$$G = 2k \, | \, \langle u_{q, k, k} \rangle | \left(\frac{2pa_i^2}{2R} \right)^{\frac{k}{2} - 1}, \qquad (3)$$

where $\langle u_{q, k, k} \rangle$ = averaged coefficients expressed in terms of floquet function f and proportional to the q-th (resonance) harmonic of the disturbance (see Table 3 in [3]); p = momentum of particle; and R = radius of orbit.

The expression $\delta' = \dfrac{d\delta}{d\vartheta}$ occurring in (2) determines the rate of change of detuning, $\delta = \nu - \nu_{res}$, in terms of the azimuthal angle, ϑ. This can be expressed as follows:

$$\delta \approx \nu \frac{\Omega}{\omega} \cdot \frac{\Delta B}{B}, \qquad (4)$$

where ΔB, Ω = amplitude and frequency of disturbing oscillations in the magnetic field, the value of which at the orbit is denoted by B. Using (4) we can easily estimate the rate of passage through a resonance and assure ourselves that, in most practical cases, we can ignore "coupling hysteresis" in the resonance and consider the passage to be rapid, satisfying (8.5) of [3] (ch. III, §8).

To simplify the calculation, we shall restrict ourselves to a cubic resonance, k = 3, ν = q/3. By (2), (3) and the above-mentioned table in [3], we have

$$J = \left[1 - \sqrt{\frac{3}{|\delta'|}} \, \frac{a_i R}{12B} \left| f^3 \frac{\partial^2 b_q}{\partial r^2} \right| \sin \left(3w_0 \pm \frac{\pi}{4} \right) \right]^{-2}, \qquad (5)$$

where b_q is the q-th harmonic of azimuthal asymmetry of the field. For the non-linearity characteristic of an ideal field we can introduce the value

$$n_{k-1} = (-1)^k \frac{R^k}{B} \cdot \frac{\partial^k B}{\partial_r^k}, \qquad (6)$$

which is a generalization of the ordinary field index $n = n_0$. In strong-focusing machines, n_k usually obeys

$$1 \ll |n_0| \ll |n_1| \ll |n_2|. \qquad (7)$$

We can assume that n_1 is approximately constant along the orbit, while n_2 is equal in magnitude and opposite in sign in consecutive sectors. Let us also assume that the field asymmetry b depends on the radius in the same way as an ideal field B, and use the approximate expression $f \approx \nu^{-1/2}$ for the floquet function.

Since, for consecutive passages through a resonance, various values of the phase ω_0 will be encountered in practically random fashion, we can use (5) to find the mean square increment of the amplitude after s passages. By (4)—(7) and our assumptions, this increment will be determined by

$$\left(\frac{1}{a_i} - \frac{1}{a_s} \right)^2 = \frac{s}{96R^2} \cdot \frac{\omega}{\Omega} \cdot \frac{B}{\Delta B} \left(n_1 \frac{b_q}{B} \nu \right)^2. \qquad (8)$$

We can, thus, find s_∞, the number of passages after which the amplitude increases appreciably in comparison to the initial value ($a_s \to \infty$), and also determine the corresponding time,

$$\tau_\infty = \frac{2\pi s_\infty}{\Omega a_i^2} \approx 10^2 T_{rev} \frac{\Delta B}{B} \left(\frac{R}{a_i} \cdot \frac{B}{b_q} \cdot \frac{1}{n_1} \nu \right)^2, \qquad (9)$$

where T_{rev} is the period of revolution of a particle in its orbit.

For our estimate we can take the following values: $\nu \approx 10$; $R \approx 10^4$ cm $\frac{\Delta B}{B} \approx \frac{B_q}{B} \approx 10^{-3} - 10^{-4}$; $n_1 \approx 10^3$; $T_{rev} \approx 10^{-6}$ sec. Substituting these values in (9) we get the required value, $\tau_\infty \approx 10/a_i^2$ sec, where a_i is taken in centimeters. It shows that, even with very modest storage times, those particles which traverse resonances will certainly be lost. These particles correspond to the interval $\Delta\nu \approx \nu \, \Delta p/p$. Therefore, if the total momentum

scatter accumulated in the magnetic track of the storage ring is Δp_0, the proportion of the particles which will be lost by passage through a resonance will be $\Delta p/\Delta p_0$. We must also remember that, besides the above one-dimensional cubic resonance, there are total cubic resonances whose intersection may also lead to losses, and also resonances of higher orders. The latter, however, have much longer times of growth to dangerous amplitudes.

To reduce losses due to passage through resonances, we must try to minimize interference oscillations $\Delta B \cos \Omega t$ in the magnetic field, and also weaken as far as possible the dependence of ν on the momentum p.

LITERATURE CITED

1. K. Johnsen et al., In: Proceedings of International Conference on Accelerators (Dubna, 1963). [Russian translation], Moscow, Atomizdat (1964), p. 312.
2. E. Courant, Ibid, p. 361.
3. A. A. Kolomenskii and A. N. Lebedev, Theory of Cyclic Accelerators [in Russian], Moscow, Fizmatgiz (1962).

805

EFFECTIVE METHOD OF SOLVING THE TWO-DIMENSIONAL DIFFUSION EQUATION FOR SQUARE AND HEXAGONAL CELLS

(UDC 621.039.51.12)

G. I. Marchuk and V. P. Kochergin

The two-dimensional one-group diffusion equation with a constant moderation source can be written in polar coordinates as follows.

$$\frac{1}{r}\cdot\frac{\partial}{\partial r} rD\frac{\partial\Phi}{\partial r} + \frac{1}{r^2}\cdot\frac{\partial}{\partial\theta} D\cdot\frac{\partial\Phi}{\partial\theta} - \Sigma_c\Phi(r,\theta) = -\xi\Sigma_s. \tag{1}$$

Much work is entailed in solving (1) by the method of finite differences with the appropriate boundary conditions—i.e., that the normal derivative of the neutron flux shall vanish at the cell boundaries, and that the neutron flux and current shall be continuous—especially when there is a large number of nodes. If we confine ourselves to the practical case when the inner zone of the cell has circular symmetry, (1) can be solved with much less labor. The essence of the method is that the two-dimensional equation (1) is reduced to a number of one-dimensional diffusion equations, which are then solved by finite-difference factorization [1].

Remembering that the neutron flux $\Phi(r,\theta)$ will be periodic in θ with period $2l$ (where $l = \pi/4$ for a square cell, $l = \pi/6$ for a hexagonal cell) and will possess several axes of symmetry, we can write $\Phi(r,\theta)$ as the following Fourier series:*

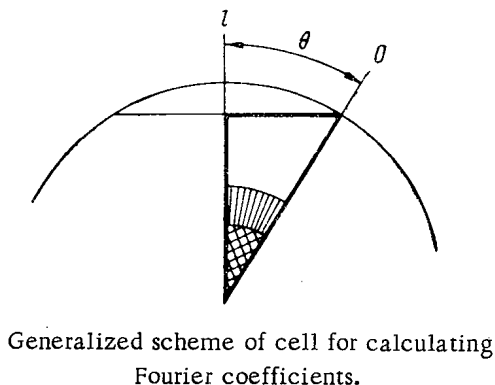$$\Phi(r,\theta) = \sum_{\nu=0}^{\infty} R_\nu(r)\cos\frac{\pi}{l}\nu\theta. \tag{2}$$

Let us extend the final cell zone to the size of the circumscribed circle. Then, substituting (2) in (1), multiplying it by $\cos\pi/l\mu\,\theta$ and integrating w.r.t. θ over the range 0 to $2l$, we get a series of one-dimensional diffusion equations for the coefficients of the expansion R (r):

$$\frac{1}{r}\cdot\frac{d}{dr} rD\cdot\frac{dR_\nu}{dr} - \left[\sum_c + \frac{D}{r^2}\left(\frac{\pi}{l}\nu\right)^2\right]R_\nu(r) = -\xi\sum_s\delta_{\nu 0}, \tag{3}$$

where $\delta_{\nu 0}$ is the Kronecker delta.

$R_\nu(r)$, the Fourier coefficients at the boundaries of the inner zone and at the center of the cell, obey the following boundary conditions, which are easily derived from the requirements imposed on the neutron flux function $\Phi(r,\theta)$:

$$\begin{cases} R_\nu(r), \quad D\frac{dR_\nu}{dr} \ -\text{ is continuous in r} \\ \frac{dR_\nu}{dr}\Big|_{r=0} = 0 \qquad (\nu = 0, 1, \ldots). \end{cases} \tag{4}$$

Generalized scheme of cell for calculating Fourier coefficients.

---

* Because of the conditions imposed on $\Phi(r,\theta)$ (see above), (2) is uniformly convergent.

806

Neutron Absorption Σ_c, Averaged Over Cell Cross Section in Various Approximations

First zone			Second zone			Shape of cell	a	Σ_c		
								cell of practical shape	equiv. cell	
D	Σ_c	$\frac{1}{3}\Sigma_s$	D	Σ_c	$\frac{1}{3}\Sigma_s$			P_1 approximation	P_1 approximation	P_3 approximation
0,22	0,05	1,0	0,2	1,5	1,0	Square	5	0,181	0,216	0,190
0,22	0,05	1,0	0,2	1,5	1,0	Hexagonal	5	0,133	0,145	0,132

Using a "continuous calculation" scheme and the method of difference factorization, we get from (3) and (4) the following system of finite-difference relations [2]:

$$\beta_{i+1}^\nu = \frac{C_{i+1}}{B_i^\nu - \beta_i^\nu}, \quad \beta_1^\nu = C_1;$$

$$Z_{i+1}^\nu = \beta_{i+1}^\nu \left(Z_i^\nu + \frac{(\xi \Sigma_s \Delta r)_i}{a_i} \delta_{\nu 0} \right), \quad Z_1^\nu = 0;$$

$$R_{\nu, i} = \frac{\beta_{i+1}^\nu R_{\nu, i+1} + Z_{i+1}^\nu}{C_{i+1}}, \quad R_{\nu, n} = \xi_\nu;$$

$$a_i = \left(1 + \frac{\Delta r_{i+1/2}}{2r_i} \right) \frac{D_{i+1/2}}{\Delta r_{i+1/2}}; \qquad (5)$$

$$C_i = \frac{1 - \frac{\Delta r_{i-1/2}}{2r_i}}{1 + \frac{\Delta r_{i+1/2}}{2r_i}} \cdot \frac{D_{i-1/2} \Delta r_{i+1/2}}{D_{i+1/2} \Delta r_{i-1/2}};$$

$$B_i^\nu = 1 + C_i + \frac{(\Sigma_c \Delta r)_i}{a_i} + \frac{1}{r_i^2} \left(\frac{\pi}{l} \nu \right)^2 \frac{(D\Delta r)_i}{a_i}.$$

Here $\Delta r_{i+1/2} = r_{i+1} - r_i$, and the brackets indicate that we take the arithmetic mean of the corresponding values to the right and left of the point i, when it coincides with the zone boundaries; the ξ_ν are the Fourier coefficients, which will be determined below, at the radius of the circumscribed circle.

After some simple transformations, the third expression of system (5) can be written as follows:

$$R_{\nu, i} = \gamma_i^\nu \xi_\nu + \varkappa_i^\nu, \qquad (6)$$

where

$$\gamma_i^\nu = \begin{cases} \prod_{l=i+1}^{n} a_l^\nu & (i = n-1, \ldots 1), \quad \varkappa_{i-1}^\nu = a_i^\nu \varkappa_i^\nu + g_i^\nu, \quad \varkappa_n^\nu = 0, \quad i = n, \ldots 1 \left(\text{here} \quad a_i^\nu = \frac{\beta_i^\nu}{C_i}, \quad g_i^\nu = \frac{Z_i^\nu}{C_i} \right). \\ 1 & (i = n); \end{cases}$$

Thus (6) gives the Fourier coefficients at the radial division points in terms of the Fourier coefficients at the radius of the circumscribed circle, together with certain quantities γ_i^ν and $\varkappa_i^\nu$, which are independent of the boundary conditions at the boundaries of the cell. (Note that, by (5), all the $\varkappa_i^\nu = 0$ when $\nu \neq 0$.)

If we introduce functions $\gamma_{(r)}^\nu$ and $\varkappa_{(r)}^0$, which coincide with γ_i^ν and $\varkappa_i^0$ respectively at the division points, while at other radii they are interpolated by polynomials of the appropriate orders, then (6), the expression for the Fourier coefficients, can be written as

$$R_\nu (r) = \gamma^\nu (r) \xi_\nu + \varkappa^0 (r) \delta_{\nu 0}. \qquad (7)$$

To determine the Fourier coefficients at the radius of the circumscribed circle, we shall use the conditions at the cell boundary (i.e., that the normal derivative vanishes); in view of the periodicity and symmetry of the solution, it is sufficient to take the boundary only from $\theta = 0$ to $\theta = l$ (see figure). Then

$$\cos (l - \theta) \frac{\partial \Phi}{\partial r} + \frac{\sin (l - \theta)}{r} \frac{\partial \Phi}{\partial \theta} = 0, \qquad (8)$$

where $r = \dfrac{a}{2 \cos (l - \theta)}$; a being the lattice step.

If we substitute (2) in (8), multiply by $\cos \frac{\pi}{l} \mu \theta$ and integrate w.r.t. θ from 0 to l, then by (7) we get a system of algebraic equations for the ξ_ν:

$$\sum_{\nu} A_{\mu\nu}\xi_{\nu} = F_{\mu},$$

where

$$A_{\mu\nu} = \int_0^l \frac{d\gamma^{\nu}(r)}{dr} \cos(l-\theta) \cos\frac{\pi}{l}\nu\theta \cos\frac{\pi}{l}\mu\theta - \frac{\pi}{l}\nu \int_0^l \frac{\gamma^{\nu}(r)}{r} \sin(l-\theta) \sin\frac{\pi}{l}\nu\theta \cos\frac{\pi}{l}\mu\theta \, d\theta;$$

$$F_{\mu} = -\int_0^l \frac{d\varkappa^0(r)}{dr} \cos(l-\theta) \cos\frac{\pi}{l}\mu\theta \, d\theta. \tag{9}$$

Note that, for μ and ν greater than zero, the integrands are of alternating sign. To obtain satisfactory accuracy by numerical integration, the range of integration must, therefore, be divided into intervals in which the integrands are of constant sign. This is done by finding the values of θ for which the integrands are zero:

$$\theta_n^{\nu} = \frac{ln}{\nu}, \quad n = 0, 1 \ldots, \nu-1 \text{ for } \sin\frac{\pi}{l}\nu\theta; \quad \theta_n^{\nu} = l\frac{2n+1}{2\nu}, \quad n = 0, 1 \ldots \nu-1 \text{ for } \cos\frac{\pi}{l}\nu\theta. \tag{10}$$

Similar relations hold for $\cos\frac{\pi}{l}\mu\theta$.

Taking a finite number of terms in the Fourier expansion [usually two or three terms, according to the existence of the second derivative w.r.t. θ of the flux $\Phi(r, \theta)$], we get from the matrix $\|A_{\mu\nu}\|$ an expression for ξ_{ν}:

$$|\xi_{\nu}| = \|A_{\mu\nu}\|^{-1} \cdot |F_{\mu}|. \tag{11}$$

By integrating the expression obtained for the neutron flux over the appropriate regions of the zones, we get the integral flux, which we need in order to determine the averages over the cell cross section:

$$\Phi_k = \begin{cases} l\int_{r_{h-1}}^{r_h} rR_0(r)\,dr & (k = 1, 2 \ldots, N-1); \\[2ex] l\int_{r_{h-1}}^{a/2} rR_0(r)\,dr + \int_{a/2}^{a/2\cos l} dr\, r \sum_{\nu} R_{\nu}(r) \\[2ex] \times \begin{cases} l - \arccos\left(\frac{a}{2r}\right), & \nu = 0; \\[1ex] \frac{l}{\pi\nu}\sin\frac{\pi}{l}\nu\left[l - \arccos\left(\frac{a}{2r}\right)\right], \\ \nu \neq 0. \end{cases} & (k = N) \end{cases} \tag{12}$$

Here, N is the number of the last zone.

The calculated results for cells of practical shape agree with the conclusions of [3, 4] that, for many such problems, the practical cell can be replaced by the Wigner-Seitz equivalent cell. However, there are problems for which the Wigner-Seitz cell leads to appreciable errors, e.g., shielding layers of reactor composed of blocks which efficiently moderate the neutrons, the gaps between the blocks being filled with absorbent material. This is illustrated in the table, which gives the mean neutron-absorption cross section over the cell in various approximations when the blocks are closely packed together (in which case the shape effect is maximal). In order to compare the effect of cell shape with the kinetic effect, the table gives corresponding values of Σ_c for the equivalent cell in the P_3 approximation. It is seen that, in this case, the cell geometry and the kinetic effects both lead to a decrease in the mean neutron-absorption cross section. For hexagonal cells these effects are equal, while for square cells the shape effect is even greater than the kinetic effect.

808

LITERATURE

1. G. I. Marchuk, Mathematical Analysis of Nuclear Reactors [in Russian], Moscow, Gosatomizdat (1961).
2. A. N. Tikhonov and A. A. Samarskii, Dokl. AN SSSR, 108, 393 (1956).
3. A. D. Galanin, Theory of Nuclear Reactors using Thermal Neutrons [in Russian], Moscow, Atomizdat (1957).
4. Ya. V. Shevelev, Atomnaya Énergiya, 2, 217 (1957).

All abbreviations of periodicals in the above bibliography are letter-by-letter transliterations of the abbreviations as given in the original Russian journal. *Some or all of this periodical literature may well be available in English translation.* A complete list of the cover-to-cover English translations appears at the back of this issue.

CRITICAL THERMAL LOAD IN BUNCHES WITH SPACER GRIDS

(UDC 621.039.517)

A. S. Kon'kov and Yu. D. Barulin

A number of authors [1-5] have studied critical thermal load, heat exchange and hydraulic resistance in a bunch of rods along which flows a heat-exchange medium. Especial attention has been paid to the critical thermal loading, as in boiling-water reactors the most widely used fuel elements are rods.

In such reactors the mechanisms of heat-exchange and hydrodynamic crises are very complex. The various methods used to determine the critical thermal loads, with various conditions of the model (contour scheme, method of heating experimental sections, measurement system, etc.) and various methods of assessing the occurrence of a crisis, often yield varying qualitative and quantitative relations which are difficult to analyze and generalize. It is,
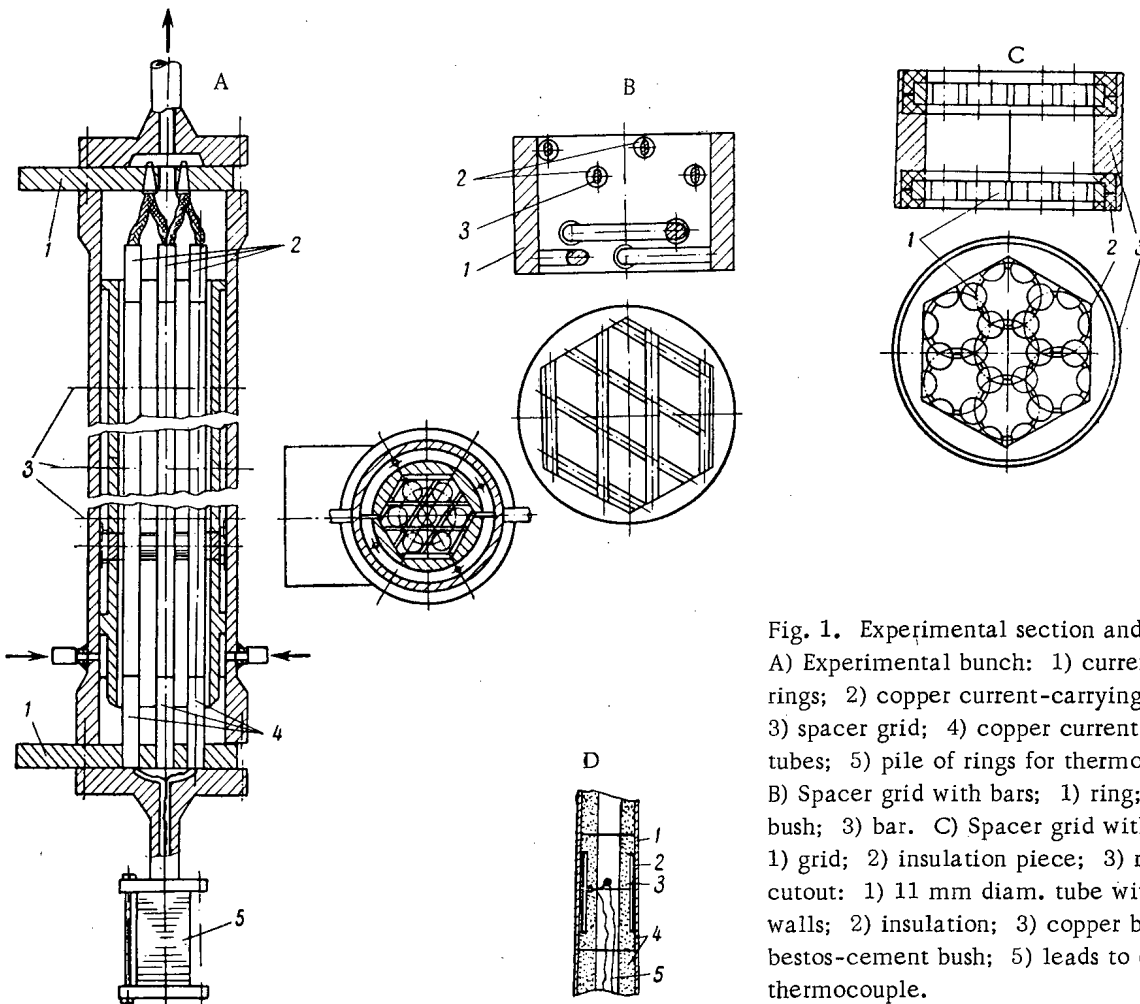

Fig. 1. Experimental section and its units.
A) Experimental bunch: 1) current-carrying rings; 2) copper current-carrying rods; 3) spacer grid; 4) copper current-carrying tubes; 5) pile of rings for thermocouple leads. B) Spacer grid with bars; 1) ring; 2) insulating bush; 3) bar. C) Spacer grid with honeycomb: 1) grid; 2) insulation piece; 3) ring. D) Safety cutout: 1) 11 mm diam. tube with 0.3 mm walls; 2) insulation; 3) copper bush; 4) asbestos-cement bush; 5) leads to differential thermocouple.
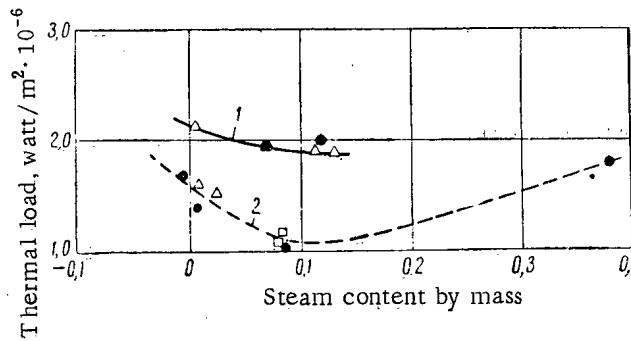
810

Fig. 2. Thermal load versus steam content by mass (1) with closed-circuit working, (2) with direct-flow working. Δ) Spacer grid with honeycomb; •) spacer grid with bars; □) 1963 experiments (spacer grid with bars and direct-flow operation).

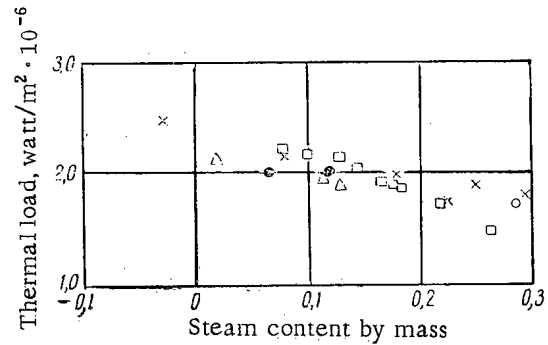Fig. 3. Experimental results of various authors on thermal load versus steam content by mass. ×) Waters; □) Polomik; O) Matzner; Δ•) results of present authors for closed-circuit system with spacer grids with honeycombs and bars.

thus, very difficult to set up the necessary model by means of which the physical and mathematical behavior of the phenomenon can be strictly determined.

The studies in [1-5] were carried out without spacer grids. However, in practice spacer grids are of course used to fix the distance between the elements of the bunch, are located in the stream of heat exchange medium, and can affect the hydrodynamics and heat exchange of the bunch.

The aim of this paper is to determine the critical thermal loads and to study how they are affected by spacer grids. The experiments were made with a bunch of seven fuel rods immersed in a current of steam and water at 98.1 bars pressure flowing at 600 kg/m$^2 \cdot$ sec and containing up to 13% by mass of steam. The experimental apparatus could be set up either for direct flow or for a closed flow circuit. We prepared a special experimental bunch simulating a bunch of fuel rods (Fig. 1A). This was 1000 mm long (over-all length 1400 mm)and was made of thin-walled tubes of steel 1Kh18N9T of diameter 11 mm and wall thickness 0.3 mm, placed in a six-sided displacer of 25.8 mm sides. The tubes were heated by a direct current. At three points along the heat-evolving rods were spacer grids with bars (see Fig. 1B) or spacer grids with honeycombs (see Fig. 1C). To protect the fuel rods from overheating, the ends of every set of seven tubes, in the heated sections of the bunch, were provided with an automatic circuit breaker transducer (see Fig. 1D). Emergency cutoff was effected by differential thermocouples, the signals from which were fed via an electronic temperature regulator to a contactor in series with the current generator excitation. The transducers were operated by changes in temperature of more than 40°C.

To record the nature of the flow and pressure changes in the coolant at the moment of crisis, the pressure selection lines were provided with low-inertia strain gauges, the signals from which were fed via an amplifier to a recording oscillograph. A heat-transfer crisis was induced by gradually increasing the thermal load (at constant temperature) and coolant flow through the experimental bunch.

Figure 2 gives experimental results obtained with both types of spacer grid and with either direct-flow or closed-circuit operation. It is seen that in the experiments with closed-circuit working the critical thermal load is higher than with direct-flow working. This is apparently due to the lower stability of the direct-flow system. In studies [6] of critical thermal loading in heated tubes, the authors discuss the effect of the flow system on the critical load. It was observed that one cause of ambiguity in the experimental results is the variations between individual methods of investigation, in particular of the thermal systems.

From [6, 7] and the results of studies of critical thermal loading of bunches, it can be inferred that the conditions obtained with direct-flow systems are more conductive to crisis phenomena than those with closed-circuit flow. The critical thermal loadings have lower absolute values with direct-flow systems.

Oscillograms recorded at 50 mm/sec show that the fluctuations in coolant flow and pressure correspond only to the moment of heat-transfer crisis. The increases in flow and pressure at the entry and output of the experimental apparatus occur about 2 sec later. For spacer grids with bars, these changes are about 10% of the values corresponding to stationary conditions. In experiments with spacer grids with honeycombs, the changes in the nature of the coolant flow and pressure fluctuations are less marked. Spacer grids with honeycombs give more stable hydrodynamic

conditions at the moment of formation of crisis phenomena than do spacer grids with bars. It was observed visually that, either with direct-flow or closed-circuit working, in experiments with bar-type spacers the crisis phenomenon (overheating of the tube bunch) occurred either at the end of the heated section of the rods or in front of it. In experiments with honeycomb-type grids it was observed only at the end of the heated part.

Figure 2 also shows that there is satisfactory agreement between results from the same apparatus on different occasions.

Figure 3 gives experimental results from bunches with spacer grids and closed-circuit working, and also experimental data obtained by other authors.

Waters [5] used a bunch of 19 rods of diameter 14.3 mm, arranged in a triangular lattice with 1.88 mm between rods and heated section 470 mm. The coils had spiral wire windings, which intensified the heat-transfer process. The mass speed of the coolant was over 600 kg/m^2 · sec, the pressure 83 bar. Polomik used nine rods arranged in a square lattice, with 4.6 mm between rods; the pressure was 96.7 bar. Matzner's experiments were made at pressure 68.7 bar with a 19-rod bunch with 2.1 mm between rods. These rods also had a wire winding.

Figure 3 shows that our results, obtained with a bunch of rods with spacer grids and with closed-circuit working, agree with the data of other investigators.

By comparing the critical thermal loads for bunches of rods immersed in a coolant current with those for steam-water mixtures flowing in tubes, we see that the former are lower than the latter.

<div align="center">LITERATURE CITED</div>

1. B. A. Zenkevich, V. I. Subbotin, and M. F. Troyanov, Atomnaya Énergiya, 4, 370 (1958).
2. V. I. Subbotin, P. A. Ushakov, and A. V. Zhukov, Inzh.-fiz. zh., 4, 3 (1961).
3. É. V. Firsova, Ibid., 6, 17 (1963).
4. S. Green and G. Mauer, Paper Amer. Soc. Mech. Engnr, No. HT—43 (1962).
5. E. Waters and D. Fitzsimmons, Nucleonics, 21, 10 (1963).
6. V. E. Doroshchuk and F. P. Frid, Teploenergetika, 9, 74 (1959).
7. V. I. Smolin, V. K. Peskov, and V. I. Esikov, Atomnaya Énergiya, 16, 417 (1964).

THERMOELECTRIC PROPERTIES OF POLYCRYSTALLINE URANIUM

(UDC 546.791:621.039.543.4)

A. A. Tsvetaev, Yu. N. Golovanov, R. K. Chuzhko,

and I. V. Kirillov

In [1, 2] the thermo-emf of uranium was measured relative to copper and platinum. These authors disagree significantly owing to impurity effects. The absolute differential thermo-emf of uranium has been measured [3] only at low temperatures (up to 300°K).

In [4, 5] it was noticed that phase changes in uranium cause no sharp changes in its thermo-emf. According to present ideas [6, 7], the absolute differential thermo-emf (ε) and the Thomson emf (σ) of a metal are governed by the entropy and thermal capacity of the mobile current carriers and are usually very sensitive to first-order and second-order phase transitions [8].

It seemed desirable to investigate the temperature dependences of ε and σ for uraniums of different purities, prepared by the usual method [8].

For these measurements we required the differential emf e of a Pt-PtRh thermocouple (40 % Rh); this was determined by precise calibration:

in the range 0-320°C

$$e_{Pt-PtRh} = 5.142 + 0.02616\, t$$
$$- 0.0000239\, t^2\ \mu V/°C$$

in the range 320-1080°C

$$e_{Pt-PtRh} = 8.362$$
$$+ 0.00900 t\ \mu V/°C$$

The curve of ε_{Pt} versus T was taken from the data of [8]. The specimens used consisted of uranium wire of different purities (99.83 and 99.98%); their diameter was 1.5 mm and length ~50 mm. The specimens, with two identical Pt-PtRh thermocouples welded one to each end, were heated in argon at about 5°C/min, with temperature drop (along the length) of about 5°C.

The differential emf of uranium paired with platinum and platinum-rhodium was measured at 20°C intervals. Figure 1 and Fig. 2 give the values of ε_U versus T for various specimens. At first these curves agree with the curves $\varepsilon_U = f(T)$ from [3]. However, our curves have discontinuities at the allotropic transition points. ε_U depends on the impurity content, but a greater effect is exerted by the textures of the specimens and (apparently) the distribution of the impurities. Thus, quenched uranium, which has maximum quasi-isotropy of its properties and fine-grained structure, has minimum ε_U. The highest values of ε_U were observed in uranium deforemd by wire-drawing or annealed after deformation. Since wire-drawing gives rise to a (010) texture along the wire axis, while annealing reinforces this texture [9], this effect can be related to anisotropy of the thermoelectric properties of the uranium crystals (by analogy with single crystals of other metals [10]).

The differences in shape of the (ε_U, T) curves during heating-cooling cycles near the phase transition points indicate that we cannot ignore the rates of phase transitions and the heredity of the texture, which influence ε_U. A similar hysteresis is observed for the thermal expansion coefficient during heating-cooling cycles near the phase transition points. The temperature dependence of ε_U must on the whole depend on variations in the properties of

813
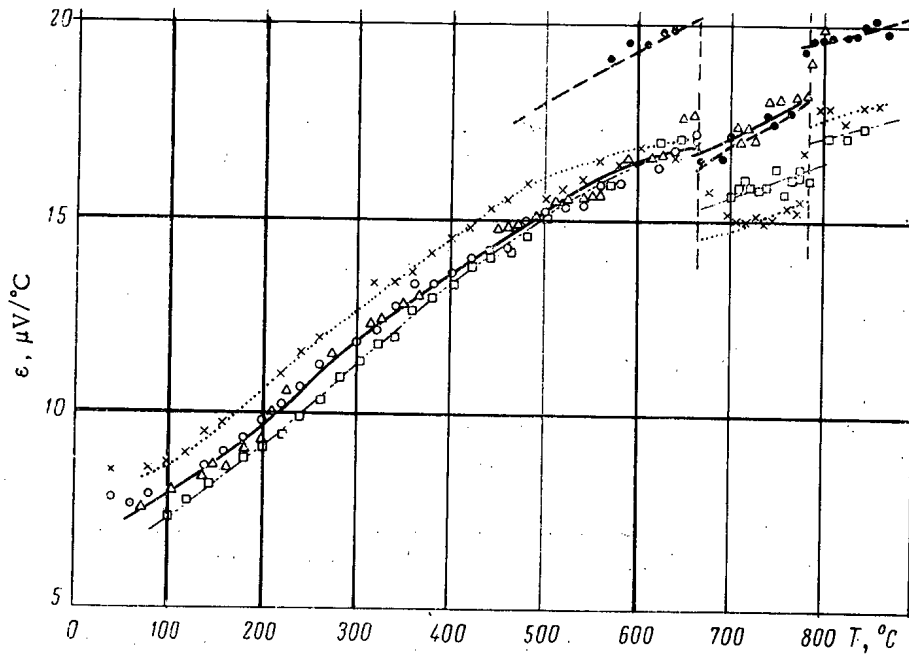
Fig. 1. Temperature dependence of ε for uranium (99.83%). Δ) Heating of quenched uranium; ●) cooling the same specimen; □) quenched uranium; O) first heating of quenched uranium (to 650°C); ×) repeated heating of same specimen.
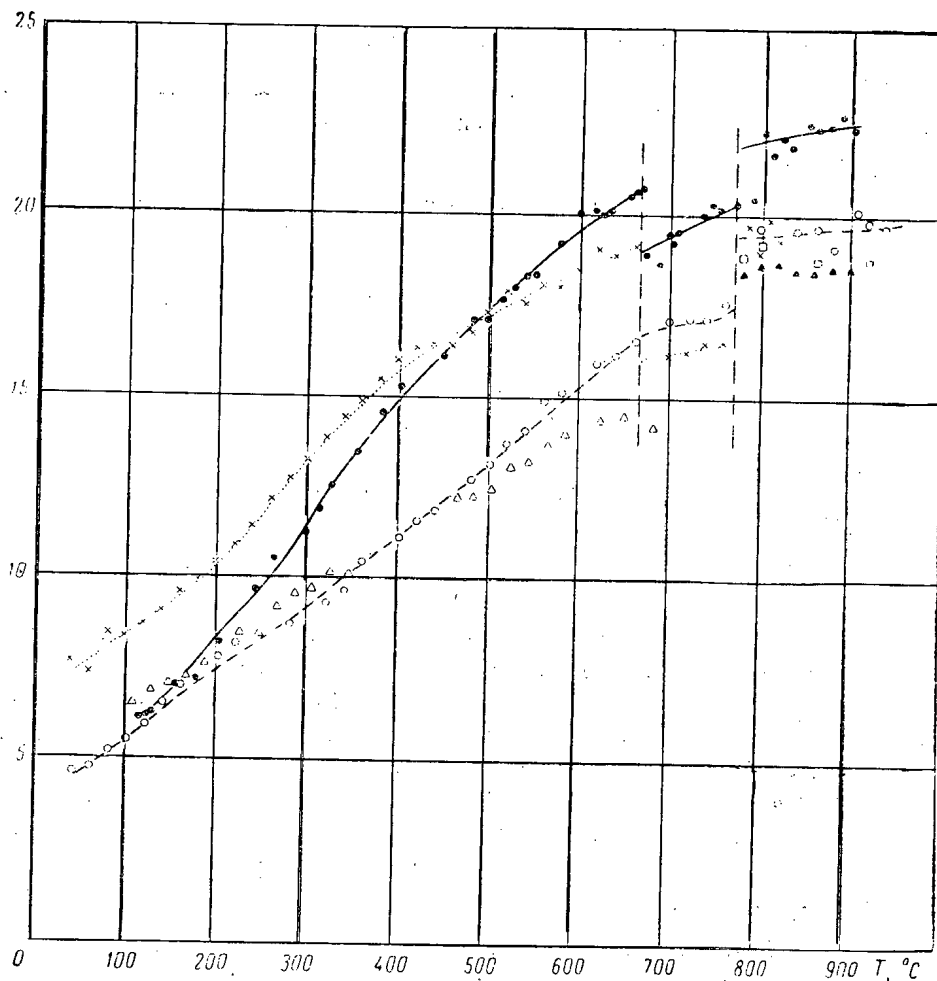

Fig. 2. Temperature dependence of ε for pure uranium (99.98%). Δ) First heating of quenched uranium (with transition to β modification); O) repeated heating of same specimen; □) first cooling in γ region; ▲) second cooling in γ region; ×) uranium deformed by drawing to α-modification; ●) uranium annealed at 600°C after deformation by drawing.

814

the uranium lattice. Increasing the temperature in the α region, which weakens the four covalent bonds in the lattice [11], ought to be accompanied by increase in entropy of the current carriers, i.e., increase of ε_U. Transition to the β - and γ -modifications, with normal metallic bonds, ought to be accompanied by increase in the entropy of the current carriers, which was in fact observed in our experiments. From this viewpoint, the lower value of ε_U in the β -modification may be linked with the stronger covalent bonds in the lattice of β -uranium, by comparison with α -uranium. As for the temperature dependence of the Thomson emf ($\sigma = T \dfrac{d\varepsilon}{dT}$, we can say in general terms that $\sigma > 0$ in the regions of existence of the α and β modifications, and suffers a discontinuous change at the transition points. the sign of σ in the γ modification was not determined unambiguously owing to the lack of experimental data. The specimen's condition affects σ more than ε. According to Ioffe [12], the sign of the Thomsom emf determines the conductivity type; it follows that hole conductivity occurs in α - and β -uranium. The Hall constant should, therefore, be positive for α -and β -uranium. (Reference [13] reports positive values for the Hall constant of α -uranium.)

LITERATURE CITED

1. H. Ebert and A. Schulze, Z. Metallkunde, 38, 46 (1947).
2. A. Dahl and M. VanDusen, J. Res. Nat. Bur. Standards, 89, 53 (1947)
3. W. Tyler et al., Trans. Amer. Inst. Mining. Met. Engrs., 197, 1238 (1953).
4. A. N. Kholden, Physical Metallurgy of Uranium [in Russian], Mowcow, Metallurgizdat (1962), p. 59.
5. J. Katz and E. Rabinovich, Chemistry of Uranium [Russian translation], Moscow, Izd-vo inostr. lit., (1954), p. 137.
6. W. Latimer, J. Amer. Chem. Soc., 44, 2136 (1922).
7. M. I. Temkin and A. V. Khoroshin, Zh. fiz. khimii, 26, 500, 773 (1952).
8. A. A. Rudnitskii, Thermoelectric Properties of Noble Metals and their Alloys [in Russian], Moscow, Izd-vo AN SSSR (1956), p. 18.
9. G. Ya. Sergeev, V. V. Titova, and K. A. Borisov, Metallurgy of Uranium and some other Reactor Materials [in Russian], Moscow, Atomizdat (1960).
10. Ya. G. Dorfan and I. K. Kikoin, Metal Physics [in Russian], Moscow-Leningrad, Gostekhizdat (1933), p. 200.
11. N. T. Chebotarev, Atomnaya Énergiya, 10, 43 (1961).
12. A. F. Ioffe, In symposium, "Electronic Current Conductors" [in Russian], Moscow, Izd-vo AN SSSR (1947), p. 305.
13. F. Boeschoten and C. Huiszoon, Physica, 23, 704 (1957).

———

———

EFFECT OF CRYSTALLIZATION RATE AND ANNEALING
ON THE PLASTIC PROPERTIES OF HIGH-BORON STEEL

(UDC 669.14:66.046.1)

R. V. Grebennikov and A. V. Chirkin

The available data indicate that, in the deformation of stainless steel (18-20% chromium and 10-16% nickel) containing more than 1.5% boron, difficulties arise owing to the material's low plasticity [1]. With boron contents > 2.2%, rolling always leads to cracking along the edges of the sheet [2].

The brittleness of boron-containing steels can be explained by their two-phase structure, in which, together with the metal base, there is a brittle, hard boride component, generally in the form of needles and plates, usually joined together. It is natural to suppose that, by breaking up the boride particles, rendering them spherical and separating them from one another, the deformability and mechanical properties of boron steel could be improved. One possible way of achieving this is to use higher crystallization rates, followed by high-temperature annealing.

The material used in our investigation was boron steel with 19.9-20.7% chromium, 14.5-17.9% nickel and 1.86 - .35% boron. The carbon and silicon contents were 0.03-0.05% and 0.40-0.61% respectively. The steel was melted in a high-frequency furnace with magnesite crucible of capacity 20 kg. Ingots of length 100-180 and width 60 mm were poured at 1450-1500°C in sand-coated molds (ingot thickness 15 mm) and slotted copper molds with

Effect of Pouring and Annealing Methods on Mechanical Properties of Boron Steel

Method of pouring	Boron content, %	Before annealing		After annealing at 1100°C for 10 min			
		σ_p, kg/mm²	l max, mm	σ_p, kg/mm²	l max, mm	σ_b, kg/mm²	δ, %
Cast material							
In sand coated molds	1,9—2,0	77	0,6	96	1,1	37,6	1 2
In copper molds with slot width 15 mm; specimens taken from middle of ingot	2,15 2,35—2,40	110,5 82,9	1,13 0,68	90,4 92	1,25 1,1	44,2 41,4	5 3,3
In copper slotted mold with slot width 8 mm	2,15 2,35—2,40	117 110	0,81 0,5	125 122,5	3,07 1,51	— —	— —
Rolled material							
In copper slotted mold with slot width 15 mm; sheet thickness 6 mm*	2,15 2,35—2,40	138,8 125,8	2,82 2,08	165,1 124	6,78 3,32	65,7 47,0	10,5 6,0

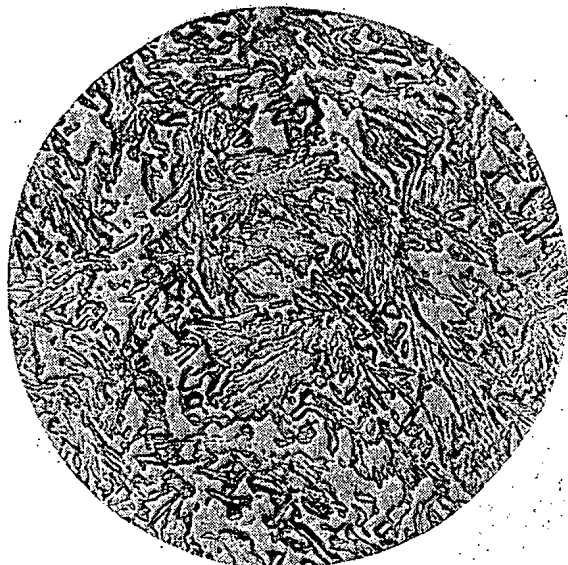* Rolled sheets of 1 mm thickness from the same melt had strength 72-82 kg/mm² for 10-11% elongation.

816

Fig. 1. Microstructure of ingot cast in sand coated mold. Boron content 1.97%; same structure at surface and inner zones of ingot (× 60).

copper walls of thickness 20 mm (ingot slits 8 and 15 mm). The ingots were rolled at 1150-950°C into sheets of thickness 6 or 1 mm. The reduction in one pass was below 0.2 mm at the beginning of rolling, and later was increased to 0.5-1 mm. The tensile strength σ_b and specific elongation $\delta\%$ were determined on ten specimens with working sections of lengths 12 and 60 mm, and the bending strength δ_p and maximum chamber l_{max} were determined on 5 × 5 mm bars with 45 mm between bearings.

The specimens were annealed for 10 min at 1100°C in conventional furnaces with Silit resistors, and were then cooled in air. The results obtained show that the rate of crystallization significantly affects the size and shape of the boride-phase grains (Fig. 1, Fig. 2) and the mechanical properties of the sheet metal (see table). For crystallization in coated molds, the mean boride thickness was about 10 μ, and for crystallization in copper slotted molds was 0.5-3 μ. This breakup of the boride phase markedly affects the rollability. Only the ingots cast in copper slotted molds could be rolled into 1 mm sheets without cracking along the edges. The different sizes of the boride particles in the outer and central parts of the ingots cast in copper slotted molds did not adversely affect the process. It seems that the outer layer with finer boride particles acts as a strong elastic stocking which makes rolling possible without cracking of the edges, whereas the coarse boride needles in the surface regions of the ingots cast in coated molds cause the formation of cracks during the first rollings.

The boride grain side in the rolled metal depends on the grain size in the initial ingots. In sheets obtained by rolling ingots from copper slotted molds, the boride grains were smaller. Subsequent high-temperature annealing affects the microstructure of the cast metal and improves its plastic properties (see Fig. 3 and table). The latter effect is apparently due to changes in the shapes of the boride grains (smoothing out of sharp edges and some spheroidization); the effectiveness of annealing decreases with increasing boride particle size in the cast metal. Annealing is also found to improve the mechanical properties of the rolled metal.

Fig. 2. Microstructure of ingot cast in copper slotted mold with slot width 15 mm [boron content 2.15%] (× 160). a) Central region; b) surface region.

817
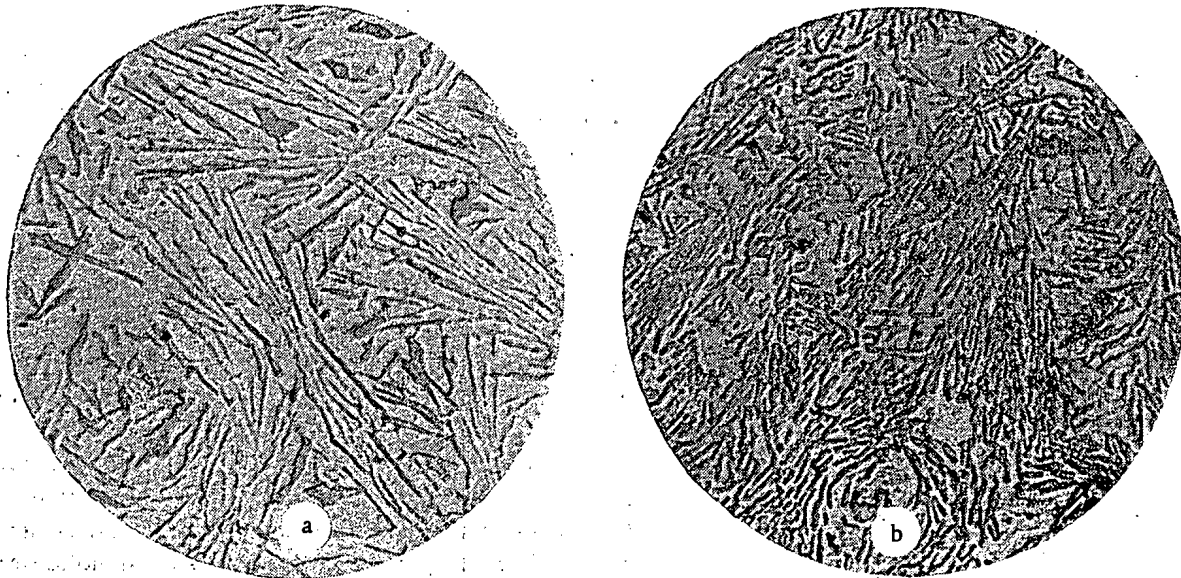
Fig. 3. Central region of ingot cast in copper slotted mold with slot width 15 mm, (a) before and (b) after annealing at 1100°C for 10 min [boron content 1.97%] (× 450).

LITERATURE CITED

1. K. Burngardt and R. Oppenheim, Arch. Eisenhuttenwesen, 32, 95 (1961).
2. D. Dunning et al., Nucl. Sci. Engng, 4, 415 (1958).

PRECIPITATION CONDITIONS FOR URANYL AMMONIUM ARSENATE AND SOME OF ITS PROPERTIES

(UDC 661.649)

M. A. Korenev, B. V. Nevskii, Z. P. Zorina,

Ts. L. Ambartsumyan, and N. G. Nazarenko

The preparation and properties of various arsenides are described in [1-8]. V. G. Chukhlantsev and A. K. Sharova showed that uranyl ammonium arsenate has a lower solubility product and lower solubility in weak solutions of mineral acids (pH $\approx$ 2.0-3.0) than the arsenates UO_2KAsO_4, UO_2NaSO_4, and UO_2LiAsO_4. They also determined the solubilities of other arsenates.

We have studied the precipitation conditions and some of the physical and chemical properties of uranyl ammonium arsenate. It was precipitated as follows. A solution of disodium arsenate added; uranyl arsenate was then precipitated with ammonia. The experiments were performed in a thermostat. The effect of temperature on the precipitation of uranyl ammonium arsenate was studied between 20 and 80°C. The uranium, arsenic and nitrogen contents of the precipitates and solutions were determined by chemical analysis.

X-ray diffraction photographs were taken with a URS-55 set with 57.3 mm diameter camera. The conditions were: Fe radiation, no filter; U = 24 kV; I = 12 mA. The relative intensities of the lines were estimated on a ten-point scale. A thermogram was plotted with a PA-1 polarograph (Pt-PtRh thermocouple, heating rate 100°/min, inert substance = calcined aluminum oxide).

It was found that, from a solution of uranyl nitrate containing 0.5 g/l uranium, at 20°C and nearly stoichiometric arsenic/uranium ratio, uranyl ammonium arsenate begins to come down as a precipitate at pH $\approx$ 1.5. With solution pH 1.5-1.9, up to 90% of the uranium is precipitated. If the pH is further increased, the degree of precipitation gradually increases, and at pH $\approx$ 2.7 the uranium content in the mother liquor is 0.003 g/l. If the uranium concentration in the solution is increased from 0.125 to 2 g/l, the pH at which precipitation begins falls from 2.3-0.7.

In studying the precipitation kinetics of uranyl ammonium arsenate at pH = 2.5, we found that most of the uranium comes down during neutralization of ammonia. Two minutes after the beginning of precipitation, the mother liquor contained 0.020 g/l uranium. Uranium precipitation then slowed down and after 90 min there was 0.004 g/l uranium left in the mother liquor.

Uranyl ammonium arsenate was obtained as a finely-crystalline lemon-yellow powder with a bright green luminescence in ultraviolet light. Its composition can be represented by the formula $UO_2NH_4AsO_4 \cdot 3 H_2O$. The refractive index of the finely-aggregated crystals was n = 1.598.

Its thermogram displays two intense endothermic effects and one exothermic peak. The first endothermic effect, at 100-300°C, is due to dehydration of the salt and formation of anhydrous uranyl ammonium arsenate. The second endothermic effect, at 400-500°C, corresponds to decomposition of uranyl

Fig. 1. Thermogram of uranyl ammonium arsenate.

819
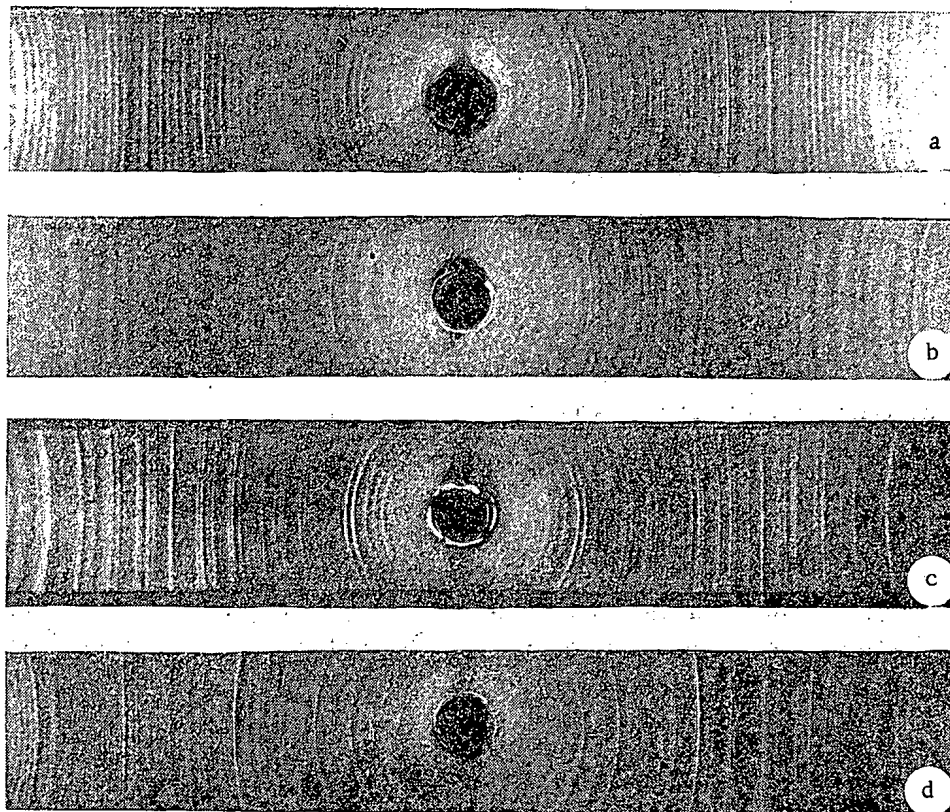
Fig. 2. X-ray powder photographs of uranyl ammonium arsenate. a) Air-dried; b, c, d) heated to 300, 800, and 1000°C respectively.
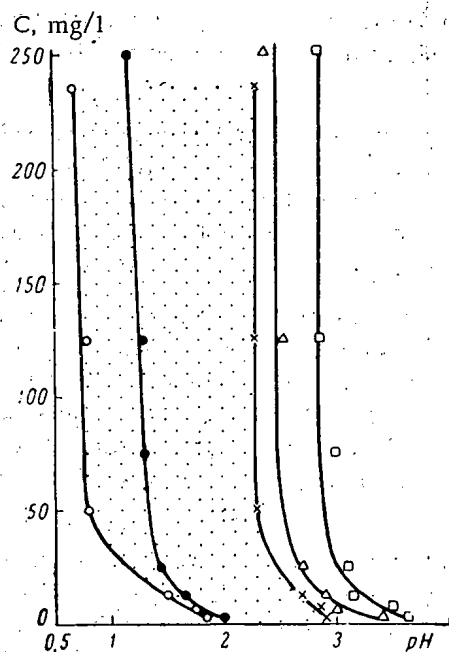
Fig. 3. Formation of ferric, ferrous, aluminum, and uranyl ammonium arsenates, versus concentrations of metals and solution pH. O) Beginning of precipitation of uranyl ammonium arsenate; ●) beginning of precipitation of ferric arsenate; ✕) end of precipitation of uranyl ammonium arsenate; △) beginning of precipitation of ferrous arsenate; □) beginning of precipitation of aluminum arsenate.

ammonium arsenate with loss of ammonia. The exothermic peak at 590°C is due to crystallization of a new phase which appears to be uranium pyroarsenate.

Thermogravimetric analysis showed that, on heating uranyl ammonium arsenate, evolution of water begins at 40°C and is completed at 300°C; 12.55% water comes off. Further heating to 500-800°C leads to almost complete driving off of the ammonia. At 900-1000°C the uranyl arsenate decomposes, gradually losing arsenic.

At higher temperatures this process accelerates. On heating ammonium uranyl arsenate to 1000°C and keeping it at this temperature, the arsenic is almost completely driven off, leaving U_3O_8.

X-ray analysis of hydrated uranyl ammonium arsenate showed that it is tetragonal, with unit cell parameters a = 7.21 A, c = 8.85 A (Fig. 2a). The crystal structure does not change up to 300°C, but at this temperature the diffraction lines are more diffuse (see Fig. 2b), and the luminescence is considerably less intense. Anhydrous uranyl ammonium arsenate is yellow.

The loss of water without disturbance of crystal structure and the ability to rehydrate show that the water in the hydrated salt is of the zeolite type. The compound decomposes at 500-800°C. The X-ray diffraction pattern of the compound at 800°C displays many sharp, intense

820

lines (see Fig. 2c); the yellow substance formed by heating to this temperature contains 58.2% uranium and 14.39% arsenic. The X-ray diffraction pattern obtained when the arsenate is heated to 1000°C corresponds to that of U_3O_8 (see Fig. 2d).

We plotted the uranium content of the solution (up to 0.250 g/l) versus the solution pH at which the arsenates of ferric iron, ferrous iron and aluminum begin to form, and the solution pH at the start anf finish of precipitation of uranyl ammonium arsenate. From the curves (Fig. 3) it is seen that uranyl ammonium arsenate and ferric arsenate are coprecipitated at similar pH values. This prevents selective separation of uranium.

Precipitation of ferrous and aluminum arsenates begins at higher pH values than precipitation of uranium. The curves for the start of their precipitation lie outside the region of uranium precipitation: thus, uranium can be selectively precipitated in the presence of ferrous and aluminum ions.

LITERATURE CITED

1. V. G. Chukhlantsev, Zh. neorgan. khimii, 1, No. 9 (1959).
2. V. G. Chukhlantsev, Zh. neorgan. khimii, 6, No. 5 (1956).
3. V. G. Chukhlantsev and A. K. Sharova, Zh. neorgan. khimii, 1, No. 1 (1956).
4. Kraft, Comptes Rendus, 20, 57 (1938).
5. Puller, Z. analyt. Chem., 10, 41 (1871).
6. A. P. Zefirov, B. V. Nevskii, and G. F. Ivanov, Factories for Uranium Reprocessing in the Capitalist Countries [in Russian], Moscow, Gosatomizdat (1962).
7. T. Arden, Industr. Chemist, 32, 202 (1956).
8. T. Arden, R. Humphries, and J. Lewis, J. Appl. Chem., 8, 151 (1958).

SOME POSSIBLE METHODS FOR PREPARING RADIOACTIVE ISOTOPES

(UDC 621.039.8)

N. P. Rudenko and A. M. Sevast'yanov

Of the known radioactive isotopes of beryllium, magnesium, and aluminum, those most suitable as tracers are given in the table, together with their properties.

We have studied the feasibility of obtaining Be^7, Mg^{28}, and Al^{26} in a nuclear reactor by means of the secondary nuclear reactions Li^6 (t, 2n) Be^7 [3-5], Mg^{26} (t, p) Mg^{28} [6], Mg^{24} (t, n) Al^{26} [7]. For this purpose, quartz ampoules containing metallic lithium, lithium compounds (for preparing Be^7) or lithium-magnesium alloys (for Al^{26}, Mg^{28}, and Be^7) were irradiated with the integral neutron flux ($\sim 10^{20}$ neutron/cm^2 for Mg^{28}).

After irradiation, the specimens were kept for a known time, then tritium was separated from the ampoules and the contents dissolved in dilute hydrochloric acid. The γ-ray spectra were then measured (Fig. 1).

To the solution containing lithium-magnesium alloy, 10-20 mg beryllium, aluminum, iron and cobalt was added as carrier. The radioactive substances present were then precipitated with excess of caustic soda. The beryllium and aluminum remaining in solution were separated with hydrochloric acid and ammonia and analyzed chromatographically by passing their solution in 1.1 N hydrochloric acid through Dowex-50 cation-exchange resin (in the H^+ form). The Be^{2+} ions were completely eluted, and the Al^{3+} ions washed out from the cation-exchange resin with 3 N hydrochloric acid. By this means we obtained radiochemically pure beryllium. Its purity was determined by taking the γ-ray spectrum (0.480 keV) and measuring the half-life (53 days). When 1 g of non-enriched lithium metal is irradiated by a neutron flux of $4.5 \cdot 10^{19}$ neutron/cm^2, the activity of the Be^7 separated is 26 μcurie.

N, pulses

Fig. 1. Gamma-ray spectrum of irradiated Li-Mg alloy, measured with a 50-channel amplitude analyzer.

Aluminum was separated from the eluant as follows. Ether was added to the solution of aluminum in conc. HCl, and cooled gaseous HCl passed until the liquid layers vanished. The precipitate of $AlCl_3 \cdot 6H_2O$ was dissolved in HCl and precipitated as aluminum hydroxide by means of ammonia. Al^{26} was identified by the γ-ray energy (1.83 MeV). From the γ-ray intensity it was found that, on irradiating 1 g lithium-magnesium alloy with 10^{20} neutrons/cm^2, $1.0 \cdot 10^{-3}$ μcurie Al^{26} is formed.

Magnesium was separated during the ion-exchange process: 0.5 N HCl was passed through the KU-2 cation-exchange resin, on which the magnesium was sorbed. The completeness of lithium separation was monitored with a flame photometer, while magnesium desorption was measured radiometrically. The chromatographic separation and purification of magnesium took about 20 h, i.e., close to the Mg^{28} half-life. We, therefore, studied the feasibility of using an extraction method.

Magnesium can be extracted and purified by means of a chloroform solution of 8-hydroxyquinoline or its derivatives, with or without the presence of an aliphatic amine [6, 10]. To an aqueous
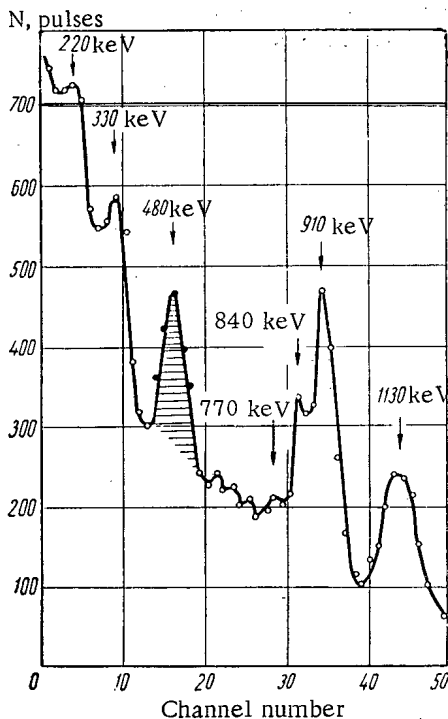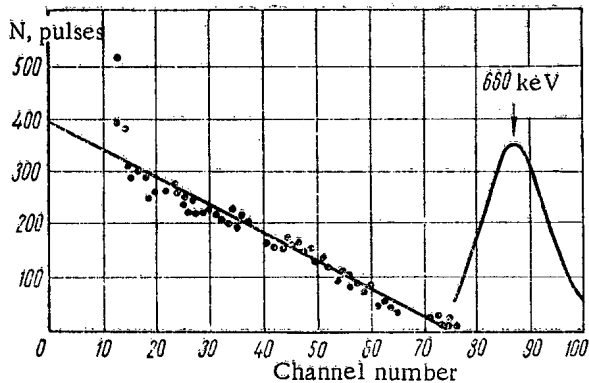
822

Some Data on Isotopes [1-9]

Isotope	Decay type	Half-life	Energy of Radiation, MeV		Preparation reaction
			β -particles	γ -rays	
Be^7	Elec. capture	53 days	—	0,480	$Li^6 (t, 2n) Be^7$
Be^{10}	β⁻	$2,5 \cdot 10^6$ years	0,535—0,560	—	$B^{10} (n, p) Be^{10}$
Mg^{28}	β⁻	21,4 h	0,3—0,4; 2,85	0,4; 0,95; 1,35; 1,80	$Mg^{26} (t, p) Mg^{28}$
Al^{26}	β⁺, Elec. capture	$7,85 \cdot 10^5$ years	~ 1,16	1,12; 1,83; 2,96	$Mg^{24} (t, n) Al^{26}$; $Al^{27} (n, 2n) Al^{26}$

Fig. 2. Upper beta-radiation limit of Be^{10}.

solution of Mg^{2+} with 0.25 M sodium acetate, ammonia solution was added until the pH was 6.5-7.0, and the heavy-metal cations extracted with 0.007 M chloroform solution of 8-hydroxyquinoline. The pH of the aqueous phase is further increased with ammonia to 11±0.5 and magnesium extracted with 0.2 M chloroform solution of 8-hydroxyquinoline containing 10 vol. % n-butylamine.

Magnesium was re-extracted with 2N HCl. During re-extraction the n-butylamine goes into the water phase, which is very undesirable. Quantitative extraction of magnesium is possible with pure 8-hydroxyquinoline solution, but at higher concentrations. The activity of the magnesium thus separated is 0.10-0.02 mcurie per 1 g magnesium in the original alloy. For alloys with Li/Mg ratios from 1/3 to 4/1, the activity is independent of alloy composition.

One method of getting Be^{10} and Al^{26} is to irradiate Be, B, Mg, and Al with fast neutrons (or, for boron and magnesium, thermal neutrons) in a reactor. From literature data [9] and experiments, it was found that the principal elements from which carrier-less Be^{10} must be freed are B, Ca, Si, Al, Co, Zn, and Fe.

Boron carbide from the spent reactor control rods was sintered with calcium hydroxide and dissolved in hydrochloric acid, and by appropriate chemical treatment a solution was obtained containing Al^{3+} and Be^{2+}.

The solution was passed through Dowex-50 cation exchange resin, in which Al^{3+} had been absorbed. The solution was then evaporated and the residue heated to 400-500°C. The Be^{10} obtained was radiochemically pure and had no γ -radiation. The Be^{10} was identified from the β -radiation spectrum, which was measured by its absorption in aluminum (560 keV). Figure 2 gives the upper boundary of the β -rays from Be^{10}, measured spectroscopically (560 keV).

LITERATURE CITED

1. B. S. Dzhelepov and L. K. Peker, Decay Schemes of Radioactive Nuclei [in Russian], Moscow-Leningrad, Izd-vo AN SSSR (1958).
2. D. Strominger, J. Hollander, and G. Seaborg, Rev. Mod. Phys., 30, 604 (1958).
3. N. P. Rudenko and A. I. Sevast'yanov, Radiokhimiya, 1, 691 (1951).
4. N. P. Rudenko and A. I. Sevast'yanov, The Radioactive Isotopes Be^7 and Be^{10} [in Russian], Moscow, Atomizdat (1964).
5. J. Roy et al., In symposium, Preparation and Uses of Radioactive Isotopes. International Conference on the Uses of Radioisotopes in Physical Science and Industry, Copenhagen, 1960 [in Russian], Izbr. dokl. inostr. uchenykh, Moscow, Gosatomizdat (1962), p. 5.
6. L. S. Kozyreva, V. V. Levin, and I. V. Meshcherova, In symposium, Methods of Preparation of Radioactive Preparations, Ed. N. E. Brezhneva [in Russian], Moscow, Gosatomizdat (1962), p. 103.

7. T. Kohman et al., International Conferences on Radioisotopes in Scientific Research, Aluminium-26, Paris (1957).
8. C. Eggler, D. Hugnes, and C. Huddeston, Phys. Rev., 74, 1239 (1948).
9. S. S. Vasil'ev et al., Atomnaya Énergiya, 11, 401 (1961).
10. F. Umland and W. Hoffman, Analyt. Chim. Acta, 17, 234 (1957).

All abbreviations of periodicals in the above bibliography are letter-by-letter transliterations of the abbreviations as given in the original Russian journal. *Some or all of this periodical literature may well be available in English translation.* A complete list of the cover-to-cover English translations appears at the back of this issue.

OPTIMUM SPECIFIC γ-ACTIVITY OF A QUASI-HOMOGENEOUS RADIATION CHEMICAL PLANT

(UDC 541.15)

V. A. Él'tekov

A radiation chemical plant may be viewed, for the purpose of designing its basic characteristics, as a radiation-absorbing system consisting of radiation sources adjacent to sources of auxiliary structures, and an irradiated medium. In most cases, this system comprises an enclosure while the sources in the form of rods are situated at the nodes of a two-dimensional lattice. The study of systems where the medium to be irradiated absorbs only γ-radiation because of adequate thickness of the auxiliary structures enclosing the sources is of practical interest. Under certain conditions which are partially examined in [1], γ-radiation energy absorbed in heterogeneous systems is distributed among the components of the system in the same way as in homogeneous systems. In what follows we shall term these systems (or radiation chemical plants) capable of homogenization quasi-homogeneous systems (or quasi-homogeneous radiation chemical plants).

We may choose as one of the parameters of quasi-homogeneous radiation chemical plants using identical sources the level of γ-activity $s = S/V$ per unit volume V of the substance irradiated, where S is the total activity of the sources in the radiation chemical plant.

A radiation chemical plant for which the losses c incurred in unit production are minimized will be termed optimal for a specific radiation chemical process. In the steady-state (time-invariant) operation of a radiation chemical plant, a quantity Q of product is produced during any unit time interval in the volume of substance irradiated, and the equipment is amortized (sources and enclosure constitute the bulk of the equipment) over the dose C; the variable c_q is the ratio C/Q. The specific capacity q equals the ratio Q/V in the case of quasi-homogeneous radiation chemical plants. It is assumed to be a known function of dose rate y_E [2] for each process, and y_E is proportional to the specific activity s, the initial energy E of the photons, and the ratio $f_E(s)$ of the energy absorbed in the medium irradiated to the γ-radiation energy generated in the exposure. The specific activity value s_0 at which the ratio c_q is minimized is determined by the common procedure for finding a minimum from the equation

$$q\,[y_E(s_0)]\,\frac{dc_V}{ds}\,(s_0) - c_V(s_0)\,\frac{dq}{ds}\,[y_E(s_0)] = 0, \tag{1}$$

where $c_V = C/V$; $y_E(s) = k_E E s\, f_E(s)$; k_E is a proportionality factor.

The cost C is broken down into two component parts corresponding to the cost of the sources and the cost of the enclosure: $C = M_s + M_e$. It is readily seen that $M_s = msV$, where m is the cost per single decay event. The value M_0 in the case where the enclosure must double as radiation shield depends on s in a fairly complex way. Equation (1) is simplified if the inequality $d/ds\,(M_0/mV) \ll 1$ holds near $s = s_0$. This inequality is valid in the case where the radiation emerging from the system is rather weak at values of s close to s_0, or where the thickness of the required shielding is less than the thickness of the enclosure required to meet the specified process conditions (e.g., high pressure). When that inequality is met, Eq. (1) becomes

$$q\,[y_E(s_0)] - (s_0 + a)\,\frac{dq}{ds}\,[y_E(s_0)] = 0, \tag{1'}$$

where $a = M_0/mV$.

825
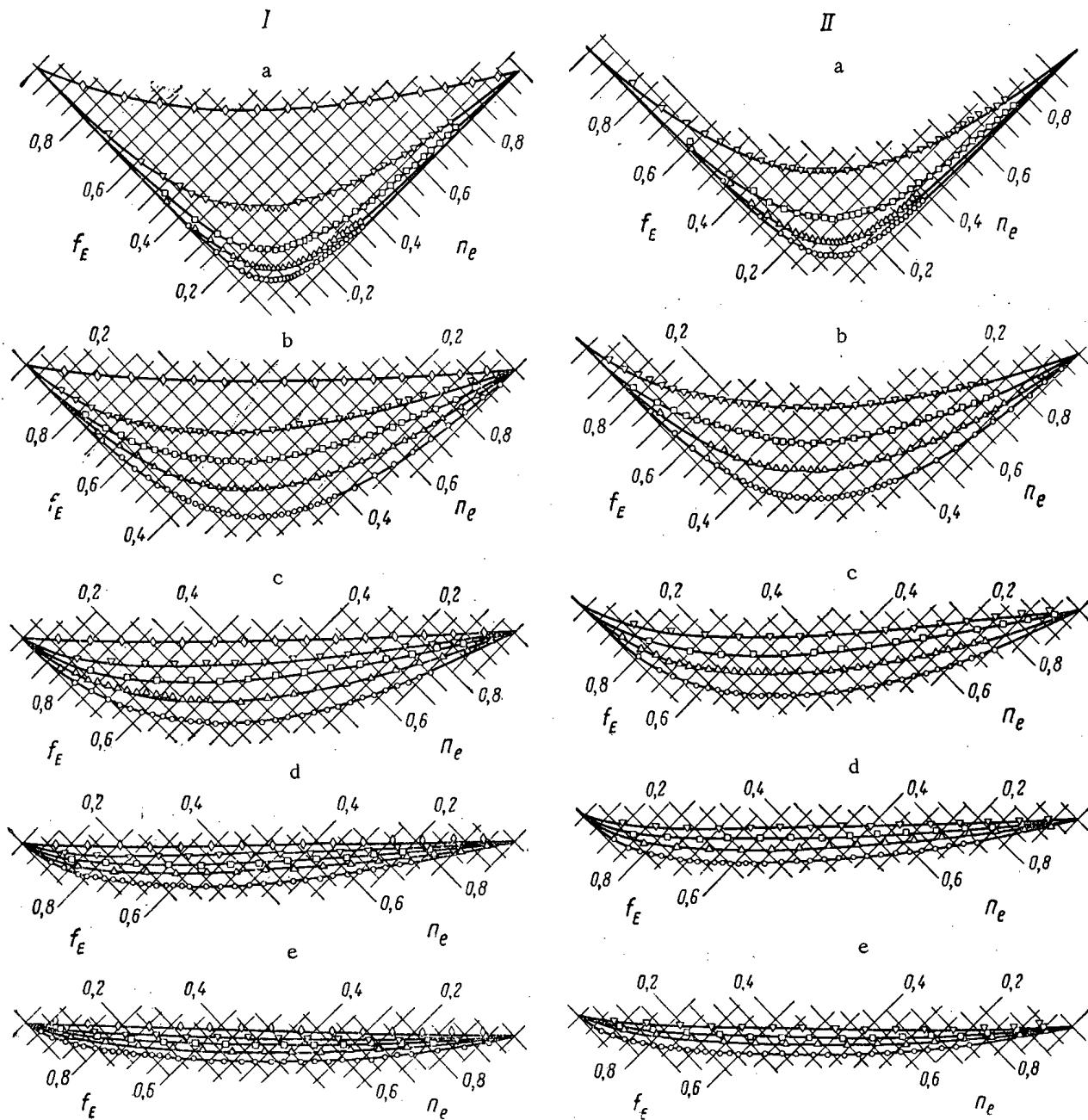
Fig. 1. Dependence of the ratio f_E of the energy absorbed in the material irradiated to the energy generated in a homogeneous mixture, for Z_{ir} = 7.5 (curve I) and for Z_{ir} = 11 (curves II) at Z_s equal to: $\diamond$) 11; ∇) 27; $\square$) 41; $\triangle$) 55; $\bigcirc$) 78. Initial energy of γ -protons: a) 123 keV; b) 316 keV; c) 660 keV; d) 1.25 MeV; e) 2.76 MeV.

In some processes, the dependence of the specific capacity on dose rate y_E is expressed by an empirical power law [2-4]: $q = ky_E^{\alpha}$ where k and α are constants for the specific process* (0 < α $\leq$ 1). Eq. (1') is, therefore cast in the form

$$y_E(s_0) = \alpha(s_0 + a)\, y'_E(s_0). \tag{1''}$$

The value of f depends on the concentration of the radioactive material (as the radiation absorber) in the system. Figure 1 shows f_E plotted as a function of the electron concentration n_e of the source material over a broad range of initial γ -photon energies and atomic numbers Z_s of the source material, and for two values Z_{ir} of the

---

* Note that α is related to the exponent e figuring in contributions [2-4] by the equation $\alpha = 1 - e$.

atomic number of the irradiated material (7.5 and 11). The electron concentration is related to s by the formula

$$n_e = \frac{s}{s+b} \,. \tag{2}$$

Here $b = \rho\, t A_s Z_{ir}/A_{ir} Z_s$, where ρ is the density of the substance being irradiated; t is the activity of unit source mass; A_s and A_{ir} are the respective atomic weights of the source material and irradiated material. The data points in Fig. 1 correspond to f_E values obtained by Monte Carlo methods, with no greater than 3% error. By interpolating the data we may find f_E for any case of practical interest.

Since no analytic expression of the function $f_E(s)$ is known, Eq. (1") must be solved numerically or graphically. In the latter case, the equation may be solved by the following construction. In a coordinate system where $\log(1 + s/a)$ is laid off as abscissa and $\log y_E$ as ordinate (the base of the logarithms is not essential), a graph of $y_E = y_E(s)$ can be plotted with the aid of the curves in Fig. 1 and Eq. (2) (see Fig. 2). The tangent to the curve, equal to α^{-1}, is then drawn. The abscissa of the tangency point will then be $\log(1 + s_0/a)$, which allows us to find s_0. Actually, of all the points on the curve $y_E = y_E(s)$, the formula (1") will hold only for the point at which this curve is tangent to some curve of the family satisfying the differential equation $y_E(s) = \alpha(s + a)\, y_E'(s)$, which turns out when plotted on a logarithmic scale to be a family of straight lines parallel to the straight line shown in Fig. 2.

The graphical method of solution referred to may also be useful when the specific capacity q does not obey a power law. This requires some constructions similar to those described above, and based on Eq. (1'), in coordinate axes along which the values of $\log(1 + s/a)$ and $\log q$ are plotted.

In the case of radiation chemical plants which do not admit homogenization, the capacity Q is determined by integrating over the volume of the irradiated material of specific capacity q, which is at each point in the volume a known function of dose rate. With the aid of the theorem of the mean, we may state: $Q = Vq\,(\tilde{y}_E)$, where $\tilde{y}_E$ is some intermediate dose rate value in the irradiated volume. Further, $\tilde{y}_E$ may be formally equated to $\varepsilon\tilde{y}_E(s)$, where ε is some function of the equipment parameters introduced to satisfy the equation.

In [2], the problem of optimizing plant design from a series of designs differing in the specific activity s and diameter D is solved under the assumption that function ε is independent of s. Roughly speaking, this assumption is equivalent to assuming γ-radiation energy leakage from the system and dose field variation at the same average dose to be independent of the density at which sources are spaced. Note that radiation chemical plants for which this assumption is valid will also permit of homogenization. Moreover, f_E is assumed independent of s in [2]. As can be readily shown, this assumption reduces to an absurdity in the case $\alpha = 1$ (this case is encountered most frequently in radiation-chemical processes). We see directly from the formulas in [2] that the optimum plant in this case must be one of zero irradiated volume and infinitely high specific activity. In our case (dependence of f_E on s taken into account), no such conclusion is reached. In the case $\alpha \neq 1$, the conclusions arrived at in [2] will not lead to contradiction, even though the parameters of the optimum plant indicated in [2] for those cases may not be considered exact. Allowing the first assumption for sake of argument, we now find the corrections dictated by the rejection of the second assumption for the optimal values of s, D, and c_q derived in [2] for a radiation chemical plant in which ethylene is radiation-polymerized ($\alpha = 0.5$). Let us denote these values as s_1, D_1, and c_{q1}. In the light of our first assumption, the equation $\dfrac{\partial c_q}{\partial s}(s_0, D_0) = 0$ is equivalent to Eq. (1"), which may be stated in the form

$$2s_0 f_E(s_0) = (s_0 + a)\,[f_E(s_0) + s_0 f_E'(s_0)]. \tag{3}$$

for $\alpha = 0.5$. Since $f_E' \equiv 0$ is assumed in [2], s_1 must satisfy the equation

$$(s_1 - a)\, f_E(s_1) = 0,$$

from which we infer $s_1 = a$. This fact is also implied in [2]. On substituting $s_0 = A + \triangle s$, Eq. (3) takes on the form
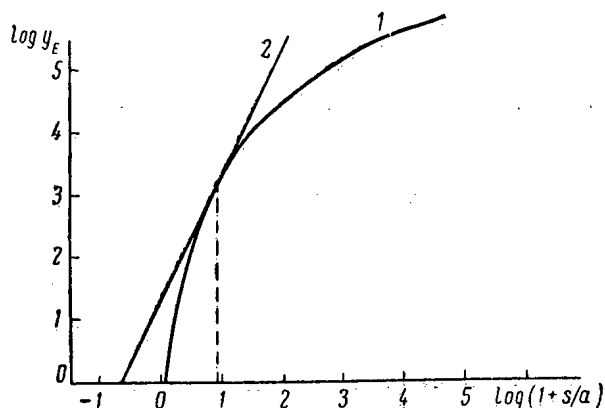

Fig. 2. Graphical method for optimizing the specific activity s_0 of a quasi-homogeneous radiation chemical plant: 1) $y_E = y_E(s)$; 2) $\log y_E = \alpha^{-1} \log(1 + s/a) + \text{const}$; $—\,—\,—\,—\,—$ $\log(1 + s_0/a)$.

827

$$\Delta s f_E(a + \Delta s) = (2a + \Delta s)\, f'_E(a + \Delta s). \tag{3'}$$

$$\Delta s = \frac{2a^2 f'_E(a)}{f_E(a)}. \tag{4}$$

holds to terms vanishing to the same order of infinity as Δs beyond the first term. The same order of exactness holds for the equations

$$\Delta D - D_0 - D_1 = - \left[\frac{\partial^2 c_q}{\partial D\, \partial s}(s_1, D_1) \Big/ \frac{\partial^2 c_q}{\partial s^2}(s_1, D_1) \right] \Delta s;$$

$$\Delta c_q = c_q(s_0, D_0) - c_q(s_1, D_1) = \frac{\partial c_q}{\partial s}(s_1, D_1)\Delta s + \frac{\partial c_q}{\partial D}(s_1, D_1)\Delta D.$$

And since $\dfrac{\partial c_q}{\partial D}(s_1, D_1) = 0$, then $\Delta c_q = \dfrac{\partial c_q}{\partial s}(s_1, D_1)\Delta s$.

From the last equation, and taking Eq. (4) into account, we may derive $\Delta c_q / c_q = -(\Delta s / 2 s_1)^2$. This implies that the correction to c_q will be consistently negative, for the procedure followed in [2] yields no minimum for c_q.

In computing $\Delta s\, s_1$, we note that $f'_E = \dfrac{d f_E}{d n_e} \times \dfrac{d n_e}{d s}$ and that, according to Eq. (2), the equation $\dfrac{d n_e}{d s} = \dfrac{b}{(s+b)^2}$ must hold. $\Delta s / s_1$ will, therefore, be determined by the equation

$$\frac{\Delta s}{s_1} = \frac{d f_E}{d n_e} \cdot \frac{2ab}{(a+b)^2 f_E(a)}. \tag{5}$$

For the system of cobalt sources, steel source holders, and ethylene discussed in [2], $f_E = 0.85$. Graph Id (cf. Fig. 1) shows that $n_e = 0.1$ while $d f_E / d n_e$ is -1.1 (Z_s is assigned the value of 27, and $Z_{ir} = 7.5$). Solving Eq. (2) for b/s we find 9.0 for the last value. Substituting all these values into Eq. (5), we then find -0.23 for $\Delta s / s_1$, which corresponds to a value of -0.013 for $\Delta c_q / c_q$. The relative difference obtained in the value of c_q does not exceed the inexactness of the calculations in this concrete case [2] brought about by some assumptions other than those already discussed. It is not excluded that this difference may be even greater in other cases.

In conclusion, note that the graphical method described above makes it possible to not only optimize the density of spacing of like sources in the medium to be irradiated, but also to choose from among various isotope preparations available for use that one for which the value of c_q characterizing the cost of producing one unit commodity will be minimized. This calls for constructing the graphs in Fig. 2 for each one of the preparations, and constructing them only near the proposed tangency points. The least c_q value will be found for in that radioactive preparation for which the tangent the curve representing log y_E as a function of log $(1+s/a)$ with a slope of α^{-1} will assume the highest position.

LITERATURE CITED

1. B. M. Terent'ev, V. A. Él'tekov, and Yu. S. Ryabukhin, Atomnaya énergiya, 13, 568 (1962).
2. M. M. Levine and M. Steinberg, Nucl. Sci. and Engng. 12, 498 (1962).
3. B. Bray et al., Chem. Engng Progr. Sympos. Series, 55, 33 (1959).
4. N. Syrkus, A. Breger, and B. Weinstein, Large Radiation Sources in Industry. Vienna, IAEA (1960), p. 15.

N-I-P GERMANIUM DETECTOR FEATURES HIGH RESOLUTION
FOR LOW-ENERGY AND MEDIUM-ENERGY GAMMAS

(UDC 539.107.4)

L. V. Maslova, O. A. Matveev, S. M. Ryvkin,

I. A. Sondaevskaya, and N. B. Strokan

Recent studies [1-4] have shown that germanium n-i-p structures can be used as spectrometric nuclear radiation detectors with high energy resolution for γ-protons.

Below we report some concise information on the fabrication technology and design of n-i-p detectors, their characteristics, and the equipment used for taking spectra.

P-type germanium of 3 to 10 ohm·cm resistivity is used in the manufacture of the radiation detectors. The n-i-p junction is brought about by thermal diffusion of lithium and subsequent drifting of the lithium ions across the n-p junction field. The width of the sensitive depletion layer (the i-layer) attained 1 mm after drifting for $\approx$10 h. Such n-i-p junction structures mounted in a leaktight enclosure have been employed to measure the energy of γ-quanta.

Further research has shown appreciably stabler results achieved with an additional electrode, the guard ring electrode. The operational reliability of the detector is increased by this device, reverse currents and noise are lowered, and operation at higher voltages becomes possible. Reverse current was $5 \cdot 10^{-5}$ A in one sample operated at 77°K and 100 V with the guard ring cut off, and dropped to 10^{-9} A when the guard ring was switched on.

The basic design of the guard ring detector and its circuitry may be seen in Fig. 1.

The detectors were checked for amplitude resolution with respect to 1.333 MeV gamma-photons and gammas of lower energies. Energy resolution of 6±1 keV was reported for 1.333 MeV (a Co^{60} source was employed). Energy resolution came to 4±1 keV at energies of $\approx$0.5 MeV and below. Resolution of 4 keV was achieved for 482 keV and 57 keV gammas emitted by an Hf^{181} preparation.

Standard circuitry was employed in measuring peak width in the pulse amplitude distribution: a pre-amplifier, amplifier, discriminator, and pulse height analyzer. Discrimination and subsequent amplification were applied to "stretch" the most interesting portions of the spectrum with the aid of an amplifier included in the AI-100 pulse height analyzer, so that the channel count-rate value determined with the aid of a generator designed to generate exact pulse amplitudes was at most 1 keV.

Detector measurements were taken with the detectors cooled to liquid-nitrogen temperatures and at bias voltage $\approx$100 V. The input stage of the amplifier section was assembled around a cascode circuit using 6Zh1P tubes. The tubes were run through quality control inspection before installation, and then specimens having a

Fig. 1. Basic design and circuitry of ion-drifted detector.

829
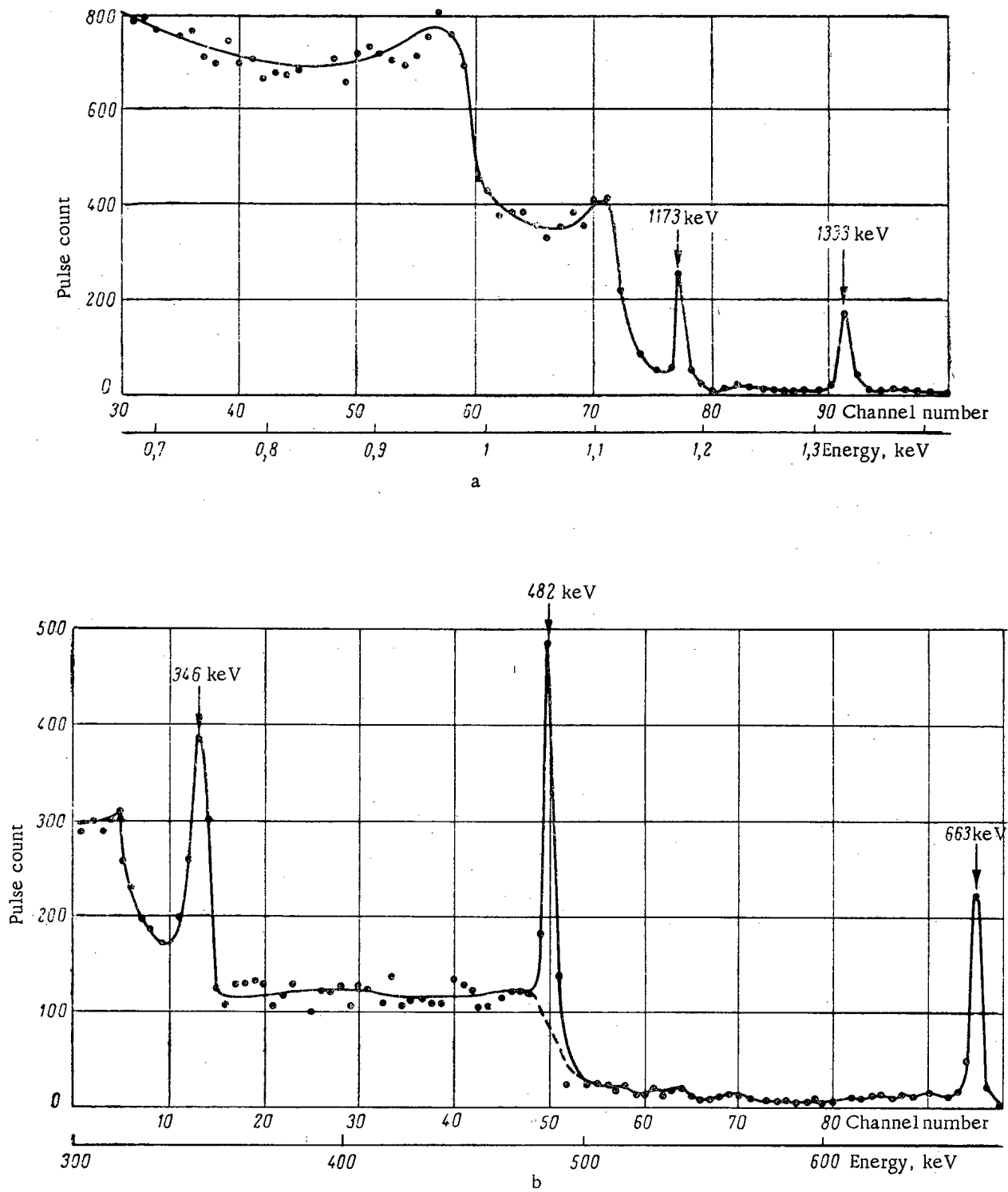
Fig. 2. Portions of the energy spectra of the gamma-photons: a) Co[60] source (T = 78°K; V = 100 V); b) Hf[181] + Cs[137] preparation (T = 78°K; V = 120 V).

transconductance $\geq$ 4.0 mA/V at grid current $4 \cdot 10^{-10}$ A were chosen. The amplifier input capacitance was 7 pf (7 $\mu\mu$f), and the amplifier noise did not exceed 2 keV when the amplifier was not working into the detector load.

Figure 2 shows the portions of the spectra referred to earlier in reduced scale. The ratio of the pulse count in the total absorption peak to the pulse count in the corresponding Compton absorption edge is strongly energy-dependent, as might be expected. (The reason for this is the energy dependence of the photoelectric absorption coefficient.)

830

Note that the relative pulse count in the full energy peak will increase in proportion to the detector sensitive volume, on account of the subsequent absorption of the Compton electron and scattered γ-ray photon.*

Finally, note that the detectors may be stored safely not only at low temperatures [2, 3], but even at room temperature when a reverse bias of 10 to 20 V is placed across the detector. But protracted shelf life still calls for a low temperature (say, 77°K).

The authors take this opportunity to thank L. P. Bogomazov and D. V. Tarkhin for their invaluable assistance in the development of the radiation detector.

LITERATURE CITED

1. O. A. Matveev, Atomnaya énergiya, 16, 362 (1964).
2. P. Webb and R. Williams, Nucl. Instrum. and Methods, 22, 2, 361 (1963).
3. A. Tavendale and G. Ewan, Ibidem, 25, 185 (1963).
4. T. Nybakken and V. Vali, Ibidem, 26, 1, 182 (1964).

---

* Actually, with the wide depletion region ($\gtrsim$ 3.5 mm) radiation detectors recently made available, the total energy peaks for the Co^{60} lines are slightly greater than the Compton absorption edge. Pulse height resolution will be less than 1% in this case, and can be brought to 0.5% if the quanta are hard enough (6.5 MeV).

RADIATION HAZARD IN IRRADIATED METAL SPECIMENS

(UDC 621.039.55.4)

M. M. Krasnoshchekov
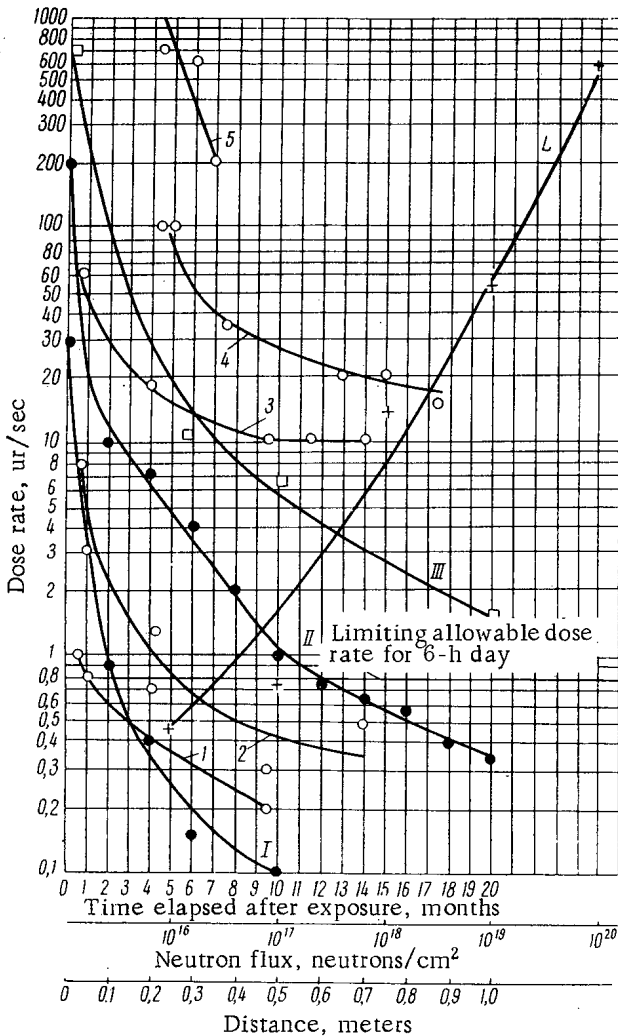
Radiation hazard in irradiated metallic specimens. Dose rate measured up to case iron specimens as a function of the time lapsed after irradiation by the following integrated doses, in neutrons/cm^2: 1) 10^{16}; 2) 10^{17}; 3) 10^{18}; 4) 10^{19}; 5) 10^{20}. Dose rate measured 7 months after withdrawal of specimens from the reactor in exposure to flux of 10^{20} neutrons/cm^2 as a function of distance from the source: I) copper; II) cast iron; III) steel. L) Dose rate measured up to case iron specimens $\frac{1}{2}$ year after extraction from reactor, as a function of neutron flux.

Reactor-irradiated alloys possess fairly high radioactivity. For that reason they can be handled for only limited time intervals. We made an experimental determination of the dose rate established in air by materials irradiated in various neutron flux levels with the object of ascertaining this allowable handling time. Specimens of 45 steel, cast iron, and technical-grade red copper were fashioned as cylinders 8 mm in diameter, 10 mm long, each weighing 4 to 4.5 g more or less. The chemical composition of these materials appears in the table.

The specimens were irradiated in vertical channels of the VVR-M reactor of the Institute of Physics (Academy of Sciences of the Ukrainian SSR) in neutron fluxes of 10^{16} to 10^{20} neutrons/cm^2. Neutrons of higher than 1 MeV energy were 9 to 10 times less numerous, and neutrons of energy greater than 3.5 MeV were 100-odd times less numerous, than thermal neutrons.

An RK-01 (open-shuttered) r-meter was employed to measure the γ dose rate of the active specimens. Results are plotted in the diagram. Curves 1– 5 show that the dose rate due to the source decayed rapidly in about a month when the flux was 10^{16} neutrons/cm^2, and decayed in 6 to 7 months for a flux of 10^{19} to 10^{20} neutrons/cm^2. After the short-lived nuclides (Mn^{56}, Si^{31}, P^{32}) had decayed, the time change in dose rate slackened off and became almost constant after a certain time.

Dose rates for samples irradiated at various neutron flux levels are entered in the table below as of 10 months following the exposure:

Neutron flux, neutrons/cm^2	Dose rate, μr/sec
10^{16}	0,2
10^{17}	0,4
10^{18}	10
10^{19}	20

832

Chemical Composition of Irradiated Specimens, %

Material	C	Mn	Si	P	Cu
Steel 45	0,49	0,56	0,27	Not deter.	—
Cast iron	3,13	0,65	3,33	0,145	—
Red copper	—	—	—	—	99,9

The decay rate of radioactive isotopes in cast iron specimens becomes negligible in 10-12 months no matter how long the specimens were exposed in the reactor. This conclusion may be extended as an approximation to other iron-carbon alloys containing no other alloying elements.

According to health physics rules for handling specimens exposed to a flux of 10^{16} neutrons/cm^2, it is safe to work with them across an entire day one month after the irradiation. Specimens exposed to a flux of 10^{17} neutrons/cm^2 may be handled an entire working day only after 5 months have elapsed since the exposure. The allowable handling time depends on the time of deactivation since the irradiation in the case of other specimens. For example, specimens exposed to fluxes of 10^{18}, 10^{19}, or 10^{20} neutrons/cm^2 may be handled for no more than 20 min, 5 min, and 0.7 min respectively out of the day even 6 months after they were withdrawn from the reactor. The dose rate measured one-half year after extraction from the reactor in the case of copper, cast iron, and steel specimens subjected to a flux of 10^{20} neutrons/cm^2 will not exceed the tolerable limit when a distance of 0.1 meter is maintained in the case of the copper specimen, 0.6 meter in the case of cast iron, and 1 meter in the case of steel.

Curves I to III may be stated in the form of the approximate formulas:

$$P_{\gamma\,(I)} = 20r^{-1.35}; \quad P_{\gamma\,(II)} = 350r^{-1.5};$$
$$P_{\gamma\,(III)} = 1.4 \cdot 10^4 r^{-2},$$

where P_γ is the γ-dose rate, in μr/sec; r is the distance from the source, in meters. At r = 0 these formulas become invalid.

For curves 1—4, similarly, these empirical formulas become valid:

$$P_{\gamma\,(1)} = 0.8t^{-0.6}; \quad P_{\gamma\,(2)} = 4.5t^{-1}; \quad P_{\gamma\,(3)} = 45t^{-0.6}; \quad P_{\gamma\,(4)} = 1000t^{-1.5},$$

where t is the time elapsed after exposure, in months. These formulas lose their validity at t = 0.

The $A = Bt^{-c}$ type equations show a certain regularity in the variation of coefficient B:

$$\frac{B_2}{B_1} = \frac{4.5}{0.8} \approx 5; \quad \frac{B_3}{B_1} \frac{45}{0.8} \approx 50 = 5 \cdot 10; \quad \frac{B_4}{B_1} = \frac{10^3}{0.8} \approx 10^3 = 5 \cdot 10 \cdot 20.$$

Taking advantage of this regularity and assigning the exponent c, a value from 0.6 to 1.5, we can tentatively find the slope of the specimens irradiated by more substantial integrated neutron fluxes.

The dose rate curve L for dose rate measured up to cast iron specimens one year after irradiation was determined is plotted as a function of neutron flux. The dose rate steps up sharply as irradiation time in increased. For specimens irradiated by fluxes of 10^{16}, 10^{17}, 10^{18}, 10^{19}, and 10^{20} neutrons/cm^2, the dose rate is respectively 0.45, $\approx$1.6, $\approx$8, 50, and 600 μr/sec. This curve fits the empirical formula

$$P_\gamma = 5 \cdot 10^{-15} \cdot n^{0.85},$$

where n is the neutron flux, in neutrons/cm^2.

In work with specimens of other dimensions, the dose rate read on the graph should be increased in proportion to the mass of the specimen; self-absorption in the source must be accounted for in dealing with larger specimen sizes.

TRACER ELEMENTS AID IN EVALUATING RADIOACTIVE
ANOMALIES IN ARID REGIONS

UDC 550.8:546.791)

V. M. Konstantinov

Geological prospecting work has shown that an impressive number of radioactive anomalies not spatially associated with uranium ore bodies in regions of arid climate has been found, in addition to anomalies in unconsolidated deposits overlying uranium ore bodies, in the course of prospecting by surface radiometric techniques. As our data show, ore anomalies in unconsolidated deposits can be distinguished from non-ore anomalies by the dispersion halos of tracer elements above ore veins.

Geochemical research was pursued in an area of low rolling topography and arid climate. Data from a local weather station over five spring and summer months in 1960 reported the amount of precipitation to be 200 mm, the average temperature 19.3°C. Most of the area investigated is covered by friable formations 1.5 to 2.0 meters thick, sometimes as thick as 10 meters. Five to 20 cm account for soils, 1.0 to 1.6 meter for talus deposits (gray loams and base rock debris) and 0.5 to 1.0 meter accounts for eluvial deposits (crumbled bedrock).

Uranium ore showings were discovered: quartz-carbonate veins containing, in addition to uraniferous minerals, galena, molybdenite, sphalerite, chalcopyrite, and in isolated instances cobalt, nickel, and bismuth minerals. Dispersion halos of uranium, lead, zinc, molybdenum, cobalt, and nickel formed around uraniferous ore bodies, halo widths being several times greater than the thickness of the ore bodies.

Trenches exposing radioactive anomalies were sampled and analyzed in detail in the study of the dispersion halos. Cores were sampled from the rims of trenches down to 1-2 meters, soil, talus waste, eluvia, and bedrock being cored separately. Each core sample weighed 250 to 300 g. Samples pulverized to 200 mesh and quartered for assay were digested for 30 min in a 2% solution of soda, after which "mobile" uranium was determined by luminescence techniques (analyzer: B. M. Eloev). Lead, zinc, cobalt, and miscellaneous metals were determined by a complete semi-quantitative spectral analysis (analyzer: E. V. Mozalevskaya). The most characteristic metal content in the particular rock facies (see table) was selected as the geochemical background.

Tracer elements were found to form dispersion halos around uranium mineralization veins in both bedrock and unconsolidated deposits. The uranium dispersion halo widths were 15 −20 times greater than the thickness of the ore veins. The uranium concentration in unconsolidated deposits over portions of most radioactive anomalies remained the same as in the primary halo, or decreased slightly (Fig. 1). In isolated cases the uranium concentration in the soils is slightly greater than uranium content in the primary dispersion halo, and drops to the background level in slide rocks.

Lead, zinc, and molybdenum form dispersion halos of width far exceeding the thickness of ore veins in unconsolidated deposits (see Fig. 1). In some sectors the width of lead dispersion halos in slide rock and in soils

Geochemical Background of the Elements*

Element	Sensitivity of method, %	Geochemical background, %
Uranium ("mobile" U)	0,00001	0,000018
Lead	0,001	0,001
Zinc	0,01	Traces (< 0,01)
Cobalt	0,001	0,001
Molybdenum	0,0003	Traces (< 0,0003)
Arsenic	0,01	0,01

* Data obtained from 260 analyses.

834

50 µr/h

30 µr/h

8 µr/h

Uranium

Lead

Zinc

Cobalt

Molybdenum

Vertical scale   1 0 1 2 3 m
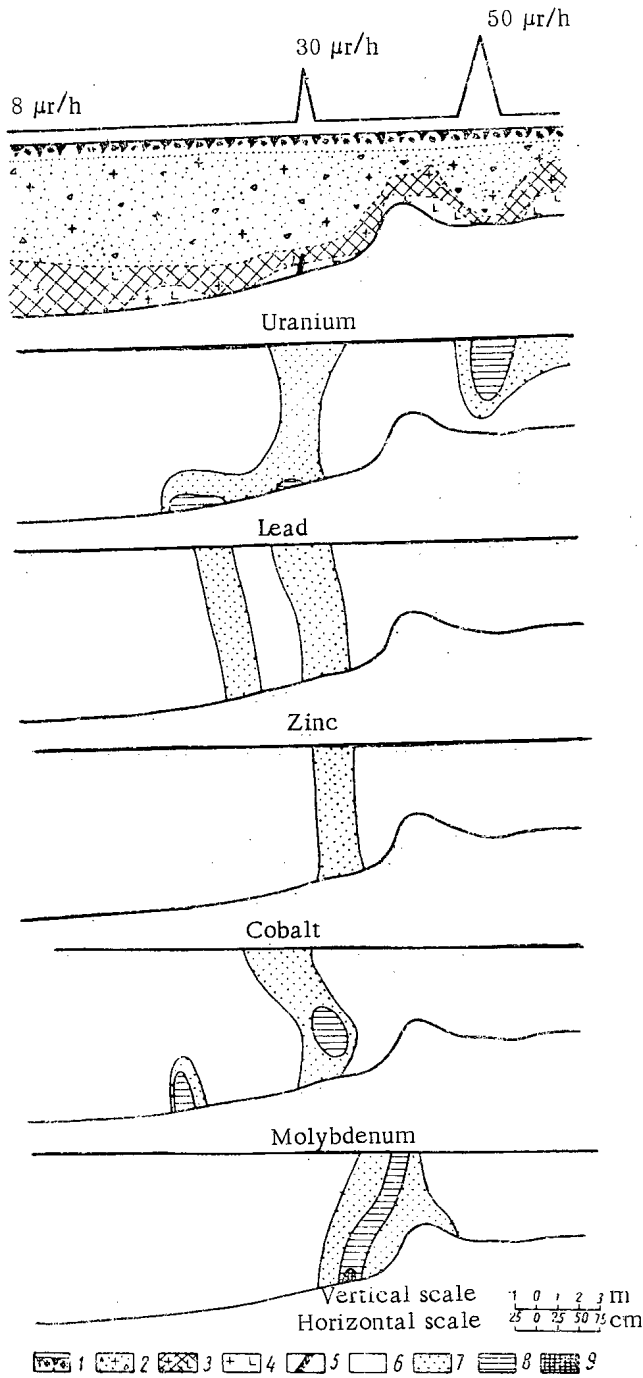Horizontal scale   25 0 25 50 75 cm

1 2 3 4 5 6 7 8 9

Fig. 1. Distribution of the chemical elements over an area featuring radioactive anomalies: 1) soil; 2) talus deposits; 3) eluvia; 4) granodiorites; 5) ore vein; content of the chemical elements in geochemical background (g.b.) units: 6) up to 3 g.b.; 7) 3 to 10 g.b.; 8) 10 to 30 g.b.; 9) 30 to 100 g.b.; —————— γ-activity curve.

tapers off abruptly. All three elements are present in the same amounts in unconsolidated deposits as they are in the primary halo, or possibly in slightly lower amounts.

Cobalt dispersion halos are usually slightly narrower than the dispersion halos of other elements. Cobalt content in unconsolidated deposits either remains the same as in the primary halo or rises slightly in eluvial formations (cf. Fig. 1).

In one of the cored trenches where the ore vein contains sizable amounts of galena and sphalerite in addition to uranium-bearing minerals, a distinct arsenic dispersion halo was found in the country rock and in unconsolidated deposits. Its width exceeded the thickness of the ore vein by 8-10 times. An abrupt widening of the dispersion halo accompanied by a slight drop in arsenic content is observed in the soil layer.

Dispersion halos of uranium, lead, zinc, cobalt, molybdenum, and arsenic, i.e., those chemical elements which also form endogenous dispersion halos, are thus observed in areas containing radioactive anomalies in unconsolidated deposits. Since the chemical properties and movability of these elements in areas of arid climate are very different in a hypergenesis zone, that their dispersion halos coincide in soils indicates that little evacuation has taken place, and implies that weathering was the main causal agent.

The top layers of cross sections through unconsolidated deposits (soil, talus drifts) in areas around non-ore radioactive anomalies are distinguished by heightened uranium concentrations (Fig. 1, Fig. 2) in most instances. Note that peak uranium content is confined to the soil layer and occasionally surpasses the uranium content in ore anomalies. Moreover, an insignificant quantity of lead is found in non-ore anomaly areas. The enhanced lead content in the soil layer is also observed on occasion in nonradioactive anomalies.

Some of the none-ore radioactive anomalies are slightly apart from the ore bodies. But in most instances there was no association with primary uranium mineralization observed. Clearly, non-ore radioactive anomalies are formed by migration and precipitation of the uranium from the soil water. Either uranium-mineralized ore veins or rock species not containing unusually large amounts of uranium could be the source of this uranium.

Accordingly, if areas featuring ore radioactive anomalies are characterized by the existence of dispersion halos of uranium, lead, zinc, cobalt, molybdenum, arsenic in unconsolidated deposits, i.e., dispersion halos of those elements which form endogenous dispersion halos around uraniferous ore bodies, then areas featuring non-ore anomalies reveal increased amounts of uranium

835
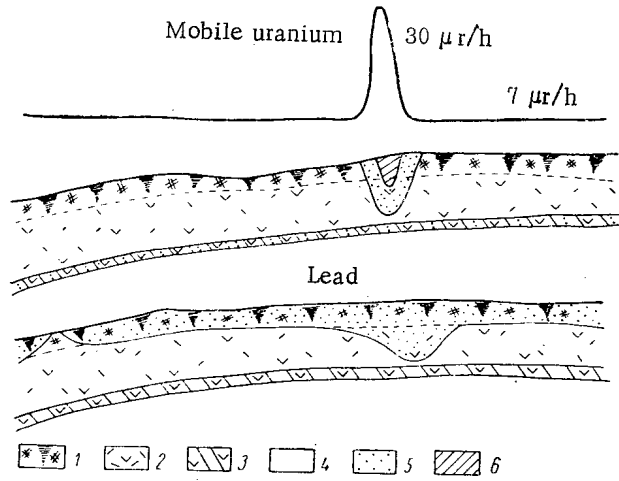
Fig. 2. Distribution of mobile uranium and lead over an area
featuring non-ore anomalies: 1) soil; 2) talus deposits; 3) bed-
rock. Content of element in geochemical background (g.b.)
units: 4) up to 3 g.b.; 4) 3 to 10 g.b.; 6) 10 to 30 g.b.;
———————— —— γ -activity curve.

alone, or sometimes lead. In an arid climate area, determination of elements acting as indicators of uranium min-
eralization may be used as a diagnostic tool for both ore associated and non-ore radioactive anomalies.

836

CONTAMINATION OF FLORA BY RADIOACTIVE FALLOUT

(UDC 551.577.7)

O. G. Mironov

Radioactive contaminants of the environment tend to accumulate in plants by the uptake of isotopes both through the soil and through falling directly on the plants [1]. Radioactive fallout is capable of adhering firmly to the surfaces of plants [2]. The artificial radioactivity consists of both accumulated and surface contamination. The relationship between the radioactive contamination level in plants and intensity of atmospheric fallout is a point of interest.

The aerial parts of plants were collected from a plot of untilled soil one meter square, in an experiment carried out in late May 1963 in the mid-European belt of the USSR, to probe into this relationship. In terms of weight, 13 species accounted for 97% of all the grasses (240 g), as shown in the table). The same species picture more or less prevailed in other lots of soil tested. Daily measurements of fallout rate by the cuvette method lasted from January through May, 1963. The grasses and collected fallout were ashed at about 500°C before radiometric, radiochemical, and γ-spectrometric measurements were taken. Sr^{90} was found from its daughter Y^{90} by tributylphosphate extraction of the latter [3]. The γ-ray spectra were recorded with an AI-100 pulse analyzer. V. P. Parchevskii was of great assistance in the γ-ray spectrometry work, and we extend him our thanks. Radiometric analyses were
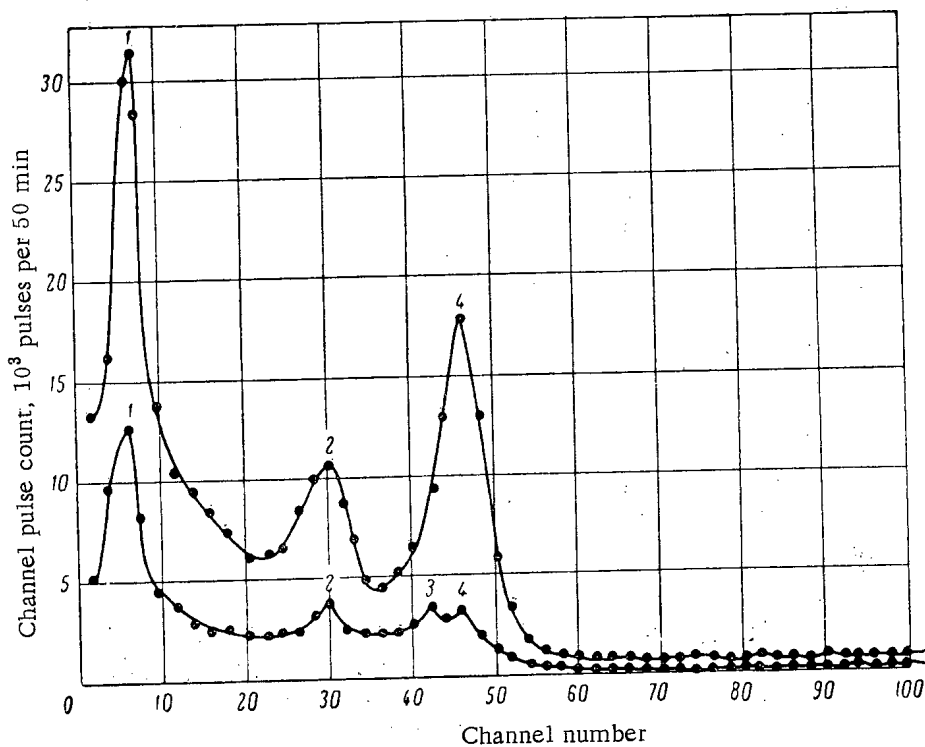
Fig. 1. γ-Emission spectrogram of radioactive fallout samples, January-May, 1963: 1) $Ce^{144}-Pr^{144}$ photopeak; 2) $Ru^{103+106}$ photopeak; 3) $Cs^{137}-Be^{137}$ photopeak; 4) $Zr^{95}-Nb^{95}$.

837

Natural and Artificially Induced Beta-Activity in Some Grasses

Plant species	Total specific activity, nCi/kg	Specific activity of K^{40}, nCi/kg	Fraction artificial radioactivity, %
Purple deadnettle (Lamium purpureum)	15.2	5.3	65.0
Stinging nettle (Urtica urens)	58.0	10.1	82.6
Quack grass (Agropyrum repens)	39.0	9.0	77.0
Ripple-seed plantain (Plantage major)	19.0	4.2	78.0
Goosefoot (Potentilla anserina)	22.0	3.8	82.7
Carrot (Daucus)	17.1	6.5	62.0
Common yarrow (Achillea millefolium)	13.0	3.9	70.0
Coltsfoot (Tussilago farfora)	22.4	6.2	72.3
Meadow clover (Trifolium pratense)	24.0	6.5	73.0
Mugwort wormwood (Artemisia vulgaris)	28.1	3.9	73.0
Common wormwood (Artemisia absinthium)	10.0	3.0	70.0
Great burdock (Arctium lappa)	18.0	6.7	62.8
Common dandelion (Taraxacum officinale)	13.5	6.5	52.0

carried out on a "Floks" arrangement using an end-window counter in a lead-shielded enclosure. Since the natural activity of the plants is due principally to K^{40}, potassium present in the plant ash was determined by flame photometry. Results of total β-activity measurements of the dominating grass species are tabulated.

As we see from the tabulated data, the artificial activity exceeded the natural activity, comprising about 70% of the total β-activity. The activity of vegetation covering a square kilometer was arrived at on the basis of the weight of plants on a square meter of soil (240 g), activity by species, and weight ratios of species. The total
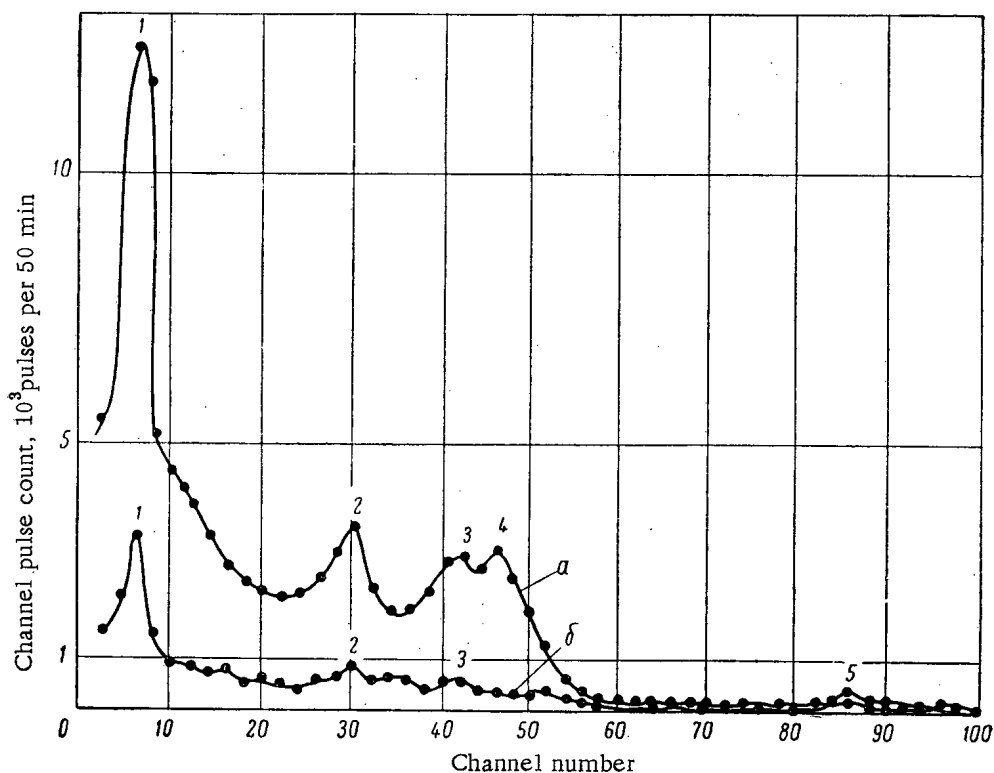
Fig. 2. Comparison of γ-ray spectrograms of fallout samples (a) and plants (b). Legend: 1—4 same as in Fig. 1; 5) K^{40} photopeak.

838

β-activity was 5.5 mCi, artificially induced activity was 3.9 mCi. Fallout density by the end of May was ≈ 200 mCi/km^2 in terms of total β-activity (decay taken into account). Contamination of environmental flora was thus found to be about 2% of the total fallout activity.

The analysis revealed about 2.0 mCi/km^2 Sr^{90} in the space of 5 months. Sr^{90} had been taken up in plants in amounts of 48.5 pCi/kg, or 11.5 mCi/km^2, i.e., about 0.5% of the total fallout Sr^{90} had been taken up.

Results of γ-ray spectroscopic studies of fallout and vegetation are shown in Figs. 1 and 2. Figure 1 shows a spectrogram of fallout collected from January through May, 1963. The analysis was performed in August, 1963 (top curve) and 5.5 months later (bottom curve). Three photopeaks whose energies correspond to the γ-emission energies of Ce$^{144+141}$–Pr^{144}, Ru$^{103+108}$–Rh^{106}, Zr^{95}–Nb^{95} appear on the top spectrum. The second spectrum shows a decrease in photopeak height and area due to radioactive decay. The photopeak for Cs^{137}–Ba^{137} energy had been masked earlier by the Zr^{95}–Nb^{95} photopeak. Comparative γ-ray spectroscopic data on fallout and vegetation appear in Fig. 2.

When we compare spectrograms of fallout and vegetation as measured in January 1964 we see the identical nature of their radioactive contamination.

The results still do not permit sweeping generalizations, but the available data do imply that the activity of the plants studied in 1963 was 70% due to artificially radioactive contaminants; about 2% of the total activity of precipitated fallout radioisotopes and about 0.5% of the fallout-derived Sr^{90} were retained on the plants.

LITERATURE CITED

1. I. V. Gulyakin and E. V. Yudintseva, Radioactive fission products present in soil and plants. Moscow State Atom Press, [in Russian] (1962).
2. R. Menzel et al., Science, 142, 3592 (1963).
3. A. K. Lavrukhina, T. V. Malysheva, and F. I. Pavlotskaya, Radiochemical analysis. Moscow, USSR Academy of Sciences Press [in Russian] (1963).

SCIENCE AND ENGINEERING NEWS

NUCLEAR ELECTRIC POWER STATIONS IN ITALY

In September 1964 a Soviet delegation headed by A. M. Petros'yanets, on invitation of the National Nuclear Energy Committee of Italy, visited nuclear electric power generating stations and nuclear research centers in that country.

The delegation visited nuclear power stations at Garigliano (160 MW), Latina (210 MW), Trino-Vercelli (272 MW), the Casaccia nuclear research center, the Frascati nuclear research institute. The delegation was also afforded the opportunity to familiarize itself with the structure and development program of the Italian National Nuclear Energy Committee (CNEN).

The Garigliano Power Station

This electric power station is sited at the mouth of the Garigliano river in Caserta province. A boiling-water reactor operates in combination with a turbine in saturated steam regime of the power station.

The nuclear instrumentation and equipment of the power station was made under contract with General Electric Co., and the remaining equipment was made under contract with Italian firms. Construction work on the power station was begun in 1960, the reactor went critical in June, 1963, and has been in operation since January, 1964.

The Garigliano nuclear power station is an improved version of the Dresden BWR power station in the USA. The principal improvements are: a) biological shielding of the power station is reduced to the least in size, thereby, reducing total power station costs; b) shielding of concrete blocks that can be dismantled and placed around the reactor to ensure the required radiation safety of the personnel; c) boron steel (2 wgt. % B) control rods are replaced by rods make of tubes with boron carbide powder; d) fission chambers are placed in the core to measure the power distribution.

The reactor is designed for easy control of the power plant during reactor transients. Even though the turbine uses the active primary-loop steam, plant personnel are free to work for a specified limited period in the machinery room. The burnout margin is 3 as against the design figure of 1.7, so that the reactor power level can be increased beyond original expectations. The power station is fairly compact, as a result of the sectionalized shielding blocks, the installation of local cranes and materials handling equipment, the placement of pure-water tanks outside the containment shell, and other features. An emergency water supply in the cooling condenser allows the reactor to cool down in 8 h in the event of a complete power failure. Equipment is checked out on models and special test rigs to ensure optimum in-pile performance of the equipment. A reloading system with a gripping rod is simple in design and easy to operate, and compact. Fuel is reloaded under water. The appreciable weight of the fuel assemblies (300 to 400 kg) facilitates reloading in a comparatively short time. The reactor and steam generator vessels are lined with stainless steel. Tubesheets in the steam generators are also stainless-steel-lined. Pretensioned bolts hold tubular seals in place to provide leaktight joints.

Rooms in the power station are planned and outfitted in a simple and economical manner. Floor, ceiling, and wall work is of excellent quality.

The large number of miniaturized transitorized and printed-circuit instruments of Italian manufacture in use at the power station is remarkable. In many instances the instruments are incorporated directly in memory circuits. Control panels do not take up much space and are easy to handle and service.

The power station performance is excellent. It operates on full power for most of the time. Operational shutdowns have not been due to any malfunctions in the basic reactor equipment.

Tests confirmed the large burnout margin permitting a 50% rise in reactor power output (i.e., a 75 MW increase). The power increase was achieved by raising the steam output of the reactor. Steam content per volume in

the most heavily stressed channel reached 70−75% instead of 61%, and averaged 23 to 32% over the entire reactor. The increased reactor power level prompted the decision to add another turbine to the station.

The power station staff numbers 110. Electric power production costs are 9.5 lire per kWh, while the regional cost of electric power produced by power plants burning fossil fuel is 5 to 6 lire per kWh.

The Enrico Fermi Power Station in Trino-Vercellese

This power station, with a water-cooled water-moderated reactor of 272 MW rating was built in Northern Italy 120 km west of Milano in the Trino-Vercellese province, on the River Po. The reactor of the Enrico Fermi Station went critical in late July, 1964. The power station is viewed by Italian specialists as the most advanced of the entire line of power stations built around water-cooled water-moderated reactors. Compared to the counterpart Yankee Power Station in the USA, the Enrico Fermi Station is almost twice the size of Yankee, as a result of some important improvements, principally in the reactor core. These improvements include:

a) the use of chemical reactor control measures;

b) three concentric uranium enrichment zones in the core. Uranium enrichment is 2.7% in the interior zone, 3.1% in the intermediate zone, and 3.9% in the exterior zone:

c) a combination of absorber and fissile materials in control rods.

The Italian SELNI firm has purchased a reactor and major primary-loop process equipment from the Westinghouse Corp. The total cost of the power station is $45 \cdot 10^9$ lire. This total includes the cost of fuel assembly fabrication, some $1.8 \cdot 10^9$ lire. The cost of the uranium is not figured in, since the USA has extended several years nuclear fuel purchase credit to Italy. The specific kilowatt cost of the power station comes to ≈175 thousand lire (257 dollars per kW).

For an installed power utilization factor of 0.7, the cost of electric power with plutonium and U^{235} buyback credit figured in, will be 7.5 to 8 lire per kWh, i.e., about one and a half times more expensive than the cost of electric power produced by regional fossil-fuel power stations.

The power station staff includes 30 shift workers, and 100 maintenance and administrative personnel. All the primary-loop equipment is designed for 843 MW(th) output. The coolant is ordinary purified water pressurized to 142 atmos. The water temperature is 266°C at the reactor entrance and 297°C at the exit.

All of the equipment and piping of the primary loop is placed inside the cylindrical containment shell. The shell is 30.5 meters in diameter, stands 58 meters high, and has wall thickness of 16 mm for the top bowl and 38 mm elsewhere. The containment sheel is designed to take a pressure of 2.3 atmos. Water spargers are installed inside the containment shell to reduce the steam pressure in the event of an accident.

Steam generators and pressurizers are located around the reactor with no special shielding. If and when required, they can be surrounded with removable concrete shielding 45 cm thick. Steam generators, pumps, piping and fittings of the primary loop are all in a single enclosure. The equipment is suspended, with pumps resting on spring suspensions. There are no expansion bends in the primary-loop pipework, given the slight difference in the temperature of the "cold" and "hot" lines. The piping layout and the lightweight transitions allow easy access to all of the equipment.

The Latina Power Station

This is an electric power station built near Latina, only 700 meters from the seacoast. A graphite-moderated gas-cooled reactor has been installed in the power station, and is a further development of the British Berkeley and Bradwell reactors. Most of the power station equipment was developed and manufactured by British industry.

Three turbogenerators each of 70 MW rating and two turbogenerators each of 70 MW rating and two turbogenerators rated at 12 MW have been built in the power station. Gas enters the reactor via six circulating loops. Gas blowers are capable of smooth change in rpm from 550 to 2500, and are provided with an oil seal.

Spadework on the power station started in 1959, and construction was completed in 1963. Startup operations commenced in November 1962 and had been completed in March 1964.

The gas temperature at the reactor exit was measured in 300 channels (10%). Temperatures were measured and recorded by computer. The temperature of the graphite did not surpass 800°C at rated power level. The reactor power rise from zero power to the monitored level takes 30 h. Gas leaks through the gas blower seals are minimal and remain below 90 kg per day; about 7 tons per day are lost at other points. Most of the gas lost is by leakage through pipe fittings, flanged joints, and other unsound spots, when the refueling machine is washed down, and in the fuel element burst-monitoring system. Soundness of the fuel elements is monitored in all reactor channels by automatic switching of a group of channels to the monitoring instrument. Rubidium and cesium activity deposited on the surface of a moving cable is monitored. The maximum fuel element temperature (450°C) makes for an exit gas temperature of 395°C. At the present time, the reactor staff is looking into the possibility of raising the fuel element temperature by another 38°, so as to boost station efficiency by 30%.

The net cost of electric power for a fairly high degree of utilization of installed power station output (7000 h) is 7.79 lire/kWh, as against a cost of 5 to 6 lire per kWh at regional fossil-fuel power generating stations.

The Latina Power Station contrasts with the Agrigliano and Enrico Fermi nuclear power stations in its much larger size, cumbersome ancillary equipment, and large servicing staff (290 persons).

From what we learned about the various nuclear power stations in Italy, it is clear that Italian specialists evinced a creative approach to power station developments proposed by the USA and by Britain, and that some of the Italian improvements in the construction and operation phases have improved station performance.

The Casaccia Nuclear Research Center

The nuclear research center at Casaccia is situated 24 km from Rome; it belongs to the National Nuclear Energy Commission (CNEN). The center was built in July 1960 and in a short time rose to the status of a major engineering and experimental center. A staff of one thousand was on duty at the center as of September 1964.

The Casaccia center is made up of 9 sectors, 7 of them devoted to scientific research projects: a reactor section (in charge of the TRIGA-II reactor, the applied nuclear physics laboratory, the reactor department, and the linear accelerator); a laboratory sector; an electronics sector; a metallurgy sector (with hot caves, laboratories fitted for work in metallurgy, industrial chemistry, and ceramics technology); a reprocessing study section (with facilities for pilot reprocessing of radioactive and ordinary wastes); a section on mineral geology and mining; a biological research sector (with laboratories facilitating research on animals and crop plants; also responsible for health physics and radiation safety monitoring).

The laboratory sector dominates the center. This sector is credited with the development of the electronic analog simulator of a nuclear power generating station, electronic manipulator gear, standard equipment and instrumentation for nuclear reactors. It has a zero-power experimental reactor with organic Santowax coolant, an experimental room for studying interactions between materials and organic liquids, and facilities for investigating heat-transfer performance of fuel elements. A critical assembly using organic moderator and ROSPO coolant has been built, as part of the investigation of fuel elements for the experimental organic-cooled organic-moderated PRO reactor. Test loop experiments designed for the PRO reactor are also underway.

Santowax and ortho-terphenyl are being given close attention as promising coolants.

Italian specialists are of the view that organic-cooled organic-moderated reactors hold forth great promise both for low-output nuclear power stations and for nuclear heat power plants and water desalinization plants.

Frascati Research Center

The Frascati Center is under the CNEN and is located in the town of Frascati 25 miles out of Rome. A staff or 270 or so serves three laboratories at the center: a synchrotron laboratory, a storage-ring accelerator laboratory, and a plasma research laboratory.

The 1100 MeV electron synchrotron has been in operation since 1959. The intensity of the internal beam is $5 \cdot 10^9$ electrons per pulse at a pulse repetition rate of 20 cps. Pulse width is 3—4 msec. A 3 MeV van der Graff accelerator with a beam current of 0.1 A/pulse functions as the electron injector. Research on four γ-radiation beams is now in progress on the synchrotron.

As yet, the Frascati center has no storage ring in actual operation. A small storage ring designed earlier for about 200 MeV electron energy has been turned over to France; now in the laboratory at Orsay, it stores 10^7 electrons at a beam cross section of $1 \cdot 0.08$ mm.

The large ADONE electron-positron storage ring is now being built at Frascati, data on this machine being:

Maximum particle energy	1.5 GeV
Bean intensity	$2 \cdot 10^{11}$ particles
Particle lifetime	1 to 1.5 h
Number of straight sections for studying beam interactions	4
Number of interactions per hour on straight section, for effective interaction cross section 10^{-32} cm^2	10
Magnetic field at injection	2.4 kG
Magnetic field when maximum energy is attained	10 kG
Average ring radius	16.2 meters
Weight of iron	322 tons
Weight of copper	31 tons
Vacuum chamber cross section	$6 \cdot 22$ cm
Vacuum	10^{-9} mm Hg

A linear accelerator purchased in the USA is proposed as the electron and positron injector.

A team of physicists engaged in plasma research at the center is still small. Their experimental equipment is quite limited. They conduct their research in two directions. One group is studying oscillations and waves in a cold plasma. Oscillations in ordinary gas discharges are being studied, as well as in cesium plasma and potassium plasma. The cesium plasma temperature is 2600°K, the density 10^{10} to 10^{11} cm^{-3}.

The second direction involves investigation of a high-temperature high-density plasma. Here, some interesting results were obtained by optical probing of a plasma with ruby lasers. Interference patterns of plasma density in a thetatron, schlieren photography of a plasma, and studies of low-angle (3°) scattering of laser emission in a plasma, are current research projects. Light scattering has been successfully observed in the last experiment not on individual electrons but on inhomogeneities of the space charge on the scale of the Debye screening radius. Both the electron temperature and the plasma ion temperature can be ascertained from studies of the scattered light spectrum.

V. V. Stekol'nikov, A. N. Grigor'yants,
and S. D. Fanchenko

843

A TRIP TO ENGLAND

O. G. Kazachkovskii

Upon invitation of the United Kingdom Atomic Energy Authority and the Central Power Authority, a group of Soviet specialists who had attended the September 1964 III Geneva Conference on the Peaceful Uses of Atomic Energy visited Britain later that month, and were brought up to date with the Berkeley power station and associated nucleonics laboratory, the Oldbury power station now under construction, the Harwell atomic research center, the Windscale complex, and the Winfrith atomic center.

Descriptions of the centers and facilities visited by this delegation have been published on various occasions elsewhere. In this article, therefore, we confine our remarks to certain details, research findings, and matters of technique of more general interest. It would be unfair to omit mention of the cordial reception accorded to our delegation.

Nuclear Power Laboratory at Berkeley

This laboratory consists of two departments: one "cold" section and one "hot" one is responsible for studying irradiation effects of magnox type fuel elements, graphite, and structural materials.

Crack formation in magnox fuel element cladding (at operating temperatures on the order of 450°C) is accompanied by intense oxidation of the uranium by carbon dioxide gas; the crack propagates speedily in the process. Since it takes a certain amount of time to record the escape of radioactivity into the loop, there is a danger of appreciable radioactivity spreading through the loop before it can be counteracted. Searches for a suitable intermediate cladding layer have spotlighted aluminum as the best added-safety material. The intermediate cladding sheath designed to take operating temperatures in the 450°—500°C range is an intermetallic uranium-aluminum compound in a $\approx 50\,\mu$ thick layer.

Radiation-induced deformation of graphite, considered a linear function of exposure dose, is being investigated. Some rather straightforward relations using empirical coefficients have been derived for estimating the expected deformation of graphite over the entire range of reactor operating conditions. The formulas take anisotropy of the specimens into account. Deformation allowances of 0.5% over 30 years time are arrived at from the calculations.

Results of research on stress relaxation reveal stresses on the order of 1 to 3 kg/mm^2 in steel undergoing complete relaxation at an integrated neutron flux on the order of $2 \cdot 10^{19}$ neutrons/cm^2. This effect is temperature-invariant, as has been demonstrated.

Hot cave equipment and facilities include the following. The inner surface of the caves is lined with epoxy coating. Most of the viewing windows are of zinc bromide. The windows are lined with ordinary iron, epoxy-painted. Front and back glasses are flange-sealed with epoxy-base resin. Manipulator passages are hermetically closed off with corrugated plastic sleeves, leading to a marked reduction in ventilation power required. Overhaul work is also greatly aided, since the sleeves simultaneously protect the manipulators from radioactive contaminants. Polyethylene film coating the surfaces exposed to contamination may be removed by the manipulator for disposal. Fine radioactive dust and powders are vitrified in a special chamber heated to 750°C in an electric furnace. Caves designed for high activity levels are fitted with access holes on top for removing equipment to be replaced or repaired. Asbestos board air filters placed directly inside the cave are removed in the same manner. Mirrors on the back walls of the caves provide an excellent survey of the entire work space; manipulators are designed to cover the entire cave area within their range. Floors in the work zone are laid with concrete and coated with epoxy resin.

In the cold section of the laboratory, research work on structural materials (for reactor pressure vessels), heat transfer (to gases), reactor physics, and dosimetry dominates the scene.

A N_2O vacuum leak detector is used, and has proven both cheaper and simpler to operate. Appearance of N_2O is recorded by an infrared spectrometer.

The Berkeley Nuclear Power Station

Two reactors have been built to serve this power generating station, each with a thermal power rating of 558 MW and an electric output of 137.5 MW. The CO_2 temperature at the reactor exit is 345°C. The total cost is 51.1 million pounds sterling. The electric power costs (at 80% load) are 1.2 penny per kWh. The power station staff numbers 500; of these 100 are engineering and technical personnel. Fifty and 7 employees respectively work each of the 5 shifts.

The actual load factor of the nuclear power station was about 40% across the past year. This is due to prolonged shutdowns caused by malfunctioning of turbine blading. The design fuel burnup is 3000 MW day/ton (and to data 1300 MW day/ton has been achieved). Refueling machines designed for on-power reloading are cumbersome and intricate, and breakdowns are frequent. Eight hundred of the 3700 reactor channels were reloaded in 1.5 year. Reloading operations were carried out with the reactor shut down. The power station personnel expressed some doubts about the feasibility of on-power refueling.

Coolant activity is low. The dose level at 100% power near the top of the steam generator is 25 to 30 $\mu r/sec$, and 5 to 6 $\mu r/sec$, near the bottom. The coolant purification system (primarily designed for moisture removal) operates on the cold-trap principle, using $\approx 5\%$ of the total flowrate.

Rotary bellows are employed to compensate for thermal expansion in the pipework. An expansion piece system with axis through the center of the bellows allows the piping to bend only, without expanding. This eliminates any need for special measures to counteract pressure drops inside the piping.

The Oldbury Nuclear Power Station

This power station is presently under construction. It will have two reactors each of 834 MW thermal output and 280 MW electrical output. Startup is scheduled for 1966. The CO_2 temperature at the exit will be 412°C. A reinforced concrete containment shell (using prestressed concrete) enclosing the reactor and the steam generators is a special feature. Special measures are for overhaul of equipment inside the containment enclosure are not provided. The power station total cost is estimated at 63.8 million pounds sterling. Power costs are to be ≈ 0.7 penny per KWh.

The Harwell Atomic Research Center

No power reactor studies are in progress at Harwell these days. Instead, the basic research trends are in nuclear physics, solid state physics, thermonuclear reactions, and radiochemistry.

The operational technology and major designs of hot caves are the same as in Berkeley.

Windscale

At Windscale, the delegation was shown the AGR reactor the Calder Hall power station, a hot metal physics laboratory, and, very fleetingly, a new plant for chemical reprocessing of spent fuel.

The AGR reactor has an output of 100,000 kW (33,000 kW electric). CO_2 temperature at the reactor exit is 575°C; the pressure is 18 atmos. Fuel elements are (2.5% enriched) uranium dioxide in stainless steel cladding. The reactor and steam generators are enclosed in a steel sphere with a pressuretight lock device. This lock is not being used at present and is always in the "open" state. A decision has been reached to discontinue the building of steel containment spheres at industrial nuclear power stations. Continued use of prestressed concrete is quite possible, nevertheless.

The reactors in the Calder Hall power station operate reliably in power transients (electric power output of 190 MW rather than the design level of 180 MW). Sufficient steam is made available for process needs. There is no automatic control system for the reactor. The power level is maintained by manual controls (an operator shifts the control rod about once every 10 min on the average). A single operator works at a common control panel serving reactor and turbine.

Fuel elements of the Calder Hall read reactors and the AGR reactor are studied in the hot metal physics laboratory. Maximum fuel burnup in the Calder Hall station reactors is 5440 MW day/ton, with figures of 3020 for average burnup and 1105 for minimum burnup. Uranium density is reduced an average of 1% per 1000 MW day/ton at these burnup levels. The temperature dependence of swelling reaches a peak at 400°C. The delegation was demonstrated a polished section of one of the fuel elements after a burnup of ≈ 7000 MW day/ton. Swelling to around 20% with conspicuous porosity was noted in the peripheral annular layer. The interior of the fuel element revealed no apparent porosity. The sharp boundary between the porous and compact regions was characteristic.

Signs of interaction between CO_2 and the fuel element cladding are evident in some of the AGR-loaded fuel elements demonstrated. It is interesting that one fuel element with a hole deliberately made through the cladding was placed in the AGR reactor. No untoward consequences were reported. Defects (pores and spalling) were observed in some fuel elements on the surface of uranium oxide pellets. No post-irradiation changes of any nature were observed in the cladding or on the pellets themselves in the vicinity of these defects.

Improved equipment is in use at the new chemical plant, and planning has been streamlined. Plant output will handle the needs of all magnox-fuel reactors in operation, under construction, or now being planned (with total ratings of 5000 MW).

The Winfrith Nuclear Research Center

Research on the physics and technology of promising power reactors is in progress at this comparatively new scientific research center. There is a large department for the theoretical and experimental engineering study of fast reactors. Experiments are conducted on the zero-power ZEBRA reactor, which simulates the cores of full-power reactors.

Clusters of square cross section fuel assemblies are used. Slab pellets of various materials are assembled into fuel elements of specified composition with the aid of a special programmed automatically operated machine. Plutonium pellets are employed as well as uranium pellets. The plutonium is clad in double-welded stainless steel.

Research on the physics of plutonium applications in thermal reactors (using heavy water or graphite moderator) is carried on in another physics department. Here, experiments are performed on two exponential graphite assemblies, one exponential fuel cluster triggered from a pile, and a heavy-water critical assembly. This research is mostly completed; it is now felt that the physics of thermal reactors burning plutonium fuel is pretty much cleared up at present. But there are still problems to be tackled in achieving economic utilization of plutonium fuel in thermal reactors.

The heat transfer department is carrying out full-scale model tests of fuel elements on test stands, and has studied the effect of finned structures on surface heat transfer. Finning was found to double the amount of heat emitted, in their experiments.

Final tests and adjustments have been carried out on the DRAGON reactor. This 20 MW reactor uses graphite-clad fuel elements cooled by helium under 20 atmos pressure. Loop tests indicate loss of $\approx 10^{-4}\%$ of the gas into the coolant. The helium loop is pressuretight. There are no rubbing packings at all in the loop. Estimates indicate helium leakage at about 0.7% annually, and the reactor itself is included with the primary loop in a pressuretight enclosure.

Plans call for discontinuing the building of magnox-fueled reactors in Britain after 1968, since it is felt that by that time their economic advantages will be obsolete (considering the large size, low fuel burnup, low efficiency). No better choice for the succeeding stage of nuclear power development has been decided upon as yet, however. The rivals furthest out in front are the improved gas-cooled graphite-moderated AGR type and a water-cooled water-moderated reactor type of American design. A heavy water-moderated reactor cooled by ordinary water is being looked at with favor. Research is being pursued in all these directions. At the same time, work on fast reactors is continuing at a fast pace; over 30% of the personnel at research centers and engineering offices of the UKAEC are engaged in this work.

A decision on the construction of a power station in Britain to be built around a 250 MW(e) fast reactor is expected in the Spring of 1965.

STANDARDIZATION OF NUCLEONIC INSTRUMENTATION*

J. Auzout

There is hardly any need at this stage to spend time proving the advantages of standardization as a principal factor in industrial development, in increased interchange between nations contributing to progress in all fields.

Electrical engineers were the first to attempt to solve this major problem on a world scale, setting up the Commission Electrotechnique Internationale (CEI) back in 1904 to deal with standardization problems affecting electrical engineering.

As engineering developed, specialized technical committees were set up within the framework of this organization to consider a strictly defined area of problems. At present there exist 60-odd such committees whose doors are open to all countries interested in participation.

Within the technical committees, problems relating to standardization are usually referred to experts combined into working teams which develop recommendations and drafts on which various countries are free to express their opinions. These drafts, after some appropriate corrections, take the form of international recommendations.

In this way, the Commission Electrotechnique Internationale constitutes an organization encompassing a wide range of problems including topics in the field of nuclear science and engineering, which have recently been assigned to a special technical committee, Technical Committee 45. A brief rundown on the activities of this committee follows.

Activities of Technical Committee 45

The complete official appelation of Technical Committee 45 reads: "Technical Committee No. 45: Electrical measuring apparatus used in connection with ionizing radiations." The committee deals principally with electronic equipment. The general feeling is that, in the field of pure electronics, an instrument becomes almost obsolete in 5 years. In nuclear electronics, this refers moreover to equipment used in a completely new field, where the overwhelming majority of instruments are as a rule still close to experimental specimens, and this accounts for the short lifetime of a particular instrument.

For standardizing these constantly evolving instruments, there is a priority need for competent experts, not simply on a national plane, where specialists are involved with a multiplicity of problems in all engineering trends and specialities at early stages in research and development. It is a well known fact that any country desirous of engaging in nuclear research faces the primary task of assembling a corps of specialists.

Uniting a group of specialists on an international plane enables each country to assign only a part of the total number of required specialists for the successful completion of a major project. Further, this is the only possible way of utilizing the accumulated experience not to be found in any one particular country.

This type of contacts on standardization problems indirectly contributes to progress in scientific research as a whole.

Another major problem is to agree upon a method of standardization. When we bear in mind that nucleonic instrumentation is a constantly evolving field of engineering, and when we consider the limited number of available specialists in that field, we realize the unfeasibility of keeping those specialists occupied with problems that hazard rapid obsolescence. We, therefore, have to concentrate our efforts on the solution of the most important problems,

---

* Article received from France, from the President of Technical Committee 45 of the Commission Electrotechnique Internationale, J. Auzout.

847

e.g., development of instrument design principles for types of instrument showing promise, or the solution of certain problems not related to instrument design procedures. At the same time, problems of too wide a scope with component parts of unequal stability are to be avoided, and preference should be given to standardization problems of more stable interest.

A further requirement in standardization work is to start work on a project as soon as possible and to complete it in as short a time as possible.

The first 4 working teams were constituted on the basis of these considerations at the first plenary session of Technical Committee 45 at New Delhi in 1960. Three other groups took form during the next session in 1961 at Rouen. An eigth team was set up at Venice in 1963, and finally a ninth team at Geneva in 1964. All these groups were assigned problems by no means identical: there are "vertical" teams dealing with very specific categories of equipment, other groups structured "horizontally" dealing with problems of a general nature of interest to teams of the "vertical" type. We are, thus clearly dealing with a quite complicated functioning plan, since mixed groups (e.g. teams 3 and 9) are assigned work which could be classified either way.

The working teams are active bodies bearing the responsibility of keeping up to data with and contributing to the evolution of problems. On that basis, a round of questions occupying the attention of several working teams (team 3, for example) was modified, and team 4 was converted to a subcommittee which in turn set up provisional working teams under itself. Further, Technical Committee 45 is connected in its activities both with other technical committees in the CEI framework, and with outside organizations of similar purpose and nature.

Résumé of Activities

The publication of CEI code 181 entitled "List of electrical measuring equipment used in connection with ionizing radiations" in less than three years from the time the project was initiated can be viewed as a great accomplishment. This publication, containing almost 200 terms and definitions of equipment, is first and foremost a document required by the Technical Committee 45 as a whole in its work.
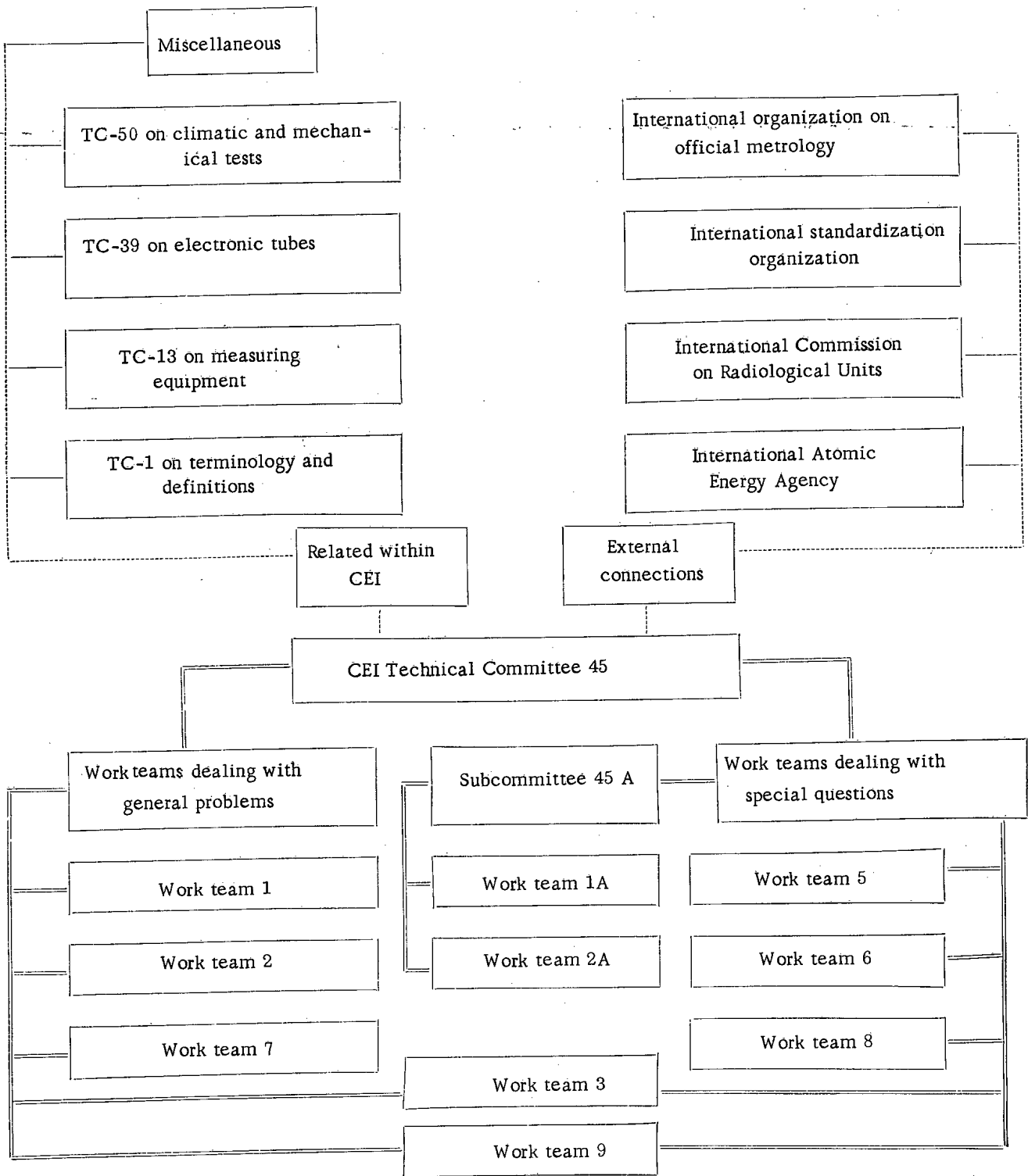
But interest in this document is by no means limited to TC-45 people. Since this document is also invaluable to other technical committees of the CEI, its publication and distribution in the various countries will necessarily make it a valuable tool in the hands of both developers and users. For the former, publication 181 will provide a common language in a field where the rapidity with which instruments evolve has left a welter of confusion. Their relationship to users and to organizations of closely allied fields will be immeasurably improved. For the latter, which to an increasing degree includes the private user as well as governmental institutions concerned with nuclear problems (scientific research institutes, universities, etc.), publication 181 cannot fail to become a source of invaluable information. Finally, this document will be highly useful for educational purposes, for translators and interpreters at international conferences, and for any persons whose interests overlap with nuclear instrumentation.

Another publication currently in press was prepared by a team working on geological prospecting equipment and mining equipment. This material is of immense value, and it is perfectly obvious that it will be needed in rapid determinations of simple and generally familiar ways of supplying ores; it is bound to aid the work of geological prospecting, by simplifying the work of raw materials reserves estimates. Publication of this document will also be of great benefit to newly constituted governments entering the field of geological prospecting work for the first time, and also to industrially developed states interested in increasing their raw materials resources.

Finally, subcommittee 45A on nuclear reactor equipment has come forth with two documents on its own: one on the basic principles of nuclear reactor instrument design and one dealing with electronic measuring equipment for control, monitoring, and scramming of reactors. These documents will be published by CEI after the usual procedure of soliciting responses and comments from the national committees.

These two documents requiring parallel work open the road for future unitization of reactor instruments, a prerequisite for further progress when we consider the great variety and proliferation of instrument types in use or in the development stage.

Taking these tangible results into account, we note that several documents which will take on the status of recommendations of a general character (dosimetry, interchangeability) or a special character (characteristics of equipment) are to be drawn up both at international conferences and as a result of exchanges of information between experts.

Miscellaneous

TC-50 on climatic and mechanical tests

International organization on official metrology

TC-39 on electronic tubes

International standardization organization

TC-13 on measuring equipment

International Commission on Radiological Units

TC-1 on terminology and definitions

International Atomic Energy Agency

Related within CEI		External connections

CEI Technical Committee 45

Work teams dealing with general problems	Subcommittee 45 A	Work teams dealing with special questions

Work team 1	Work team 1A	Work team 5

Work team 2	Work team 2A	Work team 6

Work team 7		Work team 8

Work team 3

Work team 9

Organizational Branch Chart of CEI TC-45.

This summary of CEI activities of course presents an encouraging picture. But when we consider the problem of the number of experts available, we realize that great benefits could accrue from further increases in the number of our experts, as well as in the number of nations interested in the effective work of Technical Committee 45.

It is interesting to reflect on this point, even overshadowing in importance the problem of increasing the number of specialists working on the various teams, that all countries would do well to show interest in the work of one or another team to the extent that their degree of development in the field of nuclear industry permits. Every single country could assign some experts, with no loss to itself, and thereby manifest its active interest in the over-all problem now being handled dynamically and enthusiastically by the CEI TC-45 specialists, who are inspired by the perspectives opening up.

850

PARTICIPATION OF THE USSR IN THE CEI
TECHNICAL COMMITTEE 45

N. M. Kitaev and V. V. Matveev

A delegation of USSR specialists began its participation in the work of TC-45 in September 1964 at Geneva. In addition to the USSR delegation, another ten countries participated in these sessions: Great Britain, Hungary, Italy, the Netherlands, Poland, USA, France, West Germany, Switzerland, Sweden. The participation of USSR representatives in the work of TC-45 was cordially welcomed by representations of the other nations now engaged in TC-45 activities.

Reports and projects of the work teams and subcommittee were discussed as part of the TC-45 program, as were documents prepared by the teams for publication or for formulation as CEI recommendations.

USSR representatives proposed as a basic criterion (approved by member-nations of the COMECON) for classification of nuclear instruments using the physical magnitude the instrument is designed to measure. This calls for subdividing instruments into such classes as: 1) instruments for measurement of ionizing radiations; 2) instruments utilizing ionizing radiations to measure other physical and chemical variables; 3) radio electronic units and devices in nuclear electronics, and other devices used to record ionizing radiations. Principles for further division of the instruments into subclasses were formulated in the proposals, and concrete classification of some lines of instruments was presented as an illustrative example. The basic principle underlying systematization of equipment in the CEI publication 181 groups of equipment into categories on the basis of the instrument function: 1) basic equipment for measuring radiation; 2) special devices for nuclear reactor monitoring and safety; 3) special health physics instrumentation; 4) special prospecting and mining instruments; 5) devices utilizing ionizing radiation sources. It was voted to place a detailed discussion of the Soviet proposals on the agenda of the next meeting.

Unitization of the maximum diameters of cylindrical gas-discharge and scintillation radiation detectors was discussed at the meeting of work team 3. The USSR delegation presented proposals on a preferred sequence of dimensions. These proposals, based on COMECON recommendations adopted earlier, were included in their entirety (and with one standard dimension added to the list) to the draft recommendations of CEI.

In the discussion on unitization of dimensions of electronic circuitry and equipment using semiconductors, the USSR delegation supported suggestions by Polish specialists to introduce a system of standard dimensions, a system which has been discussed and adopted by several COMECON commissions.

A Soviet TC-45 team has been set up within the framework of the State Committee of the USSR on the Uses of Atomic Energy [GKIAE SSSR] to facilitate active participation in CEI TC-45 activities, and the specialists assigned to this Soviet team have the task of familiarizing themselves systematically with the materials assembled by the TC-45 and its various teams, to prepare recommendations for joint discussion, and to popularize the CEI recommendations for widespread implementation in industry. The Soviet team will tie in its activities with those of counterpart COMECON teams and with other Soviet CEI and Standardization Committee groupings.

SOVIET JOURNALS AVAILABLE IN COVER-TO-COVER TRANSLATION

This list includes all Russian journals which—to the publisher's knowledge—were available in cover-to-cover translation on June 30, 1965, or for which definite and immediate plans for cover-to-cover translation had been announced by that date. The list reflects only *current* publication arrangements, but the date and issue listed for first publication refer to translations available from any source. Thus, earlier volumes of a translation journal may have been published by an organization other than that listed as the current publisher, and possibly under a different title (and, for *Doklady Akademii Nauk SSSR*, in a different arrangement of sections).

Five bits of information are furnished, separated by bullets:

1. The abbreviation(s) by which the journals are most frequently referred to in Russian bibliographies (if the name of the journal is customarily spelled out, no abbreviation is given).
2. The transliterated full name of the journal.
3. The full name of the translation journal (in bold type).
4. The year, volume (in parentheses), and issue of first publication of the translation (parentheses are empty if the Russian journal does not use volume numbers).
5. The current publisher of the translation [AGI—American Geological Institute, AGU—American Geophysical Union, AIP— American Institute of Physics, CB—Consultants Bureau, CH—Clearing House for Federal Scientific and Technical Information, CS—The Chemical Society (London), FP—Faraday Press, IEEE— Institute of Electrical and Electronic Engineers, ISA —Instrument Society of America, PP—Pergamon Press].

For convenience in locating bibliographic references the journals are listed in alphabetical order of the *abbreviated* titles.

AÉ • Atomnaya énergiya • **Soviet Journal of Atomic Energy** • 1956(1)1 • CB

Akust. zh. • Akusticheskii zhurnal • **Soviet Physics—Acoustics** • 1955(1)1 • AIP

Astrofiz. • Astrofizika • **Astrophysics** • 1965(1)1 • FP

Astr(on). zh(urn). • Astronomicheskii zhurnal • **Soviet Astronomy—AJ** • 1957(34)1 • AIP

Avtomat. i telemekh. • Avtomatika i telemekhanika • **Automation and Remote Control** • 1956(27)1 • ISA

Avto(mat). svarka • Avtomaticheskaya svarka • **Automatic Welding** • 1959(12)1 • British Welding Research Association

Avtometriya • **Autometry** • 1965(1)1 • CB

Biokhim. • Biokhimiya • **Biochemistry** • 1956(21)1 • CB

Byul. éksp(erim). biol. (i med.) • Byulleten' éksperimental'noi biologii i meditsiny • **Bulletin of Experimental Biology and Medicine** • 1959(41)1 • CB

DAN (SSSR) • *see* Doklady AN SSSR

Defektoskopiya • **Soviet Defectoscopy** • 1965(1)1 • CB

Diff. urav. • Differentsial'nye uravneniya • **Differential Equations** • 1965(1)1 • FP

Dokl(ady) AN SSSR; DAN (SSSR) • Doklady Akademii Nauk SSSR • The translation of Doklady is published in various journals, according to subject matter. The sections of Doklady contained in each of the translation journals are listed in parentheses.

Doklady Biochemistry (biochemistry) • 1957(112)1 • CB

Doklady Biological Sciences Sections (anatomy, cytology, ecology, embryology, endocrinology, evolutionary morphology, parasitology, physiology, zoology) • 1957(112)1 • CB

Doklady Biophysics (biophysics) • 1957(112)1 • CB

Doklady Botany (botany, phytopathology, plant anatomy, plant ecology, plant embryology, plant physiology, plant morphology) • 1957(112)1 • CB

Doklady Chemical Technology (chemical technology) • 1956(106)1 • CB

Doklady Chemistry (chemistry) • 1956(106)1 • CB

Doklady Earth Sciences Sections (geochemistry, geology, geophysics, hydrogeology, lithology, mineralogy, paleontology, permafrost, petrography) • 1959(124)1 • AGI

Doklady Physical Chemistry (physical chemistry) • 1957(112)1 • CB

Doklady Soil Science (soil science) • 1964(154)1 • Soil Science Society of America

Soviet Mathematics—Doklady (mathematics) • 1960(130)1 • American Mathematical Society

Soviet Oceanography (oceanology) • 1959(124)1 • AGU

Soviet Physics—Doklady (aerodynamics, astronomy, crystallography, cybernetics and control theory, electrical engineering, energetics, fluid mechanics, heat engineering, hydraulics, mathematical physics, mechanics, physics, technical physics, theory of elasticity • 1956(106)1 • AIP

Élektrokhimiya • **Soviet Electrochemistry** • 1965(1)1 • CB

Élektrosvyaz' • combined with Radiotekhnika in **Telecommunications and Radio Engineering** • 1957(16)1 • IEEE

Élektrotekh. • Élektrotekhnika • **Soviet Electrical Engineering** • 1965 (36)1 • FP

Éntom(ol). oboz(r). • Éntomologicheskoe obozrenie • **Entomological Review** • 1958(37)1 • Entomological Society of America

Fiz. goreniya i vzryva • Fizika goreniya i vzryva • **Combustion, Explosion, and Shock Waves** • 1965(1) • FP

Fiziol(ogiya) rast. • Fiziologiya rastenii • **Soviet Plant Physiology** • 1957(4)1 • CB

Fiz.-khim. mekh(anika) mater(ialov); FKhMM • Fizikokhimicheskaya mekhanika materialov • **Soviet Materials Science** • 1965(1)1 • FP

Fiz. met. i metallov.; FMM • Fizika metallov i metallovedenie • **Physics of Metals and Metallography** • 1957(5)1 • Acta Metallurgica

Fiz.-tekhn. probl. razr. polezn. iskopaem. • Fizikotekhnicheskie problemy razrabotki poleznykh iskopaemykh • **Soviet Mining Science** • 1965(1)1 • CB

Fiz. tv(erd). tela; FTT • Fizika tverdogo tela • **Soviet Physics—Solid State** • 1959(1)1 • AIP

FKhMM • *see* Fiz.-khim. mekhanika materialov

FMM • *see* Fiz. met. i metallov.

FTT • *see* Fiz. tverd. tela

Geliotekh. • Geliotekhnika • **Applied Solar Energy** • 1965(1)1 • FP

Geol. nefti i gaza • Geologiya nefti i gaza • **Petroleum Geology** • 1958 (2)1 • Petroleum Geology, Box 171, McLean, Va.

Geomagnet. i aéronom. • Geomagnetizm i aéronomiya • **Geomagnetism and Aeronomy** • 1961(1)1 • AGU

Inzh.-fiz. zh. • Inzhenerno-fizicheskii zhurnal • **Journal of Engineering Physics** • 1965(8)1 • FP

Inzh. zh. • Inzhenernyi zhurnal • **Soviet Engineering Journal** • 1965(5)1 • FP

Iskusstv. sputniki Zemli • Iskusstvennye sputniki Zemli • **Artificial Earth Satellites** • 1958(1)1 • CB [superseded by Kosmich. issled.]

Izmerit. tekhn(ika) • Izmeritel'naya tekhnika • **Measurement Techniques** • 1958(7)1 • ISA

Izv. AN SSSR, o(td.) kh(im.) n(auk) (*or* ser. khim.) • Izvestiya Akademii Nauk SSSR: Otdelenie khimicheskikh nauk (*or* Seriya khimicheskaya) • **Bulletin of the Academy of Sciences of the USSR: Division of Chemical Science** • 1952(16)1 • CB

Izv. AN SSSR, ser. fiz(ich). • Izvestiya Akademii Nauk SSSR: Seriya fizicheskaya • **Bulletin of the Academy of Sciences of the USSR: Physical Series** • 1954(18)3 • Columbia Technical Translations

Izv. AN SSSR, ser. fiz. atm. i okeana • Izvestiya Akademii Nauk SSSR: Seriya fiziki atmosfery i okeana • **Izvestiya, Atmospheric and Oceanic Physics** • 1965( )1 • AGU

Izv. AN SSSR, ser. fiz. zemli • Izvestiya Akademii Nauk SSSR: Seriya fiziki zemli • **Izvestiya, Physics of the Solid Earth** • 1965( )1 • AGU

Izv. AN SSSR, ser. geofiz. • Izvestiya Akademii Nauk SSSR: Seriya geofizicheskaya • **Bulletin of the Academy of Sciences of the USSR: Geophysics Series** • 1957(7)1 • AGU [superseded by Izv. AN SSSR, ser. fiz. atm. i okeana and Izv. AN SSSR, ser. fiz. zemli]

Izv. AN SSSR, ser. geol. • Izvestiya Akademii Nauk SSSR: Seriya geologicheskaya • **Bulletin of the Academy of Sciences of the USSR: Geologic Series** • 1958(23)1 • AGI

Izv. AN SSSR, ser. neorgan. mat(er). • Izvestiya Akademii Nauk SSSR: Seriya neorganicheskie materialy • **Inorganic Materials** • 1965(1) 1 • CB

Izv. AN SSSR, tekhn. kiber(netika) • Izvestiya Akademii Nauk SSSR: Tekhnicheskaya kibernetika • **Engineering Cybernetics** • 1963(1)1 • IEEE

Izv. v(yssh.) u(ch.) z(av.) aviats. tekh. • Izvestiya vysshikh uchebnykh zavedenii. Aviatsionnaya tekhnika • **Aviation Engineering** • 1963(6)1 • CH

Izv. v(yssh.) u(ch.) z(av.) fiz. • Izvestiya vysshikh uchebnykh zavedenii. Fizika • **Soviet Physics Journal** • 1965(8)1 • FP

Izv. v(yssh.) u(ch.) z(av.) geodez. i aérofot. • Izvestiya vysshikh uchebnykh zavedenii. Geodeziya i aérofotos''emka • **Geodesy and Aerophotography** • 1959(4)1 • AGU

Izv. v(yssh.) u(ch.) z(av.) priborostr. • Izvestiya vysshikh uchebnykh zavedenii. Priborostroenie • **Izvestiya VUZOV. Instrument Building** • 1962(5)1 • CH

Izv. v(yssh.) u(ch.) z(av.) radiofiz. • Izvestiya vysshikh uchebnykh zavedenii. Radiofizika • **Izvestiya VUZOV. Radiophysics** • 1958(1)1 • CH

Izv. v(yssh.) u(ch.) z(av.) radiotekhn(ika) • Izvestiya vysshikh uchebnykh zavedenii. Radiotekhnika • **Izvestiya VUZOV. Radio Engineering** • 1959(2)1 • CH

Izv. v(yssh.) u(ch.) z(av.) tekh. teks. prom. • Izvestiya vysshikh uchebnykh zavedenii. Tekhnologiya tekstilnoi promyshlennosti • **Technology of the Textile Industry, USSR** • 1960(4)1 • The Textile Institute (Manchester)

Kauch. i rez. • Kauchuk i rezina • **Soviet Rubber Technology** • 1959 (18)3 • Maclaren and Sons Ltd.

Khim. getero(tsik). soed. • Khimiya geterotsiklicheskikh soedinenii • **Chemistry of Heterocyclic Compounds** • 1965(1)1 • FP

Khim. i neft. mash(inostr). • Khimicheskoe i neftyanoe mashinostroenie • **Chemical and Petroleum Engineering** • 1965( )1 • CB

Khim. i tekhnol. topliv i masel • Khimiya i tekhnologiya topliv i masel • **Chemistry and Technology of Fuels and Oils** • 1965( )1 • CB

Khim. prirod. soed. • Khimiya prirodnykh soedinenii • **Chemistry of Natural Compounds** • 1965(1)1 • FP

Kib. • Kibernetika • **Cybernetics** • 1965(1)1 • FP

Kinet. i katal. • Kinetika i kataliz • **Kinetics and Catalysis** • 1960(1)1 • CB

Koks i khim. • Koks i khimiya • **Coke and Chemistry, USSR** • 1959( )8 • Coal Tar Research Assn. (Leeds, England)

Kolloidn. zh(urn). • Kolloidnyi zhurnal • **Colloid Journal** • 1952(14)1 • CB

Kosmich. issled. • Kosmicheskie issledovaniya • **Cosmic Research** • 1963(1)1 • CB

Kristallog. • Kristallografiya • **Soviet Physics—Crystallography** • 1957 (2)1 • AIP

Liteinoe proiz(-vo). • Liteinoe proizvodstvo • **Russian Castings Production** • 1961(12)1 • British Cast Iron Research Association

Mag. gidrodin. • Magnitnaya gidrodinamika • **Magnetohydrodynamics** • 1965(1)1 • FP

Mekh. polim. • Mekhnika polimerov • **Polymer Mechanics** • 1965(1)1 • FP

Metalloved. i term. obrabotka metal.; MiTOM • Metallovedenie i termicheskaya obrabotka metallov • **Metal Science and Heat Treatment** • 1958(6)1 • CB

Metallurg • **Metallurgist** • 1957( )1 • CB

Mikrobiol. • Mikrobiologiya • **Microbiology** • 1957(26)1 • CB

MiTOM • *see* Metalloved. i term. obrabotka metal.

Ogneupory • **Refractories** • 1960(25)1 • CB

Opt. i spektr.; OS • Optika i spektroskopiya • **Optics and Spectroscopy** • 1959(6)1 • AIP

Osnovan. fund. i mekh. gruntov • Osnovaniya fundamenty i mekhanika gruntov • **Soil Mechanics and Foundation Engineering** • 1964 ( )1 • CB

Paleon. zh(urn). • Paleontologicheskii zhurnal • **Journal of Paleontology** • 1962( )1 • AGI

Plast. massy • Plasticheskie massy • **Soviet Plastics** • 1960(8)7 • Rubber and Technical Press, Ltd.

PMM • *see* Prikl. matem. i mekhàn.

PMTF • *see* Zhur. prikl. mekhan. i tekhn. fiz.

Pochvovedenie • **Soviet Soil Science** • 1958(53)1 • Soil Science Society of America

Poroshk. met. • Poroshkovaya metallurgiya • **Soviet Powder Metallurgy and Metal Ceramics** • 1962(2)1 • CB

Priborostroenie • **Instrument Construction** • 1959(4)1 • Taylor and Francis, Ltd.

Pribory i tekhn. éksp(erimenta); PTÉ • Pribory i tekhnika éksperimenta • **Instruments and Experimental Techniques** • 1958(3)1 • ISA

Prikl. biokhim. i mikrobiol. • Prikladnaya biokhimiya i mikrobiologiya • **Applied Biochemistry and Microbiology** • 1965(1)1 • FP

Prikl. matem. i mekh(an).; PMM • Prikladnaya matematika i mekhanika • **Applied Mathematics and Mechanics** • 1958(22)1 • PP

Probl. pered. inform. • Problemy peredachi informatsii • **Problems of Information Transmission** • 1965(1)1 • FP

Probl. severa • Problemy severa • **Problems of the North** • 1958( )1 • National Research Council of Canada

PTÉ • *see* Pribory i tekhn. éksperimenta

Radiokhim. • Radiokhimiya • **Soviet Radiochemistry** • 1962(4)1 • CB

Radiotekh. • Radiotekhnika • combined with Élektrosvyaz' in **Telecommunications and Radio Engineering** • 1961(16)1 • IEEE

Radiotekhn. i élektron(ika) • Radiotekhnika i élektronika • **Radio Engineering and Electronic Physics** • 1961(6)1 • IEEE

Stal' • **Stal' in English** • 1959(19)1 • The Iron and Steel Institute

Stanki i instr. • Stanki i instrument • **Machines and Tooling** • 1959 (30)1 • Production Engineering Research Association

Stek. i keram. • Steklo i keramika • **Glass and Ceramics** • 1956(13)1 • CB

Svaroch. proiz(-vo). • Svarochnoe proizvodstvo • **Welding Production** • 1959(5)4 • British Welding Research Association (London)

Teor. i éksperim. khim. • Teoreticheskaya i éksperimental'naya khimiya • **Theoretical and Experimental Chemistry** • 1965(1)1 • FP

Teor. veroyat. i prim. • Teoriya veroyatnostei i ee primenenie • **Theory of Probability and Its Application** • 1956(1)1 • Society for Industrial and Applied Mathematics

Teploénergetika • **Thermal Engineering** • 1964(11)1 • PP

Teplofiz. vys(ok). temp. • Teplofizika vysokikh temperatur • **High Temperature** • 1963(1)1 • CB

Tsvet. metally • Tsvetnye metally • **The Soviet Journal of Nonferrous Metals** • 1960(33)1 • Primary Sources

Usp. fiz. nauk;. UFN • Uspekhi fizicheskikh nauk • **Soviet Physics—Uspekhi** • 1958(66)1 • AIP

Usp. khim.; UKh • Uspekhi khimii • **Russian Chemical Reviews** • 1960(29)1 • CS

Usp. mat. nauk; UMN • Uspekhi matematicheskaya nauk • **Russian Mathematical Surveys** • 1960(15)1 • Cleaver-Hume Press, Ltd.

Vest. Akad. med. nauk SSSR • Vestnik Akademii meditsinskikh nauk SSSR • **Vestnik of USSR Academy of Medical Sciences** • 1962(17)1 • CH

Vest. mashinostroeniya • Vestnik mashinostroeniya • **Russian Engineering Journal** • 1959(39)4 • Production Engineering Research Association

Vest. svyazi • Vestnik svyazi • **Herald of Communications** • 1954(14)1 • CH

Vysoko(molek). soed(ineniya) • Vysokomolekulyarnye soedineniya (SSSR) • **Polymer Science (USSR)** • 1959(1)1 • PP

Yadernaya fizika • **Soviet Journal of Nuclear Physics** • 1965(1)1 • AIP

Zashch(ita) met(allov) • Zashchita metallov • **Protection of Metals** • 1965(1)1 • CB

Zav(odsk). lab(oratoriya); ZL • Zavodskaya laboratoriya • **Industrial Laboratory** • 1958(24)1 • ISA

ZhÉTF pis'ma redaktsiyu • **JETP Letters** • 1965(1)1 • AIP

Zh(ur). anal(it). khim(ii); ZhAKh • Zhurnal analiticheskoi khimii • **Journal of Analytical Chemistry** • 1952(7)1 • CB

Zh(ur). éks(perim). i teor. fiz.; ZhÉTF • Zhurnal éksperimental'noi i teoreticheskoi fiziki • **Soviet Physics—JETP** • 1955(28)1 • AIP

Zh(ur). fiz. khim(ii); ZhFKh • Zhurnal fizicheskoi khimii • **Russian Journal of Physical Chemistry** • 1959(33)7 • CS

Zh(ur). neorg(an). khim.; ZhNKh • Zhurnal neorganicheskoi khimii • **Russian Journal of Inorganic Chemistry** • 1959(4)1 • CS

Zh(ur). obshch. khim.; ZhOKh • Zhurnal obshchei khimii • **Journal of General Chemistry of the USSR** • 1949(19)1 • CB

Zh(ur). org. khim.; ZhOrKh(im) • Zhurnal organicheskoi khimii • **Journal of Organic Chemistry of the USSR** • 1965(1)1 • CB

Zh(ur). prikl. khim.; ZhPKh • Zhurnal prikladnoi khimii • **Journal of Applied Chemistry of the USSR** • 1950(23)1 • CB

Zh(ur). prikl. mekhan. i tekhn. fiz. • Zhurnal prikladnoi mekhaniki i tekhnicheskoi fiziki • **Journal of Applied Mechanics and Technical Physics** • 1965( )1 • FP

Zh(ur). prikl. spektr. • Zhurnal prikladnoi spektroskopii • **Journal of Applied Spectroscopy** • 1965(2)1 • FP

Zh(ur). strukt(urnoi) khim.; ZhSKh • Zhurnal strukturnoi khimii • **Journal of Structural Chemistry** • 1960(1)1 • CB

Zh(ur). tekhn. fiz.; ZhTF • Zhurnal tekhnicheskoi fiziki • **Soviet Physics —Technical Physics** • 1956(26)1 • AIP

Zh(ur). vses. khim. ob-va im. Mendeleeva • Zhurnal vsesoyuznogo khimicheskogo obshchestva im. Mendeleeva • **Mendeleev Chemistry Journal** • 1965(10)1 • FP

Zh(ur). vychis. mat. i mat. fiz. • Zhurnal vychislitel'noi matematika i matematicheskoi fiziki • **USSR Computational Mathematics and Mathematical Physics** • 1962(1)1 • PP

ZL • *see* Zavodsk. laboratoriya

SIGNIFICANCE OF ABBREVIATIONS MOST FREQUENTLY
ENCOUNTERED IN SOVIET PERIODICALS

FIAN	Phys. Inst. Acad. Sci. USSR.
GDI	Water Power Inst.
GITI	State Sci.-Tech. Press
GITTL	State Tech. and Theor. Lit. Press
GONTI	State United Sci.-Tech. Press
Gosenergoizdat	State Power Press
Goskhimizdat	State Chem. Press
GOST	All-Union State Standard
GTTI	State Tech. and Theor. Lit. Press
IL	Foreign Lit. Press
ISN (Izd. Sov. Nauk)	Soviet Science Press
Izd. AN SSSR	Acad. Sci. USSR Press
Izd. MGU	Moscow State Univ. Press
LEIIZhT	Leningrad Power Inst. of Railroad Engineering
LET	Leningrad Elec. Engr. School
LETI	Leningrad Electrotechnical Inst.
LETIIZhT	Leningrad Electrical Engineering Research Inst. of Railroad Engr.
Mashgiz	State Sci.-Tech. Press for Machine Construction Lit.
MEP	Ministry of Electrical Industry
MES	Ministry of Electrical Power Plants
MESEP	Ministry of Electrical Power Plants and the Electrical Industry
MGU	Moscow State Univ.
MKhTI	Moscow Inst. Chem. Tech.
MOPI	Moscow Regional Pedagogical Inst.
MSP	Ministry of Industrial Construction
NI ZVUKSZAPIOI	Scientific Research Inst. of Sound Recording
NIKFI	Sci. Inst. of Modern Motion Picture Photography
ONTI	United Sci.-Tech. Press
OTI	Division of Technical Information
OTN	Div. Tech. Sci.
Stroiizdat	Construction Press
TOE	Association of Power Engineers
TsKTI	Central Research Inst. for Boilers and Turbines
TsNIEL	Central Scientific Research Elec. Engr. Lab.
TsNIEL-MES	Central Scientific Research Elec. Engr. Lab.-Ministry of Electric Power Plants
TsVTI	Central Office of Economic Information
UF	Ural Branch
VIESKh	All-Union Inst. of Rural Elec. Power Stations
VNIIM	All-Union Scientific Research Inst. of Metrology
VNIIZhDT	All-Union Scientific Research Inst. of Railroad Engineering
VTI	All-Union Thermotech. Inst.
VZEI	All-Union Power Correspondence Inst.

Note: Abbreviations not on this list and not explained in the translation have been transliterated, no further information about their significance being available to us. — Publisher.

NUCLEAR SCIENCE

MÖSSBAUER EFFECT METHODOLOGY
Volume 1
Erwin J. Gruverman, Editor
Proceedings of the First Symposium on Mössbauer Effect Methodology, held in New York City on January 26, 1965

The editor, a well-known and prolific writer in the Mössbauer field, briefly reviews applications, then clearly and accurately discusses the previously inaccessible methodology of Mössbauer-effect studies.

Because the book carefully examines the complexities of required equipment for velocity modulation, measurements of effects, and modification of external environments, the reader can find information not only for evaluating the potential of Mössbauer-effect studies, but also for estimating the merits of alternative means of applying the techniques. The comprehensive reviews by Herber and Spijkerman describe new techniques for absolute standardization of isomer shifts, using sodium nitroprusside standard absorbers. This will make possible adoption of a standard to eliminate the now-prevalent confusion in comparing work performed at different laboratories.

Chemical-process industrialists, physicists, biologists, chemists, and educators working in the Mössbauer field should find this book of immeasurable help. For example, it will aid readers in selecting a transducer system, building it, or writing specifications for its purchase; in assessing the merits of the Mössbauer technique; and in constructing and specifying measurements, calibration and environmental control systems. The excellent coverage of research and problems in this methodology includes nine carefully labeled diagrams of the apparatus and five pertinent graphs, together with legend.

CONTENTS: Mössbauer spectroscopy: some recent applications to chemical problems, Rolfe H. Herber • Review of advances in physics, S. L. Ruby • Application of the Mössbauer effect to biological systems, U. Gonser and R. W. Grant • Feedback in electrochemical drive systems, E. Kankeleit • Cam driven, constant acceleration Mössbauer spectrometer, Alan J. Bearden, M. G. Hauser, and P. L. Mattern • Constant velocity Mössbauer drive system, P. Flinn • Measurements by scattering techniques—I, J. K. Major • Measurements by scattering techniques—II, P. Debrunner • f measurement with black absorbers, J. G. Dash • Standardization of the differential chemical shift for Fe^{57}, J. J. Spijkerman, F. C. Ruegg, and J. R. DeVoe • Computation of Mössbauer spectra, J. R. Gabriel • Superconducting magnets — applications to the Mössbauer effect, Paul P. Craig • Mössbauer techniques using high field water-cooled solenoids, Norman A. Blum • Low temperature cryostats for Mössbauer experiments, Michael Kalvius • High pressure techniques, R. Ingalls.

200 pages   PP 1965 $12.50

THEORY AND METHODS OF NUCLEAR REACTOR CALCULATIONS
G. I. Marchuk, Editor

Six of the 18 papers in the collection are concerned with transport theory. The first two papers (by Marchuk et al.) deal with the properties and application of even-order P_n approximations, applying the difference equation factorization method. These papers consider the distribution of neutrons from a point source; it is shown that the techniques of renormalization, extrapolation and over-relaxation applied to S_n equations accelerate pointwise convergence. Three fundamental papers on resonance absorption are concerned with improving the treatment of deviations from the basic narrow resonance formulas, including computation of the departure of the collision density from the narrow-resonance shape. The paper (Shikhov and Abagyan) on a method for constructing multigroup constants in the resonance region, taking heterogeneous effects into account, has fundamental interest to engineering physicists. Three papers report original work on fast neutron cross sections, and six are concerned with reactor calculation methods. The papers in the collection employ unified methods of analysis based on a strict mathematical approach, with subsequent application of the results to concrete practical solutions. A Special Research Report translated from Russian.

208 pages   CB 1964 $40.00

EFFECTS OF RADIATION ON SEMICONDUCTORS
By V. S. Vavilov

Devoted to the effects of electromagnetic and corpuscular radiations on semiconductors, this new volume deals with the processes of absorption of electromagnetic radiation, photoionization and ionization by charged high-energy particles and the principal types of recombination processes by which an excited crystal returns to its original equilibrium state. Translated from Russian.

CONTENTS: Absorption of light by semiconductors • Photoionization and photoconductivity in semiconductors • Ionization of semiconductors by charged high-energy particles • Radiative recombination in semiconductors; possibility of the amplification and generation of light using semiconductors • Changes in the properties of semiconductors due to bombardment with fast electrons, gamma rays, neutrons, and heavy charged particles • Literature cited • Index.

238 pages   CB 1965 $15.00